Steinar Kristoffersen

Improved Fatigue Performance of Threaded Drillstring Connections by Cold Rolling

Dr.ing. thesis

Department of Structural Engineering
Norwegian University of Scenic and Technology
N-7491 Trondheim

January 2002

URN:NBN:no-2334

URN:NBN:no-2334

Abstract

The research work presented in this thesis is concerned with analytical, numerical and experimental studies of the effect of cold rolling on the fatigue behaviour of threaded drillstring connections.

A comprehensive literature study is made of the various effects on the fatigue behaviour of residual stresses introduced by mechanical deformation of notched components. Some of the effects studied are cyclic hardening behaviour after prestraining, cyclic creep, fatigue initiation in prestrained materials, short cracks and crack growth models including crack closure.

Residual stresses were introduced in the surface of a smooth pipe by a rolling device to simulate a cold rolling process and verify the calculated residual stresses by measurements. Strain hardening and contact algorithm of the two bodies were incorporated in the FE analyses. Two significant errors were found in the commercial software package for residual stress evaluation, Restran v. 3.3.2a also called SINT, when using the Schajer method. The Schajer algorithm is the only hole-drilling algorithm without theoretical shortcomings, and is recommended when measuring large residual stress gradients in the depth direction. Using the Schajer method solved by in-house Matlab-routines good agreement between measured residual stress gradients and residual stress gradients from FE analyses was found.

Full scale fatigue tests were performed on pipes cut from used drillstrings with notches of similar geometry as threads used in drillstring connections. The simulated threads consisted of four full depth helix notches with runouts at the surface. The pipe threads were cold rolled and fatigue tested in a full-scale four-point rotating bending fatigue testing rig. The test results showed that cold rolling had an effect on the crack initiation period. A major part of the fatigue life was with cracks observed at the notch root, but due to the increased fatigue crack propagation resistance the final fracture initiated at pits inside the pipe. Therefore, an optimisation of the roll geometry and rolling parameters was not possible. However, a significant fatigue life improvement was achieved. Based on experiments, a roller with similar profile as the thread root is recommended. A rolling force of maximum 20 kN is recommended to minimise the possibility of damaging the thread profile. Shallow cracks were observed typically when 5% of the fatigue life had expired. Re-rolling after 50% of expected improved fatigue life, when also short cracks were observed in the notch roots further increased the fatigue improvement.

Pretensioned small steel specimens with a notch were used to simulate cold rolled threads. The specimens were fatigue tested in tension with minimum load close to zero. Pretensioning increased the fatigue life from approximately 50 000 cycles to an infinite number of cycles. In these tests non-

URN:NBN:no-2334

propagating cracks of typically 0.4 mm length were found. The benefit from pretensioning gradually disappeared with increasing mean stress. FE analyses indicated that an almost instant relaxation of residual stresses to a level with no monotonic strain hardening from preloading would take place when cycled at moderate mean stress. Cycled at low mean stress, an instant relaxation of the surface layer was found in analysis. All observations from notched pretensioned fatigue specimens were in good agreement with the available literature. However, preloading was found to be strain rate dependent in tests where a pretension load held for 2 minutes gave a longer fatigue life than a sinusoidal loading-unloading cycle performed over a one minute interval.

Strain hardening was found not contributing to the fatigue life improvement, whereas the polishing effect from improved surface quality after cold rolling increased the fatigue initiation period. However, residual stress and subsequent early crack closure was the dominating effect at moderate cyclic mean loads.

The material data required to perform FE fatigue simulation studies of a full threaded cold rolled coupling incorporating make-up torque, include cyclic stress strain behaviour at various amplitudes and mean stress caused by various degrees of prestraining. Such data are not readily available today, and are only possible to obtain in carefully planned and executed experiments. Also, 3D FE model required for cold rolling analysis is extremely CPU time consuming. Consequently, cold rolling simulations could not be successfully implemented in this work.

One of the main conclusions from this work is that drillstring connections will respond differently to thread rolling at the pin or box. A significant improvement in the fatigue life of box threads from residual stresses is expected mainly from increased resistance to crack propagation. However, the compressive residual stress is sensitive to overloading in compression, and the improvement from residual stress depends strongly on the mean stress (or R-ratio). At values of R of approximately 0.6 or higher the beneficial of rolling therefore tends to disappear. At the critical locations of the pin, which are the last engaged thread or the stress relief groove, the effect of residual stresses introduced by rolling is therefore likely to be severely reduced by the high mean stress imposed during make-up of the connection. However, a beneficial effect of rolling is expected to remain due to the improved surface condition, and due to a possible effect of strain hardening. The net results of these factors on the fatigue performance of actual drillstrings can only be determined in full scale rotating bending tests.

Acknowledgements

I would like to express my gratitude to my supervisor Professor Per J. Haagensen, Department of Structural Engineering, for his initiation and supervision of this study. His valuable advice is greatly acknowledged as are several proposals for improvements to the original manuscript.

The experimental work has been carried out in the laboratories of the Department of Structural Engineering. The assistance, hard work and interest of all the laboratory staff is very much appreciated. In particular I would like to thank Mr. Hans Tømmervold and Mr. Ole Aunrønning for their help replacing the full scale fatigue test specimens.

I also acknowledge the fruitful and instructive collaboration with Mr. Kjell Müller at the Department of Machine Design and Materials Technology, and all help in the last phase of the project from Dr. Ken Macdonald.

This research was made possible by a scholarship from Statoil and The Research Council of Norway. The interest and support from Mr. Terje Grøttum, Statoil, was much appreciated.

Donations of used drillstring elements by Independent Oil Tools, Stavanger, and the cutting and thread profiling done at Gefro, Stavanger, at reduced costs are very much appreciated. Also, all the help from Karsten Moholt AS in Bergen making the full scale four-point bending rig is acknowledged.

I would also like to thank: Professor Jussi for physical and social training; my father Kåre for all his support and encouragement during this period, particularly in the later months; my sister Elisabeth for the dinners where I invited myself, and her great care; and the rest of my family and in-laws for the positive and excellent private environment.

Most of all, I would like to thank my wife Vigdis for all her patience and understanding on the occasions where I spent most of the time at the University and the remainder with a physical presence at home, but with my thoughts still at work.

URN:NBN:no-2334

Table of contents

1 General introduction

1.1 Notation

AHD	along-hole depth
BEM	boundary element method
BHA	bottom hole assembly
FEM	finite element method
HSLA	high strength low alloy
LET	last engaged thread
MWD	measurement-while-drilling
ROP	rate of penetration
SCC	stress corrosion cracking
SRG	stress relief groove
TOB	torque on bit
TVD	true vertical depth
WOB	weight on bit

1.2 Motivation for this thesis

Offshore oil field drilling operations are extremely costly, and a drillstring failure will have severe economic consequences. A typical day-rate for drilling operations on a fixed production installation is of the order of $100,000 and about twice as much if performed on a floating deep-water exploration drilling rig. A drillstring downhole failure, defined as complete separation of the drillstring or the bottom hole assembly (BHA), may necessitate the drilling of a new hole parallel to the section filled with the abandoned drillstring where the remaining drillstring cannot successfully be fished out. Such an operation will typically take from two or three up to 12 days. The cost for replacing lost equipment is typically of the order of one million dollars.

1.3 Introduction to oil field drilling

The oil well is made by a rock cutting tool called the drill bit, supported from the surface through the drillstring. Drilling fluid called mud is pumped inside the drillstring with a specified density to ensure a slightly higher hydrostatic pressure in the well compared to the fluid pressure in the formation being drilled. The mud pressure must be sufficient to prevent an uncontrolled intrusion of hydrocarbons into the well, which can lead to an extremely dangerous situation called blow-out, where hydrocarbons (mix of oil and gas) flow uncontrolled through the bore-hole all the way up to the surface. If the hydrostatic pressure is too high, fracturing of the formation may occur, allowing the mud to escape, leading to loss of mud and possibly loss of control of the operation. During drilling mud flows back in the annulus between the drillpipe and the borehole wall all the way back to the drilling rig with a typical flow rate of 10-50 L/sec. Maximum differential pressure between the bottom of the hole and the drilling rig where the pressure is atmospheric can reach more than 200 Bar. A large amount of the energy used in rock cutting stems from highly erosive turbulent jets of mud emanating from nozzles in the bit (see Figure 1-1). The mud also cools and lubricates the bit and transports the cuttings to surface. The cuttings are separated from the mud in a solids-removal system on the rig before reuse. The mud usually consists of water with viscosifiers and weighting materials. However, oil-based mud can also be used.

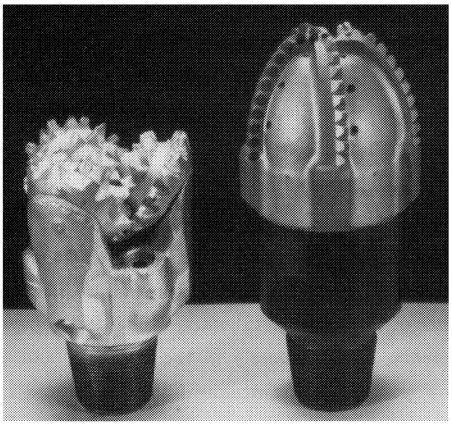

Figure 1-1. Two types from the wide range of bits available. The nozzles are easily visible on the PDC (polycrystalline diamond cutter) bit to the right. To the left is a roller-cone bit. [2]

The drillstring normally consists of 10 m long tubulars called drillpipes, coupled by conical threaded connections with typically 5 or 5.5 in. diameter and 9 mm wall-thickness. All the drillpipe used in a string have the same diameter, however, as well pressure increases, reduction of the drillstring diameter must take place to avoid collapse. Located at the lower end of the drillstring are various elements and the drill bit, collectively termed the bottom hole assembly (BHA). Heavyweight drillpipe is used in a transition zone before the thick-walled drill collars to obtain a smooth change in stiffness from the drillpipe to the tools close to the bit, and to add weight to the bit. Typical drill collars have an outer diameter up to 250 mm and a wall thickness up to 85 mm. The BHA often contains various crossover elements to accommodate different thread profiles and diameters. Behind the bit, various sophisticated downhole tools can also be elements in the BHA, e.g. turbines and measurement-while-drilling (MWD) equipment.

Drillstrings of more than 9000 m in length are used today; this is an extremely slender construction with a diameter/length-ratio much less than for a long human hair. The drillpipes are loaded in tension, supported by the drilling rig, and only the lowest few hundred meters of the drillstring is in compression during vertical and directional drilling. Horizontal drilling has obviously no use for the heavy parts to add weight on the bit, and the entire horizontal portion of the drillstring is loaded in compression. To minimise lateral motion of the drillstring loaded in compression, elements called stabilisers are used. Stabilisers are cylindrical elements that fit loosely in the borehole with a coarsely grooved blade length up to 1 m and a diameter that is 5 to 50 mm less than the borehole diameter to allow passage of the mud.

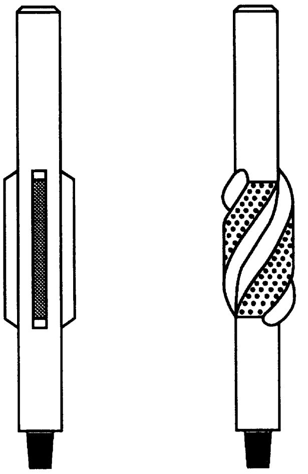

Figure 1-2. Two types of stabilisers; straight bladed and spiral bladed.

Usually torque is transmitted from the drilling machine at the top of the drillstring. Typical rotation speeds are 50 – 200 revolutions per minute. Another technique used to generate rotation of the bit employs downhole motors that can be either a turbine or a positive-displacement mud motor.

To isolate the various pressurised layers in the formation, a casing, which is a high strength steel tube, is lowered into the borehole and fixed in place by cement. The casing also offers protection against mechanical damage of the hole by the drillstring and erosion of the hole by the mud.

In directional drilling, MWD instruments are placed in the BHA as close to the bit as possible and transmit data to the surface by pressure pulses that travel through the mud in the drillpipe and the annulus (mud-pulse telemetry). The measurements are based on magnetic, gyroscopic or inertial techniques and measure parameters such as inclination (vertical deviation; angle with respect to the vertical), azimuth (angle from magnetic north) and along-hole depth (AHD). This gives enough information to reconstruct the position of the borehole in North, East and true vertical depth (TVD). Modern survey tools can reach an accuracy in the order of 1 to 10 m lateral error per 1000 m AHD. Measurement-while-drilling technology enables the measurement of data such as averaged weight on bit (WOB), torque on bit (TOB), temperature, pressure and petrophysical data. Typically WOB is 0 to 250 kN, with more than 3000 kN weight on the drillrig-hook. Torque-on-bit is typically between 0.5 and 10 kNm, while the torque at the rotary table is higher because of the frictional losses along the borehole and may be in the range of 0.5 and 70 kNm. During drilling by downhole motor, MWD is used to measure the angle of the bent drillstring in a plane perpendicular to the borehole.

The rate of penetration (ROP) and drillstring rotational speed are dependent on the type of well and formation drilled. Typically penetration rate is 1 to 50 m per hour.

1.4 Fatigue loading on the drillstring

In general, there are two types of fatigue loading on the drillstring. Often the most severe fatigue loading is caused by doglegs, the curved part of the well where directional changes take place with a typical radius of 300 – 850 m. (2°100 ft.$^{-1}$ - 5°100 ft.$^{-1}$). Because of this curvature, the drillstring will be alternating in tension and compression as it is rotated, shown in Figure 1-3. During the planning of the well profile, engineers attempt to maximise the dogleg radius. However, different circumstances might give unavoidable short dogleg radii, e.g. side tracking where a well is drilled out from an existing borehole; and in avoiding other wells.

Other sources of fatigue loading are three types of dynamic vibration:

- *torsional vibrations* from stick-slip where the bit in extreme cases becomes stuck while the drilling rig continues to apply torque to the string. After reaching a critical value, the bit loosens and spins out the stored energy in the string. Typical frequency is 0.05 to 0.5 Hz.
- *lateral vibration* due to the difference in diameter between the drillstring and the borehole which allows the BHA to oscillate laterally. This is in contrast to the part of the drillstring that is loaded in tension and therefore is forced into continuous contact against the curved well wall. Other sources are from the unbalanced forces in the drillcollars giving whirling - much like an unbalanced centrifuge - and from the backward rolling motion of the drillstring along the borehole wall caused by friction. Typical lateral vibration frequencies are from 0.5 to tens of Hz.
- *longitudinal vibration* called bit-bouncing that occurs when the bit cuts through loose formations with high speed and suddenly hits a hard formation, such as large stones. Typical frequencies are 1 to 10 Hz.

Dynamic vibration in the BHA will generally decrease the ROP and can cause damage to the borehole wall giving a collapsed or oversized borehole. The very complex dynamic behaviour[1] of the BHA is not easily recognised at the surface because of the remoteness and damping from friction between the drillstring and the borehole wall. Changing the rotation speed is the easiest and first step in reducing the vibrations, but often the whole drilling operation must be halted until all the vibrations are dissipated before continuing drilling operations.

---

[1] Jansen presents numerical models in his PhD thesis [2].

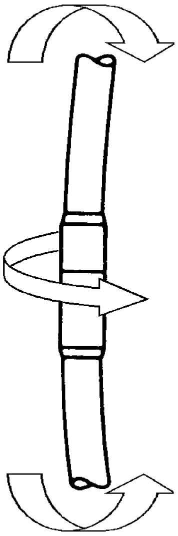

Figure 1-3. Cyclic bending stress from dog-legs.

1.5 Fatigue failure of downhole equipment

Systematic failure analyses of downhole equipment are not easily available, but drilling contractors and oil companies suffering from frequent failures confirm that downhole failures are a costly problem. Continuous work on optimising the geometry, welding processes and materials technology has improved the fatigue performance of drillstring components since the early 1990's when the failure investigations reported later in this chapter were performed. As an example, the high number of failures at the taper runout (see Figure 1-6) has been reduced by optimising the taper length and radius to reduce the stress concentration factor. The data collected by Dr. Kenneth A. Macdonald in his PhD thesis [3] are interesting in this context of this thesis and will be summarized in this chapter.

1.5.1 UK drillstring failures in the period 1989 - 1994.

Macdonald [3] made a comprehensive review of the failure data available from a leading North Sea operator's drilling programme between 1989 and mid-1993. The critically stressed parts of almost all BHA equipment are the threaded connections and this is where most failures occur. The failure mechanisms commonly encountered are (in no particular order): fatigue, corrosion fatigue, stress corrosion cracking and ductile fracture from overloading. Fatigue and ductile fracture are by far the most common failure modes in ferritic-pearlitic drilling components, with stress corrosion cracking then claiming most casualties in austenitic drill collars. The make-up torque leaves the pins in particular with a locked-in tensile preload, giving a permanent mean stress of about half the yield strength in the case of drillcollars [1]. The data presented by Macdonald were collected from 157 wells totalling 550 km in length where 63% was directional or horizontal wells. BHA accounted for 79% of the failures balanced by 21% failure of drillpipe. Connection fatigue failure totalled 58% of all BHA failures confirming fatigue as the main cause of failure in drillstring equipment over the period. Approximately equal proportions of pin and box failures occurred. This is supported by two other investigations listed by Macdonald in which 1785 and 76 failures were investigated.

Fatigue failures in BHA threaded connections invariably start at either of the pin or box last engaged thread (LET), consistent with the known distribution of load and stress in such connections. The cracks initiate at the LET root and grow both circumferentially along the helix and radially across the section wall. See Figure 1-4.

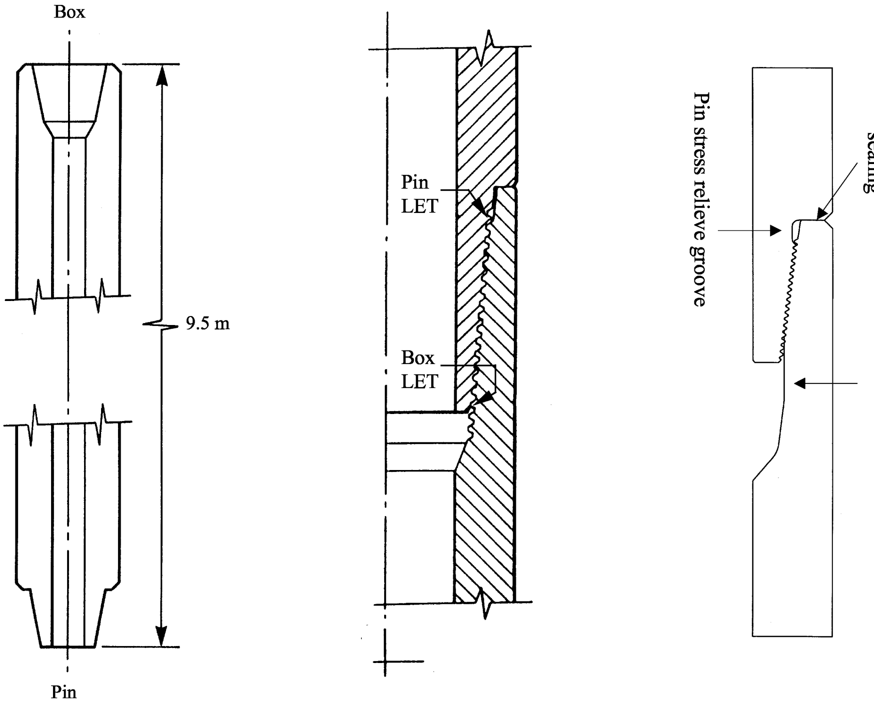

Figure 1-4. Drillcollar, connection critical thread sites (LET) and stress relief features. [8]

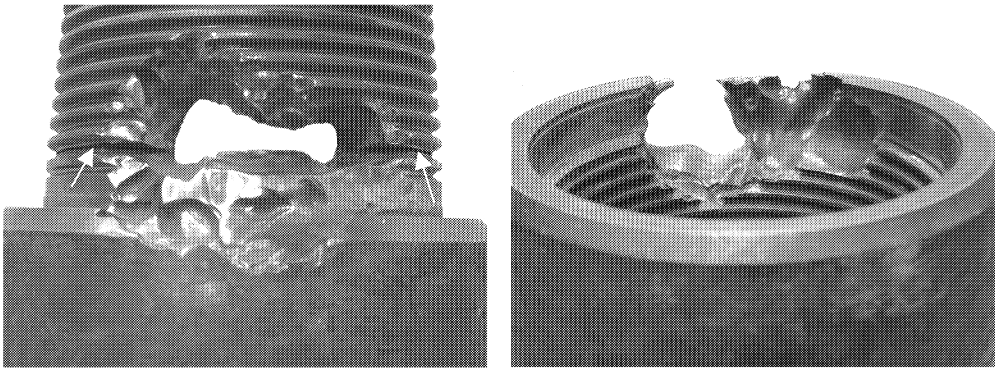

Figure 1-5. Crack initiated in pin LET (white arrows) leading to leakage in the sealing and subsequent erosion. 5.in drillpipe connection from the Norwegian sector. (T. Grøttum, Statoil, 2001)

The failure of BHA components – defined as either loss of pressure containment (washout) or complete separation (twistoff) – may occur with little or no indication at the drillfloor, primarily due to the remoteness of the equipment from the drilling rig. Failures in upper regions of the drillstring are easier to detect as differential pressure between drillpipe and annulus are higher.

1.5.2 Drillstrings

The majority of fatigue failures of the drillpipe generally occurs at locations away from the connections (see Figure 1-6) and as such is not directly of interest in this thesis, it is nonetheless an important cause of failure.

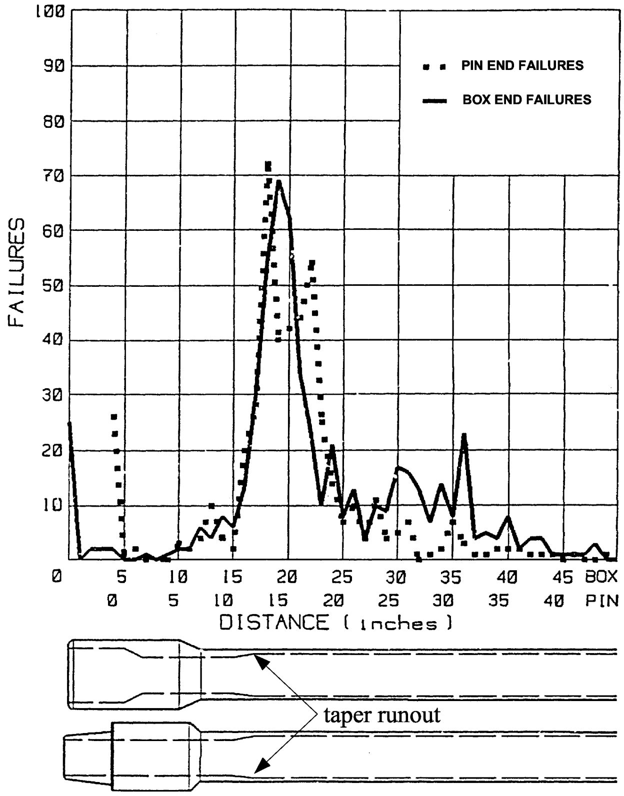

Figure 1-6. API/IADC database failure distribution of drillpipe box and pin-end failure locations (1,785 failures). [5]

Drillpipe failures can be categorised in two groups: Plain fatigue; and corrosion fatigue. Once a leak path exists across the pipe wall both types of failure are prone to washout. In ordinary fatigue, cracks initiate at the internal taper runout (see Figure 1-6) and are oriented circumferentially. The pipe bore and particularly the plastic coating is typically in good condition with damage localised around the crack or the washout. Under conditions of corrosion and fluid turbulence, surface damage develops rapidly promoting general material loss and pitting. The reduced section consequently gives increased stresses, which exacerbate the fatigue process and self-acceleration occurs. Fatigue or corrosion assisted fatigue cracks are initiated and subsequent crack propagation eventually produces washout or twistoff. The damage to the pipe bore under such conditions is characteristically extensive around the bore circumference and is easily distinguished from plain fatigue.

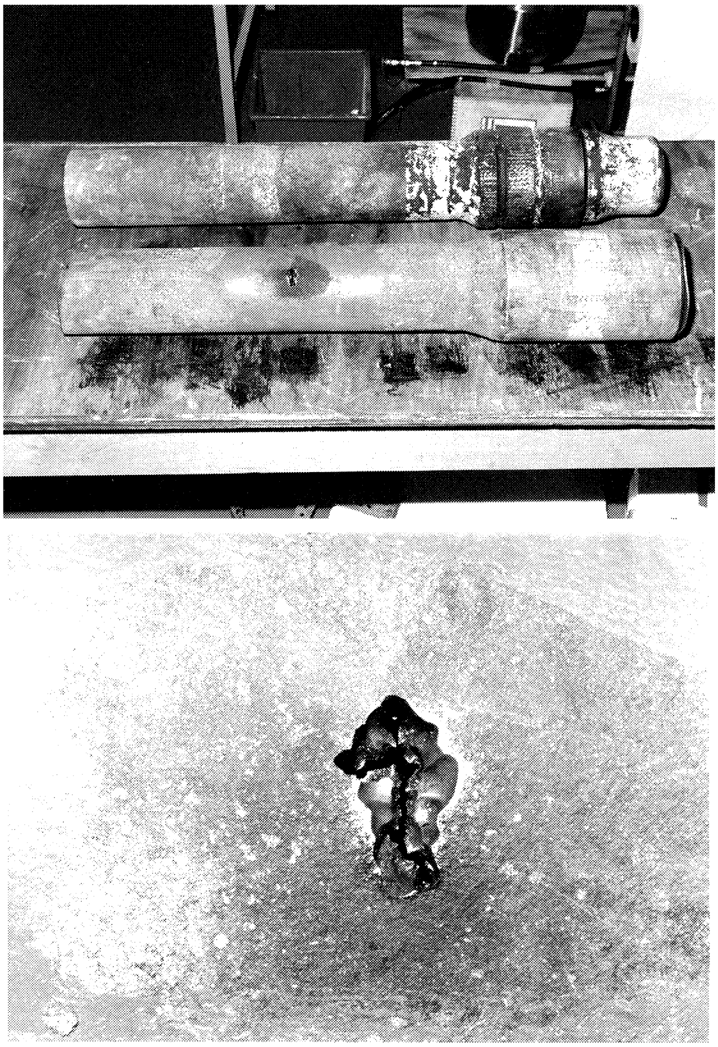

Figure 1-7. Example of washout failure in 5in. drillpipe. [3]

1.5.3 Drill collars

Fatigue and ductile fracture (from overload) are by far the most common failure modes in general ferritic drilling equipment with SCC (stress corrosion cracking) presently claiming most casualties amongst austenitic drill collars. High strength stainless steel drillstring components suffer the same set of problems in terms of failure modes as their ferritic counterparts, but additionally present some unique and distinct difficulties in corrosion-fatigue and SCC damage associated with exposure to highly aggressive mud. Fatigue failures in high strength nonmagnetic connections occur at identical sites to those in HSLA components: the critical LETs and sometimes the stress relief groove (SRG) if present. Stress-corrosion cracking normally starts at the bore of the pin and the cracks are oriented transverse to the drillstring longitudinal axis, and caused by the permanent mean stress of about half the yield strength from the tooljoint make-up.

Some manufactures hammer peen the bore to introduce compressive residual stresses to lower the average surface stress below the threshold level for SCC. Where satisfactory service performance relies on a layer of compressive residual stress from hammer peening-treatment to help inhibit the onset of SCC, the connections are at risk if the pin bore surface becomes corroded or eroded and the beneficial layer is damaged or lost altogether.

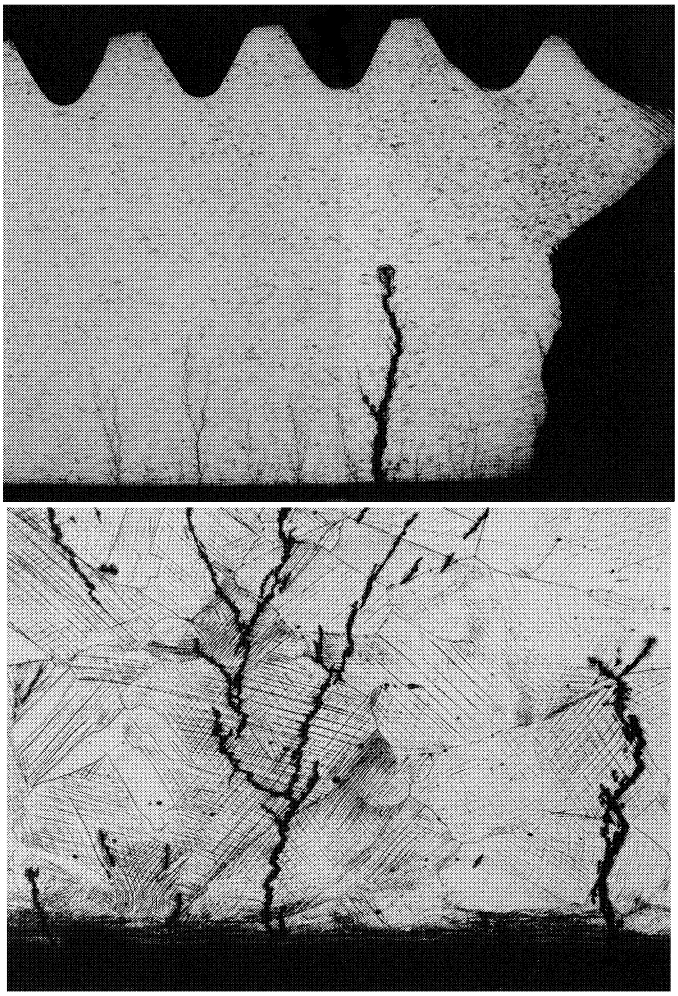

Figure 1-8. SCC failure of a 6 ½in. nonmagnetic drillcollar pin connection. 5x and 100x. [3]

1.6 Objectives, scope and organisation of the thesis

During recent decades there has been an increased general interest in residual stresses and their effects on fatigue and fracture. Numerical simulations by FEM (finite element method) and BEM (boundary element method) have been used in addition to experimental investigations. As an example of the large amount of work carried out recently, in the period from 1998 to first quarter of 2000 179 references on the analysis and modelling of residual stresses by means of FEM or BEM are listed in a biography study by Mackerle [4].

Residual stresses have long been known to influence fatigue performance. In API Spec 7 [1], cold rolling is mentioned as a method to increase the fatigue performance of threaded drillstring components. However, it is very difficult to find scientific work where the cold rolling process applied to drillstring threaded connections have been studied. The intent of this thesis has been to increase the understanding of the cold rolling process and factors affecting the degree of improvement that is possible to obtain, within the limitations set by the resources available, with regard to finances and time. In addressing these matters, the main objectives of the present study were:

- To simulate and verify by experiments the introduction of residual stresses by cold rolling.
- To improve the understanding of the physical processes that influence long-term decay of residual stresses.
- To study the influence of residual stresses on the fatigue performances of pipes with thread profiles and to optimize the cold rolling process of the thread profile

Full-scale tests were performed on simulated threads rather than on threaded connections due to constraints imposed by the time frame and the financial budget.

This thesis consists of nine chapters including this one. The thesis is organized as follows:

Chapter 2 gives a brief introduction to general fatigue with the aim of giving necessary background to read this thesis.

Chapter 3 presents basic aspects of linear elastic fracture mechanics considered necessary to read this thesis.

Chapter 4 reviews and presents the state of the art for issues influencing the cold rolling process. Some of these issues are: cyclic stress-strain behavior of steel; crack initiation; plastic deformation at the crack tip; relaxation of residual stresses; crack closure; overloads; the behaviour of short fatigue cracks; and short crack propagation models.

Chapter 5 presents in detail the hole drilling method and verification of residual stresses computed by FE analysis.

Chapter 6 reports full-scale rotating bending fatigue tests of rolled and unrolled thread profiles in drill pipes undertaken in this study.

Chapter 7 reports the 3D FE analysis of simulated thread profile rolling.

Chapter 8 discusses the results from the study of a small scale notched fatigue specimen preloaded to introduce residual stresses, FE simulations of the preloading, and crack growth calculations in residual stress fields under different levels of mean stress.

Chapter 9 gives the conclusions of the study and makes recommendations for further work regarding cold rolling of drillstring threads.

1.7 References:

1 American Petroleum Institute (1997) API specification 7, 39'th edition. Specification for Rotary Drill Stem Elements.

2 Jansen J.D. (1993) Nonlinear dynamics of oilwell drillstrings. PhD-thesis. Delft University Press, Delft.

3 Macdonald K.A. (1996) Fatigue of drillstring threaded connections. PhD Thesis, Aberdeen University.

4 Mackerle J. (2001) FEM and BEM analysis and modelling of residual stresses. A bibliography (1998-1999). *Finite Elements in Analysis and Design* 37, 253-262.

5 Seshadri P.V. and Allwin R.P. (1992) API/IADC Drillstring failure database: What do we learn? Proc.SPE Drilling conf., New Orleans, 18-21 Feb. IADC/SPE 23842. pp 17

2 Basic fatigue

2.1 Notation

σ	stress [MPa]
$\Delta\sigma$	nominal stress range = σ_{max} - σ_{min} [MPa]
σ_a	fatigue stress amplitude [MPa]
σ_e	fatigue limit for completely reversed loading [MPa]
σ_m	mean stress [MPa]
σ_{max}	maximum cyclic stress [MPa]
σ_{min}	minimum cyclic stress [MPa]
ρ	material constant
S_u	ultimate tensile stress = $F_{ultimate}$ / A_0 [MPa]
D	damage
D_f	damage at fracture
FE	finite element
K_f	fatigue-notch factor
K_t	stress concentration factor
m	inverse slope in the S-N curve
N_f	total cycles to failure
N_i	number of cycles in initiation
N_p	number of cycles in propagation
n_i	number of cycles in a block
q	fatigue-notch sensitivity factor
R	stress ratio = $\sigma_{min}/\sigma_{max}$
r	radius of notch root [m]

2.2 Introduction

Fatigue cracking and failure have been recognised and studied since the 1830's [1, 2, 8, 12]. Fatigue has gradually become more prevalent as better materials have been developed and more accurate analysis tools have been developed for analysing complex and highly optimised structures. It is often stated that fatigue accounts for at least 90 percent of all service failures due to mechanical causes. Many serious incidents with loss of human life are caused by fatigue, such as railway accidents, airline crashes, and loss of ships and oilrigs.

In an uncracked component fatigue fracture generally occurs in three stages; a fatigue crack is initiated and grows in a shear mode in *stage I*, the crack propagates for most of it's length in *stage II* in a direction that is perpendicular to the principal stress and final fracture takes place in *stage III*. Metallic fatigue is often spilt into two categories; welded and non-welded structures. The reason is the different proportions of the fatigue life spent in stage I. Non-welded structures will typically spend 90% [1, 8] of life in stage I, whereas fatigue cracks normally initiate at small weld defects and start growing very early in the service life in welded structures. The fatigue life of welded structures is therefore spent almost entirely in crack growth, and the initiation portion is normally neglected. This document will focus on non-welded structures unless clearly stated otherwise.

Even today, after 170 years of research, engineers are often dependent on fatigue testing to determine a structure's resistance to fatigue. Fatigue testing can roughly be split into three categories:

1. Full scale testing with an actual load sequence or a representative load spectrum.
2. Component testing with constant- or variable amplitude load cycles.
3. Small scale testing with constant- or variable amplitude load cycles.

Full scale testing is only applicable for relatively small fixed structures e.g. pedestrian bridges [7] or vehicles on test stands. Larger structures must be scaled down, and components of special interest are studied separately. Downscaling has several problems such as different natural frequencies, mechanical scaling factors and load distributions. Full scale testing and even component testing are expensive with regard to the cost of the test object and the test itself. The number of specimens available is therefore often limited and typically of the order of one or two, up to about ten.

2.3 High cycle and low cycle fatigue

Fatigue crack initiation in smooth parts is associated with local plastic deformation, as discussed in Section 4.3 and 4.4. At small defects or inclusions macroscopic elastic strain will intensify and lead to microscopic plastic deformation initiating a fatigue crack. Under high-cycle, low stress fatigue, the material deforms primarily elastically; the failure time or the number of cycles to failure under such *high-cyclic fatigue* has traditionally been characterised as a function of the stress range. However, the stress associated with *low cycle fatigue* is generally high enough to cause appreciable plastic deformation prior to failure. Under these circumstances, the fatigue life is characterised in terms of the strain range. Low cycle fatigue will lead to fracture within a few thousand cycles.

The work in this study is concerned mainly with high cycle fatigue.

2.4 Factors effecting the fatigue strength

The mechanical properties of the material influence in particular the crack initiation period, as seen in Figure 2-1, and almost insignificantly influences the crack propagation, as seen in Figure 2-2.

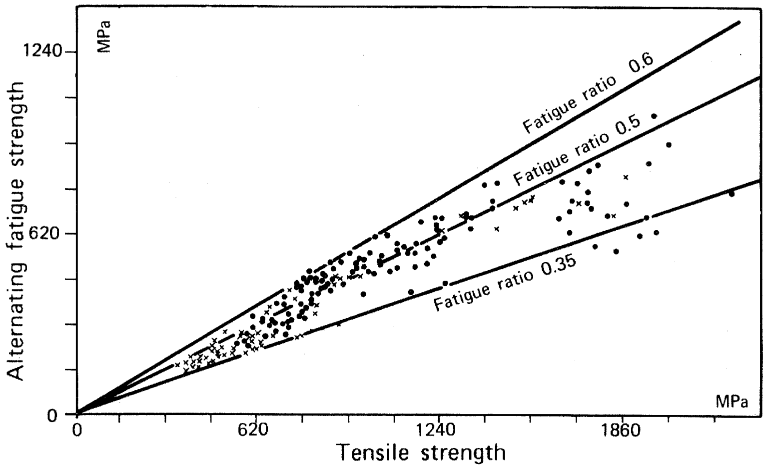

Figure 2-1. Fatigue endurance limit vs tensile strength. Carbon and alloy steels. [4]

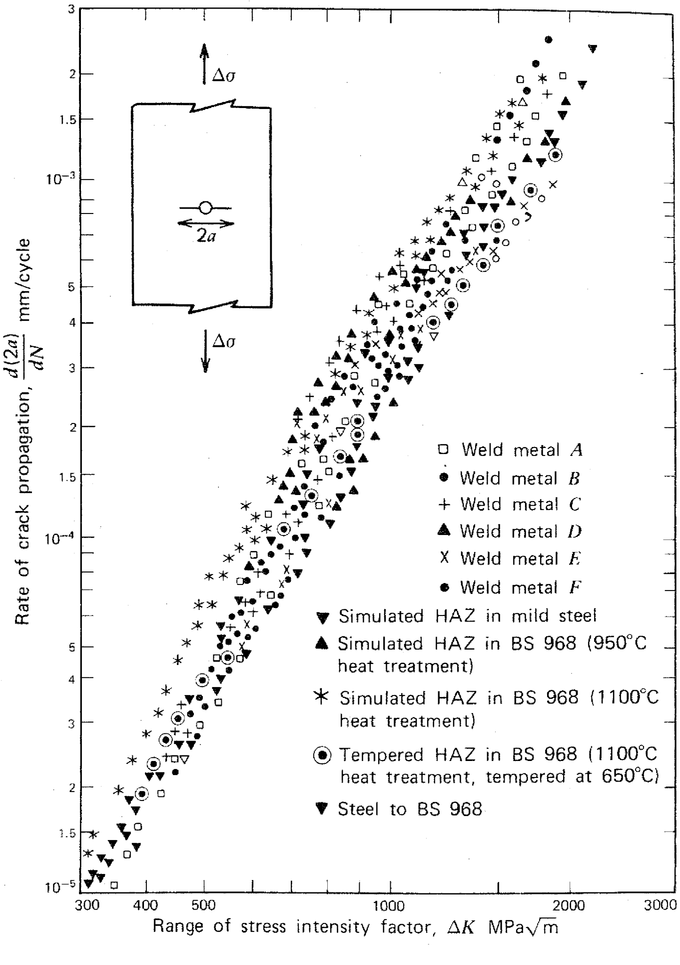

Figure 2-2. Crack growth data for C-Mn steel weld metals, HAZ and base materials. [4]

Type of loading and loading history, geometry, surface condition, environment and residual stress (Section 4.6) are all factors influencing the fatigue life and will be briefly discussed in this Chapter.

2.5 Fatigue testing

Ever since the earliest days of fatigue testing it has been known that in order to determine the fatigue strength of a particular component it is necessary to test several identical specimens due to the large scatter in the test results. A number of tests are performed to determine an S-N curve, typically between eight and twenty. Tested at different stress ranges, a relationship is established between nominal stress range, $\Delta\sigma$, (or stress amplitude σ_a) and number of cycles to failure, N_f. By plotting $\Delta\sigma$ against N_f the *S-N curve* is obtained. Under constant amplitude conditions the endurance (in cycles) at failure rapidly increases with decreasing magnitude of the stress range applied. The curve, however, subsequently becomes progressively flatter and parallel to the life axis for ferrous alloys. In this region, small decreases in stress produce disproportional large increases in life, eventually implying infinite life below *the endurance limit* as shown in Figure 2-3

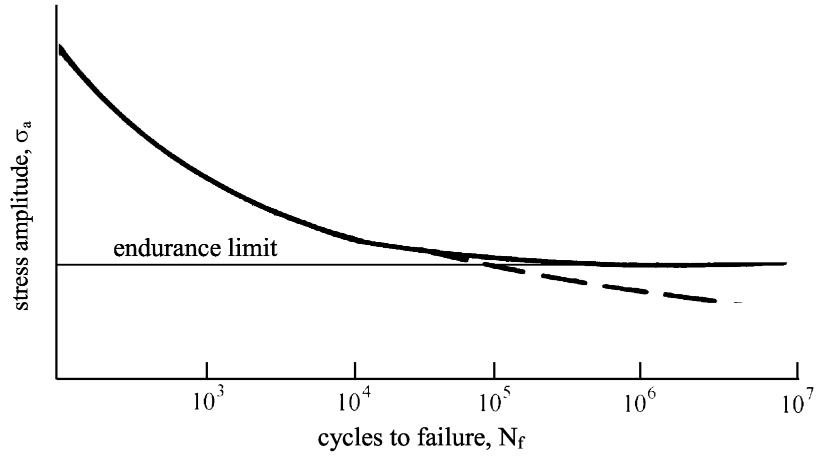

Figure 2-3. Typical S-N diagram showing the variation of the stress amplitude for fully reversed fatigue loading of nominally smooth specimen as a function of the number of cycles to failure for ferrous and nonferrous alloys. [12]

The total fatigue life is the sum of the initiation and propagation stages as follows:

$$N_f = N_i + N_p \qquad \text{Equation 2-1}$$

where N_i is the number of cycles to crack initiation and N_p it the number of cycles spent in propagation. As discussed in Section 4.10 there is no strict definition of initiation, but generally the crack length at the end of initiation is of the order of a few grains. The S-N curve will not give the portion of fatigue life in initiation and propagation.

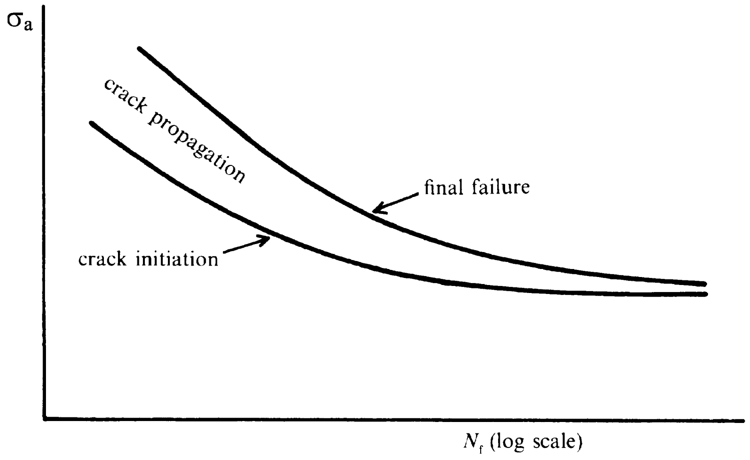

Figure 2-4. Total fatigue life is the sum of crack initiation and propagation. [12]

Stress-life fatigue data are now conventionally plotted with double logarithmic scales where the resulting curve is close to a straight line, and is described by Basquin's equation (1910) of the form

$$\Delta\sigma^m N_f = \text{constant} \qquad \text{Equation 2-2}$$

where m is the inverse slope.

The straight lines seen in Figure 2-5 are best-fit curves for the test points available, and there is always scatter which generally increases with increasing fatigue life. The scatter means that particular design S-N curves have associated probabilities of survival based on statistical analysis of the test data.

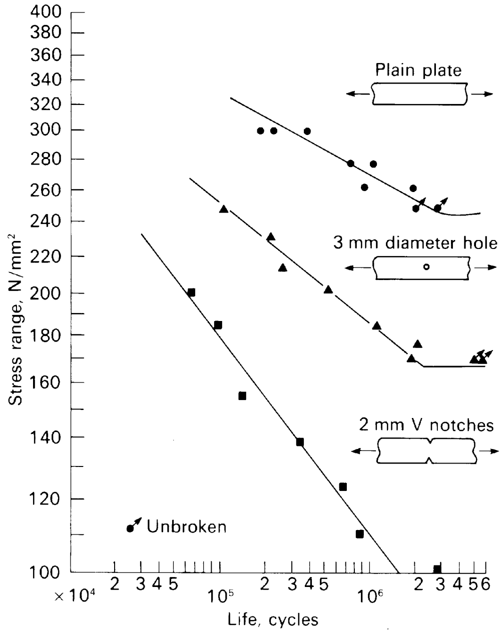

Figure 2-5. Effect of stress concentrations on the S-N curves of mild steel plate at R = 0. [10]

In addition to the applied stress range, fatigue is also sensitive to the mean stress, and the test data for the endurance limit can be presented in a modified *Goodman diagram* [5], see Figure 2-6. Test data for ductile metals generally fall closer to the parabolic curve proposed by Gerber. However, due to the scatter in the results and the fact that tests on notched specimens fall closer to the Goodman line [2], the linear relationship is usually preferred in engineering design. These relationships may by expressed by the following equation,

$$\sigma_a = \sigma_e \left[1 - \left(\frac{\sigma_m}{S_u} \right)^x \right] \qquad \text{Equation 2-3}$$

where x = 1 for Goodman line, x = 2 for Gerber parabola. The fatigue limit, σ_e, for steel is usually 35% or more of the ultimate tensile strength [6].

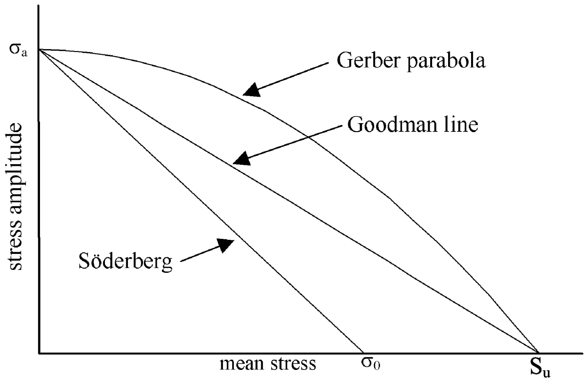

Figure 2-6. Modified Goodman diagram, also called Haigh diagram.

An alternative to constant mean stress testing, and a more common way, is to perform fatigue testing by constant *stress ratio*, R:

$$R = \frac{\sigma_{\min}}{\sigma_{\max}} \qquad \text{Equation 2-4}$$

The S-N-diagram from a constant mean stress test will differ from the diagram representing the constant stress ratio as seen in Figure 2-7.

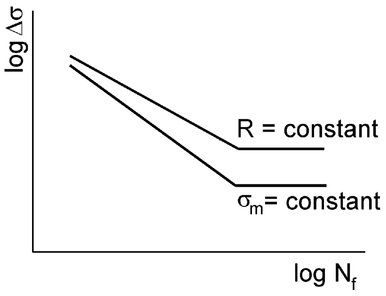

Figure 2-7. Difference in S-N curve from constant R and constant σ_m testing of the same specimen.

2.6 Fatigue life estimation based on S-N curves

Most fatigue failures occur at stress raisers, and this is the location of particular interest for the design engineer. A definition of the severity of the stress raiser assuming elastic material is the *stress concentration factor*, K_t, defined as max stress / nominal stress. There will often be no S-N curve available for the particular detail of interest. The solution is to find K_t from various publications or a detailed finite element (FE) analysis, and use a S-N curve for a smooth specimen, $K_t = 1$.

The effect on notches on fatigue strength is determined by comparing the S-N curves of notched and unnotched specimens. The effectiveness of the notch in decreasing the fatigue limit is expressed by the *fatigue-strength reduction factor*, or *fatigue-notch factor*, K_f. This factor is simply the ratio of the fatigue strength of unnotched specimens to the fatigue strength of notched specimens. Values of K_f have been found to vary with:

- severity of the notch
- material
- type of loading
- stress level

The value of K_f published in the literature has considerable scatter. However, two general trends are usually observed for test conditions of completely reversed loading. First, K_f is usually less than K_t. and second, the ratio of K_f / K_t decreases as K_t increases. Thus, very sharp notches have less influence on fatigue than expected from K_t. The notch sensitivity of a material in fatigue is expressed by a *notch-sensitivity factor* q

$$q = \frac{K_f - 1}{K_t - 1} \qquad \text{Equation 2-5}$$

Equation 2-5 was chosen so that a material which experiences no reduction in fatigue due to a notch ($K_f = 1$) has a factor of q = 0, while a material in which the notch has its full theoretical effect ($K_f = K_t$) has a factor q = 1. However, q is not a true material constant since it varies with the severity and type of notch, the size of specimen, and the type of loading. The notch sensitivity increases with tensile strength.

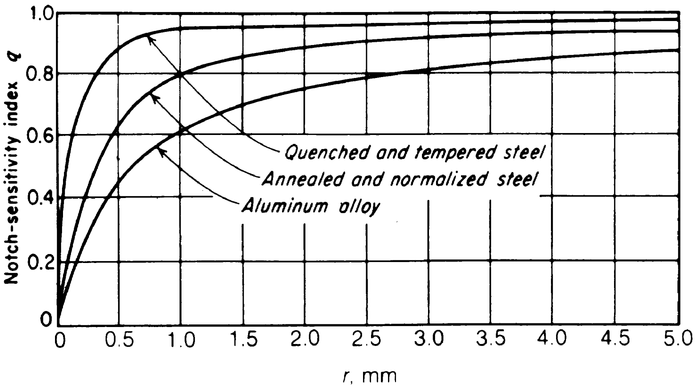

Figure 2-8. Variation of notch-sensitivity index with notch radius for materials of different tensile strength. [11]

Neuber proposed another approach in 1946 where K_f is expressed

$$K_f = 1 + \frac{K_t - 1}{1 + \sqrt{\rho / r}} \qquad \text{Equation 2-6}$$

where r = radius of the notch root and ρ = a material constant related to the strength of the material.

Material	Strength level [MPa]	ρ [mm]
Steel	Su = 552	0.15
	Su = 896	0.07
	Su = 1310	0.01
Aluminum alloy	Su = 150	2
	Su = 300	0.6
	Su = 600	0.4

Table 1. Some values of Neuber's constant ρ [2]

2.7 Surface condition

The most common machining operations such as sawing, grinding, polishing and milling cause different degrees of surface roughness. The valleys of the rough surface serve as stress concentrations, which, in turn, induce different levels of resistance to fatigue crack nucleation.

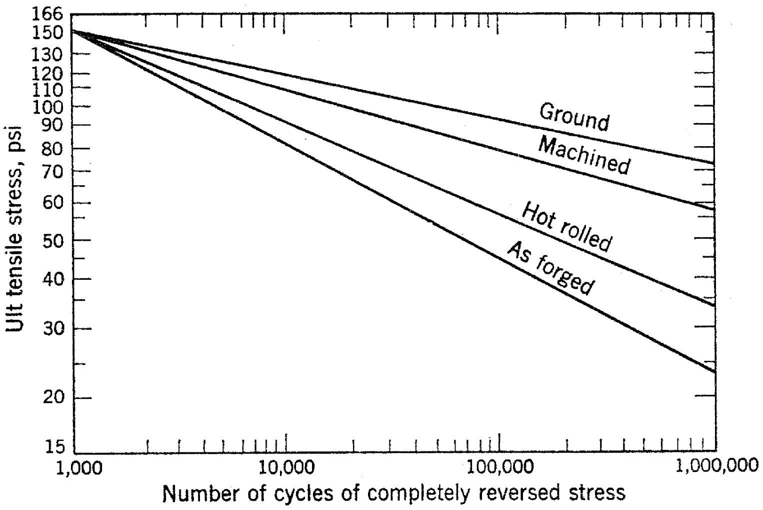

Figure 2-9. Influence from surface condition on fatigue resistance. [9]

2.8 Size effect

There are considerable problems related to performing size effect studies. It is very difficult, if possible, to manufacture geometrically similar specimens of increasing dimensions that have the same metallurgical structure and residual stress distribution throughout the cross-section. There are two other important factors influencing the scaling of fatigue specimens. First, the possibility of defects at the surface increases with increasing surface area, and second, generally the stress gradient is steeper through the cross-section for a smaller specimen compared to a large one. Increased dimensions will always tend to decrease the resistance to fatigue and brittle fracture.

2.9 Environmental effect

A corrosive environment will deteriorate a smooth surface and reduce the fatigue initiation period, which is the dominant period for unwelded components with a smooth surface. Also the crack propagation rate will be influenced by corrosion. However, a corrosive environment will have a much stronger effect on the fatigue life of unwelded smooth components than on notched components, as seen in Figure 2-10. Temperature influences corrosion and hence the fatigue life, and also the mechanical properties of the material. Environmental effects are further discussed in Section 4.3, 4.4, 4.7, and 4.8.

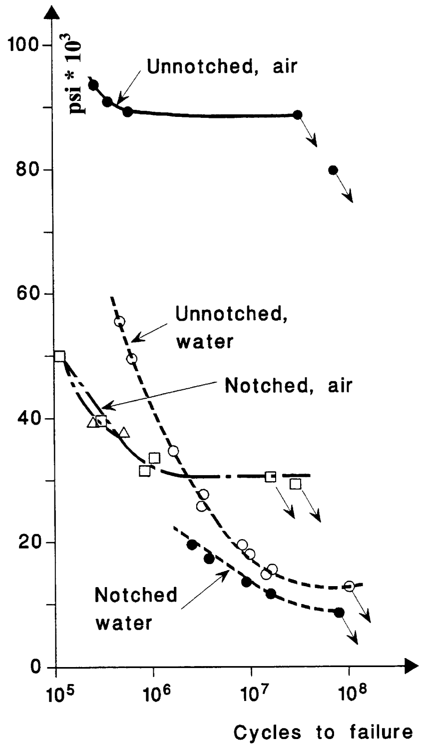

Figure 2-10 Corrosion fatigue of notched and unnotched specimens of quenched and tempered SAE 3140 steel in water. [3]

2.10 Other influencing factors

Depending on the processing history rolled, forged or extruded material exhibit varying degrees of anisotropy, i.e. directional dependence of many strength properties, including fatigue strength. In some cases reduction factors are used to correct for anisotropy in fatigue.

2.11 Cumulative damage

Fatigue tests are normally done with constant amplitude loading, and design based on these data will only be relevant for constant amplitude loading. Most structures will however experience a load history of a stochastic nature.

The development of fatigue damage under stochastic or random loading is in general termed *cumulative damage*. Numerous theories for calculating cumulative damage from S-N curves may be found in the literature. However, the procedure independently presented by Palmgren in 1924 and by Miner in 1945, called Miner-Palmgren cumulative damage rule, is widely used in engineering design, despite serious shortcomings.

The basic assumption in the Miner-Palmgren cumulative damage method is that the "damage" to the structure per load cycle is independent of the load history, which is not true, (see Section 4.9 Overload) and hence constant at a given stress range and equal to

$$D = \frac{1}{N_f} \qquad \text{Equation 2-7}$$

In a stress history of several stress ranges $\Delta\sigma_i$, each with a number of cycles n_i, the damage sum follows from

$$D = \sum_i \frac{n_i}{N_{f,i}} \qquad \text{Equation 2-8}$$

where $N_{f,i}$ is the number of cycles for $\Delta\sigma_i$ alone giving fracture. The failure criterion is

$$D_f \leq \delta \qquad \text{Equation 2-9}$$

where normally $\delta = 1$, but in some applications additional conservatism is obtained by decreasing δ.

Fatigue is a consequence of cycle-by-cycle plastic strains at a notch or at a fatigue crack tip. The state of stress and strain in the damage area is a result of the preceding stress-strain history. Hence, the damage in one cycle is not a function of that stress cycle only, but also of the preceding cycles, leading to interaction or load history effects.

It is well known that tensile overloads applied to notched and cracked metallic materials temporarily reduce the rate of subsequent fatigue crack growth and that the application of compressive overloads generally has the opposite effect. These topics will be discussed in more detail in following chapters.

2.12 References:

1 Colangelo V.J. and Heiser F.A. (1986) Analysis of Metallurgical Failures, second edition. John Wiley & Sons.

2 Dieter G.E. (1988) Mechanical Metallurgy, SI metric edition. McGraw-Hill, Singapore.

3 ESDEP European Steel Design Education Programme, Fatigue I.

4 Fuchs H.O. (1959) Techniques of surface stressing to avoid fatigue. In Metal Fatigue. Edited by Sines G. and Waisman J.L. McGraw-Hill book company, Pennsylvania. pp 197-231.

5 Goodman J. (1899) Mechanics Applied to Engineering. Longmans Green & Co., London.

6 Lawson L., Chen E.Y. and Meshii M. (1999) Near-threshold fatigue: a review. *International Journal of Fatigue* 21, 15-34.

7 Lotsberg I., Karlsen A. and Oma Å., Fatigue life evaluation and full scale testing of an aluminium bridge., Det Norske Veritas.

8 Macdonald K.A. (1996) Fatigue of drillstring threaded connections. PhD Thesis, Aberdeen University

9 Madayag A.F. (1969) Metal Fatigue: Theory and Design. John Wiley & Sons.

10 Maddox S.J. (1991) Fatigue Strength of Welded Structures. Second edition. Abington Publishing, Cambridge.

11 Peterson R.E., Sines G. and Waisman J.L. (1959) Metal Fatigue. McGraw-Hill Book Company, New York.

12 Suresh S. (1998) Fatigue of Materials, second edition. Cambridge University Press, Cambridge.

3 Linear elastic fracture mechanics

3.1 Notation

Γ	perimeter [m]
Π	potential energy [J]
δ_{ij}	Kronecker delta
γ_p	plastic work required to extend crack [J/m^2]
γ_s	surface energy per unit crack area [J/m^2]
ν	Poisson's ratio
θ	angle from x-axis
ρ	crack curvature [mm]
σ	stress [MPa]
σ_c	critical stress [MPa]
σ^∞	far-field stress [MPa]
A	area [m^2]
a	crack length, major axis in an ellipse [m^2]
B	plate thickness [m^2]
b	minor axis in an ellipse [m^2]
C	material parameter
E	Young's modulus [MPa]
E	total energy [J]
h	weight function
K	stress intensity [Nm$^{-3/2}$]
K_c	critical stress intensity factor [Nm$^{-3/2}$]
ΔK_{th}	stress intensity threshold [Nm$^{-3/2}$]
m	material parameter
N	no of cycles
p	crack face traction [N]
r	radius from crack tip [m]
u	displacement [m]
W_s	work required creating new surfaces [J]
x_0	atomic spacing [m]

3.2 Introduction

Until the sudden and completely unexpected separation of a Liberty ship in 1943 fracture mechanics was a scientific curiosity. The Liberty ships were among the first ships fabricated with an all-welded hull. Of the approximately 2700 ships that were built, 400 sustained fractures while 20 ships suffered total failure. Previously, similar types of steel had already been used successfully in riveted ships, where the steel quality was adequate because fractures could not propagate across panels that were joined by rivets. Welded structure is essentially a continuous plate of metal in which a fracture will have no crack growth barriers. Most of the fractures in Liberty ships initiated at the corners of square hatches with high stress concentrations; thus high local stresses were a contributing factor.

In 1960 Paris and co-workers [9] applied fracture mechanics to fatigue crack growth. The resistance to this work was so intense that they could not find a technical journal willing to accept the paper. The work was then published in a University of Washington periodical entitled “The Trend in Engineering” [9]. The aerospace industry first adopted the method, whereas the Liquid Nitrogen Gas (LNG) tankers approved by Veritas (DNV) was one of the first applications of fracture mechanics based fatigue analysis within the offshore and shipping industries

Figure 3-1. Norman Lady is the first LNG carrier built with the Moss Rosenberg spherical tank design, this type of design was demonstrated by fracture mechanics methods to have adequate fatigue and fracture strength.

3.3 Theoretical cohesive strength of metals

A common model of *cohesive strength* of metals with a perfect atomic lattice is

$$\sigma_c = \sqrt{\frac{E\gamma_s}{x_0}} \qquad \text{Equation 3-1}$$

where E is Young's modulus, γ_s is the surface energy per unit crack area and x_0 is the atomic spacing.[2] γ_s is equal to one half the fracture energy because two surfaces are created when a material fractures. Engineering materials typically have values of fracture toughness that are 10 to 1000 times lower than the theoretical value. Leonardo da Vinci (1452-1519) observed the same phenomena in his experiments on strength of iron wires, where the strength varied inversely with wire length and hence the increased possibility of flaws. A longer wire will have an increased probability of flaws, which implies that the maximum flaw size is controlling the wire strength.

3.4 Griffith fracture theory

In 1913 Inglis [6] published his work on the stress concentration at an elliptical hole in an infinite plate. The stress at the tip of the major axis at point A in Figure 3-2 is

$$\sigma_A = \sigma\left(1 + \frac{2a}{b}\right) \qquad \text{Equation 3-2}$$

With decreasing b the elliptical hole will gradually be shaped like a crack and by introducing the radius of the curvature

$$\rho = \frac{b^2}{a} \qquad \text{Equation 3-3}$$

Equation 3-2 can be written as

$$\sigma_A = \sigma\left(1 + 2\sqrt{\frac{a}{\rho}}\right) \qquad \text{Equation 3-4}$$

Equation 3-4 predicts an infinite stress at the tip of an infinitely sharp crack.

---

[2] For detail see Anderson, T.L. *Fracture Mechanics. Fundamentals and Applications. Second edition.* (CRC press LCC, Boca Raton, 1995) or Dieter, G.E. *Mechanical Metallurgy, SI metric edition.* (McGraw-Hill, Singapore, 1988).

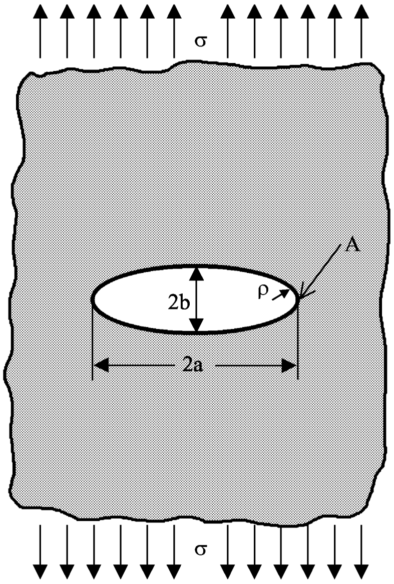

Figure 3-2. Elliptical hole in an infinite plate.

Griffith [5] used the First Law of Thermodynamic when in 1920 he published his theory applicable to brittle materials such as glass. He suggested that in a brittle material a population of fine cracks exist. At the crack tip the stresses will locally reach the theoretical cohesive strength at a nominal stress that is well below the theoretical value. The crack will propagate when the decrease in elastic strain energy is at least equal to the energy required to create the new crack surface. The Griffith energy balance for an incremental increase in the crack area, dA, under equilibrium conditions can be expressed in the following way

$$\frac{dE}{dA} = \frac{d\Pi}{dA} + \frac{dW_s}{dA} = 0 \qquad \text{Equation 3-5}$$

where E is the total energy, Π is the potential energy supplied by the internal strain energy and external forces, and W_s is the work required to create new surfaces. Griffith used the stress analysis of Inglis to show that

$$\Pi = \Pi_0 - \frac{\pi\sigma^2 a^2 B}{E} \qquad \text{Equation 3-6}$$

where Π_0 is the potential energy for an uncracked plate of thickness B. The energy required to develop the crack is

$$W_s = 4aB\gamma_s \qquad \text{Equation 3-7}$$

since the formation of a crack requires the creation of two surfaces.

Thus

$$\frac{d\Pi}{dA} = -\frac{\pi\sigma^2 a}{E} \qquad \text{Equation 3-8}$$

and

$$\frac{dW_s}{dA} = 2\gamma_s \qquad \text{Equation 3-9}$$

From Equation 3-8 and Equation 3-9 the fracture stress is given as

$$\sigma_f = \left(\frac{2E\gamma_s}{\pi a}\right)^{1/2} \qquad \text{Equation 3-10}$$

For a thick plate (plane strain) the Griffith equation is given by

$$\sigma = \left[\frac{2E\gamma_s}{(1-\nu^2)\pi a}\right]^{\frac{1}{2}} \qquad \text{Equation 3-11}$$

Griffith's equation was independently modified by Irwin [7] and Orowan [8] to account for brittle fracture in metals. This was done by inclusion of a term, γ_p, expressing the plastic work required to extend the crack.

$$\sigma_f = \left[\frac{2E(\gamma_s + \gamma_p)}{\pi a}\right] \approx \left(\frac{E\gamma_p}{a}\right)^{\frac{1}{2}} \qquad \text{Equation 3-12}$$

The surface-energy term can be neglected since estimates of the plastic-work term are about 10^2 to 10^3 J/m^2 compared with values of γ_s of about 1 to 2 J/m^2 [3].

3.5 Limitation of linear elastic fracture mechanics (LEFM)

The Griffith's model (Equation 3-10) in particular, but also the modified Griffith model (Equation 3-12), must be used with care. They are both only recommended for cracks with a small plastic region at the crack tip. In high-cyclic fatigue the plastic zone at the crack tip tends to be small compared with the crack length, and it is possible and adequate to calculate the conditions around the crack by linear elastic stress analysis. The reason for this is three-fold. Firstly, the load level is low or moderate, and the crack tip stresses are proportional to the nominal stresses, according to linear elasticity. Secondly, the triaxiality of the crack tip stress field acts to reduce plasticity. Thus, the crack tip plastic zone is smaller in plane strain than in plane stress. Thirdly, the cyclic plastic zone size is known to be only about one quarter the size of the monotonic plastic zone. This is discussed in more detail in Chapter 4.

3.6 Stress intensity factor

Before considering the variation of stress and displacement field adjacent to a crack, it is appropriate to consider the three basic types of loading a crack can experience, as illustrated in Figure 3-3. The superposition of the three loading *modes* describes the general case of cracking. Mode I (tensile opening mode) is technically the most important, as it is the most common mode, particularly in fatigue.

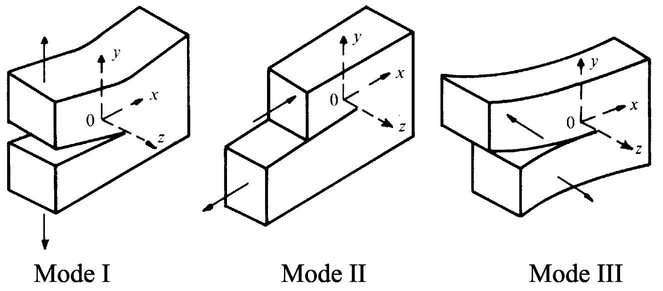

Figure 3-3. The three modes of cracking. [11]

For a certain crack configuration subjected to external forces, is it possible to derive closed-form expressions for the stresses in the body, assuming isotropic linear elastic material behaviour. The stresses and displacements for such configurations at any point near the crack tip can be derived using theory of elasticity and complex stress functions. It can be shown that the stress field in any linear elastic cracked body is given by [1, 11][3]:

$$\sigma_{ij} = \frac{K_I}{\sqrt{2\pi r}} f_{ij}(\theta) + T\delta_{ix}\delta_{jx} + (\text{terms that vanish at the crack tip}) \qquad \text{Equation 3-13}$$

where σ_{ij} is the stress tensor, r and θ as defined in Figure 3-4, K is the *stress intensity factor*, f_{ij} is a dimensionless function of θ and δ_{ij} is the Kronecker delta. The first term is the leading singular term. The second term refereed as the *T-term* contains a non-singular stress. In most linear elastic fatigue crack growth problems the usual omission of the T-stress is adequate, but in some situations significant errors can be introduced. One example is short cracks [11].

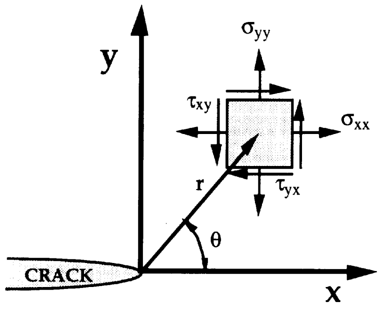

Figure 3-4. Definition of the coordinate axis ahead of a crack tip. The z-direction is normal to the paper. [1]

Each type of loading produces a 1/√r singularity at the stress tip, but K and f_{ij} depend on mode. The stress intensity factor is usually given a subscript to denote the mode of loading. Thus the stress fields ahead of a crack tip in an isotropic linear elastic material can be written as

---

[3] For detail see Anderson, T.L. *Fracture Mechanics. Fundamentals and Applications. Second edition.* (CRC press LCC, 1995) and Suresh, S. *Fatigue of Materials, second edition.* (Cambridge University Press, Cambridge, 1998).

$$\lim_{r\to 0}\sigma_{ij}^{(I)} = \frac{K_I}{\sqrt{2\pi r}} f_{ij}^{(I)}(\theta)$$ Equation 3-14a

$$\lim_{r\to 0}\sigma_{ij}^{(II)} = \frac{K_{II}}{\sqrt{2\pi r}} f_{ij}^{(II)}(\theta)$$ Equation 3-14b

$$\lim_{r\to 0}\sigma_{ij}^{(III)} = \frac{K_{III}}{\sqrt{2\pi r}} f_{ij}^{(III)}(\theta)$$ Equation 3-14c

for Modes I, II and III, respectively. For linear elastic material, individual components of stress, strain and displacement are additive within each mode. An arbitrary crack can be separated into the three different modes, and the stress field for each mode calculated. The individual contributions to a given stress field component are then summed

$$\sigma_{ij}^{total} = \sigma_{ij}^{(I)} + \sigma_{ij}^{(II)} + \sigma_{ij}^{(III)}$$ Equation 3-15

Equation 3-15 is only valid near the crack tip, where the 1/√r singularity dominates the stress field. Stresses far from the crack tip are governed by remote boundary conditions. We can define a *singularity dominated zone* as the region where Equation 3-15 and Table 3-1 describes the crack tip fields. The stress distribution in the crack plane, θ = 0, will for a mode I crack according Table 3-1 be:

$$\sigma_{xx} = \sigma_{yy} = \frac{K_I}{\sqrt{2\pi r}}$$ Equation 3-16

which is illustrated in Figure 3-5.

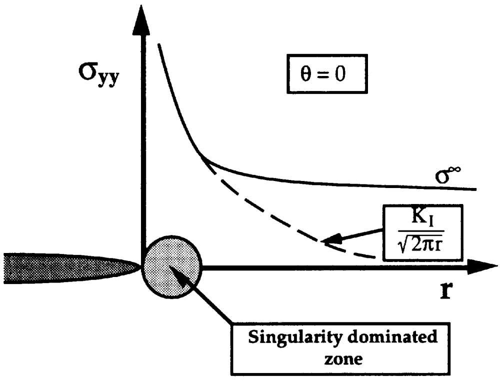

Figure 3-5. Stress field at the crack tip from remote load. [1]

	Mode I	Mode II	Mode III
σ_{xx}	$\frac{K_I}{\sqrt{2\pi r}}\cos\left(\frac{\theta}{2}\right)\left[1-\sin\left(\frac{\theta}{2}\right)\sin\left(\frac{3\theta}{2}\right)\right]$	$-\frac{K_{II}}{\sqrt{2\pi r}}\sin\left(\frac{\theta}{2}\right)\left[2+\cos\left(\frac{\theta}{2}\right)\cos\left(\frac{3\theta}{2}\right)\right]$	0
σ_{xx}	$\frac{K_I}{\sqrt{2\pi r}}\cos\left(\frac{\theta}{2}\right)\left[1+\sin\left(\frac{\theta}{2}\right)\sin\left(\frac{3\theta}{2}\right)\right]$	$\frac{K_{II}}{\sqrt{2\pi r}}\sin\left(\frac{\theta}{2}\right)\cos\left(\frac{\theta}{2}\right)\cos\left(\frac{3\theta}{2}\right)$	0
σ_{xy}	$\frac{K_I}{\sqrt{2\pi r}}\cos\left(\frac{\theta}{2}\right)\sin\left(\frac{\theta}{2}\right)\cos\left(\frac{3\theta}{2}\right)$	$\frac{K_{II}}{\sqrt{2\pi r}}\cos\left(\frac{\theta}{2}\right)\left[1-\sin\left(\frac{\theta}{2}\right)\sin\left(\frac{3\theta}{2}\right)\right]$	0
σ_{zz}	0 (Plane stress) $\nu(\sigma_{xx}+\sigma_{yy})$ (Plane strain)	0 (Plane stress) $\nu(\sigma_{xx}+\sigma_{yy})$ (Plane strain)	0
σ_{xz},	0	0	$-\frac{K_{III}}{\sqrt{2\pi r}}\sin\left(\frac{\theta}{2}\right)$
σ_{yz}	0	0	$\frac{K_{III}}{\sqrt{2\pi r}}\cos\left(\frac{\theta}{2}\right)$

Table 3-1. Stress field ahead of a crack tip for Mode I , II and III in a linear elastic, isotropic material.

K must be determined from remote load and geometry to be useful for the stress intensity factor. Closed-form solutions for K have been derived for a number of different configurations, but for complex situations the stress intensity factor must be estimated by use of FE analysis.

Two simple configurations where closed forms are available is a crack in an infinite plate in tension and an edge crack in an infinite plate in tension. The stress intensity factor is

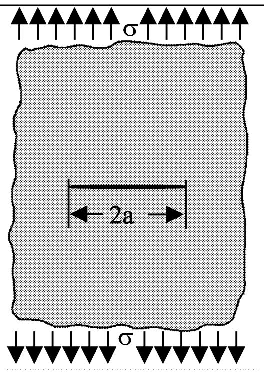 Figure 3-6. Centre crack in infinite plate.	$K_I = \sigma\sqrt{\pi a}$	Equation 3-17
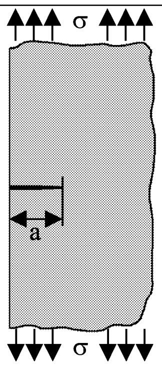 Figure 3-7. Edge crack in infinite plate.	$K_I = 1.12\sigma\sqrt{\pi a}$	Equation 3-18

The 12 % increase in K_I for the edge crack is caused by difference in compliance in the two configurations as illustrated in Figure 3-8.

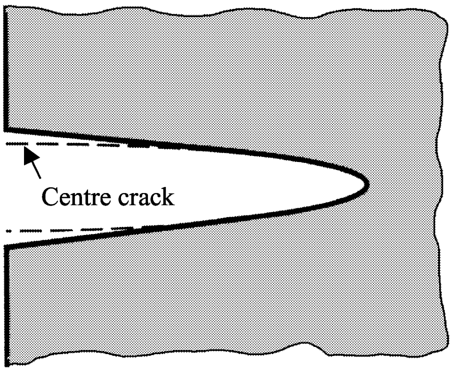

Figure 3-8. Different compliance from an edge-crack and crack in infinite plate.

3.7 Principle of superposition and similitude

The principle of superposition is generally used in linear elastic mechanics. Individual components of stress, strain and displacement are additive. This principle is used in LEFM by adding stress intensity factors of the same mode from decomposed loads as:

$$K_I^{(total)} = K_I^{(A)} + K_I^{(B)} + K_I^{(C)} + ... \qquad \text{Equation 3-19}$$

Another fundamental principle in LEFM is the principle of similitude: two cracks in a particular material-environment system will at load – geometry conditions giving similar K behave similar. However fracture mechanics will in general be load history dependent, which is not incorporated in K and hence the principle is only valid at constant amplitude testing or load history effects is incorporated. See Section 5.9 Overload.

3.8 Weight functions

The K solution is dependent on the applied boundary load. It turns out, however, that the solution to one set of boundary conditions contains sufficient information to obtain K for any other loading condition on the same geometry. Assume two arbitrary boundary load conditions and for simplicity mode I, Rice [10] showed $K_I^{(1)}$ and $K_I^{(2)}$ are related as follows:

$$K_I^{(2)} = \frac{E}{2K_I^{(1)}} \left[\int_\Gamma T_i \frac{\partial u_i^{(1)}}{\partial a} d\Gamma + \int_A F_i \frac{\partial u_i^{(1)}}{\partial a} dA \right] \qquad \text{Equation 3-20}$$

where Γ and A are the perimeter and area of the body, respectively, and u_i is the displacement in the x and y directions. Since loading system (1) and (2) are arbitrary, it follows that $K_I^{(2)}$ cannot depend on $K_I^{(1)}$ and $u_i^{(1)}$. Therefore, the function

$$h_I(x_i) = \frac{E}{2K_I^{(1)}} \frac{\partial u_i}{\partial a} \qquad \text{Equation 3-21}$$

where x_i represents the x and y coordinates, must be independent of the nature of loading system (1).

Any loading configuration can be represented by appropriate tractions applied directly on the crack face as illustrated in Figure 3-9.

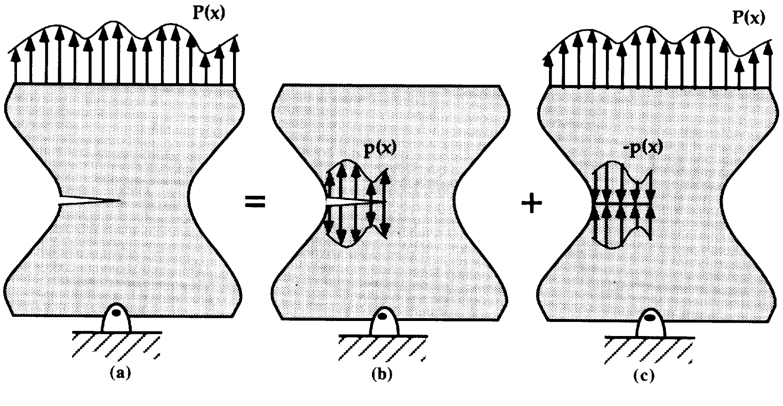

Figure 3-9. Application of superposition to replace a boundary traction P(x) with a face traction p(x) that results in the same K_I. [1]

There is no singularity for a closed crack, hence $K_I^{(c)}$ is 0 and $K_I^{(a)} = K_I^{(b)}$.

The *weight function* (Equation 3-21) is dependent on geometry only, and given the weight function for one crack configuration it is possible to calculate the K for any load condition. Thus K_I for a two-dimensional cracked body can be obtained as

$$K_I = \int_{\Gamma_c} p(x)h(x)dx \qquad \text{Equation 3-22}$$

where p(x) is the crack face traction (equal to the normal stress acting on the crack plane when the body is uncracked) and Γ_c is the perimeter of the crack. The weight function, h(x), can be interpreted as the stress intensity from a unit force applied to the crack face at x. The weight function concept works also on three dimensional, non-isotropic and mixed mode cracks.

3.9 Crack growth by LEFM

Fatigue fracture is split into three *stages*, where the first stage is crack nucleation and initiation. The second stage is stable crack growth until stage III with rapid crack growth. There are different crack growth mechanisms in the different stages. The crack growth rate in stage II, which will be the one of most interest in this work, has been investigated in thousands of investigation for various alloys. The crack rate is normally presented in log-log diagram with da/dN vs ΔK. See Figure 3-11.

The general shape of the log da/dN vs log ΔK, is a sigmoidal curve with three distinct regions. The linear portion in the intermediate part of the curve is Region II. At low ΔK values da/dN approaches zero, termed ΔK_{th}, the stress intensity threshold, where no crack growth will take place below this value. This part of the da/dN curve is Region I. At the other extreme, in Region III, the curve deviates from the linear curve and the crack growth rate accelerates approaching K_c, the critical stress intensity factor. A schematic log-log plot of da/dN versus ΔK for typical fatigue crack growth behaviour is shown in Figure 3-10.

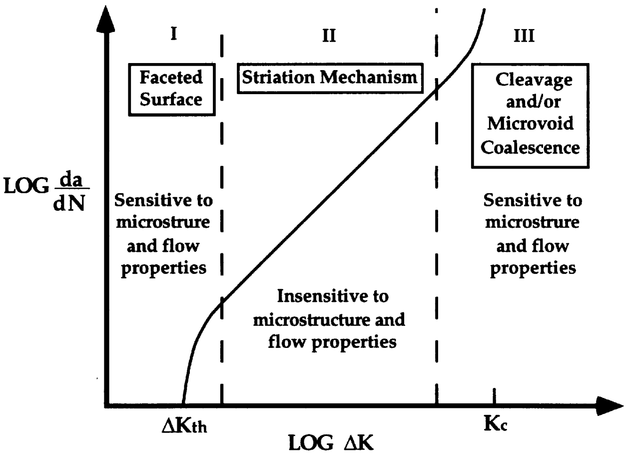

Figure 3-10. Typical crack growth behaviour in metals. [1]

Paris et al. [9] first observed and described the linear part of the log-log plot by a power law

$$\frac{da}{dN} = C\Delta K^m \qquad \text{Equation 3-23}$$

where C and m are material constants that are determined experimentally. The slope of the linear stage II varies from two to seven for various materials, mean load and environment. See Figure 3-11 and Figure 3-12. There are a number of different related equations where the non-linear parts are modelled. Many of these are empirical, although some are semi-empirical based on physical considerations. In general, the descriptions of stage II assume elastic similitude of the growing crack, ignoring the history dependency and are therefore strictly valid only for constant amplitude loading. It is important to bear in mind the possibility of history dependency when used with variable amplitude loading. See Section 4.9.

The crack growth rate is influenced by microstructure. A coarse-grained material will generally produce a higher degree of surface roughness in fatigue, and correspondingly the crack closes at higher loads that will give a reduced effective stress range. This is illustrated in Figure 3-11. At the lower R-ratio, where the closure effects are most pronounced, the coarse grained material has a higher ΔK_{th}, due to a higher closure load caused by greater surface roughness.

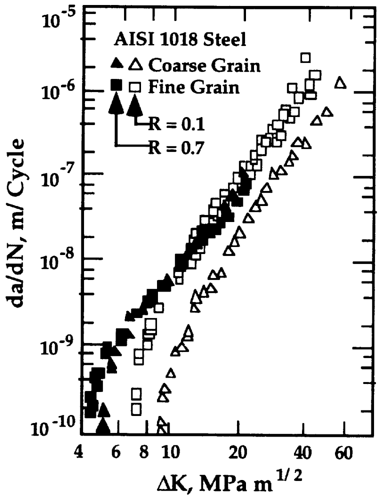

Figure 3-11. Influence from grain size and r-ration on crack propagation in steel. [4]

The ΔK_{th} is influenced by surface roughness, stress ratio, environment (corrosion, hydrogen) and microstructure. These issues will be handled in Section 4.8. K_c is also strongly influenced by microstructure, but will not be discussed in this work.

Factors such as temperature, hydrostatic pressure, load frequency and pH will influence the crack propagation rate [2] with exposure to seawater. Corrosion products will decrease the effective stress range by crack closure. Hydrogen at the crack tip will for some alloys embrittle the material at the crack tip, and increase the crack propagation rate. This is illustrated by the higher growth rates for steel in seawater exposed to cathodic overprotection, see curves for potential levels of – 850MV and -1100MV in Figure 3-12.

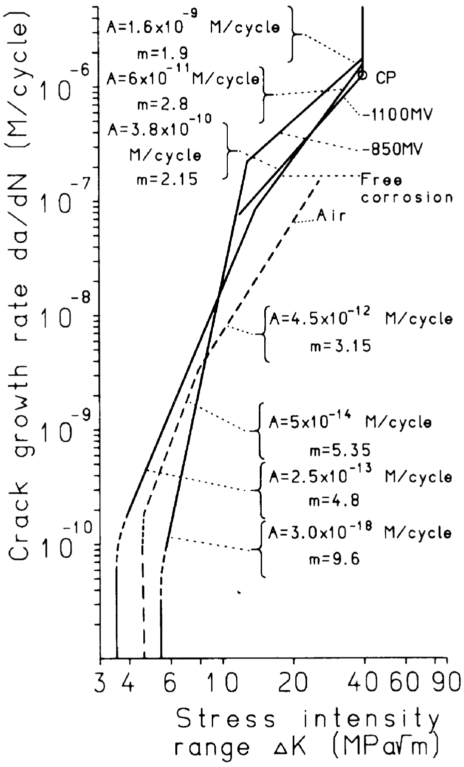

Figure 3-12. Crack growth rate for various environmental exposures. [2]

3.10 References:

1 Anderson T.L. (1995) Fracture Mechanics. Fundamentals and Applications. Second edition. CRC press LCC.

2 Bardal E. (1985) Effect of marine environment and cathodic protection on fatigue of structural steel. In Fatigue Handbook, offshore steel structures. Edited by Almar-Næss A. Tapir, Trondheim. pp 291-312.

3 Dieter G.E. (1988) Mechanical Metallurgy, SI metric edition. McGraw-Hill, Singapore.

4 Gray G.T., Williams J.C. and Thompson A.W. (1983) Roughness Induced Crack Closure: An explanation for microstructurally sensitive fatigue crack growth. *Metallurgical Transaction A* 14, 421-433.

5 Griffith A.A. (1920) The Phenomena of Rupture and Flow in Solids. *Philosophical Transaction, Series A* 221, 163-198.

6 Ingles C.E. (1913) Stresses in a Plate Due to the Presence of Cracks and Sharp Corners. *Transaction of the Institution of Naval Architects* 55, 219-230.

7 Irwin G.R. (1948) Fracture dynamics. *Fracturing of Metals* 147-166.

8 Orowan E. (1948) Fracture and Strength of Solids. *Reports of Progress in Physics* 185.

9 Paris P.C., Gomez R.E. and Anderson W.E. (1961) A rational analytic theory of fatigue. *The Trend in Engineering* 13, 9-14.

10 Rice J.R. (1976) Some remarks on elastic crack-tip stress fields. *International Journal of Solid and Structures* 8, 751-758.
11 Suresh S. (1998) Fatigue of Materials, second edition. Cambridge University Press, Cambridge.

4 High cycle fatigue of machined steel components in residual stress field: A state of the art literature survey.

4.1 Notation

δ	crack tip opening [m]
ε	strain
$\dot{\varepsilon}$	strain rate [1/s]
ε_{ap}	plastic strain amplitude
ε_e	elastic strain amplitude
ε'_f	material parameter in Coffin-Manson law
ε_{pl}	plastic strain
ν	Poisson's ratio
ρ	plastic yield zone at crack tip from the Dugdale Model [m]
$\Delta\sigma$	stress range = σ_{max} - σ_{min} [MPa]
$\Delta\sigma_{eff}$	effective stress range = σ_{max} - σ_{op} [MPa]
σ_a	stress amplitude [MPa]
$\sigma_{a,s}$	stress amplitude at surface [MPa]
σ_{cl}	crack closure stress [MPa]
σ_e	fatigue limit [MPa]
σ_{op}	crack opening stress [MPa]
σ^{res}	residual stress [MPa]
σ_s	saturation stress [MPa]
$\Delta\sigma_{th}$	threshold stress [MPa]
σ_y	yield stress [MPa]
a	crack length [m]
A	empirical fatigue material constant
a_0	critical crack length [m]
a_{eff}	effective crack length [m]
$a_{non\ prop}$	Non-propagating crack length
ACR	adjusted compliance ratio
ASTM	American Society for testing and materials
BCC	body centered cubic
c	material parameter in Coffein-Manson law
CSS	cyclic stress-strain

CT	compact tension
CTOD	crack tip opening displacement
d_g	grain size dimension [m]
E	Young's modulus [MPa]
EPFM	elastic-plastic fracture mechanics
FCC	face centered cubic
FE	finite element
G	Shear modulus [MPa]
HCF	high cycle fatigue
K	stress intensity factor [$MNm^{-3/2}$]
ΔK	stress intensity range = $K_{max} - K_{min}$ [$MNm^{-3/2}$]
K_c	material and thickness dependent fracture toughness [$MNm^{-3/2}$]
K_{cl}	closure stress intensity factor [$MNm^{-3/2}$]
ΔK_{eff}	effective stress intensity range = $K_{max} - K_{op}$ [$MNm^{-3/2}$]
$\Delta K_{eff,\, th}$	effective stress intensity threshold [$MNm^{-3/2}$]
$\Delta K_{eff,\, th\infty}$	effective stress intensity threshold, long crack [$MNm^{-3/2}$]
$K^*_{max,\, th}$	stress intensity threshold value in Unified Approach model [$MNm^{-3/2}$]
K_{op}	opening stress intensity factor [$MNm^{-3/2}$]
$K_{op,\, th}$	opening stress intensity factor at threshold [$MNm^{-3/2}$]
K_t	stress concentration factor
ΔK_{th}	stress intensity threshold [$MNm^{-3/2}$]
ΔK^*_{th}	threshold value in Unified Approach model [$MNm^{-3/2}$]
LEFM	linear-elastic fracture mechanics
n	empirical fatigue material constant
N	number of cycles
N_f	number of cycles to fracture
P	far-field load [N]
PSB	persistent slip band
Q	LEFM finite size correction factor
R	load ratio = P_{min} / P_{max}
r	crack tip/notch tip radius
r_c	cyclic plastic zone at crack tip for growing crack from FE analysis [m]
R_{eff}	effective R-ratio including crack closure
r_p	plastic yield zone at crack tip satisfying stress equilibrium [m]
r_y	zone at crack tip with stress above σ_y [m]
S	far-field stress [MPa]
S_{cl}	far-field crack closure stress [MPa]
S_{res}	residual stress [MPa]
T_0	transition temperature [K]
T_m	melting temperature [K]

4.2 Introduction

In previous chapters several well-known and accepted classical theories that are available in most textbooks on fatigue have been discussed. There is not much controversy amongst researchers regarding the basic aspects of these theories. In this Chapter the state of the art of crack initiation and growth in residual stress fields will be presented. Topics on which some researchers around the world may disagree are discussed in some detail.

4.3 CSS –curve

Microplastic cyclic strains of the order of 10^{-5} to 10^{-4} at microscopic irregularities will lead to fatigue fracture at applied loads that are well below yield. The relationship between the cyclic plastic strain amplitude ε_{ap} and the fatigue life N_f was first expressed 45 years ago by the empirical *Coffin-Manson-law* [69, 99]:

$$\varepsilon_{ap} = \varepsilon_f'\left(2N_f\right)^c \qquad \text{Equation 4-1}$$

where ε'_f is the strain at fracture, and c is a constant. From the Coffin-Manson-law the crucial loading variable is the cyclic plastic strain amplitude rather than the stress amplitude. The total accumulated plastic strain, ε_f', before fracture is of the order 10^2 - 10^3 for various metals. At high plastic strain amplitudes the accumulated plastic strain will not accurately capture the extent of permanent damage where a significant fraction of dislocation[4] motions can be reversible [94]. The fatigue limit is plastic strains in the order of 10^{-5} to 10^{-4}.

A stress-strain loop for constant strain cycling is shown in Figure 4-1. The test starts at O. The load is increased and reaches the yield stress at A. With still increasing load the plastic strain dominates until the test strain is reached at B. The load is then decreased and the material yields in compression at an absolute value less than the stress in B at C. This is due to the *Bauscinger effect*[5]. This effect is seen in all metals [25], but not always with the magnitude seen in Figure 4-2. After the test strain is reached in compression, the specimen is loaded in tension until test strain is reached for second time. The hysteresis loop is now developed. The dimension of the hysteresis loop is described by its width $\Delta\varepsilon$, its height $\Delta\sigma$ and the area fraction[6]. The total strain range $\Delta\varepsilon$ consists of the elastic strain component $\Delta\varepsilon_e = \Delta\sigma / E$ plus the plastic strain component $\Delta\varepsilon_p$.

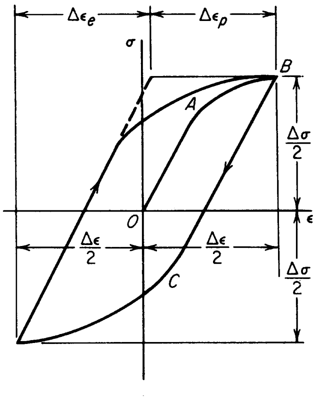

Figure 4-1. Cyclic stress-strain curve. [25]

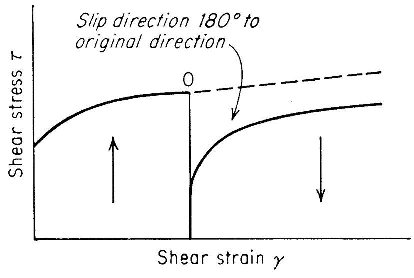

Figure 4-2. The Bauschinger effect. [25]

---

[4] Line defect in the atomic lattice of metal.

[5] A dislocation pileup at a barrier will need less energy to move away from the barrier than passing it.

[6] Area inside the hysteresis loop divided by the square defined by $\Delta\sigma*\Delta\varepsilon$.

The dislocation motion is not completely reversible. The dislocation density and structure will be modified giving changes in the stress-strain response during cyclic straining. Depending on the initial state a metal may undergo *cyclic hardening, softening* or remain *cyclically stable.* If σ_{max} increases during constant strain amplitude testing, the material is cyclic hardening, conversely the material will undergo cyclic softening. This is illustrated in Figure 4-3 and Figure 4-4.

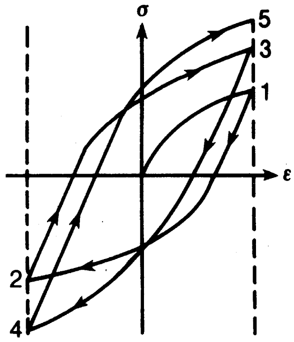

Figure 4-3. Cyclic hardening. [25]

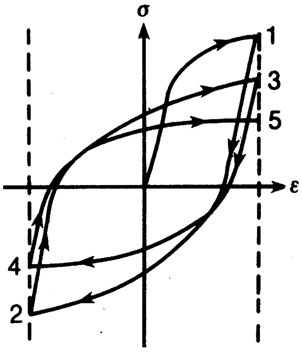

Figure 4-4. Cyclic softening. [25]

Strain hardened metals typically fatigue soften before the hysteresis loops stabilise. Further rapid change at the end of the fatigue life is often observed resulting from macroscopic crack propagation. The number of cycles to saturation depends on the material's inherent slip system[7]. From the ability for a dislocation to cross-slip, change slip system, all metals can roughly be divided into two groups: wavy-slip[8] and planar-slip[9]. All BCC[10] metals and FCC[11] metals with high stacking fault energy [25, 52] have wavy-slip. Generally, wavy-slip systems will cyclic-saturate faster than planar-slip systems [52].

In both stress controlled and strain controlled tests, the respective strain or stress amplitude reach a stable saturation value after an initial shake-down period. Connecting the tips for the different stabilised hysteresis loops gives the *cyclic stress-strain curve (CSS).* Only a part of the total number of cycles to fracture will show hardening/softening. The majority of fatigue life is under steady-state conditions. During the saturation period the dislocation structure is modified until a stable structure representative for the applied load is reached, where after the structure essentially remains the same throughout the fatigue life. The CSS curve is often quite different from the monotonic stress-strain curve, as illustrated in Figure 4-6.

---

[7] Plane and direction of dislocation movement dependent on the atomic structure of specific metal.

[8] Wavy-slip material: Aluminium, copper, pure iron, carbon steels, nickel [52]

[9] Planar-slip metail: e.g. Austenitic steel, α-brass, Fe-Si alloys [52]

[10] Body-centered cubic atom-lattice system. (e.g. alpha-iron, columbium, tantalum, chromium, molybenum and tungsten)

[11] Face-centered cubic system. (e.g. Aluminium, copper, gold, lead, silver and nickel)

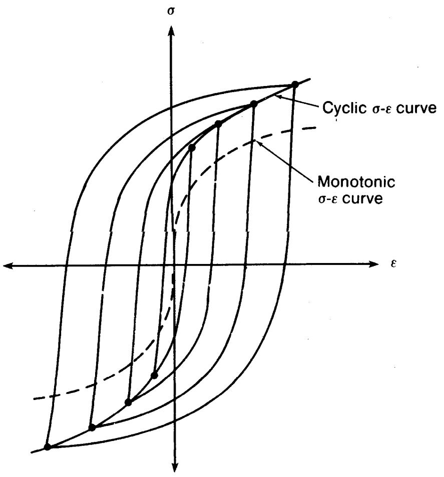

Figure 4-5. Cyclic stress-strain curve. [25]

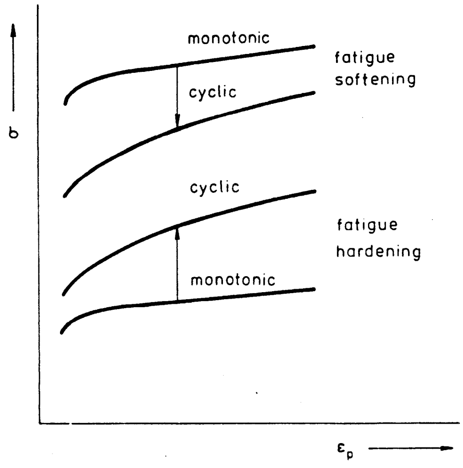

Figure 4-6. Comparison of tensile (monotonic) and cyclic stress-strain curve. Schematic. [52]

The most important difference between BCC- versus FCC-metals is the strong temperature- and strain dependence in BCC, and BCC is strongly dependent on interstitial atoms such as C, N and O [79]. A transition temperature T_0, where a change in dislocation movement mechanism takes place is

$$0.1T_m \leq T_o \leq 0.2T_m \quad \text{Equation 4-2}$$

according Mughrabi [79]. Also, T_0 will increase with increasing strain rate, $\dot{\varepsilon}$. This will give transition temperature around room temperature for steels[12] at $\dot{\varepsilon} < 10^{-4}\ s^{-1}$. Normally fatigue testing is done at frequency giving $\dot{\varepsilon} \approx 10^{-2}\ s^{-1}$ rising T_0 above room temperature [79] for steel. At $T > T_0$ the BCC will behave much like FCC [79, 90] especially with small amounts of interstitial atoms present [79, 89]. Cycled at $T < T_0$ and low $\Delta\varepsilon_{pl}$ no microstructural changes takes place, and the CSS-curve has a small plateau without any noticeable hardening. See Figure 4-7. A well developed dislocation cell structure is however observed at the surface with a significant hardening, but in the bulk the dislocation density is very low and hence no hardening occurs. Mughrabi [79] estimates the hardened layer to be 10 μm, which will be insignificant for the behavior of a test specimen showing no hardening at the plateau. The hardened cell structure layer is expected to increase the fatigue resistance if the cell structure is developed before fatigue initiation. The cell structure follows approximately the trace of the primary glide plane. The ill-defined surface slip bands at which the fatigue cracks initiates in BCC metals is possibly linked to this phenomena [79].

---

[12] Typical melting temperature for steel is 1750K.

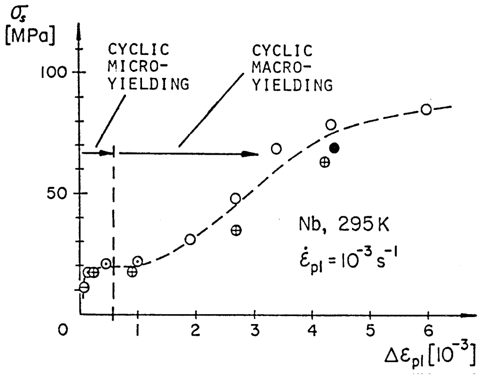

Figure 4-7. CSS-curve for a single Nb crystal. [79]

A wavy-slip material will saturate relatively fast, in contrast to planar-slip materials. As an example pure copper in the high cycle region saturates after 1 - 4% of fatigue life (In Figure 4-26 a cyclic stress-strain evolution as a function of cycles is shown), whereas a planar-slip Cu-30%Zn alloy takes 30-40% of fatigue life before saturation [52]. When saturation of the hysteresis loop is not obtained the maximum hardening/minimum softening before fracture, or the value at 50% of fatigue life is normally used to establish a CSS-curve.

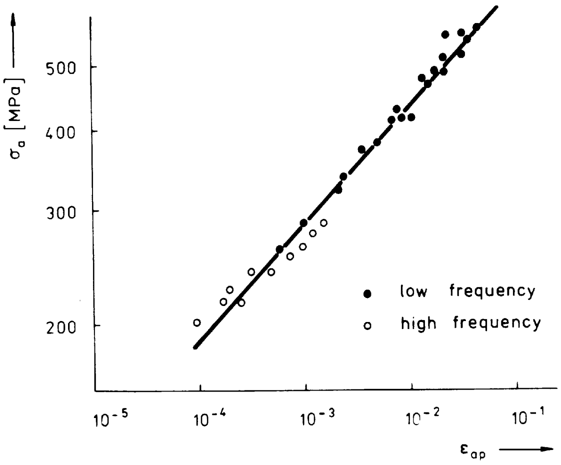

Figure 4-8. Cyclic stress-strain curve for carbon steel 11423 covering both high- and low cycle regions. [52]

At the end of the fatigue life in wavy-slip materials secondary hardening is observed [18, 105]. In order to study this effect, polycrystalline copper was fatigued in vacuum to prolong the life by excluding environmental effects. As indicated in Figure 4-9 the change is seen to be small and the effect is considered insignificant for this study.

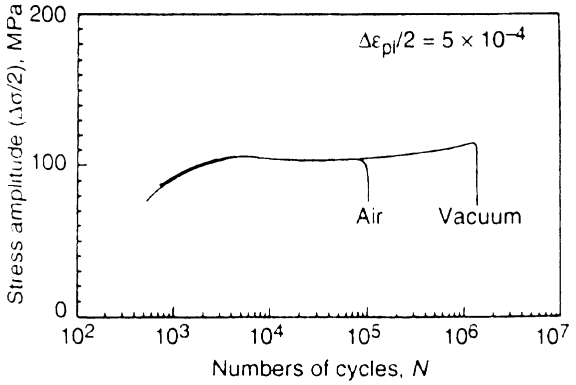

Figure 4-9. Deformation curve for polycrystalline copper in air and vacuum. [18]

The cyclic stress-strain curves depend on the temperature and strain rate in a similar way to the monotonic curves. The lower the temperature, the higher the saturated-stress amplitude for a given strain amplitude. This holds true in general for all metals.

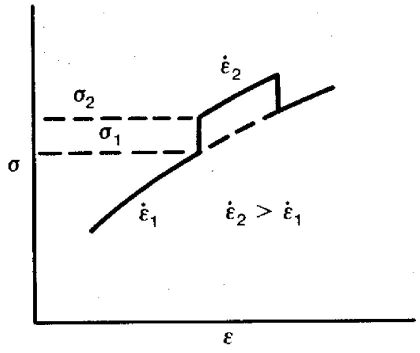

Figure 4-10. Influence of strain rate. [25]

By changing the temperature during fatigue wavy-slip material have shown no, or only small, temperature historic dependency [52], as seen in Figure 4-11 for a low-carbon steel. This is not valid for material undergoing phase transformation within the investigated range of temperature.

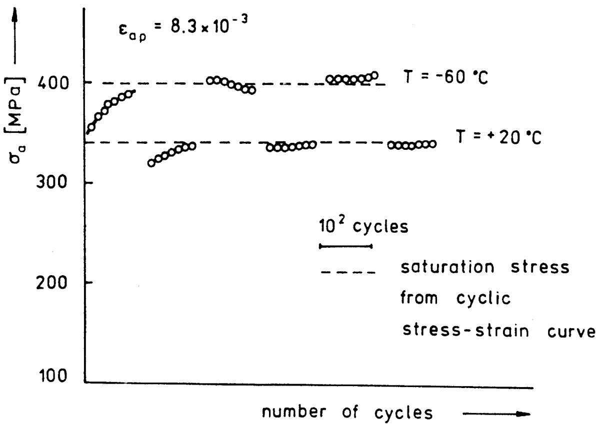

Figure 4-11. Behaviour of stress amplitude during changes in temperature. Plastic-strain amplitude held constant, carbon steel. [52]

4.4 Crack initiation

Crack initiation is a definition strongly linked to the scale of observation. A material scientist is likely to define crack initiation to end at the formation of flaws along persistent slip bands, whereas a mechanical engineer may define end of fatigue crack initiation when the crack is observed through a magnifying glass.

Cyclic loading of high purity wavy-slip material at low- or moderate strain amplitudes will develop slip bands at the surface in grains with favourable orientation. This is in contrast to monotonic strain where the same slip systems are active, but usually widespread throughout all the grains [25]. After removing the slip bands by electropolishing some of the slip bands will reappear at the same locations, thereby the name persistent slip bands (PSB). A PSB consists of lamellas of high local dislocation motions parallel to the active slip plane and is typically ≥ 1 μm in FCC. The strain is localised in the soft PSB ladder structure (See Figure 4-12), whereas the surrounding matrix of rigid vein structure does not absorb much strain (See Figure 4-13). Microhardness measurements on fatigue induced slip bands shows that the PSBs are much softer than the matrix [45]. Cyclic slip at PSBs is partly irreversible forming extrusions, intrusions and protrusions consisting of several intrusions and extrusions (See Figure 4-14). A protrusion is a surface uplift from tens of PSBs and/or matrix lamellas.

Dilute FCC solid solution alloys show similar cyclic strain localisation in PSB. The precipitation-hardened[13] alloys are of particular interest. The reason is the coherent precipitates, which are easily shearable. The repetitive cutting of the precipitates during cycling from to-and-fro degrades the strengthening precipitates and localises the strain to a persistent slip band. The PSBs are very thin, ≤ 0.1 μm [79]. As a consequence of the strain localization is an initial period of hardening observed, following by drastic cyclic softening leading to fracture before saturation is obtained [79]. In alloys with large shearable particles where planar-slip is favoured due to the composition of the matrix an

---

[13] Precipitation hardening, or age hardening, is produced by solution treating and quenching an alloy in which a second phase is in solid solution at the elevated temperature but precipitates upon quenching and ageing at a lower temperature. The age-hardened aluminium alloys and copper-beryllium alloys are common examples.

immediate very severe strain localization is observed. Examples of such alloys are nickel-based superalloys and austenitic steels hardened by coherent particles [79].

In materials where PSBs are formed, cracks nucleate at the PSB/matrix glide plane and particular for small grained polycrystals at the intrusions [79]. See Figure 4-15. The early crack propagation, stage I, along the PSB is very slow and may extend for only a few grain diameters before the crack propagation changes into stage II crack and growth takes place normal to the maximum applied stress.

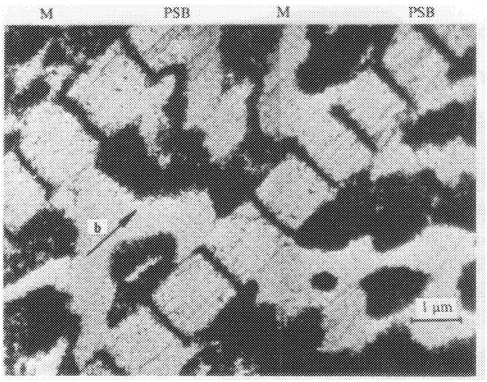

Figure 4-12. Persistent slip band in fatigued copper. M: matrix, PSB. [79]

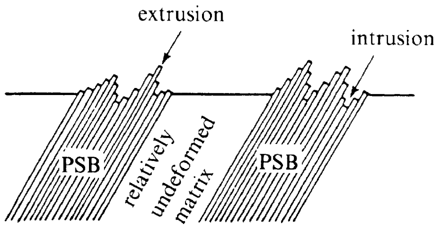

Figure 4-13. Rough surface containing extrusions and intrusions by PSB from cyclic plastic strains. [94]

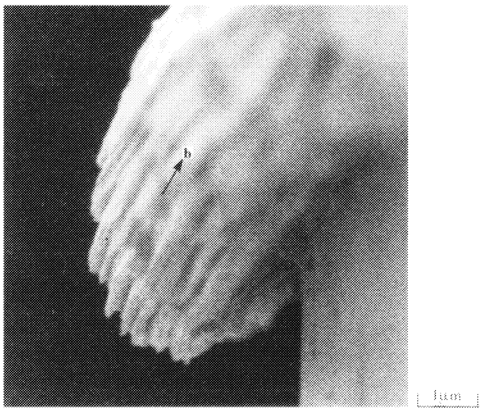

Figure 4-14. Protrusion of PSBs in copper single crystal. N = 40 000. [79]

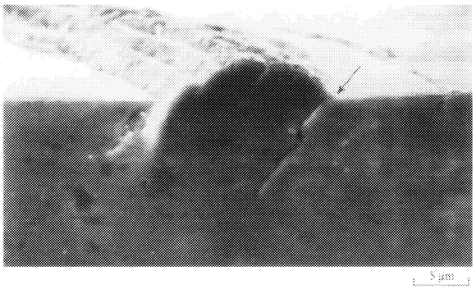

Figure 4-15. Fatigue crack initiation (denoted by an arrow) at PSB after 60 000 cycles in a copper crystal. [68]

The surface roughness has a strong influence on the fatigue initiation life. See also Figure 2-9. Basinski et al. [9] found in single crystal copper with coarse PSBs traverse the bulk, elimination of the surface roughness from PSBs by electropolishing drastically increased the fatigue life.

It is well known that the environment influences the fatigue initiation. Fatigue life is markedly improved in vacuum or in dry, oxygen-free environment compared to moist laboratory air. See Figure 4-9. Oxide layers form in a chemically aggressive environment (e.g. air) on the extruded fresh material surface from slip, making reverse slip difficult, or embrittling substances (such as hydrogen and oxygen) are transported to the bulk along the PSB, and thereby facilitating crack nucleation.

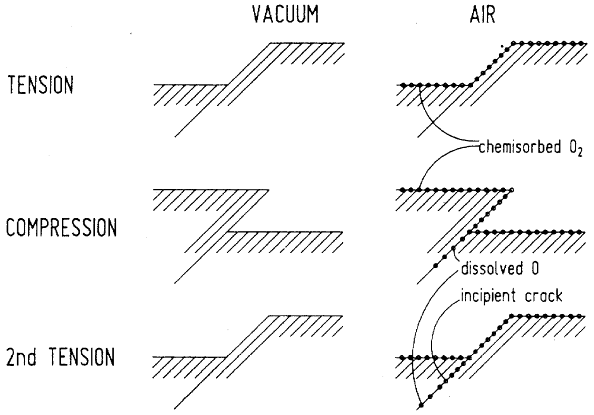

Figure 4-16. Transportation of oxygen along a slip systems. [58]

At T > T_0 BCC metals will develop PSB, especially with small amount of interstitial atoms present [79]. Channels with few dislocations having the appearance of PSBs embedded in a matrix of veins are observed. PSB are generally not observed in pure BCC-metals fatigued below T_0 where a thin cell-structure at the surface will be established [89].

Crack initiation in α-Fe and low carbon steel at "normal" fatigue testing strain rates is at ill-defined slip-band and intergranular [79]. The reason for intergranular crack initiation is the unsymmetrical dislocation motions occurring in BCC giving distorted surface grains where crack might initiate at the grain boundary. This is particularly observed at $T < T_0$ and high ε_{ap}.

In commercial alloys fatigue crack nucleation often takes place at irregularities such as gas entrapments, inclusions, dents and regions with microstructural and chemical nonuniformity. While cracks nucleate at the surface for high purity alloys, near-surface and interior nucleation is possible in commercial alloys. The mechanics of crack nucleation at inclusions and pores (defects) is dependent on the matrix-inclusion bonding strength, the relative strength of the matrix and the defect and the susceptibility of matrix and inclusion corrosion.

Nucleation of fatigue cracks is often found in the bottom of pits. A form of localised corrosion with numerous small cavities takes place on the metal surface. Pits are typically smaller than a millimetre in depth and have a length/depth ratio equal or greater than one. They occur most frequently in solutions of near neutral pH, containing chloride, bromide and hypocloride ions [22]. The most common structural materials susceptible to pitting are stainless steels and aluminium alloys [22]. In the pit the concentration of metal chlorides will increase from chemical reactions and the surroundings will be cathodic suppressing the formation of nearby pits. The increased pH level of the corrosive medium inside the pit will furthermore increase the fatigue crack growth rate. High velocity of the solution will decrease the concentration of chlorides and retard pit and crack growth [22]. In narrow gaps between contacting plates and in threaded connections the solution velocity is small, and consequently pitting attacks is often found.

4.5 Plastic deformation at crack tip

The singularity at the crack tip will cause yielding. By substituting σ_{xx} in Equation 3-16 by the yield stress, $\sigma_{y,}$ is a first approximation of the plastic zone size for elastic-perfect-plastic material in plane stress obtained

$$r_y = \frac{1}{2\pi}\left(\frac{K_I}{\sigma_y}\right)^2 \qquad \text{Equation 4-3}$$

Plane strain will due to the triaxial stress state have a reduced plastic zone size, and the approximate plastic zone correction is reduced by a factor of three [6, 96].

$$r_y = \frac{1}{6\pi}\left(\frac{K_I}{\sigma_y}\right)^2 \qquad \text{Equation 4-4}$$

Also, the shape of the plastic zone will change from plane stress to plane strain. The zone in which $\sigma > \sigma_y$ from Table 3-1 using von Mises yield criterion is shown in Figure 4-17.

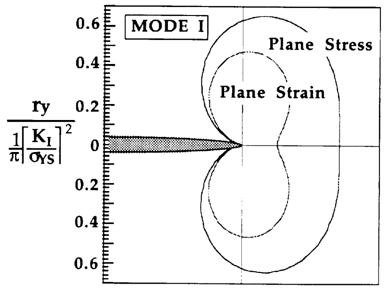

Figure 4-17. Plastic zone calculated from Table 3-1 and von Mises yield criterion. [6]

The simple approximation giving Equation 4-3 is only valid for limited yield zone because it is based on elastic crack tip solution where no redistribution of the stresses is incorporated in order to satisfy equilibrium. In Figure 4-18 the hatched area is truncated, and the plastic zone must increase to give a new stress distribution which integrated will give the same force as the original elastic distribution. A force balance considering the yield zone

$$r_p\sigma_y = \int_0^{r_y} \sigma_{yy}dr = \int_0^{r_y} \frac{K_I}{\sqrt{2\pi r}}dr \qquad \text{Equation 4-5}$$

integrated and replacing r_y with Equation 4-3

$$r_p = \frac{1}{\pi}\left(\frac{K_I}{\sigma_y}\right)^2 \qquad \text{Equation 4-6}$$

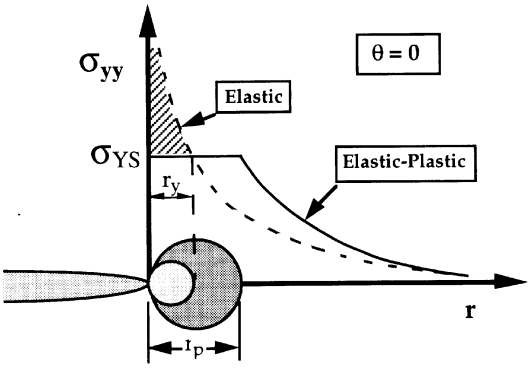

Figure 4-18. Stress distribution at crack tip. [6]

As seen in Figure 4-18 the stress in the redistributed area is higher than the elastic solution predicts (Equation 3-16), which will be described by a higher effective stress intensity factor. A good approximation was proposed by Irwin (1961) where an effective crack length

$$a_{eff} = a + r_p \qquad \text{Equation 4-7}$$

is used. This is illustrated in Figure 4-19.

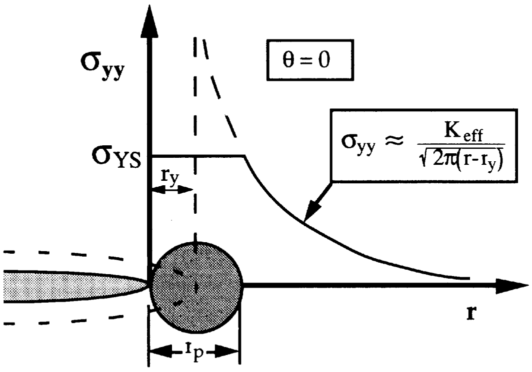

Figure 4-19. Effective crack length proposed by Irwin used to get a effective stress intensity factor. [6]

For the geometry of interest the effective crack length is used and K_{eff} is

$$K_{eff} = F(a_{eff})\sigma\sqrt{\pi a_{eff}} \qquad \text{Equation 4-8}$$

which normally must be solved by iteration.

Another model used to predict the plastic zone and K_{eff} is the *Dugdale Model* also called the *Strip Yield Model*. A plastic zone in the crack plane of a thin plate with length ρ is added to the crack length giving an effective crack length similar to the Irwin model, see Figure 4-20. Perfect linear elastic-plastic material and plane stress is assumed and LEFM is used by adding two elastic solutions, the remote applied stress and the constant stress in the yield zone of opposite sign to the applied stress equal to σ_y in magnitude (The principle of superposition is valid for elastic models. See Section 3.7). In the plastic model there will not be a singularity at the crack tip, and the stress concentration factors from the two load conditions must balance each other. From this condition the size of the plastic zone is obtained:

$$\rho = \frac{\pi}{8}\left(\frac{K_I}{\sigma_y}\right)^2 \qquad \text{Equation 4-9}$$

for $\sigma \ll \sigma_y$ and consequently $\rho \ll a$. Note the difference (20%) between Equation 4-6 and Equation 4-9.

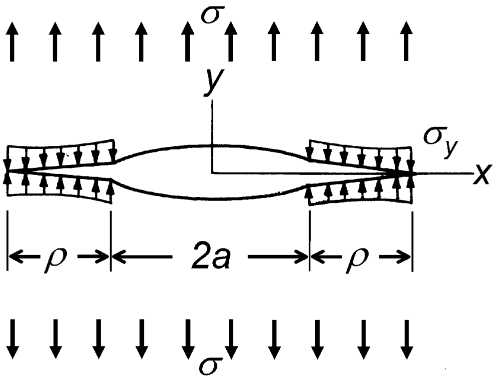

Figure 4-20. Dugdale plastic zone model.

As seen in Figure 4-21 LEFM is approximately valid for $\sigma / \sigma_y < 0.5$. The Irwin and Dugdal model gives the same K_{eff} at $\sigma / \sigma_y < 0.85$. The Dugdale model is not representing the plastic zone in metals well, but is better suited for polymers [6]. With strain hardened materials the plastic zone be will smaller, for engineering materials typically 70-80% smaller than the cyclic plastic zone for perfect plastic materials [72].

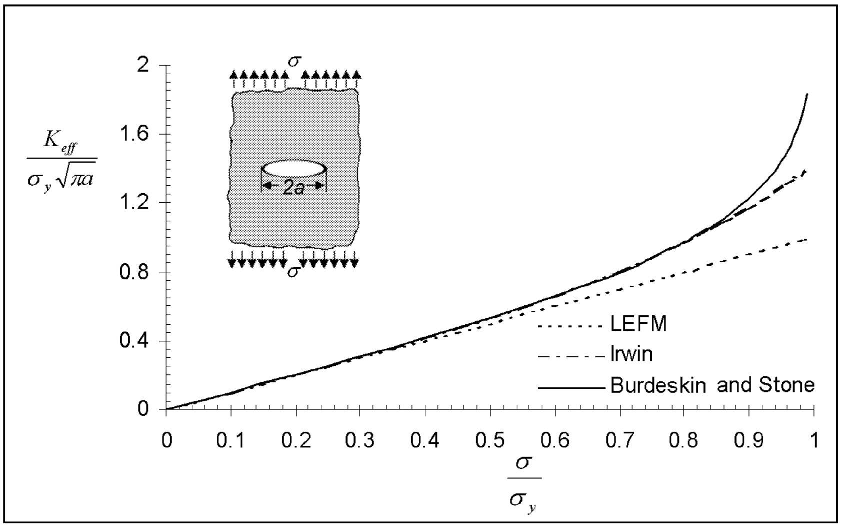

Figure 4-21. Comparison of the effect from plastic zone correction[14].

The existence of a reversed plastic zone in front of a fatigue crack has been known for a long time [94]. Looking at an elastic-perfect plastic material without crack closure and with no crack tip blunting this phenomenon is easy to explain. Under far-field tension load (P) a plastic zone will form, with size approximated by Equation 4-6 or Equation 4-9. At unloading with ΔP plastic yielding will take place once more, but at a smaller scale depending on the magnitude of ΔP compared to P and the "new" yield stress of $2\sigma_y$ as indicated in Figure 4-22. Using Equation 4-6 or Equation 4-9 to calculate the extend of the monotonic plastic zone where r_p and K are replaced by Δr_p and ΔK respectively, and replacing σ_y with $2\sigma_y$ gives

$$\Delta r_p = \frac{1}{4} r_p \qquad \text{Equation 4-10}$$

At unloading an initial load in tension to zero far-field load a residual stress[15] field in compression will remain near the crack tip, and remain at cycling where $\Delta P < P$ assuming elastic-perfect material without hardening. With $\Delta P > P$ and neglecting crack closure the initial residual stress field in compression will decrease in magnitude and become residual stress field in tension depending on ΔP. This will influence crack growth in compression. (See Section 4.13 Crack growth in residual stress fields)

Residual stress at the crack tip can also influence the phenomena of transient crack growth in variable fatigue loading [94]. (See Section 4.9 Overload)

---

[14] Burdeskin F.M and Stone D. E. W. "The crack opening displacement approach to fracture mechanics in yielding materials", Journal of Strain Analysis, **1**, 1966, pp. 145-153 is a more realistic model than the model related to the Strip Yield Model.

[15] Described in chapter 4.6 Residual stress.

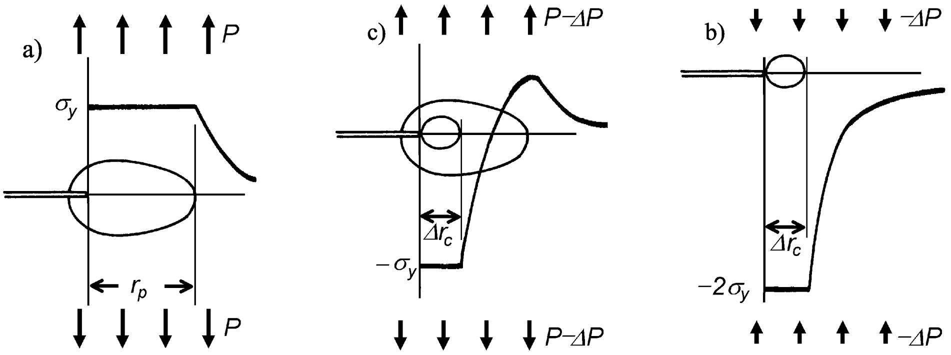

Figure 4-22. Schematic presentation of plastic yield zone in front of a crack in a linear-perfect plastic solid neglecting crack closure. a) monotonic yield zone, b) subsequent plastic yield zone and stress distribution after load reduction of ΔP and c) superimposed stress distribution from a and b.

Budiansky and Hutchinson [15] performed in 1978 an analysis based on the Dugdale Model of cyclic plastic zone in an ideally plastic solid under plane stress including crack closure. At R=0, they found the cyclic plastic zone was less than 10% of the monotonic cyclic zone which is mostly caused by the premature contact of the crack surfaces from residual displacement in the wake of the crack.

This is supported by a FE plastic analysis done by McClung [72] on steel with high kinematic hardening and aluminum with low kinematic hardening. He found the estimate in Equation 4-6 to be valid for low hardening rates. As expected the plastic zone was smaller for a material with higher strain hardening where less redistribution of the stress will take place. The plastic size was found to be 5% higher for a growing crack compared to a stationary crack. See Figure 4-23.

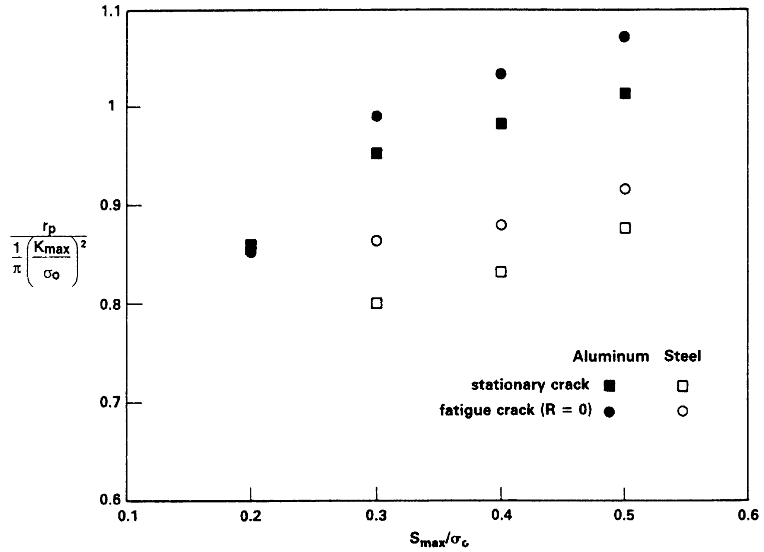

Figure 4-23. Normalized plastic zone widths along the crack plane at maximum load for stationary and growing crack. [72]

The reversed plastic zone size found was in good agreement with Equation 4-10 fatigued at R = 0, where $r_c = 0.22\ r_p$ compared to 0.25 calculated in Equation 4-10 where closure is ignored. Crack closure can generally not be ignored, but the approximation proposed by McClung indicates limited crack closure for plane stress. The values for growing crack r_c / Δr_p was from 0.09 to 0.16 which is in good agreement with the approximation by Budiansky& Huchinson of 0.1 [15].

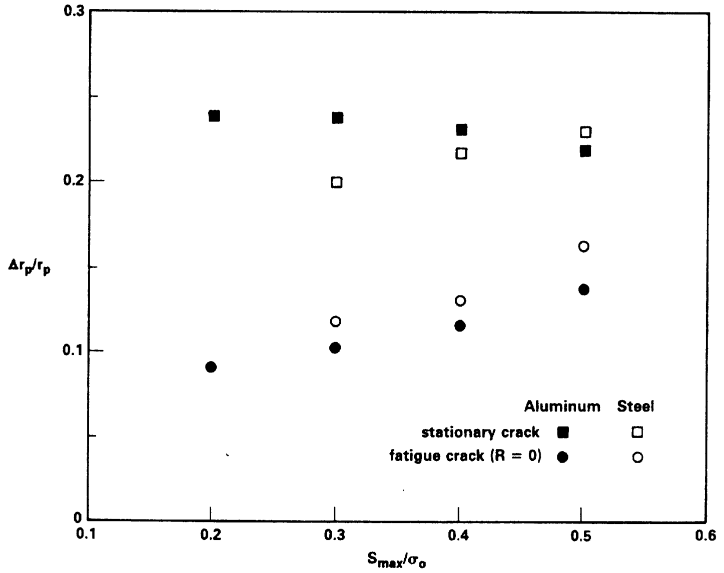

Figure 4-24. Ratio of reversed plastic zone size to forward plastic zone size for stationary and growing crack. [72]

McClung proposed a simple approximate model where closure and kinematic hardening is incorporated.

$$U = \frac{S_{\max} - S_{cl}}{S_{\max} - S_{\min}} \qquad \text{Equation 4-11}$$

$$\frac{\Delta r_p}{r_p} = \left(\frac{U}{2 - (1 - U)\frac{S_{\max}}{\sigma_y}} \right)^2 \qquad \text{Equation 4-12}$$

A closure far-field stress at which the crack is starting to close must be either calculated by FEM or measured in test. The McClung model was found to give excellent agreement compared to FE analyses. Closure will be discussed further in Section 4-8 Crack closure.

4.6 Residual stress

Residual stresses have for a long time been known to influence fatigue performance. Residual stresses are internal local structural stresses in self-equilibrium through the cross-section. In contradiction to primary loads residual stress will never lead to plastic collapse of a structure. However, residual stresses can contribute significantly to the stress state near a crack tip, thereby influencing the possibility of complete fracture.

Residual stresses are generally differentiated in two groups; microstress and macrostress, the latter one generally referred to as residual stresses in literature.

Microstresses are found in two-phase material, where the microstress must balance between the phases. Microstresses can be determined by diffraction measurement (see Section 5.3.4). In contrast to macrostresses microstresses may be evenly distributed over the cross-section and will be different in the phases present. Generally steel will have two phases: ferrite and carbide structure, thus, both macrostress and microstress will be present. Microstresses will not influence the fatigue initiation [4, 106], nor the crack propagation rate [5] because they fade out rapidly in contrast to macrostresses.

By definition, macrostresses are the same in all the phases present in the material. Macrostresses are normally caused by thermal expansion during solidification (from melting or welding), from local plastic deformation from surface preparation (e.g.: cutting, milling, turning, grinding, rolling, sandblasting and hammering) or overload. In general macrostress is introduced in a macrostress-free structure after solidification by introducing a plastic strain gradient locally.

Tensile residual stresses are known to decrease fatigue life, whereas compressive residual stresses will increase the fatigue life. Mechanical industry has long been aware of the benefit from sandblasting, hammering and rolling of threads. During the Second World War cracks in the teeth of a large gear were cut out and peened to extend the life of a part difficult to replace due to the war [38]. In the last decade there has been an increased use of hammer peening of welds in the ship and offshore industry [43, 50]. Cold expansion of bolt and rivet holes after repair and life extension has become a standard procedure in the aircraft industry.

4.7 Relaxation of residual stresses

A crucial question regarding the effectiveness of compressive residual stresses is the stability of these stresses during fatigue and factors influencing a possible relaxation. Superimposed thermal and mechanical loading is of decisive importance for the stability of the residual stresses. The relaxation of residual stress can be split into two categories. First, immediate relaxation due to yielding. This relaxation is reasonably easy to estimate using non-linear FE analysis [4] and proper material data for actual temperature. Secondly, and the one that is mostly debated in the literature is the long-term residual stress decay.

One important material characteristic controlling the long term relaxation is the ability to cross slip, which is also the most important parameter determining the number of cycles spent to saturation [52].

Planar-slip material exhibits strain history dependence as illustrated in Figure 4-25. After prestrain some softening will take place at a slow rate [52, 67, 89].

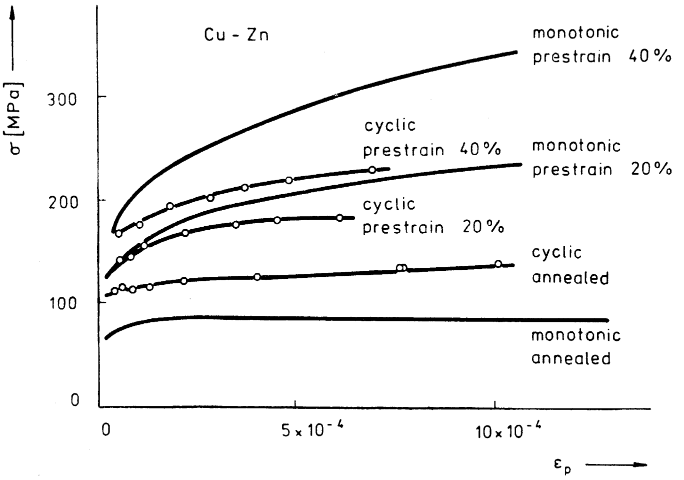

Figure 4-25. Cyclic and monotonic stress-strain curves for the planar-slip FCC Cu-Zn (α-brass). [67]

Wavy-slip material with moderate prestrain or cycling will relatively fast after prestrain reach the cyclic stress-strain curve of a virgin cycled specimen, and hence be strain history independent [20, 67]. The same holds true for higher degrees of prestrain cycled at high plastic amplitudes [30].

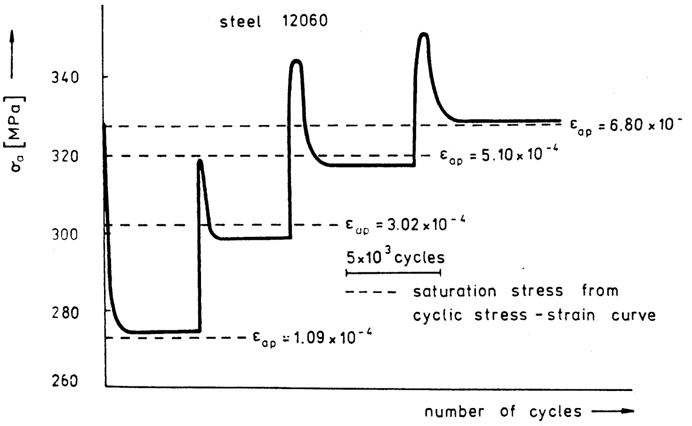

Figure 4-26. After a short transition region is the FCC steel attaining the same cyclic stress-strain curve as a virgin specimen cycled at the same amplitude level [52]. Plastic strain amplitude of 10^{-3} corresponds roughly to fatigue life of 10^5 cycles.

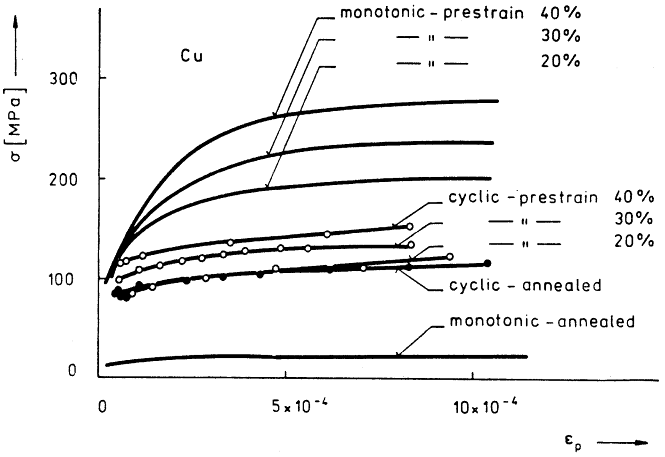

Figure 4-27. History dependence for prestrained FCC copper. 20% prestrain has same CSS-curve as a virgin cycled annealed specimen. High cyclic fatigue region. [67]

The history dependency can be explained by the dislocation structure. A wavy-slip material will exhibit vein or bundle dislocation structure (Figure 4-28) at low cyclic plastic strain amplitudes, whereas the same material will exhibit cell structure (Figure 4-29) at higher plastic strain amplitudes. Depending of the degree of prestrain a cell structure with rather broad walls with dislocation will be found [17, 20, 30, 67] (Figure 4-30, Figure 4-31 and Figure 4-32). After pretension wavy-slip materials will at high strain amplitudes clean up the cell structure, the walls sharpen to a similar dislocation structure as a virgin cycled annealed specimen (Figure 4-29), and the material will be slightly strain history dependent. However, at lower amplitudes that will give a vein structure in an annealed specimen, a cell structure will be found. Once a stable cell structure is established either from cycling at high amplitude or prestrain, it can not be removed by cycling at low amplitude [17, 20, 67], i.e. the material is strain history dependent. The strain limit after which the cell structure is too well formed and can not return to a vein structure is for steel [17] and copper [20] approximately 10% plastic strain, but Belassel & Lebrun [11] measured no stress relaxation in 3.5% prestrained steel after 100 000 cycles. A fast relaxation was however found (~10 000 cycles) with lower stress amplitudes and prestrained at 1.5%.

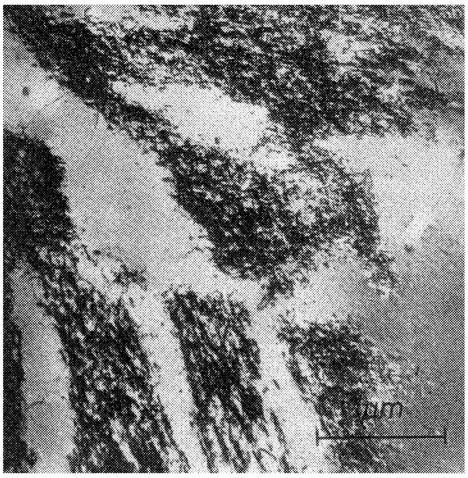

Figure 4-28. Dislocation vein structure in copper cycled at $\varepsilon_{ap} = 3.25 * 10^{-4}$. [67]

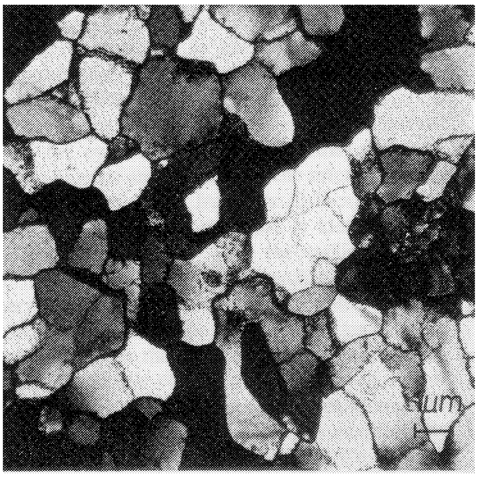

Figure 4-29. Dislocation cell structure in copper cycled at $\varepsilon_{ap} = 9.1 * 10^{-4}$. [67]

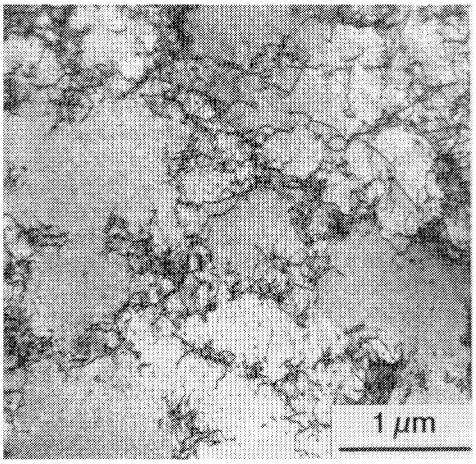

Figure 4-30. Cell structure in copper after 5% prestrain. [20]

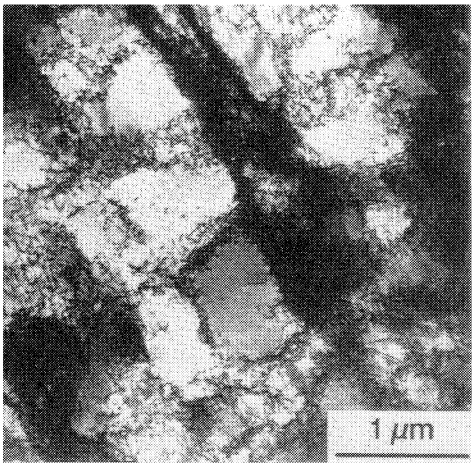

Figure 4-31. Cell structure in copper after 20% prestrain. [20]

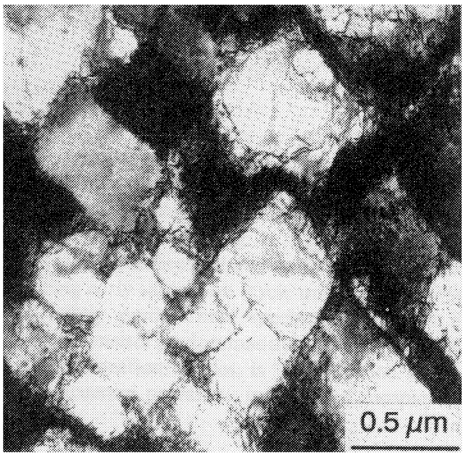

Figure 4-32. Cell structure in copper after 87% prestrain. [20]

Chai & Campbell [17] studied cyclic stress-strain curves for a low-carbon steel on small cylindrical specimens with varying prestrain. They found the same dislocation structure behavior as in copper which is supported by [29, 70], but they also found cyclic creep. As seen in Figure 4-34 the creep rate is decreasing with number of cycles even after softening has saturated. The creep rate was large in the first few cycles and then decreased with increasing cycling. The authors suggest that the creep always was in the opposite direction of the prestrain. A high degree of prestrain significantly decreased the amount of creep. Also, cyclic creep was found to depend on stress amplitude, with larger creep rates for high stress amplitudes. Chai & Campbell suggested that the cyclic creep of prestrain to be caused by an internal back-stress caused by dislocation pile-ups and bundles that favourise dislocation movements in opposite direction of the prestrain. The cyclic creep is then associated with the *Bauschinger effect,* whereas the cyclic softening is a process in which dislocation annihilation and re-arrangement into structures of lower energy take place. Softening and creep are thus two parallel cyclic behaviours caused by two different dislocation mechanisms. Cyclic creep is also reported in [19, 39] and [94], and is a phenomenon dependent on temperature.

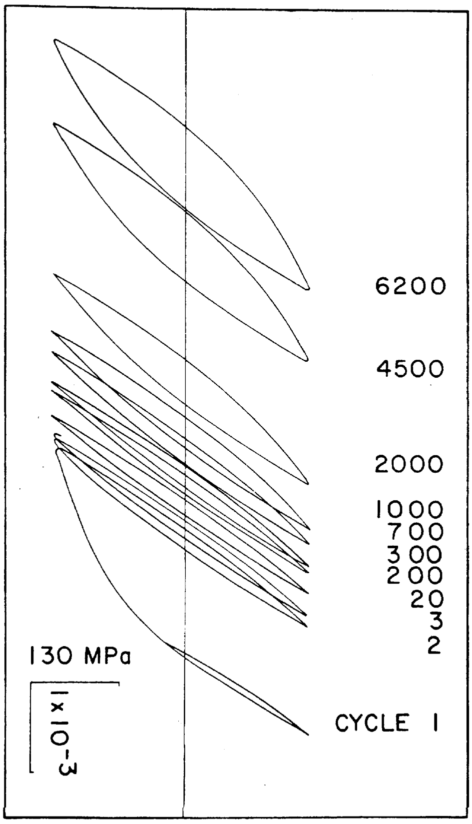

Figure 4-33. Cyclic creep. [17]

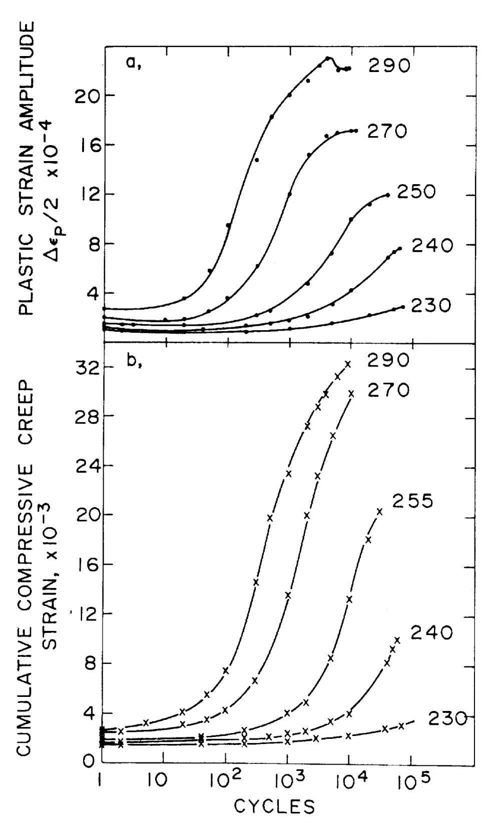

Figure 4-34. Cyclic creep after 15% prestrain depending on the stress range. Fatigue threshold is 205 MPa. [17]

Chai & Campbell also studied the influence from mean stress on cyclic creep and cyclic softening on a 6% prestrained un-notched specimen in a low-carbon steel. Even a low mean stress of 32 MPa caused a relatively large amount of creep, with a relatively small influence seen on cyclic softening (Figure 4-35). However, this observation was made in low-cyclic fatigue tests with a fatigue life of approximately 5 000 cycles.

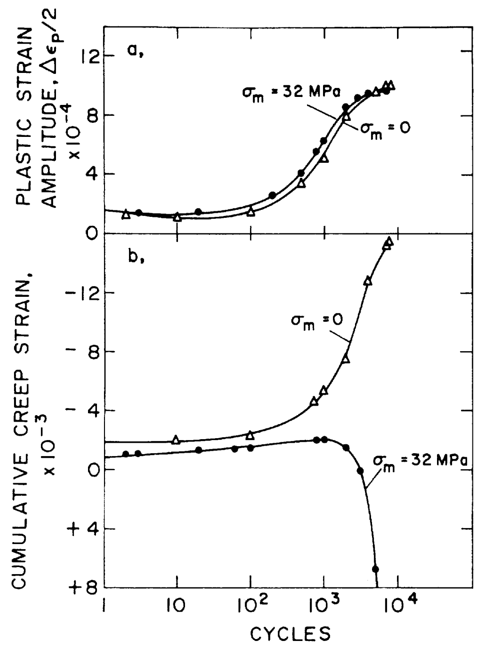

Figure 4-35. The effect of a small mean stress (a) on softening behaviour and (b) on creep behaviour in a low-carbon steel. The specimens, subjected to 6% prestrain, were tested at stress amplitude of 214 MPa, with and without a mean stress of 32 MPa. Fatigue threshold is 156 MPa. [17]

Another interesting observation is that Chai & Campbell found that softening was an exponential function of the number of cycles, and also that softening increased at higher stress amplitudes. Holzapfel et al. [48] studied shot peened steel with two temperature treatments, quenched and tempered steel specimens and normalised specimens that were austenitized, under alternating bending ($R = -1$, $K_t = 1.0$). They found the residual stress decay to be linear with log(N). Similar results is found in [24, 29, 55, 57], for shot peened steel specimen at $R = 0$ [71], cold expanded holes in steel at $R = 0$ [4] and $R = 0.1$ [33], and prestrained steel at $R = -1$ [11]. Close to the fatigue limit other researchers also have very small or no decay in steel [4, 108] and aluminium specimens. By use of x-ray diffraction Xu et al. found a complete relaxation of residual stresses in notched ($K_t = 2.85$) specimens tested at $R = -1$ close to the fatigue limit [108]. This effect is most likely caused by an instant relaxation by plastic deformation in the surface layer, which is observed by FE analysis in Section 8.6.

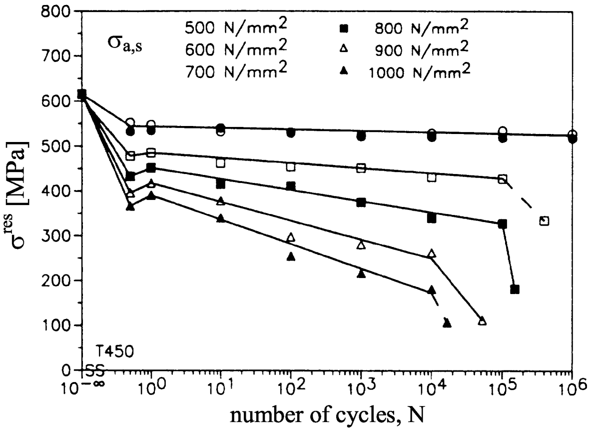

Figure 4-36. Residual stress decay as a function of constant stress amplitude and number of cycles in shot peened steel. [48]

Holzapfel et al. also found that the yield strength decreased with increasing temperature for the quenched and tempered material, which reduced the residual stress initially as seen in Figure 4-37. For the normalised austenititic steel the yield stress was much less influenced by temperature and the initial residual stress was consequently almost independent of temperature. The long-term decay was independent of temperature for both materials, which is illustrated by almost identical slopes for all temperatures tested, as indicated in Figure 4-37.

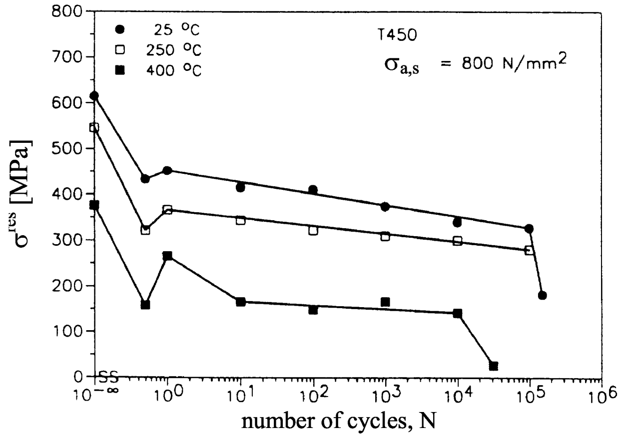

Figure 4-37. Residual stress decay as a function of temperature and number of cycles in shot peened steel. [48]

The residual stress decay from softening is proportional to the difference between monotonic and cyclic yield stress. Cyclic creep will cause additional decay. The two residual stress relaxation mechanisms decrease with increasing prestrain.

In some studies crack initiation and small crack growth influence the amount of decay that is found, as illustrated by the sudden drop at the end of the fatigue life in Figure 4-36 and Figure 4-37. Especially residual stresses measured by x-ray diffraction, which measures no deeper than 0.05mm [32], will be influenced if careful inspection for small crack prior to residual stress measurement is not done. Good correlation between relaxation and crack initiation was found in aluminium by Özdemir & Edwards [110].

To summarise relaxation of residual stresses:

1. The instant relaxation of residual stress from plastic deformation is well known and easy to incorporate into an analysis.
2. Long term decay is material dependent, where material effects can be split into two categories determined from the material's resistance to dislocation cross-slip. In planar-slip materials the decay is strain history dependent, with a slow softening process and small total softening. In wavy-slip materials the decay is history independent for low prestrain, $\varepsilon_p < 10\%$. Fast cyclic softening will give an almost instant residual stress drop proportional to the difference in monotonic and cyclic yield stress. At high prestrain the cyclic softening increases linearly with log(N), starting at zero at small plastic amplitudes, and almost immediate for large plastic strain amplitude. For HCF the relaxation from cyclic creep as well as cyclic softening is small.

4.8 Crack closure

Several situations exist in which the crack growth rate can be markedly different from the normal value, such as:

- premature crack closure of the crack surfaces
- wavy crack plane decreases the ratio of crack growth due to effective area reduction
- crack tip shielding from branching or residual stress generating within the cyclic plastic zone

Crack closure explains several important load effects, including those of overload and stress ratio. Some reasons for premature crack closure are illustrated in Figure 4-38. The development of the different closure and retardation mechanisms for variable and constant amplitude testing is not possible to quantify accurately. The processes are strongly dependent on small variations in the path of the crack, environmental conditions, loading conditions and testing methods. Additionally, these mechanisms can simultaneously influence the crack growth and it is often impossible to identify the contributions of the various mechanisms [94].

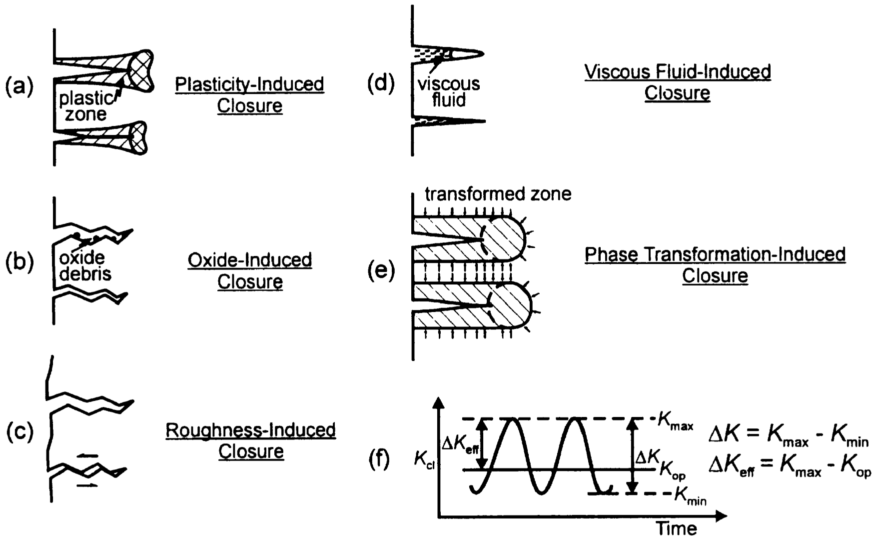

Figure 4-38. Schematic illustration of the various mechanisms of crack closure. [76]

It is extremely difficult to measure the far-field closing and opening stress as both opening and closing is a “zipping” process, which gradually moves the contact surface respectively from or towards the crack tip. This process will however occur relatively rapidly, and hence the “zipping” process has likely only a second order effect [72].

Since closure may involve contact beneath the observed surface planes, the only truly direct method for observing crack closure are techniques that can “see” beneath the surface. Such methods are electrical potential and ultrasonic transmission or diffraction techniques [64] (See Section 5.3). Both can identify contact at points away form the crack tip, but lose sensitivity as the crack tip is approached [64]. Most observations available in the literature on closure are made by observing variations in specimen compliance. Change in compliance is investigated by a fixture where the applied force or far-field stress is monitored together with the displacement. To illustrate the procedure a far-field stress – grip displacement fixture is used. The far-field stress vs. displacement curve obtained for a specimen containing a crack which is unloaded is schematically presented in Figure 4-39b. At unloading a constant stress-displacement rate will initially be obtained when the crack is fully open, A-B. As the unloading continues from B to C the second derivative of the curve becomes negative, and the fixture becomes stiffer. In this region the crack is gradually closing, and is finally closed at C. Once more a constant stress/displacement ratio is obtained at further unloading with a stiffness identical to a similar specimen without crack.

The variations in compliance are very small and must be measured near the crack in order to show distinct changes. Crack tip opening gauges have been criticised for giving opening/closing stress values far different from those observed at the crack tip [26, 64]. A single strain-gauge mounted near the crack tip in the path of the crack is another used method to measure the compliance. See Figure 4-39a. However, such tests that are simple in principle are difficult to perform due to the small change in compliance. The first ASTM round-robin test on crack closure did not show a high degree of reproducibility [26, 64], but the second ASTM round-robin performed presented in 1993 with an reanalysis of data in [26] showed a marked improvement. The improvement was mainly from more stringent reject/acceptance criteria. Generally the opening load is overestimated and non-conservative [26, 64, 92], but small changes in the analysis procedure giving the adjusted compliance ratio (ACR) method have reduced the scatter and conservatism [26]. Five more methods to determine ΔK_{eff} from the same set of compliance measurements are presented in [27]. The most broadly accepted closure measurement technique (the ASTM 2% offset standard) is typically only sensitive to closure 10 μm or more behind the crack tip [56].

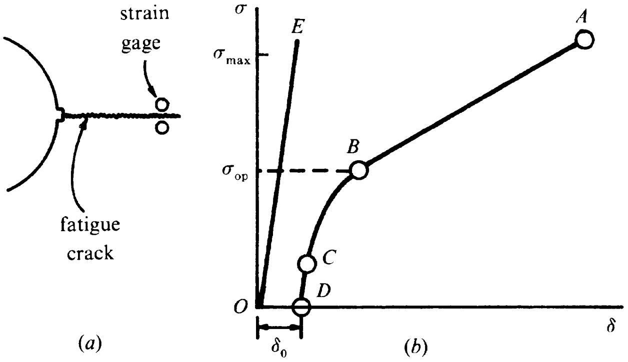

Figure 4-39. An illustration of stress-displacement obtained from a strain-gauge attached behind a fatigue crack. [94] (After Elber, 1970)

Generally, the closing stress where the crack starts closing at unloading, σ_{cl}, is lower than the opening stress, σ_{op}, where the crack tip is fully open at increased tension loading [94], as illustrated in Figure 4-40. This is also seen in FE analyses [74].

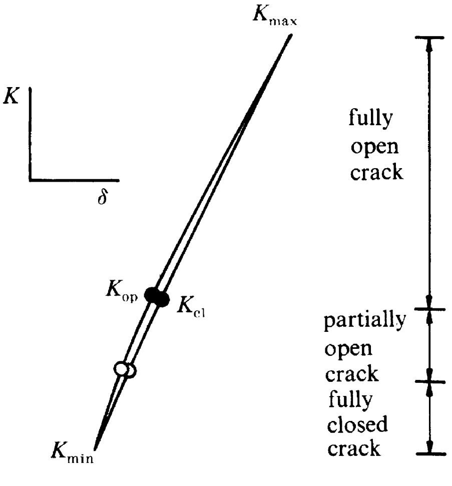

Figure 4-40. Stress intensity factor vs displacement across the crack for loading (K_{op}) and unloading (K_{cl}). [94]

By using the portion of the fatigue cycle where the crack is open

$$\Delta\sigma_{eff} = \sigma_{\max} - \sigma_{op} \qquad \text{Equation 4-13}$$

$$\Delta K_{\text{eff}} = K_{\max} - K_{\text{op}} \qquad \text{Equation 4-14}$$

the crack growth curve, da/dN curve, for various R-ratio will collapse into one [64, 95, 109].

During crack growth the material at the crack tip is cyclically plasticized, leaving a band of previous plasticized material in the wake as the crack propagates. The size of the band containing residual tensile strains depends on the load history, but will generally be wider as the crack advances due to increased stress intensity giving increased cyclic plastic zone size in the front of the crack tip. As already stated in Section 4.5 Plastic deformation at crack tip, Budiansky and Hutchinson [15] found the residual tensile strain in the crack wake to be a very important closing mechanism. Since volume must be conserved, out-of-plane plastic displacement is necessary to provide closure in the wake. This cannot take place in pure plane strain. However, specimens sized for nominally plane strain conditions may be in plane stress near the surface, but the effect of closure is then markedly reduced [64, 94]. Another important difference from plane stress is the effect from the T-term in Equation 3-13, which normally vanishes [94].

Louat et al. [66] used a dislocation model in plane strain, and found the closure non-existing or insignificant, but a mathematical mistake [88] was later found in their work. After correcting the mistake, closure was found to be of similar magnitude as in finite element studies. Several papers suggest that plastic closure does not exist at all or on very small scale [91, 92, 102, 103], but they all rely on the erroneous results from Louat et al. [66]. These papers are strongly criticised by [56, 76] and several authors listed in [64].

Numerical models based on continuum-mechanics are not accurate and in particular for crack growth near threshold, since the material locally at the crack tip is not homogeneous as long as preferred dislocation glide systems are present and randomly oriented along the crack front [87]. However, FE analysis performed by McClung et al. [73-75] observed reduced crack closure in plane strain compared to plane stress as expected. Their interesting finding was that the closure in plane strain was drastically reduced in test performed at R = 0.1 compared to R = 0, and only 2% of the crack was closed at R = 0.1. This is in good agreement with the dislocation model that Riemelmoser & Pippan found to give 1.3 μm closure near the crack tip at R = 0.1 [88]. Fatigue tests are often performed at R from 0.05 to 0.1 to avoid practical test control problems, and the resulting small portion close to the crack tip closed is difficult to measure in a compliance method for crack closure detection. This is where the strongest effect on thresholds and propagation is observed for crack closure [64, 86]. Biaxial loading, which is difficult to perform experimentally, has been investigated by FE analysis and found to play a significant role in crack closure were equi-biaxial load increases the opening level. Pure shear load lowers the opening stress compared to uniaxial loading [74, 86].

During crack propagation, presence of moist atmosphere leads to oxidation of the freshly formed crack surfaces. At low ΔK and R-ratio repeated crack face contact in mixed mode (some shear displacement of the crack surfaces) and microscopic roughness will be abrasive on the oxide layer. Fresh surfaces will oxidize and a process of build-up of oxide layers that are much thicker than a freshly prepared surface exposed to the same moist environment for the same time will take place. Oxide-layers up to

0.2 μm thick in low strength steel tested have been found, which is of the same magnitude as the maximum crack tip opening displacement at threshold for most low strength steels [94]. A total wedging ensuing crack arrest may then take place [94].

Roughness-induced crack closure depends on microstructural dimensions, ΔK and the R-ratio. With small cyclic plastic zones compared to microstructural features such as grain size, a crystallographic fracture process is promoted [94]. Stage I crack growth, which increases with planar-slip, gives a highly serrated or faceted crack surface. Crack mismatch from e.g. plastic zone and irreversible slip in front of the crack tip will lead to early crack closure and elevate the crack closure stress. Significantly higher fatigue thresholds are found in coarse-grained material at low R-ratio, but similar thresholds at high R-ratios compared to fine-grained material [94] suggesting roughness to be the main closing effect. Periodic deflection in the crack path induced by grain boundaries (see Figure 4-45) and second phase particles will also promote crack closure.

Fluids in fatigue cracks are often water or oil. Crack propagation is sensitive to hydrogen embrittlement at the crack tip, which will be suppressed by oil. Also, oxidation of the crack as described above will influence the crack propagation. One last fluid property of interest is the viscosity, which will control the ability to crack penetration and hence crack closure from hydrodynamic wedging. Experiments and calculation both indicate less closure promoted by viscous fluids compared to the effects of roughness and oxidation [94].

To summarise: In general crack closure is more dominant at low ΔK values and lower R-ratio because of the smaller minimum crack opening displacement. Consequently near threshold fatigue crack propagation rates (generally less than 10^{-9} m/cycle [64]) will be most susceptible to crack closure. As the fatigue crack propagates in depth from a free surface the extent of crack closure generally increase until a saturation level where after the closure is crack-length independent. Under strictly near-threshold crack growth conditions plastic closure will not be significant even if its existence had not been questioned [64]. The predominance of the evidence show that crack closure due to oxidation and surface roughness dominates over plasticity induced closure [64, 76, 92]. In many cases ΔK_{eff} is greatly underestimated because the contact stress when contact first occurs is used and initial contact at isolated points is partial [64]. For a partly closed crack some of the remote loading is transferred across the crack and will contribute to the crack propagation. Using opening or closing stress will then give to small ΔK_{eff} [64, 92]. For these reasons partial crack closure is of great importance. Because of the small plastic zone in front of the crack at near fatigue threshold LEFM can be used successfully.

4.9 Overload

Crack growth rate is affected by superimposed overloads both in tension and compression, and under variable amplitude and block loading. Overloads in tension are known to retard crack growth, while overloads in compression accelerate the crack growth. The effect of overloads on crack growth rate is transient and diminishes after a certain distance of crack growth. The crack grows two to four plastic zones before the retardation vanishes [64]. The retardation effect following an overload depends on several load factors, material flow parameters, slip planarity and microstructure.

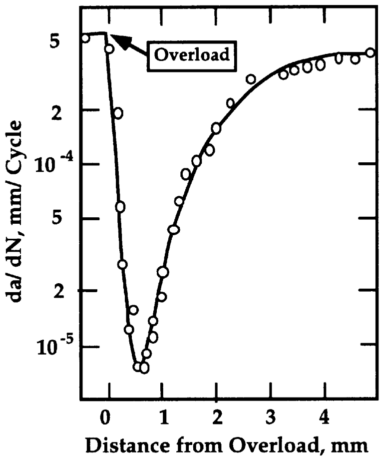

Figure 4-41. Retardation of crack growth after a tensile overload. [6]

There are several effects from overload that can contribute to the observed retardation. These are [92]:

1. Crack blunting
2. Crack deflection, branching and secondary cracking
3. Crack tip strain hardening or residual stress ahead of the crack tip
4. Plasticity-induced closure
5. Roughness-induced closure

Plastic deformation at the crack tip blunt the tip and reduces the stress intensity factor until the crack has advanced a distance approximately equal to the crack tip radius. There are reports listed in [92] where an important effect is observed in ductile materials, however, the mechanism is not capable to explain the sudden initial acceleration after overload and effect beyond the blunt crack tip radius.

Crack tip deflection, branching and secondary cracking will affect the crack tip driving force and is important for significant planar-slip material. This phenomena is, however, not sufficient general and thereby not the main effect for the generic behaviour observed under overloads [92].

Crack tip strain hardening will decrease slip at the crack tip and decrease crack propagation if the crack growth is slip controlled. Therefore, brittle material growth mechanism can have the opposite effect [92]. Residual stress will be introduced from the plasticity, and several publications supports residual stress as the major source for retardation [92]. First, residual stress will lower both K_{max} and K_{min} and hence leave ΔK_{eff} unchanged and thereby supporting two-parameter crack growth models (da/dN dependent on ΔK_{eff} and K_{max}. See Section 4.11.1 Two-parameter LEFM based crack growth model) which is debated. Second, delayed retardation is not supported as the largest residual stress is adjacent to the tip and delayed retardation persists even after the crack has propagated out of the compressive residual stress zone [92].

The factors discussed so far (numbered 1-3 in the list above) is influencing the front of the crack tip, whereas the plasticity-induced (4) and roughness-induced (5) crack closure are factors affecting the wake of the crack. This is in agreement with the observed delayed retardation and will also be effective after the crack has grown through the reversed plastic zone as the extended monotonic zone is controlling closure. Also, the closing model will reduce the driving ΔK_{eff}. Once more, the crack path tortuosity is controlled by slip planarity and can not explain the generally observed retardation. Material that shows a significant crack plane tortuosity can show a larger retardation due to the roughness-induced closure. The closure contribution should be considered as an additive mechanism where several mechanisms adds up simultaneously [92]. See Section 4.8 Crack closure.

Hammouda et al. [44] studied CTOD in plane stressed steel with $\sigma_y = 350$ MPa with hardening after overloads. With physical short cracks (see definitions in Section 4.10 Short fatigue cracks) crack blunting was the main mechanism after overloads above yield stress, where as strain hardening and crack tip closure at the crack tip plays an additional role at overloads $< 0.5\ \sigma_y$. This can be explained by the absence of wake where the crack will close (see Section 4.10 Short fatigue cracks).

From this discussion crack closure is the most obvious reason for crack retardation after overload where the crack has a length before overloading sufficient for closing.

4.10 Short fatigue cracks

In non-welded components with smooth surfaces, e.g. drillstring threads, a major part of the fatigue life is spent in the development and growth of small cracks. However, once initiated small cracks grow at higher rates than long ones [95]. Up to two orders of magnitude compared to the one calculated from continuum approaches using material properties obtained from long crack growth tests have been found [94]. Crack growth data for short cracks exhibit considerably higher scatter than crack growth data for long cracks, and the use of LEFM is questioned [64, 86, 87, 95]. Differences in crack closure, microstructure, microstructural stresses, crack growth mechanisms, environmental susceptibility and relative plastic zone size are the reasons most often given for differences between small and large crack behaviour [64, 86, 95].

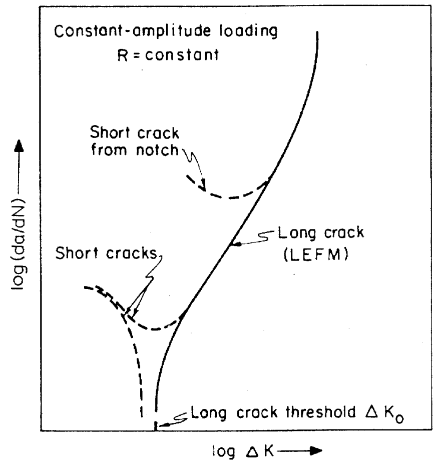

Figure 4-42 Typical short crack propagation rates for long and short cracks as function of stress intensity factor range. [95]

There is no strict definition of short cracks. Short cracks can be broadly classified as [94]:

1. Microstructurally short cracks whose length are comparable to microstructural dimensions such as grain size.
2. Mechanically short cracks for which the near-tip plasticity zone is comparable to the crack size or the crack is surround by the plastic strain field caused by a notch.
3. Physically short cracks that are significantly larger than the characteristic microstructural dimensions and the crack tip plastic zone, but are merely physically small with typical length less than a millimetre or two.
4. Chemically small crack that exhibits different chemical susceptibility than a long crack does.

One major challenge is to perform reproducible crack growth measurements. The low magnification optical techniques used for long crack growth measurements are not suited to detect the presence and monitor the growth of short cracks during a fatigue test. Normally thin CT[16] specimens are used with plane stress condition at the surfaces where observations are made. Other techniques that are suitable for observing the crack front in the bulk, e.g. potential resistance, ultrasonic and testing compliance techniques, suffer from lack of reproducibility and low resolution.

Normally the crack growth threshold is determined using the load shedding procedure. After initial growing of a fatigue crack in a CT- or centre-notched specimen the far-field load is reduced stepwise by an amount not more than 10% after growing of a crack of at least four times the maximum plastic zone size for each amplitude level [94]. This will necessarily end up with a non-propagating crack of some size. A method to avoid this problem is to remove material in the wake by machining until a short crack is obtained. By plotting the rate crack growth threshold / fatigue limit ($\Delta\sigma_{th}$ / $\Delta\sigma_0$) as a function of the crack length, a, was a critical crack length, a_0, found where after the crack propagation threshold stress was found to decrease linearly. See Figure 4-43a. This diagram is called *Kitagawa-Takahashi diagram* [51]. The rate stress intensity threshold representative for the actual crack size / long crack stress intensity threshold (ΔK_{th} / ΔK_0) increases until it reaches a length a_0 after which the ratio is constant. With the crack approaching zero length the crack propagation threshold stress approaches the fatigue limit for smooth specimen. See Figure 4-43b. This is true for a wide range of engineering alloys as seen in Figure 4-43.

---

[16] Compact tension test specimen.

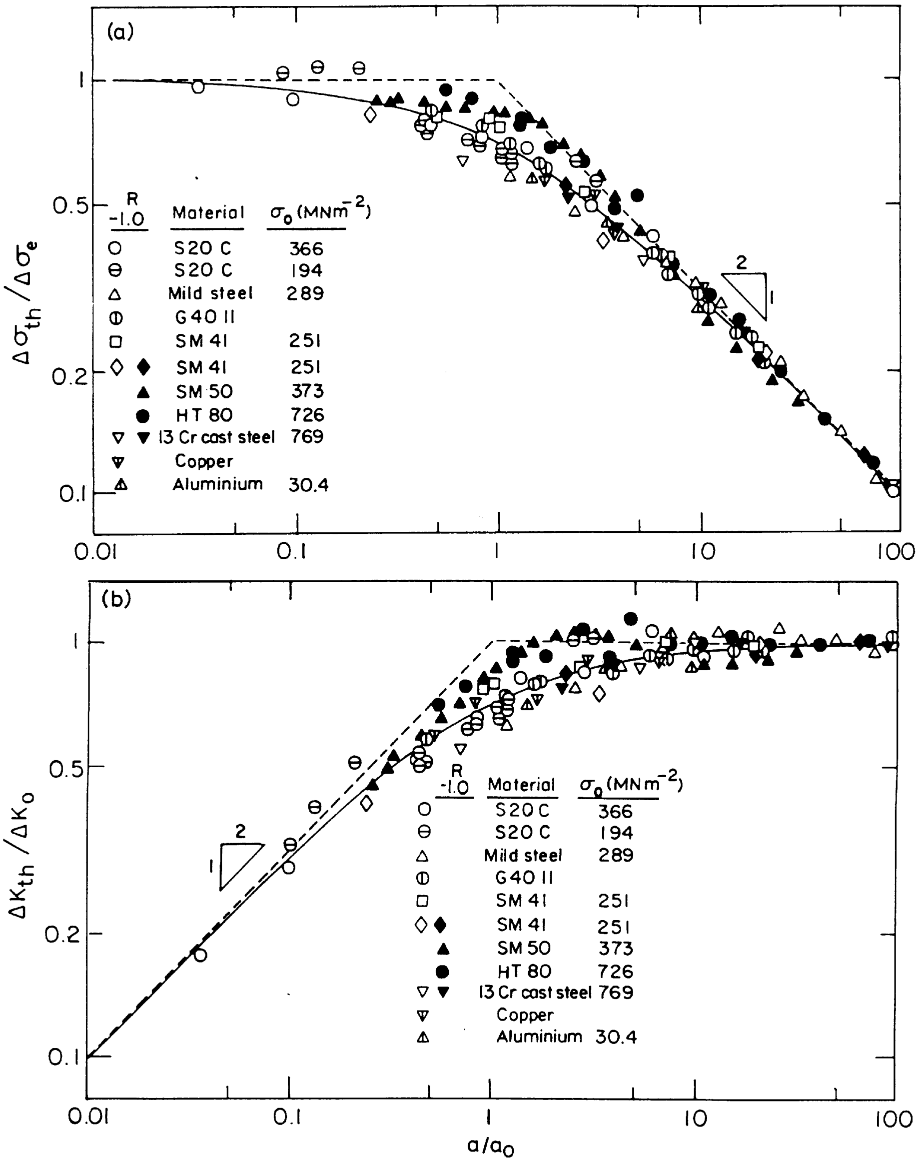

Figure 4-43. The effect of crack size on (a) threshold stress and (b) threshold stress intensity factor range for a wide range of engineering alloys. [95] (After Tanaka, Nakai & Yamashita, 1981)

The LEFM is built upon the principle of similitude (see Section 3.7), whereby a particular material and environment system subject to some particular loading history giving identical near-tip conditions will prevail same characterising crack driving parameter (e.g. ΔK) independent of geometry and crack size. The observation of a different crack growth behaviour for a < a_0 violates the concept of similitude in fracture mechanics which implies that the intrinsic threshold stress intensity factor, $\Delta K_{th,}$, should be crack size independent.

a_0 is alloy-dependent, but can be estimated from [94]:

$$a_0 = \frac{1}{\pi}\left(\frac{\Delta K}{\sigma_e}\right)^2 \qquad \text{Equation 4-15}$$

where

$$\Delta K = \Delta K_{th} \text{ for } a > a_0$$
$$\sigma_e = \Delta\sigma_{th} \text{ for } a < a_0$$

The concept of similitude cannot be applied when [95]:

1. The crack size approaches local microstructural dimensions.
2. The crack size is comparable with the extent of local plasticity.
3. Through thickness, out of plane stresses which are independent of K_I are different.
4. Extensive fatigue crack closure is observed.
5. Environmental conditions that significantly influence the crack growth.

It is important to bear in mind that the near tip parameters are governing the crack tip, and not the nominal "far-field stresses" and macroscopic crack length.

To account for the differences in growth rates between long and short fatigue crack El Haddad et al. [28] proposed the use of an effective crack length $a_{eff} = a + a_0$

$$\Delta K = Q\Delta\sigma\sqrt{\pi(a + a_0)} \qquad \text{Equation 4-16}$$

where $\Delta\sigma$ is the far-field stress range and Q is the geometry correction factor. As a increases the contribution from a_0 drops and ΔK approaches the Paris equation (Equation 3-23). This approach is purely empirical with no physical explanation [94].

Premature contact of the crack surfaces will decrease the effective stress intensity range as described in Equation 4-14. An infinitesimal small crack from a smooth surface will have no wake where premature closure can take place. It is therefore reasonable to believe that a short crack is less sensitive to closure compared to a long crack, and hence has a higher crack propagation rate. This is observed in several investigations[17] of physical short crack of typically 0.5 – 1 mm compared to long cracks under a nominally identical driving force (See Figure 4-42). By using Equation 4-14 short cracks are found to obtain the same crack growth rate behaviour as long crack as seen in Figure 4-44. Once the mean stress is increased the anomalous sub-threshold short crack growth is found to disappear and obtain the same behaviour as long cracks [95]. Cracks of this size are expected to satisfy both continuum mechanics and LEFM requirements [95].

---

[17] Five listed in [95].

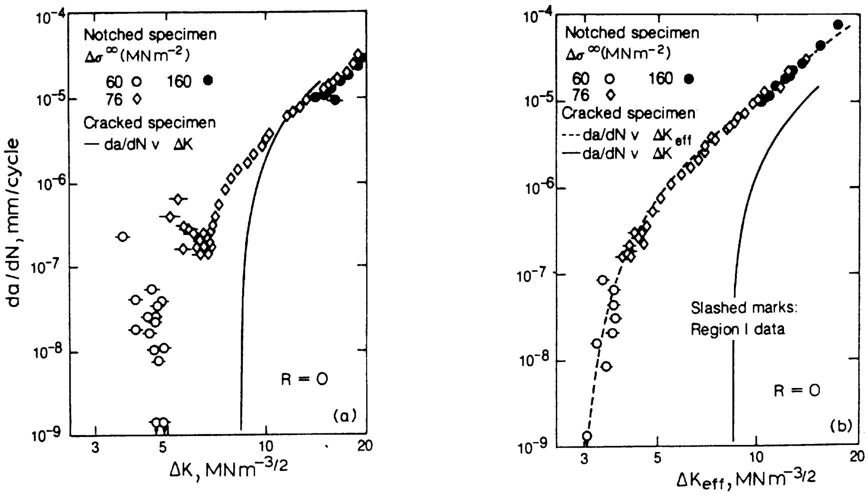

Figure 4-44. Variation of crack propagation rate with stress intensity rage in a mild structural steel. (a) nominal stress intensity and (b) effective stress intensity from crack closure. Note the correspondence with conventional obtained crack growth data for long cracks once the closure is accounted for. [95]

The interaction crack tip – grain boundary have the following consequences [94]:

1. Cessation of propagation into a neighbouring grain until a sizeable plastic zone is established.
2. Slip bands emanating from the crack tip are pinned at the grain boundary.
3. Change in the driving crack force as the crack deflects when it crosses the grain boundary into the neighbouring grain, due to the change in grain crystallographic orientation.

An increase in the crack closure stress takes place with increasing crack length as the crack deflects at the grain boundaries and decomposition of far-field stress into mode I and mode II cracking leads to a shear motion. See Figure 4-45. This is supported by fractographic studies that show a practically featureless fracture surface in Stage I crack growth, whereas stage II crack propagation frequently shows a pattern of ripples or striations [25, 79]. The presence of striations unambiguously proves that crack propagation was caused by fatigue, but their absence does not preclude fatigue as the failure mechanism. E.g. in martensite striations is very difficult to find.

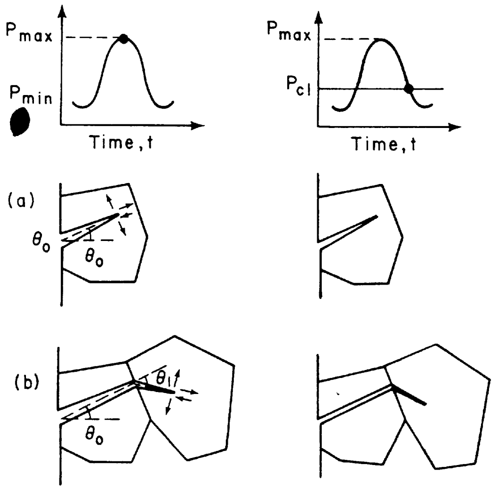

Figure 4-45. Deflection at grain boundaries as the crack traverses though grain boundaries. [95]

The minimum crack propagation rate is obtained at a crack size, a, that is equal to the smallest grain dimension, d_g, which also appears to be equal to the critical crack size in the Kitagawa-Takahashi diagram [64, 95]. The grain boundaries are unlikely to affect the crack growth of a long crack significantly. The increased restraint on cyclic plasticity in the bulk compared to the surface grains tends to activate more slip systems, leading to a non-crystallographic mode of crack advance [95]. At near-threshold levels the cyclic plastic zone is small enough to remain within a single grain, and even long cracks might propagate by one active single slip system which will deflect at each grain boundary giving a zigzag crack path morphology [95].

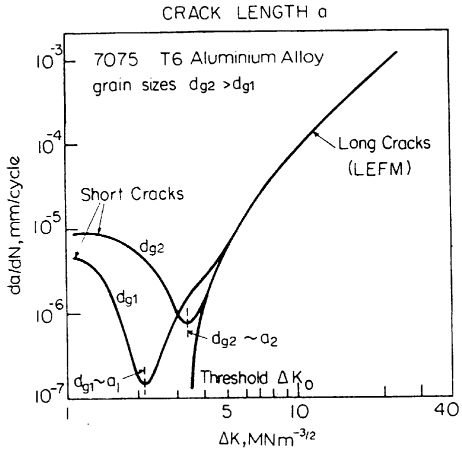

Figure 4-46. Effect of grain size d_g on growth of microstructurally short cracks below long crack threshold. [95]

Chemical and electrochemical effects can also influence the growth rate of small cracks, in particular physically short cracks in aggressive environments as seen in Figure 4-47. The following corrosion fatigue crack size dependent mechanisms are influencing the propagation rate:

1. Oxide- and roughness-induced crack closure of cracks with sufficient wake [94].
2. Hydrogen embrittlement of crack tip [3].
3. Blunting of crack tip from corrosion [64].
4. Mass transport/reaction to produce hydrogen within cracks.

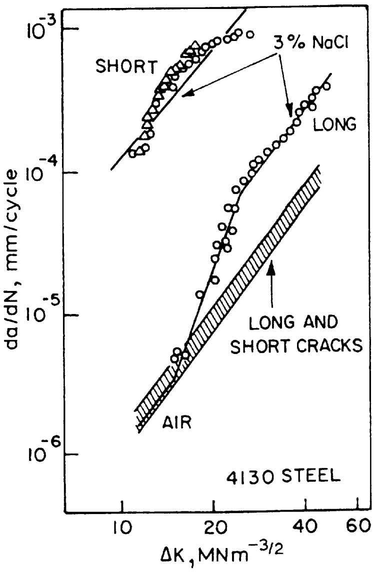

Figure 4-47. Fatigue crack propagation rate as a function of ΔK for long (a ~50 mm) and physically short (~ 0.1 – 0.8 mm) cracks in steel, tested in moist air and in 3% NaCl solution. [97]

For mechanically short cracks where the near-tip plasticity is large compare to the crack size elastic-plastic fracture mechanics (EPFM) or crack tip opening displacement (CTOD), δ, is often used. One EPFM method is the J-integral, which uniquely and autonomously characterises the crack tip field under elastic-plastic conditions. For small scale yielding J can be directly related to the strain energy rate G, and hence to K_I:

$$J = G = \frac{K_I^2}{E'} \qquad \text{Equation 4-17}$$

where

$$E' = E \quad \text{for plane stress}$$

$$E' = \frac{E}{1-\nu^2} \quad \text{for plane strain} \qquad \text{Equation 4-18}$$

Cracks that are comparable in size with the extent of the local yielding can be treated by using ΔJ. J and δ can be taken as measures of the intensity of the elastic-plastic crack tip field. It is therefore feasible to correlate rates of fatigue crack growth to the range of δ, i.e. the cyclic CTOD Δδ. Approaches based on J and δ are basically equivalent for proportional loading [94], and are valid under both elastic-plastic and linear elastic conditions. Part of the reason for anomalous short crack growth behaviour lies in the inappropriate use of LEFM analysis [95]. The stress distribution ahead of the crack tip is described in Equation 3-13. One fundamental assumption in LEFM is small scale yielding ahead of the crack tip compared to the crack size. For long fatigue cracks, the size of the K-dominance is typically 10% of the characteristic dimension [94]. As the length of the crack is decreasing, the zone of K-dominance is also reduced, and the T-term in Equation 3-13 should be incorporated into the expressions of the near-tip fields [86, 94, 95]. The T-term not only influences the stress and elastic strain field in front of the crack tip, but also influences the size of the plastic zone. The short - long crack transition is different for uniaxial compared to biaxial and equibiaxial loading [74, 86]. LEFM can be inappropriate for short cracks, even under nominally elastic conditions, since the use of linear elastic singularity to characterise the local stresses on the basis of K_I invariably involves neglecting the T-term. The T-term can have an appreciable effect on short cracks with significant contributions from the remote loading [86, 95].

The solution often used to increase the fatigue limit of steel components is to increase the yield stress and reduce the grain size, which will increase the small crack growth resistance. This can have a detrimental effect on the growth of long cracks, however, its effect on crack propagation rates above threshold is generally small [64, 94]. By use of discrete dislocation model $\Delta K_{eff,\,th}$ is found to be nearly independent of yield stress and also nearly independent of R-ratio [87]. $\Delta K_{eff,th}$ is in [87] found to be 2.6 for Fe-alloys which is in good agreement with measured values of 3.0 ± 0.6 MPa√m [2, 87].

To summarise; there is no strict definition of short cracks. Microstructure and plasticity at the crack tip either the stress concentration from the crack it self or from a notch limits the use of LEFM. Microstructural barriers e.g. grain boundaries decreases the crack propagation rate. Physically short cracks (typical 0.5-2 mm) are in many cases significantly longer than the scale of microstructural barriers and the size of the crack-tip yield zone. These cracks can be treated by LEFM [96], and have in many investigations [96] been shown to propagate considerably faster than long cracks subjected to the same nominal value of ΔK. Since a short crack has a limited wake, crack closure effects are less pronounced for a short crack. This is a rational explanation of the observations.

4.11 Crack growth models

Since the introduction of the LEFM concept to calculate crack growth first was introduced by Paris et al. [80], have the original proposed model and related models[18] trying to describe the entire crack growth curve (see Figure 3-10) been used. In this Section more refined models will be briefly presented.

4.11.1 Two-parameter LEFM based crack growth model

In regime 3 a change in crack growth mechanism is taking place (see Figure 3-10), and K_{max} will be an important parameter together with ΔK. Traditionally ΔK has alone been the driving parameter in regime 2. However, in the Forman equation [34] the mean stress is incorporated as:

$$\frac{da}{dN} = \frac{A(\Delta K)^n}{(1-R)K_c - \Delta K} \qquad \text{Equation 4-19}$$

---

[18] See Anderson, 1995 [6]

where A and n are empirical fatigue material constants and K_c is the fracture toughness for the material and thickness. Vasudevan, Sandananda and Louat have in a series of papers (some: [66, 91, 92, 102, 103]) presented the two-parameter Unified Approach model also applicable in regime 2 based on ΔK and K_{max}, and its ability to incorporate different observations. This model is a further development of two-parameter models earlier proposed and listed in [64]. Riemelmoser et al. have in [86] shown the paper of Louat et al. [66] to contain a mathematical mistake which makes the paper to draw the conclusion that closure does not exist or is insignificant. By correcting this mistake closure is found to exist, and contributes significantly at near threshold loading [86]. Many publications presenting various topics of the Unified Approach have heavily argued that traditional approach have exaggerated the closure and also referred to the incorrect conclusion of Louat et al. [66].

The fundamental difference between the traditional one parameter model where ΔK_{eff} is the only driving parameter and the Unified Approach model is the use of both ΔK and K_{max} in the latter. The stress intensity at the crack tip must simultaneously exceed lower critical values of ΔK and K_{max}, ΔK^*_{th} and $K^*_{\mathrm{max,th}}$ respectively, in order to have crack growth. These values are asymptotic values in the ΔK - K_{max} plot presented in Figure 4-48. In [102] five different classes are proposed to categorise different material behavior in particular environments leading to differences in the L-shape presented in Figure 4-48.

If crack closure is present, a third parameter is necessary to fully describe the fatigue process. The observed importance of crack closure in the literature is contradictory to the Unified Approach, in which no or only a very limited crack closure is found from analytical dislocation models [66] (As noted earlier this work contains a mathematical error). The crack closure observations are assumed to be exaggerated or wrong, based on the complexity of measurement and the huge scatter found in general and particularly in the first ASTM round-robin test performed.

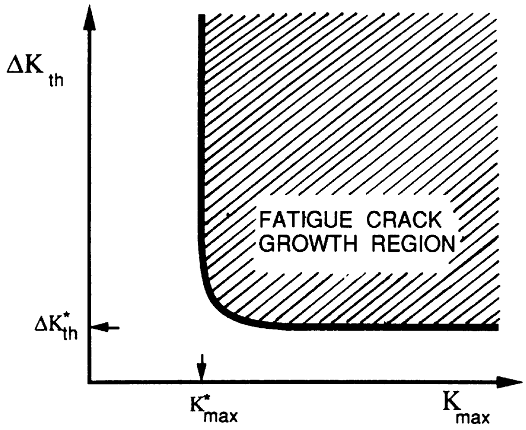

Figure 4-48. Schematic figure of a typical fundamental fatigue threshold curve plotted in terms of ΔK_{th} vs K_{max}. [102]

The superposition of the externally applied stresses and any internal stress is the driving force in the model. The internal stresses will influence K_{max} only as also K_{min}, which is not a driving parameter in the model, will be influenced and thereby not influence ΔK. The size of the monotonic plastic zone is controlled by $K_{max,}$, which influences the residual stresses locally at the crack tip. This model is supported by Lang and Marci among others in a series of papers according [92], which have shown the importance of what happens is in front of the crack tip rather than the crack closure behind the crack tip.

Sadananda et al. [92] found residual stress to be the major factor contributing to the crack growth retardation from overloads, rather than the crack closure behind the crack tip. By using the two-parameter crack growth model the unchanged driving parameter ΔK_{eff} is not an argument against residual stress based model, where the other parameter in the model K_{max} will be lowered from residual stresses and influence the crack propagation rate.

Sadananda and Vasudevan [91] explained the anomaly high growth rates for short cracks in terms of internal stresses. Tests involving specimens only slightly thicker than a few grain sizes indicated that decreased growth rate and arrest of short cracks in specimens thicker than several grain sizes could not be explained by grain boundaries or other microstructural obstacles [91]. The rapid deceleration of short cracks are found to be related to the internal stresses, and total arrest occurred when the total force due to internal and applied stresses fell below $K^*_{\max,th}$. It is however very difficult to perform measurements to determine the internal stresses [91].

In a critical review of the two-parameter model McEvily and Ritchie [76] refer to Pippan [83] who found a constant ΔK_{th} in the absence of crack closure at the R-range –2 to 0.1. McEvily and Ritchie concluded that only one parameter, ΔK_{th}, is controlling the rate of crack growth in ductile materials, except for high growth rates during which static fracture modes occur as K_{max} approaches instability.

4.11.2 Load history dependent empirical model

Lang and co-workers [60-62]have proposed a model in which the effect of load history is incorporated. Depending on the load history the crack growth is split into two; cyclic dependent and crack growth dependent behaviour. The model is based upon experiments on aluminium alloy Al 7475-T7351, and has a series of input requirements from tests. At present time this rather complicated model is lacking general experimental evidence to be interesting in this work.

Hammouda et al. [44] have performed numerical analysis with overloads of steel with $\sigma_y = 350$ MPa including hardening, and proposed a crack growth model for short cracks. Crack closure is a variable in this model, but is incorporated through FE analysis. This model requires far less testing in advance than the Lang model, but is also lacking general experimental evidence to be interesting in this work.

4.11.3 Crack closure models

After further development of the work by Tanaka and Nakai [98] Tanaka and Akiniwa proposed the resistance curve method (R-curve) in 1988. In [1, 2, 109] the same authors have further developed the model which is based upon the long crack stress intensity threshold and crack closure as

$$\Delta K_{eff,th} = \Delta K_{eff,th\infty}$$ Equation 4-20

$$\Delta K_{\text{eff}} = K_{\max} - K_{\text{op}}$$ Equation 4-21

Their work is based on numerical analysis on three different steel grades and tests involving one of them with yield stress of 316 MPa. The fatigue test was done at R = -1, and the crack length on the specimen surface was measured by a travelling microscope. They found that ΔK_{eff} unique describes the crack propagation rate irrespective of stress amplitude or crack length. From their work an empirical crack opening stress intensity factor at the threshold, $K_{\text{op,th}}$ is determined, but this is only valid for the material and test environment used because of crack closing factors other than plasticity, which is difficult to incorporate in an FE analysis, are not included. (See Section 4.8 Crack closure) According the R-curve method, the condition for crack propagation can be described as

$$K_{\max} \geq K_{\max,\text{th}} = \Delta K_{\text{eff,th}} + K_{\text{op,th}}$$ Equation 4-22

According Lawson et al. [64] ΔK_{eff} in most cases used able to collapse the data taken from different R-ratios into a single line of the da/dN plot, but the success of the approach is largely dependent upon the skill with which K_{op} is chosen.

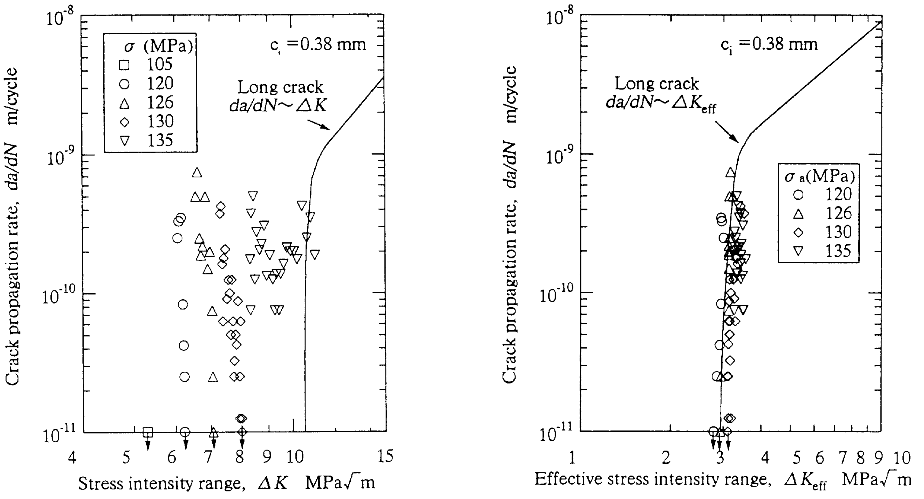

Figure 4-49. a) Crack growth rate for various crack length and stress amplitudes, and b) effective stress intensity range. [109]

Lam et al. [59] studied variable amplitude loading on steel specimens, and by the use of ΔK_{eff} the fatigue life was successfully calculated by LEFM. By assuming load histories that included frequent overloads where the largest compressive cycle determined crack closure was not unduly conservative fatigue life obtained.

4.12 Crack initiation and growth of short cracks in strain hardened material and in residual stress fields

Residual stress is normally introduced during solidification or plastic strain. Plastic deformations will generally both lead to strain hardening and introduce residual stresses, effects very difficult to separate in analyses of fatigue tests.

By cutting specimens out of compressed bars that have been uniformly plastically deformed over its cross-section, the specimens will have no residual stress. As discussed in Section 4.7, the wavy-slip material history is independent at prestrain below 10%, and hence no increased fatigue life from strain hardening is expected. Above 10% prestrain wavy-slip material will be history dependent as planar-slip material, and an increased fatigue life from strain hardening is possible. At 15% strain Chai and Campbell [17] increased the fatigue threshold in AISI 1018[19] steel with 30%. Frost et al. [37] have reported from several investigations where the fatigue threshold for mild and austenitic steel are found to increase 40% after 50% prestrain tested at R = -1, but the fatigue limit of alloy steels showed little difference (~10% increase) from that of the unworked. Kuo and Cohen [57] found and 10% increased fatigue life near fatigue life of 10^5 cycles after severe prestrain from deep rolling of AISI 1008 steel tested at R = -1. All the tests discussed in this paragraph have been strained above the limit for history dependence in wavy-slip material, and they have all reported increased fatigue limit from strain hardening in the region of 10-40% with the majority around 15% increase. However, in some of these investigation the test specimens might not have been cut out of a prestrained bar, and hence residual stresses might have been present without being determined or reported.

Fang et al. [29] reported 7% increase in fatigue threshold of shot-peened steel specimen tested at R = -1 and K = 1.0 where Densvignes et al. [24] found 20% increase in another test under similar conditions. Berstein and Fuchsbauer [13] reported 90% increase in fatigue strength after cold rolling of steel with 300 MPa in yield stress and 20% increase with 1000 MPa in yield stress. In general care should be taken when utilising an increased fatigue strength from strain-hardening as it varies significantly between different metals and alloys ([37] reported decrease of 10-20% for high-strength aluminium alloys), and also within different steels.

All investigation reported so far in this Section have all been performed on smooth specimens ($K_t = 1.0$). An interesting observation is crack nucleation reported at various sub-surface depths for un-notched surface treated specimens [23, 54, 77, 104]. Crack nucleation below the surface can be explained by the relative flat slope of the local stress for un-notched specimen compared to the steep slope of the residual stresses, and the increased fatigue resistance of the surface layers from strain hardening. Notches will have a steep applied stress gradient and hence initiate the crack at the surface where sub surface cracks have not been found reported. See Figure 4-50.

---

[19] 0.17% C, 0.78% Mn, 0.09% S, 0.01% P. Annealed at 910 °C for 30 min. before testing.

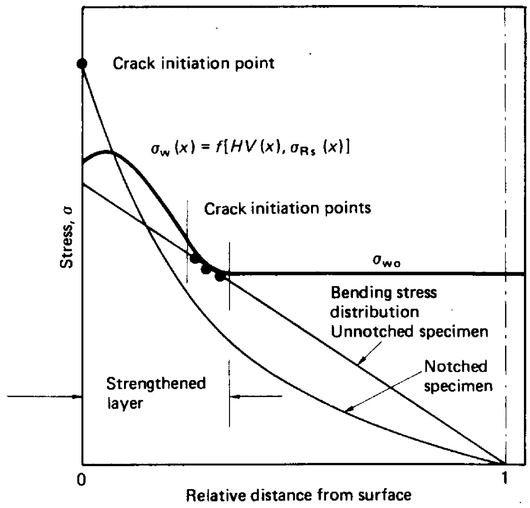

Figure 4-50. Schematic description of sub-surface nucleation occasionally observed for smooth specimen compared to the surface nucleation of notched specimen. [54]

For notched specimens the high local stress reduces the residual stress when local yielding in compression takes place [8]. At $R \geq 0$ a reduction from overload will not take place. Attention should therefore be paid to the type of loading and geometry of the specimens when the effects of residual stresses are examined.

The amount of literature on cold rolling of notches is limited, some are [7, 13, 47, 53, 54, 104, 107]. In general K_t for the notches are in the range of 2-3, which is close to an infinite plate with hole for which $K_t = 3.0$ (Ref. Equation 3-2 with $a = b$). In the aircraft industry considerably research has been made on cold expanded holes [4, 8, 12, 16, 21, 33, 40-42, 46, 65, 81, 82, 110] mostly in aluminium. Cold expansion has become a standard procedure in the aerospace industry to increase the fatigue performance of bolted or riveted plate joints, especially in connection with repair and upgrading of ageing aircraft structures.

Ghfiri et al. [40, 41] tested aluminium 6005-T6 and 6082-T6 at $R = 0.57$ to avoid crack closure and found an increased fatigue initiation (crack < 0.2 mm deep) from $3.4*10^5$ to $1.2*10^6$ and $6.1*10^5$ to $2.2*10^6$ cycles, respectively, after cold expansion (High K_t, probably round 3). Özdemir and Edwards [110] tested Al. 7050-T6 with expanded hole at the fatigue threshold and $R = 0.1$. The crack initiated at 45 000 for the reference test and 250 000 for the expanded hole (and the crack was arrested at 0.45 mm). Bernard et al. [12] tested Al. 7475-T7351 at $R = 0.05$ and found an increased fatigue initiation from 9 200 to 10 500 cycles from cold expansion, and an increase in fatigue life from 9 700 to 24 300 cycles. Ball and Lowry [8] refer to studies of Chandawanich and Sharpe (1979) and the "Fastner Hole Quality Program" (1978) in which a small effect of cold worked holes, if any, on crack initiation life of 7075-T6 and 7475-T6 was reported. The R ratio is not known, but probably low. In a study with a flight-by-flight loading sequence on cold expanded holes in an Al A7-U4SG-T651 [82] an increased initiation life of a factor approx. 4 was observed, but 89% of the total increased fatigue was from prolonged propagation. Almer et al. [4] investigated a cold expanded hole in 1080-steel tested at R = 0 and doubled the fatigue initiation from 45 400 to 91 000 cycles with an increased fatigue life from 88 000 to 209 000.

Ferreira et al. [31] studied A515 Grade 70 notched shot peened steel (389 MPa in yield stress) with R = 0 and K_t = 1.7. A 25% increase in fatigue initiation (crack = 0.15 mm) was found in fatigue threshold stress. The increase is from strain-hardening and residual stresses whereas the surface roughness introduced by shot peening will lower the improvement. See Figure 4-51.

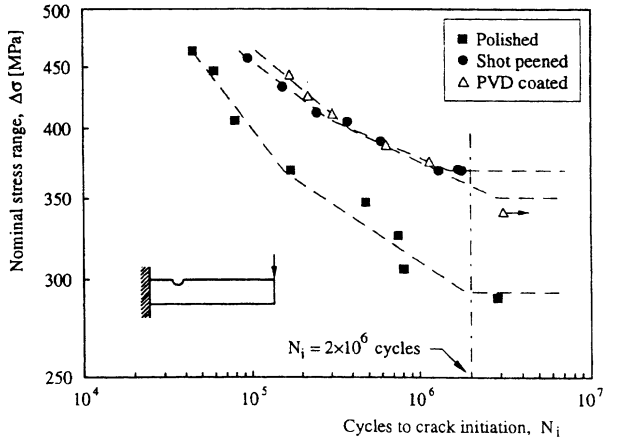

Figure 4-51. Increased fatigue initiation from shot peening compared to polished surface. R = 0. [31]

Several investigations without residual stress have shown non-propagating cracks present after infinite fatigue testing. The first observations of non-propagating cracks emanating from notches were published by Frost and Dugdale in 1957 [36] and Frost in 1960 [35]. Vallellano et al. [100, 101] proposed a mathematical model which was compared to experimental data describing the fatigue initiation threshold and propagating threshold, depending on the severity of the stress concentration and plastic slip barriers (e.g. grain boundaries). For smooth specimen under constant amplitude loading the fatigue threshold will be similar for initiation and failure, $\Delta\sigma_0 = \Delta\sigma_{th}$, whereas $\sigma_0 < \sigma_{th}$ for a notched components with K_t above a critical value. This model will also calculate the non-propagating crack length, which is less accurate than the determination of the K_t-limit where non-propagating fatigue threshold exists. As seen in Figure 4-53, at critical stress the length of non-propagating crack will increase with increasing K_t. Another remarkably observation is that for K_t where propagating threshold exists; the threshold is almost independent of K_t. Microstructural size will influences the length of non-propagating cracks in this model, which is also observed in testing [63, 84]. This mathematical model is also applicable for residual stress fields.

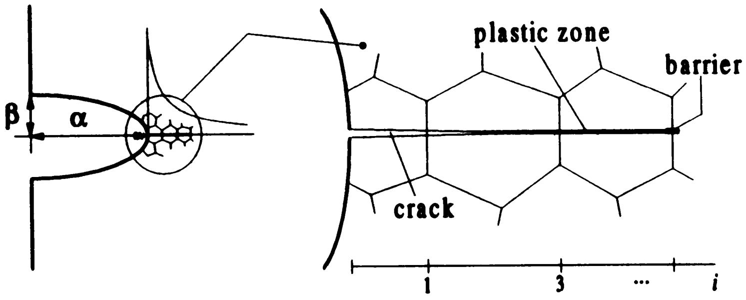

Figure 4-52. Schematic crack growth and grain boundary barriers. [101]

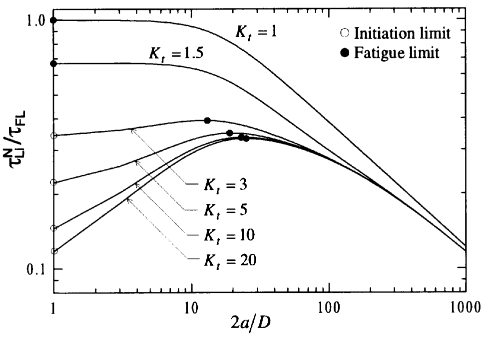

Figure 4-53. Variation of the non-dimensional threshold stress as a function of the non-dimensional crack length for different notch severities. [101]

Kloos et al. [54] studied the effect of repeated over-rolling a notch in a German grade 37CrS4 rolled steel that was heat treated to three strength levels, and GTS 55 steel. The results are shown in Figure 4-54. As seen, better performance is obtained from 45 passes compared to 15. Broszeit et al. [14] tested the same steel as Kloose et al. with a heat treatment giving $R_{p,\,0.2}$ = 243 MPa, showing optimum fatigue treatment close to 40 overpasses. (See Figure 4-55.) One explanation for this behaviour is cyclic work-hardening of a history dependent material, in which development of a more stable cell structure may occur. The dynamic hardening rate will decrease with increasing number of cycles, and will typically be small from 0.1 N_f in steel. Over-rolling will add low cycle fatigue damage to the total damage, and there will be an optimum number of passes, beyond which the low cycle fatigue damage is greater than the beneficial effect of dynamic strain–hardening. The tests where performed with $R = -1$ and no distinction was made between crack initiation and propagation. Most likely the strain-hardening increased the fatigue limit, but a hardening will also increase the residual stresses and hence the crack closure stress in crack propagation. However, Kloos et al. concluded that the major part of the life improvement was due to reduced crack growth.

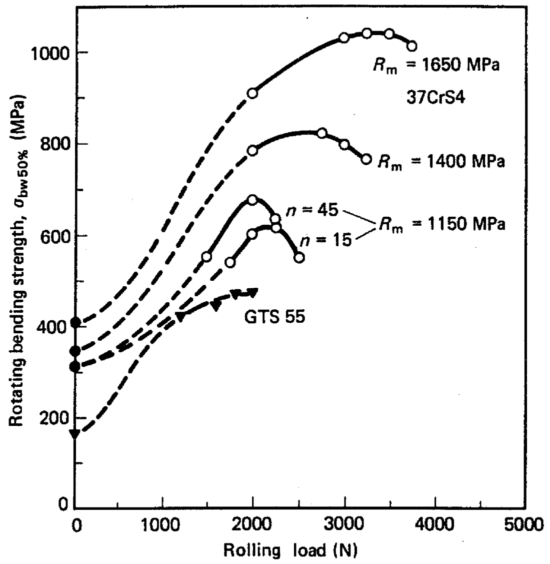

Figure 4-54. Optimised bending fatigue strength on notched steel specimen. $K_t = 2$. n = number of rolling passes. [54]

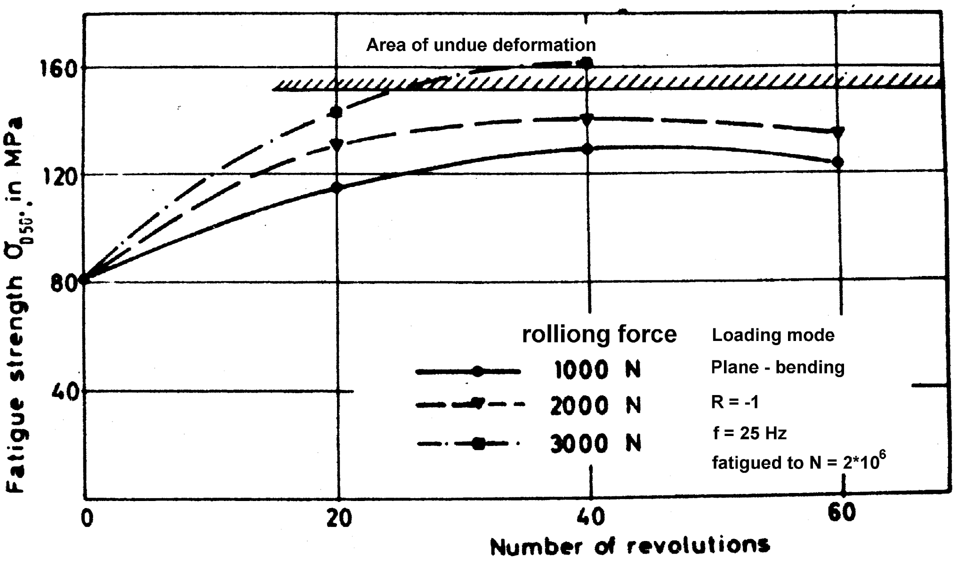

Figure 4-55. Influence of rolling force and number of rolling passes on smooth steel specimen. [14]

Flizpatrick and Edwards [33] found in an expanded hole the residual stress relaxation dependent on the applied stress level and number of cycles as already seen in Section 4.7 Relaxation of residual stresses, even below the fatigue limit. By comparing crack opening measurements on specimen with residual stress fields and stress relieved specimens, Flizpatrick and Edwards found a positive influence from compressive residual stress fields on crack closure.

From a survey of the available literature it may therefore be concluded that reduced crack propagation rate is the major contributing factor to the fatigue improvement that is reported for tests on cold-rolled notched specimens. After an initial fast crack growth a remarkably reduction in crack growth rate takes place before an acceleration after the crack has grown through the residual stress field (see Figure 4-56). Very often a fatigue crack will initiate early (~10 000 cycles, R = -1, K = 2.5 – 3.0 [54, 107]) and grow to a length of some tens of a mm, where a total crack growth stop takes place. Increasing non-propagating crack length is found with decreasing material toughness [54], with 0.38 mm maximum non-propagating crack after cold rolling for a steel with 1040 MPa in yield stress, $K_t = 3.0$ and R = -1. Another cold rolling investigation of steel with 765 MPa yield stress, $K_t = 2.85$ and R = -1, where the improvement was not optimised, 0.7 – 1.0 mm maximum non-propagating cracks were found [107]. This is the length where the crack growth suddenly accelerates for higher constant stress amplitudes (above the fatigue endurance limit), see Figure 4-56. The length of the non-propagating crack depends on material, residual stress, K_t and applied stress.

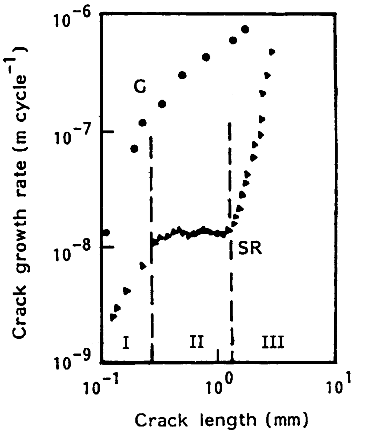

Figure 4-56. Crack growth rate versus crack length for ground (G) and subsequent surface rolled (SR). Steel (SAE5140), R = -1, $K_t = 2.85$. [107]

An important issue is crack closure. At low stress ratios a crack is partly closed (see Section 4.8 Crack closure.) and reduces ΔK to an effective value, ΔK_{eff}. From this it will be obvious that the R-ratio and residual stress profile including possibly relaxation (hence cyclic loading and K_t) are important parameters. Ghfiri et al [40, 41] found R-ratios of 0.5-0.6 to be sufficient to have a open crack during fatigue testing in residual stress fields. This agrees well with tests done in the present work where no further benefit from cold working was found at R-ratios higher than 0.5 (see Section 8.5).

Moshier and Hillberry [78] performed numerical analysis of the residual stress in a notched aluminium specimen with $K_t = 3.17$ which was compared to experimental results. They found a linear relationship between ΔK_{th} and R_{eff}

$$\Delta K_{th} = 1.338 - 0.85 R_{eff} \qquad \text{Equation 4-23}$$

where

$$R_{eff} = \frac{S_{\min} + \frac{S_{res}}{K_t}}{S_{\max} + \frac{S_{res}}{K_t}}$$ Equation 4-24

and S_{res} is the local compressive stress at the notch. It is important to bear in mind that these continuum mechanics based results are incorporating only residual stresses and residual stress based closure mechanisms.

To summaries; in most cases large improvements in fatigue life are found from cold working. One has even found higher fatigue strength after rolling of notch than without notch, fully removing the effect of the notch tested at R = -1 (High strength steel) [54]. But for smooth specimen a reduction from surface cold working is also found in the low cycle, high stress region of the S-N diagram in some cases, e.g. surface rolling of steel [54], shot peening of steel [55, 71]. All lives were ~< 100 000. From strain hardening of high strength steel with K_t = 1.0 a 10 - 20% increased fatigue strength will be expected, which will give 2.4 – 5.2 times increased life with a slope of 9 (See Figure 2-9, ground surface). This agrees with the results of improved initiation life from notched cold worked tests, where residual stress is present. From the fact that increasing the residual stress did not seem to further improve the fatigue initiation life, and that R was in the range 0 to 0.57 without any pattern in improved initiation, it is reasonable to believe that the fatigue initiation is mean stress insensitive for strain hardened steel and aluminium. The "fatigue crack initiation S-N curve" for a cold-worked axial loaded specimen has a lower slope compared to a non-cold worked specimen (see Figure 4-57). For low R-ratio (R < 0.5) the major part of the improvement is caused by decreased crack propagation rate and crack arrest from crack closure. As an example, an increase in the fatigue endurance limit of 230% or more than 100 times increase in fatigue life was found for high strength steels, K_t = 2.0, R = -1 [54]. Similar results are achieved for rolled aluminium [104]. At higher R ratios, and especially above R ~> 0.5 where no closure takes place, the increased fatigue life will "exclusively" be from an increased fatigue crack initiation phase due to strain-hardening, and a possible improved surface finish as long as the residual stress is not found to influence the fatigue initiation as discussed above.

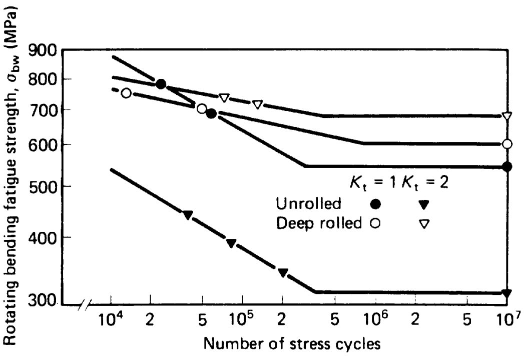

Figure 4-57. S-N curves for smooth and notched cold rolled specimen including residual stress and hardening (notched specimen rolled 45 passes). Notice the small improvement for smooth specimens, and the very large increase for notched specimens. [54]

4.13 Crack growth in residual stress fields

Compressive residual stresses will premature close the crack, giving decreased crack growth rate, whereas tensile residual stresses will keep the crack open at low or even compressive nominal stress and increase the growth rate. This was demonstrated in the work by Hubbard and Reid et al. [49, 85] where residual stresses in tension was introduced by overload in compression, and subsequent crack initiation and growth until 10 mm length under cyclic compressive loading.

Fatigue test by Beghini et al. on compact tension (CT) specimens [10] showed an increased crack growth with increasing R up to a R-ratio between 0.1 and 0.3, where after (R > 0.3) no change was apparent indicating total open crack under the fatigue testing. Similarly, welded CT-specimens with residual stress in tension showed an increased crack growth rate and CT-specimens with residual stress in compression a decreased crack growth rate. In Figure 4-58 the crack growth rate for R = 0.1 is presented. With residual stresses in tension the crack is open during the whole load cycle, and have a higher crack growth rate compared to base material which had a small portion of the cycle with closed crack. The opposite will happen with residual stress in compression, and as seen in Figure 4-58 the effect is more pronounced.

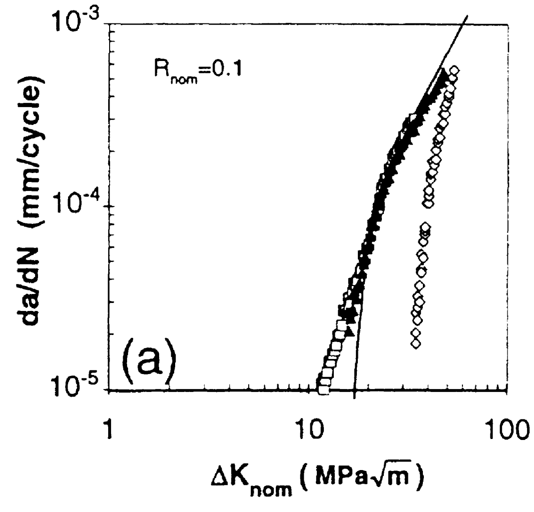

Figure 4-58. Crack growth in residual stress fields from welds. Solid line: base material, Open circles: compressive residual stress, Filled triangles and open squares: tension residual stress. [10]

Residual stress field at a notch can be altered by three different ways; from overload giving plasticity at the notch, long-term decay as described in Section 4.7 Relaxation of residual stresses, and by passage of a crack. Once a crack has passed through a region with residual stress, it is possible that there will be some relaxation of the preexisting residual stress field. It is not clear as to what degree this will occur.

Attempts at modelling the crack growth life in residual stress fields have met with mixed success. The use of weight functions with the initial residual stress field is not applicable in cases when the initial residual stress field changes. A proper description of the stress intensity factor requires a good approximation of the residual stress field at each stage as the crack grows [33], but weight functions can be used to calculate the upper bound to the effect of the residual stress field [81]. Beghini et al. [10] used the weight function method on welded CT-specimen with residual stress, and found the method to give acceptable results for engineering purposes.

Cracks can also initiate in cyclic compression [83, 93]. Suresh [93] and Pippan [83] studied crack growth in compression in both CT and CCT[20] and made similar observations. In stage I crack growth cyclic shear propagated a short crack 45% on the principal load axis. After initiation of a microstructural short crack cyclic plasticity at the crack tip lead to crack growth in stage II, even in compression for mechanical short cracks where no crack closure in the wake takes place. The assumption of no crack closure is fundamental for the crack growth model in compression illustrated in Figure 4-59. Equal crack growth rate for cyclic compression and tension for very short cracks as seen in Figure 4-60 supports this model. The similar fracture surface of cyclically compression and tension is also supporting the model of equal crack growth mechanisms [93]. With increasing crack growth crack closure will be more pronounced, and crack growth rate will decrease and finally stop. See Figure 4-61.

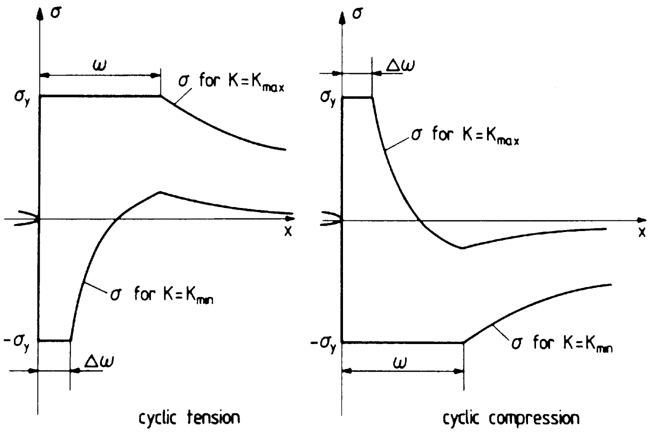

Figure 4-59. Schematic stress distribution in front of a sharp notch for an elastic ideally plastic material for a) cyclic tension and b) cyclic compression. [83]

---

[20] center cra cracked specimens

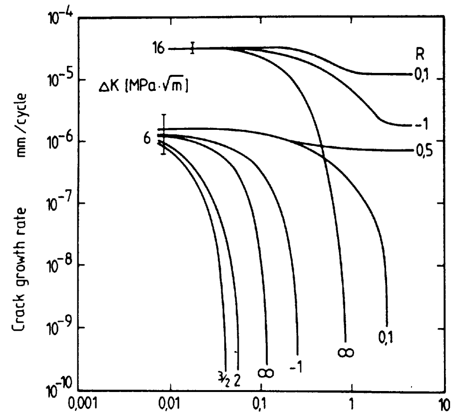

Figure 4-60. Crack growth rate as function of the crack length, l, measured from the notch root for various R under constant ΔK test. [83]

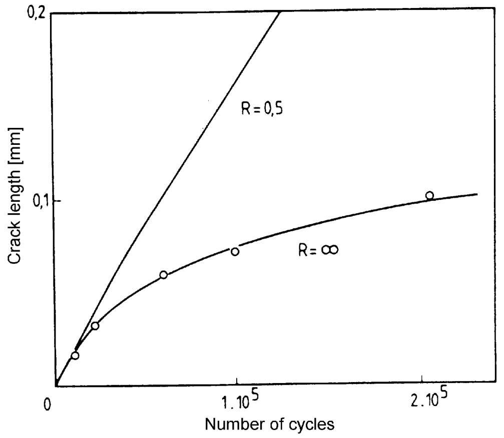

Figure 4-61. Fatigue crack length as function of N, in a compression and tension test with ΔK = 6 MPa√m. [83]

Pippan [83] found the equation

$$a_{\text{non prop}} = \frac{1}{5\pi}\left(\frac{\Delta K}{\sigma_y}\right)^2 \qquad \text{Equation 4-25}$$

to represent the length of a non-propagating crack in compression. From this equation it is reasonable to assume that the length of the non-propagating crack is proportional to the plastic zone size. Suresh found in contradiction to Pippan a critical length of non-propagating cracks beyond which after an increase in ΔK did not increase $a_{\text{non prop}}$. From this observation cyclic compressive load on a fatigue crack of several mm length will not contribute to crack advance, this is explained by complete crack closure taking place for the longer crack.

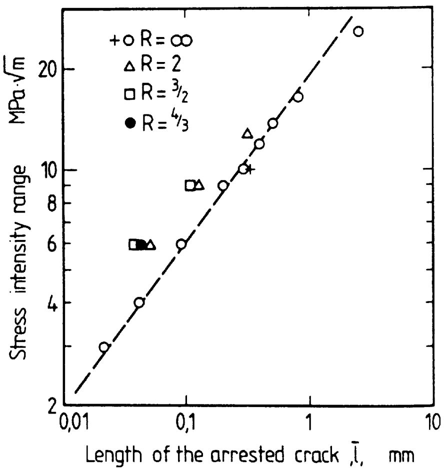

Figure 4-62. Length of arrested cracks as a function of ΔK and R. [83]

The use of cyclic compression fatigue is interesting in crack growth measurements. Precrack preparation in compression for crack growth measurement on CT specimens will give a considerably smaller plastic zone at the tip of the fatigue crack [93]. This method gave crack growth rates for smaller cracks and with 30 % reduction in test time. The traditionally used method for crack growth measurement is presented in Section 4.10. The use of crack initiation by cyclic compression appears to provide a conservative estimate of the crack growth threshold [93]. This is obtained by avoiding too rapid decrease in ΔK, corrosion layer when the decrease in ΔK is too small, and by reducing the role of plastic-induced crack closure.

4.14 Conclusions

BCC and FCC have different atomic structure that controls the dislocation slip systems. In FCC metals with low stacking fault energy dislocation movements give planar-slip pattern that produce PSB's under cyclic strain. Under further cycling strain is localised in the PSB's and cracks are formed. In contrast, dislocation motion in BCC metals gives wavy-slip that is temperature dependent. However, cycling at low strain rates and at high temperatures give dislocation motion much like that found in planar-slip FCC, and PSB's will develop.

Cracks are initiated in the PSB/matrix transition or at intrusions for small grain sizes in metals where PSB's are formed. The PSB's are developed in dislocation systems having high shear stresses, and are therefore close to 45° at the principal load axis. The initial crack is susceptible to environment as new surface material is exposed. Stage I cracks will grow along the PSB and will generally propagate very slowly. When the crack has reached a length of a few grain diameters, the crack growth direction will be normal to the applied stress and is then defined as a stage II crack.

Depending on the degree of prestrain wavy-slip metals will at high plastic prestrain develop dislocation cell structures with broad dislocation walls that decrease in width with increasing prestrain. Once the cell structure is developed, a veinstructure will not be introduced at cyclic strain-rates that would produce veinstructure in a virgin specimen. During strain cycling the cell structure will be cleaned up and the dislocation bands become more pronounced. Consequently, wavy-slip metals will as planar-slip metals be history dependent and the cyclic stress-strain curve will softens linearly with log(N), but insignificantly for HCF. However at prestrains below approximately 10%, cell structure will not develop and wavy-slip metals will remain history independent and the cyclic stress strain curve will approach the monotonic stress-strain curve within a short transition period. The long-term residual stress relaxation is proportional to the softening as indicated by the change in the cyclic stress-strain curve.

The crack growth rate increases with increasing R-ratio until a limit value (R~0.2) after which no increase will take place. This indicates the important effect of crack closure and not factors at the crack tip. Crack closure can explain several important effects observed in fatigue, but the extent of crack closure is debated. The measurement of crack closure is notoriously difficult, but the reproducibility has increased in later years. Presence of crack closure will reduce ΔK_{eff}, but in many studies of the closure phenomenon the closure stress has been overestimated and thus a non-conservative ΔK_{eff} has been predicted. There are several sources for crack closure, and residual stress is dominating in situations where residual stresses exist. When a compressive residual stress is present, the residual stress acts as an external closing mechanism, opposite to the applied load, forces the crack closed and reduces the amount of plastically deformed material. The result is an opening stress that is less than the original opening stress when residual stress was not present. When residual stress is not present scientific work has shown that the main contribution to crack closure are crack surface roughness and crack surface oxidation. Generally crack closure will be most dominant at low values of ΔK and R, and therefore influences crack growth in the threshold and during HCF. This will give a rather small plastic zone at the crack tip, which makes LEFM applicable and the most convenient tool for analysis. Cracks initiated at stress concentrations and later arrested are non-propagating as long as the compressive residual stress field does not relax due to plasticity or temperature effects. The great number of scientific work which have observed crack closure makes, as some claims, the total absence of crack closure or insignificant closure to be unrealistic in author's view.

For many years the improvement from a residual stress field on fatigue life was taken to be a suppression of crack initiation, but it is now clear that effects on fatigue crack growth rate and subsequent crack arrest is most dominant at least for $R \stackrel{\sim}{<} 0.4$. However, strain hardening has been shown to increase the fatigue threshold for most common steels with approximately 10-15%. The effect seems to be R independent, but the amount of data studied regarding this effect during the present work is not sufficient. In some investigations the improvement might be from residual stress introduced during strain hardening. However, there are reports where a decrease of the fatigue threshold is seen which makes strain hardening induced fatigue improvement dangerous as a general fatigue improvement technique.

Some studies on repeated cold rolling have shown an increase in fatigue life until a number of over-rolls where the amount of damage introduced from each over-roll exceeds the benefit. This limit is found at approximately 40 passes. The most plausible explanation of this observation is cyclic hardening, which will contribute both to increased initiation and increased residual stress. The increased residual stress will increase the closure effect and hence increase fatigue propagation life.

There is no clear definition of short cracks. However, short cracks have both a considerably higher scatter in crack growth data than long cracks and higher crack growth rates. The higher growth rate is best explained by lack of a significant wake behind the crack where contact between the crack surfaces can take place. This model is supported both by similar crack growth rate for short cracks cycled at similar ΔK in cyclic compression and cyclic tension load, and similar fracture surface of from both load cases. By using the concept of crack closure several investigators have crack growth data for short cracks equal the curve obtained from long cracks. Use of LEFM on short cracks is debated, as the requirement of small plastic zone compared to crack size often fails. Higher T-term that vanished in the expression for K for long cracks will influence K for short cracks. These problems are reduced by use of EPFM or CTOD.

Continuum mechanics is not incorporating discrete dislocation motion, and hence not appropriate used at crack propagation rates near threshold [87]. However, the computer capacity required to perform 2D analysis of discrete dislocation model is massive [87], and the CPU required for a 3D analysis with crack not easily accessible. From discrete dislocation analysis $\Delta K_{eff,\,th}$ is found nearly independent of R and yield stress. However, since the inaccuracy introduced by plasticity in continuum mechanics is smaller than the inaccuracy from random orientation of slip system across grains, oxidation and roughness induced closure, it is considered unnecessary to model the exact plastic motion from dislocation theory at the crack tip.

4.15 References:

1 Akinawa Y., Tanaka K. and Taniguchi N. (1990) Prediction of propagation and nonpropagation of short fatigue cracks at notches under mean stress. *JSME International Journal* 33, 288-269.

2 Akiniwa Y., Zhang L.M. and Tanaka K. (1997) Prediction of the fatigue limit of cracked specimens based on the cyclic R-curve method. *Fatigue Fract Engng Mater Struct* 20, 1387-1398.

3 Almar-Næss A. (Editor)(1985) Fatigue Handbook, offshore steel structures. Tapir.

4 Almer J.D., Cohen J.B. and Moran B. (2000) The effect of residual macrostresses and microstresses on fatigue crack initiation. *Materials Science and Engineering* A284, 268-279.

5 Almer J.D., Cohen J.B. and Winholtz R.A. (1998) The effects of residual macrostresses and microstresses on fatigue crack propagation. *Metallurgical and Materials Transaction A* 29, 2127-2136.

6 Anderson T.L. (1995) Fracture Mechanics. Fundamentals and Applications. Second edition. CRC press LCC.

7 Bai-ping D. and Nian L. (1992) Relation between fatigue threshold and fatigue limit for surface-rolled specimens. *International Journal of Fatigue* 14, 403-409.

8 Ball D.L. and Lowry D.R. (1998) Experimental Investigation on the Effects of Cold Expansion of Fastener Holes. *Fatigue Fract Engng Mater Struct* 21, 17-34.

9 Basinski Z.S., Pascual R. and Basinski S.J. (1983) Low amplitude fatigue of copper single crystals - I. The role of the surface in fatigue failure. *Acta metallurgica et materiala* 31, 591-602.

10 Beghini M., Bertini L. and Vitale E. (1994) Fatigue crack growth in residual stress fields: experimental results and modelling. *Fatigue Fract Engng Mater Struct* 17, 1433-1444.

11 Belassel M. and Lebrun J.L. (1997) Micro residual stress evaluation during elastic and elastoplastic fatigue tests in two-phase eutectoid steel. In The fifth international conference on residual stresses, ICRS-5. Edited by Ericsson T., Odén M. and Andersson A. pp 1174-1179.

12 Bernard M., Bui-Quoc T. and Burlat M. (1995) Effect of re-coldworking on fatigue life enhancement of a fastner hole. *Fatigue Fract Engng Mater Struct* 18, 765-775.

13 Berstein G. and Fuchsbauer B. (1982) Festwalzen und Schwingfestigkeit. *Z Werkstofftech* 13, 103-109.

14 Broszeit E., Hauk V., Oudelhoven R. and Steindorf H. (1989) Residual stress state after roll-peening of sintered Fe-Cu material. In International conference on residual stresses, ICRS-2. Edited by Beck G., Denis S. and Simon A. Elsevier science publishers, London. pp 46-51.

15 Budiansky B. and Hutchinson J.W. (1978) Analysis of closure in fatigue crack growth. *Journal of Applied Mechanics* 45, 267-276.

16 Buxbaum O. and Huth H. (1987) Expansion of cracked fastener holes as a measure for extension of lifetime to repair. *Engineering Fracture Mechanics* 28, 689-698.

17 Chai H.-F. and Laird C. (1987) Mechanisms of cyclic softening and cyclic creep in low carbon steel. *Materials Science and Engineering* 93, 159-174.

18 Christ H.-J. (1996) Microstructural aspects of cyclic loading. In ASM Handbook. Edited by Lampmam S.R. Metals Park, Ohio. pp 76-86.

19 Christ H.-J. (1996) Cyclic stress-strain response and microstructure. In ASM Handbook, Fatigue and fracture. Edited by Lampman S.R. Metals Park, Ohio. pp 73-76.

20 Christ H.J., Hoffmann G. and Öttinger O. (1995) History effects in metals during constant and variable amplitude testing. I: Wavy dislocation glide behaviour. *Materials Science and Engineering* A201, 1-12.

21 Clark G. (1991) Modelling residual stresses and fatigue crack growth at cold-expanded fastener holes. *Fatigue Fract Engng Mater Struct* 14, 579-589.

22 Colangelo V.J. and Heiser F.A. (1986) Analysis of Metallurgical Failures, second edition. John Wiley & Sons.

23 De la Cruze P., Odén M., Billenius A. and Ericsson T. (1997) Fatigue behaviour and residual stress relaxation of a plasma nitrided B-Mn steel. In The fifth international conference on residual stresses, ICRS-5. Edited by Ericsson T., Odén M. and Andersson A. pp 1162-1167.

24 Desvignes M., Gentil B. and Castrex L. (1989) Fatigue with residual stresses due to shot peening: effects and evolution. In International conference on residual stresses, ICRS2. Edited by Beck G., Denis S. and Simon A. Elsevier science publishers, London. pp 791-796.

25 Dieter G.E. (1988) Mechanical Metallurgy, SI metric edition. McGraw-Hill, Singapore.

26 Donald J.K. and Phillips E.P. (1999) Analysis of the second ASTM round-robin program on opening-lad measurement using the adjusted compliance ratio technique. In Advances in fatigue crack measurement and analysis. Edited by McClung R.C. and Newman J.C. ASTM. pp 79-93.

27 Donald K. and Paris P.C. (1999) An evaluation of ΔK_{eff} estimation procedures on 6061-T6 and 2024-T3 aluminum alloys. *International Journal of Fatigue* 21, 47-57.

28 El Haddad M.H., Tropper T.H. and Smith K.N. (1979) Prediction of nonpropagating cracks. *Engineering Fracture Mechanics* 11, 573-584.

29 Fang G., Xu K.W. and Zhang D.Q. (1989) Effect of cyclic stress and temperature on residual stress relaxation. In International conference on residual stresses, ICRS2. Edited by Beck G., Denis S. and Simon A. Elsevier science publishers, London. pp 759-764.

30 Feltner C.E. and Laird C. (1967) Cyclic stress-strain response of F.C.C. metals and alloys - II Dislocation structures and mechanisms. *Acta Metallurgica* 15, 1633-1653.

31 Ferreira J.A.M., Borrego L.F.P. and Costa J.D.M. (1996) Effects of surface treatments on the fatigue of notched bend specimens. *Fatigue Fract Engng Mater Struct* 19, 111-117.

32 Finch D.M. (1994) A review of non-destructive residual stress measurement techniques. ERA Report 94-0101R. ERA Technology Limited, Surry.

33 Flitzpatrick M.E. and Edwards L. (1998) Fatigue crack/residual stress field interactions and their implications for damage-tolerant design. *Journal of Materials Engineering and Performance* 7, 190-198.

34 Forman R.G., Kearney V.E. and Engle R.M. (1967) Numerical analysis of crack propagation in cyclic-loaded structures. *Transactions of the ASME* 89, 459.

35 Frost N.E. (1960) Notch effects and the critical alternating stress required to propagate a crack in an aluminium alloy subject to fatigue loading. *Journal of Mechanical Engineering Science* 2, 109-119.

36 Frost N.E. and Dugdale D.S. (1957) Fatigue tests on notched mild steel plates with measurements of fatigue cracks. *Journal of the Mechanics and Physics of Solids* 5, 182-192.

37 Frost N.E., Marsh K.J. and Pook L.P. (1973) Metal Fatigue. Oxford University Press, Belfast.

38 Fuchs H.O. (1959) Techniques of surface stressing to avoid fatigue. In Metal Fatigue. Edited by Sines G. and Waisman J.L. McGraw-Hill book company, Pennsylvania. pp 197-231.

39 Garcia-Granada A.A., Lacarac V.D., Holdway P., Smith D.J. and Pavier M.J. (2001) Creep relaxation of residual stresses around cold expanded holes. *Journal of Engineering Materials and Technology* 123, 125-131.

40 Ghfiri R., Amarouche A., Imad A. and Mesmacque G. (2000) Fatigue life estimation after crack repair in 6005 A-T6 aluminium alloy using the cold expansion hole technique. *Fatigue Fract Engng Mater Struct* 23, 911-916.

41 Ghfiri R., Shi H.-J., Guo R. and Mesmacque G. (2000) Effects of expanded and non-expaned hole on the delay of arresting crack propagation for aluminium alloys. *Materials Science and Engineering* A286, 244-249.

42 Goto M., Miyagawa H. and Nisitani H. (1996) Crack growth arresting property of a hole and brinell-type dimple. *Fatigue Fract Engng Mater Struct* 19, 39-49.

43 Haagensen P.J., Gunleiksrud Å., Ludvigsen J.A. and Larsen J.E. (2000) Repair and strengthening of the Veslefrikk B floating production platform. In Proceedings of OMAE 2000, 14-17 February, New Orleans.

44 Hammouda M.M.I., Ahmad S.S.E., Sherbini A.S. and Sallam H.E.M. (1999) Deformation behaviour at the tip of a physically short fatigue crack due to a single overload. *Fatigue Fract Engng Mater Struct* 22, 145-151.

45 Helgeland O. (1965) Cyclic hardening and fatigue of copper single crystals. *Journal of the Institute of Metals* 93, 570-575.

46 Heller M., Jones R. and Williams F. (1991) Analysis of cold-expansion for cracked and uncracked fastner holes. *Engineering Fracture Mechanics* 39, 195-212.

47 Heywood R.B. (1962) Design against fatigue in metals. Reinhold, New York.

48 Holzapfel H., Schulze V., Vöhringer O. and Macherauch E. (1998) Residual stress relaxation in an AISI 4140 steel due to quasistatic and cyclic loading at higher temperatures. *Materials Science and Engineering* A248, 9-18.

49 Hubbard R.P. (1969) Crack growth under cyclic compression. *ASME Journal of Basic Engineering* 91, 625-631.

50 Kirkhope K.J., Bell R., Caron L., Basu R.I. and Ma K.-T. (1999) Weld detail fatigue life improvement techniques. Part 2: application to ship structures. *Marine Structures* 12, 477-496.

51 Kitagawa H. and Takahashi S. (1976) Applicability of fracture mechanics to very small cracks or the cracks in the early stage. In Proc. of second international conf. on mechanical behavior of materials. American society for metals. pp 627-631.

52 Klesnil M. and Lukas P. (1992) Fatigue of metallic materials, second revised edition. Elsevier, Amsterdam.

53 Kloos K.H., Broszeit E., Fuchsbauer B. and Schmidt F. (1981) Optimierung von Schwingfestligkeitseigenschaften beim Oberflächendrücken gekerbter Umlaufbiegeproben unter Berücksichtigung der Probengrösse. *Z Werkstofftech* 12, 359-365.

54 Kloos K.H., Fuchsbauer B. and Adelmann J. (1987) Fatigue properties of specimens similar to components deep rolled under optimized conditions. *International Journal of Fatigue* 9, 35-42.

55 Kodama S. (1971) The behaviour of residual stress during fatigue stress cycles. In Mechanical behaviour of materials. Proc. of the int. conf. on mech. behaviour of materials. The society of materials science. pp 111-118.

56 Krenn C.R. and Morris J.W. (1999) The compatibility of crack closure and K_{max} dependent models of fatigue crack growth. *International Journal of Fatigue* 21, 147-155.

57 Kuo H.K. and Cohen J.B. (1983) Changes in residual stress, domain size and microstrain during the fatigue of AISI 1008 steel. *Materials Science and Engineering* 61, 127-136.

58 Laird C. (1996) Fatigue. In Physical Metallurgy. Edited by Chan R.W. and Haasen P. Elsevier Science, Amsterdam. pp 2293-2397.

59 Lam T.S., Topper T.H. and Conle F.A. (1998) Derivation of crack closure and crack growth rate data from effective-strain fatigue life data for fracture mechanics fatigue life predictions. *International Journal of Fatigue* 20, 703-710.

60 Lang M. (2000) A model for fatigue crack growth, part II: modelling. *Fatigue Fract Engng Mater Struct* 23, 603-617.

61 Lang M. and Huang X. (1998) The influence of compressive loads on fatigue crack propagation in metals. *Fatigue Fract Engng Mater Struct* 21, 65-83.

62 Lang M. and Marci G. (1999) The influence of single and multiple overloads on fatigue crack propagation. *Fatigue Fract Engng Mater Struct* 22, 257-271.

63 Lankford J. (1977) Initiation and early growth of fatigue cracks in high strength steel. *Engineering Fracture Mechanics* 9, 617-624.

64 Lawson L., Chen E.Y. and Meshii M. (1999) Near-threshold fatigue: a review. *International Journal of Fatigue* 21, 15-34.

65 Leon A. (1998) Benefit of split mandrel coldworking. *International Journal of Fatigue* 20, 1-8.

66 Louat N., Sadananda K., Duesbery M. and Vasudevan A.K. (1993) A theoretical evaluation of crack closure. *Metallurgical Transaction A* 24A, 2225-2232.

67 Lukas P. and Klesnil M. (1973) Cyclic stress-strain response and fatigue life of metals in low amplitude region. *Materials Science and Engineering* 345-355.

68 Ma B.-T. and Laird C. (1989) Overview of fatigue behaviour in copper single crystals - II. Population, size, distribution and growth kinetics of stage I cracks for tests at constant strain amplitude. *Acta metallurgica et materiala* 37, 337-348.

69 Manson S.S. (1962) discussion of reference no. 99. *Transactions of the ASME* 84, 537.

70 Martin U., Oettel H., Schreiber G. and Mühle U. (1997) Microstructure related mechanicms of residual stress relaxation in metals. In The fifth international conferance on residual stresses, ICRS-5. Edited by Ericsson T., Odén M. and Andersson A. pp 1121-1126.

71 McClinton M. and Cohen J.B. (1982) Changes in residual stress during the tension fatigue of normlized and peened SAE 10400 steel. *Materials Science and Engineering* 56, 259-263.

72 McClung R.C. (1991) Crack closure and plastic zone sizes in fatigue. *Fatigue Fract Engng Mater Struct* 14, 455-468.

73 McClung R.C. and Sehitoglu H. (1989) On the finite element analysis of fatigue crack closure - 1. Basic modeling issues. *Engineering Fracture Mechanics* 33, 237-252.

74 McClung R.C. and Sehitoglu H. (1989) On the finite element analysis of fatigue crack closure - 2.Numerical results. *Engineering Fracture Mechanics* 33, 253-272.

75 McClung R.C., Thacker B.H. and Roy S. (1991) Finite element visualization of fatigue crack closure in plane stress and plane strain. *International Journal of Fracture* 50, 27-49.

76 McEvily A.J. and Ritchie R.O. (1998) Crack closure and the fatigue-crack propagation threshold as a function of load ratio. *Fatigue Fract Engng Mater Struct* 21, 847-855.

77 Meguid S.A., Shagal G., Stranart J.C. and Daly J. (1999) Three-dimentional dynamic finite element analysis of shot-peening induced residual stresses. *Finite Elements in Analysis and Design* 31, 179-191.

78 Moshier M.A. and Hillberry B.M. (1999) The inclusion of compressive residual stress effects in crack growth modelling. *Fatigue Fract Engng Mater Struct* 22, 519-526.

79 Mughrabi H. (1985) Dislocation in fatigue. In Proc. of the 50th anniversary of the concept of dislocations in crystals. The Institute of Metals, London. pp 244-262.

80 Paris P.C., Gomez R.E. and Anderson W.E. (1961) A rational analytic theory of fatigue. *The Trend in Engineering* 13, 9-14.

81 Pavier M.J., Poussard C.G.C. and Smith D.J. (1999) Effect of residual stress around cold worked holes on fracture under superimposed mechanical load. *Engineering Fracture Mechanics* 63, 751-773.

82 Pell R.A., Beaver P.W., Mann J.Y. and Sparrow J.G. (1989) Fatigue of thick-section cold-expaned holes with and without cracks. *Fatigue Fract Engng Mater Struct* 12, 553-567.

83 Pippan R. (1987) The growth of short cracks under cyclic compression. *Fatigue Fract Engng Mater Struct* 9, 319-328.

84 Radhakrishnan V.M. and Mutoh Y. (1986) On Fatigue Crack Growth in Stage I. In The behaviour of Short Fatigue Cracks. Edited by Miller K.J. and Mutoh Y. Mechanical Engineering Publication Limited, London. pp 87-99.

85 Reid C.N., Williams K. and Hermann R. (1979) Fatigue in compression. *Fatigue of Engineering Materials and Structures* 1, 267-270.

86 Riemelmoser F.O., Gumbsch P. and Pippan R. (2000) Plastic deformation at short edge cracks under fatigue loading. *Engineering Fracture Mechanics* 66, 357-374.

87 Riemelmoser F.O., Gumbsch P. and Pippan R. (2001) Dislocation modelling of fatigue cracks: An overview. *Materials Transactions* 42, 2-13.

88 Riemelmoser F.O. and Pippan R. (1999) On the ΔK_{eff} concept: An investigation by means of a discrete dislocation model. In Advances in fatigue crack closure measurement and analysis. Edited by McClung R.C. and Newman J.C. ASTM. pp 1-13.

89 Roven H.J. (1986) Utmatting - Mikrostruktur, en litteraturundersøkelse. SINTEF, Trondheim, Norway.

90 Roven H.J. and Nes E. (1991) Cyclic deformation of ferritic steel - I. Stress-strain response and structure evolution. *Acta metallurgica et materiala* 39, 1719-1733.

91 Sadananda K. and Vasudevan A.K. (1997) Short crack growth and internal stresses. *International Journal of Fatigue* 19, 99-108.

92 Sadananda K., Vasudevan A.K., Holtz R.L. and Lee E.U. (1999) Analysis of overload effects and related phenomena. *International Journal of Fatigue* 21, 233-246.

93 Suresh S. (1985) Crack initiation in cyclic compression and its applications. *Engineering Fracture Mechanics* 21, 453-463.

94 Suresh S. (1998) Fatigue of Materials, second edition. Cambridge University Press, Cambridge.

95 Suresh S. and Ritchie R.O. (1984) Propagation of short fatigue cracks. *International Metals Reviews* 29, 445-476.

96 Tada H., Paris P.C. and Irwin G.R. (2000) The Stress Analysis of Cracks, Handbook. Professional Engineering Publishing, Edmunton, UK.

97 Tanaka K. (1987) Mechanisms and mechanics of short fatigue crack propagation. *JSME International Journal* 30, 1-13.

98 Tanaka K. and Nakai Y. (1983) Propagation and non-propagation of short fatigue cracks at a sharp notch. *Fatigue of Engineering Materials and Structures* 6, 315-327.

99 Tavernelli J.F. and Coffin L.F. (1962) Experimental support for generalized equation predicting low cyclic fatigue. *Transactions of the ASME* 84, 533.

100 Vallellano C., Navarro A. and Domínguez J. (2000) Fatigue crack growth threshold conditions at notches. Part II: generalization and application to experimantal results. *Fatigue Fract Engng Mater Struct* 23, 123-128.

101 Vallellano O., Navarro A. and Domínguez J. (2000) Fatigue Crack Growth Threshold Conditions at Notches. Part I: Theory. *Fatigue Fract Engng Mater Struct* 23, 113-121.

102 Vasudevan A.K. and Sadananda K. (1995) Classification of fatigue crack growth behaviour. *Metallurgical and Materials Transaction A* 26A, 1221-1234.

103 Vasudevan A.K., Sadananda K. and Louat N. (1994) A review of crack closure, fatigue crack threshold and related phenomena. *Materials Science and Engineering* A188, 1-22.

104 Wagner L., Müller C. and Gregory J.K. (1993) Influence of surface rolling on notched fatigue strength of Al2024 in two age-hardening conditions. In Fatigue 93 - Proceedings of the Fifth International Conference on Fatigue and Fatigue Threshold, 3-7 May 1993, Montreal, Canada. Edited by Bailon J.-P. and Dickson J.I. Engineering Materials Advisory Services Ltd, Cradley Heath. pp 471-476.

105 Wang R. and Mughrabi H. (1984) Secondary cyclic hardening in fatigued copper monocrystals and polycrystals. *Materials Science and Engineering* 63, 147-163.

106 Winholtz R.A. and Cohen J.B. (1992) Changes in the macrostresses and microstresses in steel with fatigue. *Materials Science and Engineering* A154, 155-163.

107 Xu K., He J. and Zhou H. (1994) Effect of residual stress on fatigue behaviour of notches. *International Journal of Fatigue* 16, 337-343.

108 Xu K., Hu N. and Zhou H. (1996) Prediction of notch fatigue limits in a compressive residual stress field. *Engineering Fracture Mechanics* 54, 171-176.

109 Zhang L., Akiniwa Y. and Tanaka K. (1997) Fatigue strength evaluation of cracked components. *JSME International Journal* 40, 445-452.

110 Özdemir A.T. and Edwards L. (1997) Relaxation of residual stresses at cold-worked fastener holes due to fatigue loading. *Fatigue Fract Engng Mater Struct* 20, 1443-1451.

5 Residual stress measurements and verification

5.1 Notation

α	angle between x-direction to max principal stress
α_j	angle between x-direction to max principal stress in increment j
ε_θ	tangential strain
$\varepsilon_{k,nj}$	surface strain at gauge No. k = 1,2 or 3 from j'th layer of n total layers
$\bar{\varepsilon}_{k,n}$	measured surface strain at gauge No. k = 1,2 or 3 after n layers
$\hat{\varepsilon}_{k,n}$	calculated surface strain from layers 1..n-1 at n total layers
ε_k	strain from gauge k = 1,2 or 3 respectively
ε_r	radial strain
ε_x	strain in x-direction
ε_y	strain in y-direction
ϕ	dimensionless hole diameter = $2R_0/D$
ν	Poisson's ratio
$\sigma_r^{'}$	radial stress prior to hole drilling [MPa]
$\sigma_r^{''}$	radial stress after hole drilling [MPa]
$\sigma_\theta^{'}$	tangential stress prior to hole drilling [MPa]
$\sigma_\theta^{''}$	tangential stress after hole drilling [MPa]
σ_x	stress in x-direction [MPa]
σ_y	stress in y-direction [MPa]
σ_1	max principal stress [MPa]
$\sigma_{1,j}$	max principal stress in layer j [MPa]
σ_2	min principal stress [MPa]
$\sigma_{2,j}$	min principal stress in layer j [MPa]
$\tau_{r\theta}^{'}$	shear stress prior to hole drilling [MPa]
$\tau_{r\theta}^{''}$	shear stress after hole drilling [MPa]
A	hole drilling coefficient
A_0	original tensile-test cross-section area
$\bar{A}$	blind-hole drilling coefficient
$\bar{A}_{nj}$	incremental hole drilling coefficient for j'th layer of total n layers in hole

$\bar{a}$	material independent blind-hole drilling coefficient
$\bar{a}_{jn}$	material independent incremental hole drilling coefficient for j'th layer of n layer in hole
B	hole drilling coefficient
$\bar{B}$	blind-hole drilling coefficient
$\bar{B}_{nj}$	incremental hole drilling coefficient for j'th increment of total n increments in hole
$\bar{b}$	material independent blind-hole drilling coefficient
$\bar{b}_{nj}$	material independent incremental hole drilling coefficient for j'th layer of n layer in hole
D	gauge diameter [m]
E	Young's modulus [MPa]
F	Force [N]
FE	finite element
H	dimensionless stress depth = 2h/D
h	stress depth [m]
HBM	Hottinger Baldwine Messtechnik
K	stress intensity factor [$Nm^{-3/2}$]
K_{eff}	effective stress intensity factor [$Nm^{-3/2}$]
M&M	Micro-Measurements Group
R	stress ratio = $\sigma_{min}/\sigma_{max}$
R	radial distance [m]
R_0	hole radius [m]
r	dimensionless distance = R/R_0
$Rp_{0.2}$	yield stress [MPa]
UTS	ultimate tensile stress = F/A_0
Z	dimensionless hole depth = 2z/D
z	hole depth [m]
z_j	depth of increment j [m]

5.2 Introduction

Residual stresses in structures are of great importance for resistance to fatigue and brittle failure, and have been widely investigated. Residual stresses may be accounted for through the influence on K, ΔK_{eff} and R in fracture and fatigue assessments.

All residual stress systems have zero resultant force, the body being in self-equilibrium [17]. The distance or range over which the stresses achieve this balance may be grouped into two classes. The first kind of residual stress termed macrostress, is long range in nature, extending at least over several grains and is easily measured by destructive mechanical methods such as machining or chemical milling. Macrostresses are caused by thermal treatment, mechanical operations including machining and forming, chemical processes, or combinations of these. The second type of residual stress termed microstresses, range over dimensions of approximately one grain and may be generated by a difference in mechanical properties of different phases in a material or by yield anisotropy between individual grains. See also Section 4.6.

In many situations, residual stresses have a negative impact on the behaviour of a structure, e.g. residual stresses caused by welding. These stresses can be utilised as a positive influence by employing one of the many mechanical treatments available such as rolling or any of the various peening techniques that introduce compressive residual stresses. However, relaxation of surface residual stresses under cyclic loading will reduce their effectiveness. See Section 4.7.

Since residual stress is a very important factor in increasing fatigue strength by surface rolling of threads, a major part of the present work was focused on verification of the FE analysis of residual stresses. The first part of this Chapter describes in detail the integral hole drilling method. A test procedure for the introduction of residual stress is presented, the procedure is simulated by FE analysis, and the results are verified by the integral hole drilling method. The results are then compared.

5.3 Residual stress measurement techniques

Residual stress measurements are complicated, and highly accurate techniques should be used to minimize experimental errors. Unfortunately, measurements are often performed without proper regard for the limitations of each technique; and the interpretation of the results may be wrong, and the results are therefor useless [14].

The only equipment available for residual stress measurements at NTNU is for the hole drilling method, and this was therefore used in the work presented in this thesis. However, other residual stress measurement techniques exists and these will also be discussed briefly in this Section.

5.3.1 Classification of Measurement Techniques

There are several relatively well-developed non-destructive and semi-destructive measurement techniques. These methods can be grouped in four major generic categories [11]:

- Strain gauge stress relief
- Diffraction
- Ultrasonic
- Magnetic

In fact, no technique can measure stresses directly. Strain gauge and diffraction techniques measure the mechanical and lattice deformations, respectively, while the other techniques measure physical or mechanical properties that are changed by stress, and these measurements are then used to determine the nature and the magnitude of the stress distribution.

Strain gauge techniques are destructive or semi-destructive and involve removal of material at the position of residual stress measurement near to a set of strain gauges. These methods are based on the principle that the removal of stressed material disturbs the equilibrium of stresses in it's vicinity, thus resulting in a measurable change of strain at the location of the strain gauge. These strains can then be used to calculate the residual stresses that existed prior to the removal of the material.

5.3.2 Trepanning or ring-core drilling

A strain gauge is placed at the position where the residual stress is to be determined. A circular groove is then cut around the strain gauge. The method in its original form is only valid for a residual stress field that is constant in the depth direction.

If the groove is made deep enough, no further strain relief will take place at the surface where the strain gauge is located. Elastic stress-strain analysis is then used to calculate residual stresses. However, if the groove is not deep enough for complete strain relief, a calibration-routine must be established. This can be done either experimentally or by FE analysis. The same basic equations are used, but with a hole geometry reduction factor. The basic equation can be written as

$$\sigma_{1,2} = f(\varepsilon_{1,2,3}, z, K_1, K_2, E, \upsilon) \qquad \text{Equation 5-1}$$

where K_1 and K_2 are reduction factors that depend on the machining depth, the ring core geometry and the strain gauge rosette arrangement. The assumption of constant in-depth residual stress can be controlled in the same way as in the blind-hole method (see Section 5.4.2) by performing incremental drilling with subsequent strain readings. Ajovalasit et al. [2] have further developed the original ring core method to accommodate stress gradients in the depth direction.

The main advantage with this method is it's greater sensitivity compared to the hole drilling methods. The original ring core method is also insensitive to minor diameter errors or eccentricity of the annular hole with respect to the strain gauge. The main disadvantage of the method is the relative large area measured, typically about 15 mm in diameter and from 2 to 20 mm in depth for metals, and the need to disconnect the gauge wires before drilling. No standard procedure or commercial equipment is available, and the method has not been verified as widely as the hole drilling technique. This method is primarily used for very large components.

5.3.3 Chip removal

The technique was developed at Battelle Columbus Division [31] and involves cutting a pyramid of material (chip) by use of a high-speed dental drill and carbide burrs. Typical dimension of the removed chip is of the order of 5 mm on the four sides with a height of approximately 0.15 mm. An ordinary strain-gauge rosette is attached to the specimen where the residual stresses are to be examined and the strain relief is then measured after chip removal.

The degree of relaxation depends on the shape of the chip and the nature of the stress field. The strain relieved by this technique is far greater than by the blind hole drilling technique. It is straightforward to determine the residual stress from strain, and measurement accuracy is claimed to be within ±30 microstrain. Measurement accuracy depends on operator skill, avoiding the introduction of residual stresses during the cutting process, and the stress gradient perpendicular to the surface. This technique is not widely used and very few publications on the technique exist [11.

A very similar technique is to cut out the strain gauge by sawing. This is a very simple and rough method, which again depends strongly on operator skill and the stress gradient perpendicular to the surface

5.3.4 Diffraction techniques

The diffraction techniques are non-destructive. Two types of diffraction techniques are presently in use: *x-ray diffraction* standardised by ASTM [5] and *neutron diffraction*. The techniques exploit the fact that when metal is under stress, applied or residual, the resultant elastic strains cause the atomic planes in the metallic crystal structure to change their spacing.

The use of x-ray diffraction is well established and often used as a reference for other residual measurement techniques. Lately, portable x-ray devices have been developed for on-site measurements. The conventional technique is capable of measuring the stresses in a surface layer approximately 0.05 mm deep [11]. The accuracy is very good, in the region of 2-3% [5]. To measure residual stresses in the depth direction, the electrolytic layer removal method is often used. Strictly speaking the residual stresses measured in the depth should be corrected for the redistribution after material removal. A high-energy dispersive x-ray diffraction method has been developed to obtain stress information in the interior of the material [11].

The neutron diffraction method measures the atomic spacing in a small volume deep in a material, and a full 3D residual stress field can be determined. The high-flux reactor or neutron accelerator source that is necessary limits the use of the neutron diffraction method [33] to nuclear laboratories.

5.3.5 Ultrasonic technique

Ultrasonic techniques for residual stress measurement are based on the changes in velocities of ultrasonic waves as a result of stress. On a microscopic basis, a stress applied to a solid causes a change both in the elastic modulus and in the interatomic distance, which in turn produces a change in the velocity of sound. Stress is measured by introducing a sound wave into the specimen and measuring the time of flight or some other velocity-related parameter. The great interest in ultrasonic techniques for residual stress measurement stems from the promising results obtained for three-dimensional non-destructive measurements within the material [11].

5.3.6 Magnetic techniques

The physical basis of magnetic techniques for residual stress measurements is complex because a number of magnetic properties are sensitive to stress as well as microstructure. Nonetheless, in simple terms, the physical origin of the stress dependence is the magnetoelastic effect whereby deformation of the material produces changes in the relative energies of various magnetic domain configurations, which consequently influence the macroscopic magnetic response [11].

5.4 The hole drilling method

The hole drilling method in its original form is based on analytical solutions for a uniform field of elastic stresses and strains in an infinite thin plate with a through thickness hole. Mathar [18] introduced the concept of determining the residual stresses based on these solutions in 1933. Over time, however, significant improvements have been made in the theory behind the method so it can now be used for blind holes, and to provide information of the in-depth distribution of residual stresses. Current research is also trying to improve the measurement accuracy [27, 35], the effect of plasticity around the hole [6] and analytical expressions for the calibration surfaces [7, 9]. Moreover, standardised procedures, commercially available drilling equipment, special strain gauge rosettes and stress evaluation software have greatly increased the availability and use of the hole drilling method. The accuracy of the standardised blind-hole method is reported to be of the order of 15 MPa in standard deviation in a uniaxial, elastic stress field [4]. However, the many steps in the non-uniform in-depth residual stress measurement and evaluation procedure are prone to errors and noise.

During verification of the commercial hole drilling software Restran distributed by Hottinger Baldwin Messtechnik (HBM), two significant mistakes were found in the software. This is the reason for the detailed presentation of the hole drilling technique in this Chapter.

5.4.1 Through hole method

Assume a uniform residual stress σ_x. See Figure 5-1

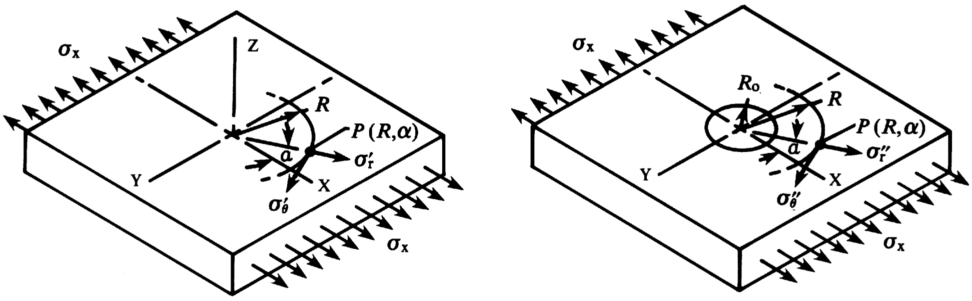

Figure 5-1. Stress states at P(R,α), before and after the introduction of a hole. [20]

The initial stress at any point P (R,α) can be expressed in polar coordinates by:

$$\sigma'_r = \frac{\sigma_x}{2}(1+\cos 2\alpha) \qquad \text{Equation 5-2a}$$

$$\sigma'_\theta = \frac{\sigma_x}{2}(1-\cos 2\alpha) \qquad \text{Equation 5-2b}$$

$$\tau'_{r\theta} = -\frac{\sigma_x}{2}\sin 2\alpha \qquad \text{Equation 5-2c}$$

After the hole is drilled, the hole surface will have σ_r and $\tau_{r\theta}$ equal to zero. A solution of this situation was obtained by G. Kirsch in 1898, and yields the following expressions for the stresses at the point P(R,α):

$$\sigma''_r = \frac{\sigma_x}{2}(1-\frac{1}{r^2}) + \frac{\sigma_x}{2}(1+\frac{3}{r^4}-\frac{4}{r^2})\cos 2\alpha \qquad \text{Equation 5-3a}$$

$$\sigma''_\theta = \frac{\sigma_x}{2}(1+\frac{1}{r^2}) - \frac{\sigma_x}{2}(1+\frac{3}{r^4})\cos 2\alpha \qquad \text{Equation 5-3b}$$

$$\tau''_{r\theta} = -\frac{\sigma_x}{2}(1-\frac{3}{r^4}+\frac{2}{r^2})\sin 2\alpha \qquad \text{Equation 5-3c}$$

where

$$r = \frac{R}{R_0}(R \geq R_0) \qquad \text{Equation 5-4}$$

Subtracting Equation 5-2 from Equation 5-3 into Equation 5-5 yields the full expressions for the relaxed stresses at point P(R,α) after drilling due the hole. That is:

$$\Delta\sigma_r = \sigma_r^{''} - \sigma_r^{'} \qquad \text{Equation 5-5a}$$

$$\Delta\sigma_\theta = \sigma_\theta^{''} - \sigma_\theta^{'} \qquad \text{Equation 5-5b}$$

$$\Delta\tau_{r\theta} = \tau_{r\theta}^{''} - \tau_{r\theta}^{'} \qquad \text{Equation 5-5c}$$

If the plate material is homogenous and isotropic in its mechanical properties, and linear-elastic in its stress/strain behaviour, these equations can then be substituted by the biaxial Hook's law to solve for relieved normal strains at the point P (R,α). The resulting expressions are as follows:

$$\varepsilon_r = -\frac{\sigma_x(1+\upsilon)}{2E}\left(\frac{1}{r^2} - \frac{3}{r^4}\cos 2\alpha + \frac{4}{r^2(1+\upsilon)}\cos 2\alpha\right) \qquad \text{Equation 5-6a}$$

$$\varepsilon_\theta = -\frac{\sigma_x(1+\upsilon)}{2E}\left(-\frac{1}{r^2} + \frac{3}{r^4}\cos 2\alpha - \frac{4\upsilon}{r^2(1+\upsilon)}\cos 2\alpha\right) \qquad \text{Equation 5-6b}$$

The preceding equations can be written in a simpler form, demonstrating that along a circle at any radius R (R≥R$_0$) the relieved radial and tangential strains vary in a sinusoidal manner:

$$\varepsilon_r = \sigma_x(A + B\cos 2\alpha) \qquad \text{Equation 5-7a}$$

$$\varepsilon_\theta = \sigma_x(-A + C\cos 2\alpha) \qquad \text{Equation 5-7b}$$

Comparison of Equation 5-6 with Equation 5-7 demonstrates that coefficients A, B and C have the following definitions:

$$A = -\frac{1+\upsilon}{2E}\left(\frac{1}{r^2}\right) \qquad \text{Equation 5-8a}$$

$$B = -\frac{1+\upsilon}{2E}\left[\left(\frac{4}{1+\upsilon}\right)\frac{1}{r^2} - \frac{3}{r^4}\right] \qquad \text{Equation 5-8b}$$

$$C = -\frac{1+\upsilon}{2E}\left[-\left(\frac{4\upsilon}{1+\upsilon}\right)\frac{1}{r^2} + \frac{3}{r^4}\right] \qquad \text{Equation 5-8c}$$

In the strain gauge rosette used to measure strain relief the three gauge elements are radially oriented. That means only Equation 5-7a is of interest, hence from now on only radial strain will be considered. The preceding expressions considered only the simplest case, uniaxial residual stress. In practice, however, residual stresses are more often biaxial, with two non-zero principal stresses. This condition can readily be incorporated in the analysis by employing the superposition principle, which is applicable to linear-elastic material behaviour. Referring to Figure 5-1 again, it is apparent that if the uniaxial residual stress had been along the Y axis instead of the X axis only, Equation 5-2 and Equation 5-3 would still apply, with cos 2α replaced by cos 2(α+π/2), or by the equivalent, -cos 2α. Thus, the relieved radial strain at the point P(R,α) due to uniaxial residual stress in the Y direction can be written as:

$$\varepsilon_r^y = \sigma_y(A - B\cos 2\alpha) \qquad \text{Equation 5-9}$$

And, employing the corresponding notation, Equation 5-7a becomes:

$$\varepsilon_r^x = \sigma_x(A + B\cos 2\alpha)$$ Equation 5-10

When both residual stresses are present simultaneously, the superposition principle permits algebraic addition of Equation 5-9 and Equation 5-10, so the general expression for the relieved radial strain due to a plane biaxial residual stress state is:

$$\varepsilon_r = \sigma_x(A + B\cos 2\alpha) + \sigma_y(A - B\cos 2\alpha)$$ Equation 5-11

Or, in a slightly different form:

$$\varepsilon_r = A(\sigma_x + \sigma_y) + B(\sigma_x - \sigma_y)\cos 2\alpha$$ Equation 5-12

Equation 5-12 represents the basic relationship underlying the hole-drilling method of residual stress analysis. In general, neither the direction nor the magnitudes of the principal stresses are known. To solve for these three unknown quantities, three strain measurements are required. The rosette configurations with 0, 45 and 90 degree will give the easiest equation to solve, and has been standardised [3]. Figure 5-2 shows the strain gauge rosette arrangement for determining residual stresses. The numbering in this work is clockwise, and position 2a and 2b will give identical results.

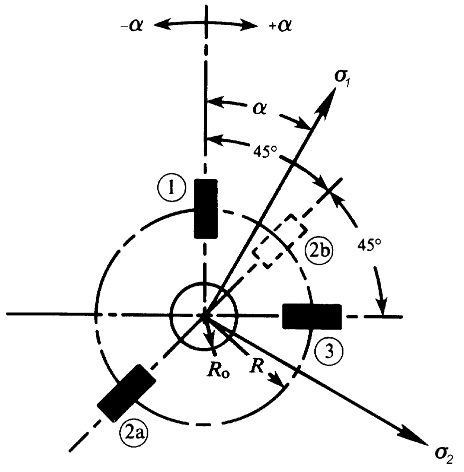

Figure 5-2. Strain gauge rosette arrangement for determining residual stress. [20]

Equation 5-12 will then give the following set of equations:

$$\varepsilon_1 = A(\sigma_x + \sigma_y) + B(\sigma_x - \sigma_y)\cos 2\alpha$$ Equation 5-13a

$$\varepsilon_2 = A(\sigma_x + \sigma_y) + B(\sigma_x - \sigma_y)\cos 2(-\alpha + \frac{\pi}{4})$$ Equation 5-13b

$$\varepsilon_3 = A(\sigma_x + \sigma_y) + B(\sigma_x - \sigma_y)\cos 2(-\alpha + \frac{\pi}{2})$$ Equation 5-13c

Inverting this set of equations yields:

$$\sigma_1 = \frac{\varepsilon_1 + \varepsilon_3}{4A} - \frac{1}{4B}\sqrt{(\varepsilon_3 - \varepsilon_1)^2 + (\varepsilon_3 + \varepsilon_1 - 2\varepsilon_2)^2} \qquad \text{Equation 5-14a}$$

$$\sigma_2 = \frac{\varepsilon_1 + \varepsilon_3}{4A} + \frac{1}{4B}\sqrt{(\varepsilon_3 - \varepsilon_1)^2 + (\varepsilon_3 + \varepsilon_1 - 2\varepsilon_2)^2} \qquad \text{Equation 5-14b}$$

The negative square root in this equation is associated with σ_1 because the calibration constants A and B have negative numerical values.

The principal stress σ_1 is located at an angle α measured clockwise form the direction of gauge No. 1 in Figure 5-2

$$\alpha = \frac{1}{2}\arctan\left[\frac{\varepsilon_3 + \varepsilon_1 - 2\varepsilon_2}{\varepsilon_3 - \varepsilon_1}\right] \qquad \text{Equation 5-15}$$

Direct calculation of the angle α using the common one-argument arctan function; such as found on an ordinary calculator, can give an error of ± 90°. The result form the one-argument calculation can be adjusted by ± 90° as necessary to place α within the appropriate range defined in Table 5-1.

	$\varepsilon_3 - \varepsilon_1 < 0$	$\varepsilon_3 - \varepsilon_1 = 0$	$\varepsilon_3 - \varepsilon_1 > 0$
$\varepsilon_3 + \varepsilon_1 - 2\varepsilon_2 > 0$	$45° < \alpha < 90°$	45°	$0° < \alpha < 45°$
$\varepsilon_3 + \varepsilon_1 - 2\varepsilon_2 = 0$	90°		0°
$\varepsilon_3 + \varepsilon_1 - 2\varepsilon_2 < 0$	$-90° < \alpha < -45°$	-45°	$-45° < \alpha < 0°$

Table 5-1 One-argument arctan function adjustment table

For any given set of material properties E and ν, the coefficients A and B are simple geometric functions, and thus constant for all geometrically similar cases[21]. This means that once the coefficients have been determined for a particular rosette configuration, the rosette geometry can be scaled upward or downward and the same coefficients will still apply when the hole diameter and depth are similarly scaled (assuming the same material). It is convenient to introducing the material independent a and b (which is only geometric dependent), as:

$$a = \frac{2AE}{1+\upsilon} \qquad \text{Equation 5-16}$$

$$b = 2BE \qquad \text{Equation 5-17}$$

The measured strain from a strain gauge is the average strain over the strain gauge filament, and not the infinitely small point used in the preceding presentation. The resistance wires in each filament are oriented in parallel, hence only the central resistance wire will not have a contribution from σ_θ''. The integrated values over the filament area for a through hole are [3]:

---

[21] The constants vary by less than 1% for Poisson's ratio in the range 0.28 to 0.33 [4] and less than 2% in the range 0.25 to 0.35 [28].

$$a = -\frac{D_0^2}{2GW(R_2 - R_1)}(\theta_1 - \theta_2) \qquad \text{Equation 5-18}$$

$$b = -\frac{D_o^2}{2GW(R_2 - R_1)}(p - q) \qquad \text{Equation 5-19}$$

where

$$p = 2(1-\upsilon)(\theta_1 - \theta_2) + (1+\upsilon)(\sin 2\theta_1 - \sin 2\theta_2)$$

$$q = \frac{(1+\upsilon)D_0^2}{32}\left(\frac{2\sin 2\theta_1 + \sin 4\theta_1}{R_1^2} - \frac{2\sin 2\theta_2 + \sin 4\theta_2}{R_2^2}\right)$$

with definitions given in Figure 5-3.

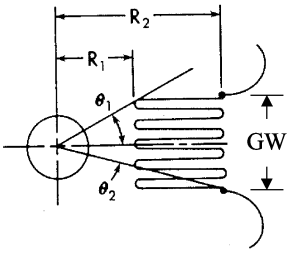

Figure 5-3. Definition of filament geometry. [4]

5.4.2 The standardised ASTM method

In the standardised blind-hole drilling technique the assumption of constant in-depth stress is verified by performing the drilling procedure incrementally. By drilling the hole in intervals with subsequent strain readings, a strain relief profile as a function of depth is obtained. The fundamental assumption of constant residual stress in the depth might be verified by comparing this profile with a profile obtained from a constant stress calibration test. Another method also found in [4] is to independently calculate the average residual stress in the hole at each new increment and thereby verify the assumption of no stress gradient. This is the *Average Strain Method* and is approximate if a gradient is present (See Section 5.4.3). If the residual stress turns out to be inconstant, only the residual stress in the first very shallow layer will be known. The theoretical background for the standardised hole-drilling method was developed in the preceding discussion on the basis of a small hole drilled completely through a thin (plane strain) and wide plate subjected to uniform residual stresses (Section 5.4.1).

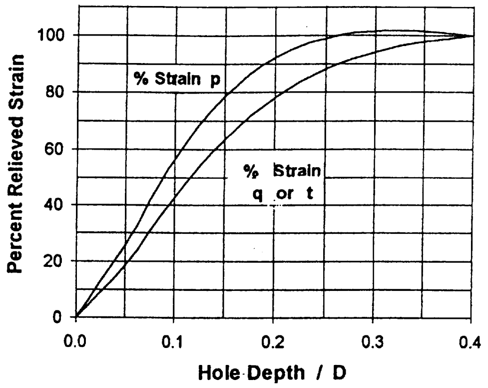

Figure 5-4 Strain relaxation with constant in-depth stress for Measurements Group gauge 031RE, 062RE and 125RE. $p = (\varepsilon_1 + \varepsilon_3) / 2$, $q = (\varepsilon_3 - \varepsilon_1) / 2$, $t = (\varepsilon_3 + \varepsilon_1 - 2\varepsilon_2) / 2$ [4].

The introduction of a blind hole into a field of plane stress produces a very complex local stress state, for which no exact solution is yet available from the theory of elasticity. Rendler and Vigness [25] demonstrated the close relationship in the general nature of the stress distribution between through hole and blind hole. The relieved strain due to drilling of a blind hole varies sinusoidally along a circle concentric with the hole, in the manner described by Equation 5-12. Equation 5-14 and Equation 5-15 are applicable to the blind-hole implementation when appropriate blind-hole coefficients $\bar{a}$ and $\bar{b}$ are employed. Since these coefficients cannot be calculated directly from theoretical considerations, they must be obtained by empirical means; that is, by experimental calibration or by numerical procedures such as FE analysis.

Compared to the through-hole procedure, blind-hole analysis involves one additional independent variable; namely, the dimensionless hole depth, z/D.

$$\bar{a} = f_a(r, z/D) \qquad \text{Equation 5-20 a}$$

$$\bar{b} = f_b(r, z/D) \qquad \text{Equation 5-20 b}$$

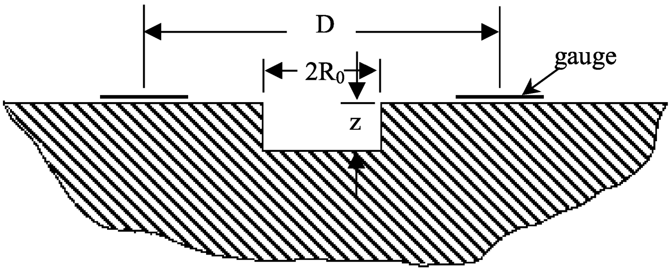

Figure 5-5 Blind hole notation.

For any given initial state of in-depth-constant residual stress and a fixed hole diameter, the relieved strains generally increase (at a decreasing rate) as the hole depth is increased. Therefore, in order to maximise the strain signals, and thereby minimise noise, the hole is normally drilled to a depth corresponding to at least z/D = 0.4.

Experimental calibration of $\bar{a}$ and $\bar{b}$ is particularly attractive since it automatically accounts for the mechanical properties of the test material, strain gauge rosette geometry, hole shape, hole diameter and depth, and the strain-averaging effect of the strain gauge grid. When performed correctly, and with sufficient attention to detail, it is potentially the most accurate means for determining the coefficients. It's principal disadvantage is the requirement for a new calibration for each new set of geometric parameters involved.

FE analysis is the other method for determining $\bar{a}$ and $\bar{b}$. Consider the material in the gauge area before the hole is drilled. A cross-section view is shown in Figure 5-6, where the boundary curve is assumed to be sufficiently distanced from the hole that the drilling does not significantly influence the stresses at the boundary.

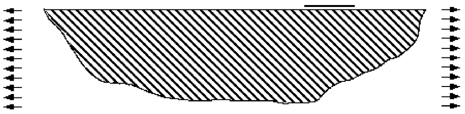

Figure 5-6 Cross-section of strain gauge area before hole is drilled.

Now imagine drilling the hole, and externally loading the hole surfaces with the same stresses as previously experienced. Under these conditions, the stress distribution in the remaining material is unchanged. Consider Figure 5-7, where the material with the loading applied to the hole surface is shown in (a). Since the system is linear elastic, the loading shown in (b) may be superimposed. The stresses in (b) are equal and opposite to those in (a), but with zero stress at the distant boundary. The sum of these two, shown in (c), is the stress distribution that exists after the hole has been drilled. Thus, loading (b) corresponds to the redistribution of stresses due to the drilling of the hole, and the associated strains are those that are measured by strain gauges. It also follows that the measured strain relaxation depends only on the original residual stresses at the hole boundary. An analysis of loading case (b) using finite element techniques gives the relaxed surface displacements, which from numerical integration over the gauge area is compared to the actual strain measured.

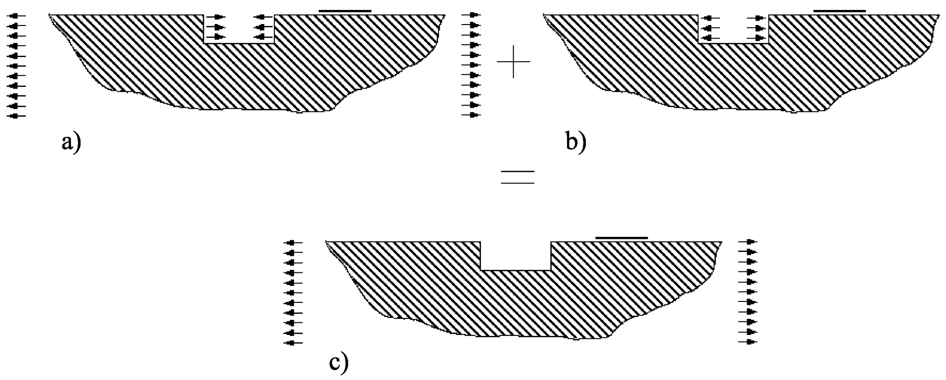

Figure 5-7 Superposition of loading to find the strain relaxation due to hole drilling (a) original stresses, (b) stress change due to drilling, (c) final stresses

It should be noted that values for the basic coefficients $\overline{A}$ and $\overline{B}$ obtained from a particular calibration test are strictly only applicable for residual stress measurements exactly matching the calibration conditions with regard to:

- rosette geometry
- hole size
- hole form
- uniform stress with depth
- nominally no stress gradient
- homogeneous, isotropic linear-elastic material considered

$\overline{a}$ and $\overline{b}$ are tabulated in discrete dimensionless z / D depth intervals in the ASTM standard [4] for a selected number of Measurement Group [19] strain gauges.

5.4.3 Incremental hole drilling method

One major disadvantage with the through hole drilling method and blind-hole drilling method is the assumption of uniform residual stresses parallel to the surface. There are a number of analogous non-uniform in-depth hole-drilling methods. The *Incremental strain method* also called *Differential strain method* and the *Average strain method* require experimental calibration and also have some theoretical shortcomings [29]. A *Power series method* introduced by [28] is an approximate method based on FE analysis that is only suitable for small gradient stress fields [17, 29].

Niku-Lari et al. [21] and Flaman and Manning [12] introduced the *incremental hole drilling method* in 1985 which is based on coefficients from FE analysis and can be used to determine in-depth residual stress gradients without theoretical shortcomings and approximations. The coefficients are geometry dependent, and must be calculated for each new strain gauge geometry, hole radius and depth increment if complete geometric scaling does not take place.

The easiest way to describe the method is by an idealised 2D example:

1. drill a hole with depth z_1, this is the first increment: $j = 1$, of total increments $n = 1$
2. replace the removed mass with a unit-stress on the hole surface in a FE analysis and read the average strain, ε_{nj}, over the filament area
3. measure the relieved strain, $\bar{\varepsilon}_n$
4. uniform residual stress in layer $j = 1$ is calculated

$$\sigma_{n=1} = \frac{\bar{\varepsilon}_n}{\varepsilon_{nj}} \qquad \text{Equation 5-21}$$

5. drill next layer: $n = n + 1$
6. insert unit-stress exclusively at each layer $j = 1$ to n, and calculate ε_{nj}. See Figure 5-9
7. calculate the strain from previous solved "layer-stress"

$$\varepsilon_n = \sum_{j=1}^{n-1} \varepsilon_{nj}\sigma_j \qquad \text{Equation 5-22}$$

8. measure strain relief $\bar{\varepsilon}_n$
9. additional strain from the last drilled layer, n

$$\hat{\varepsilon}_n = \bar{\varepsilon}_n - \varepsilon_n \qquad \text{Equation 5-23}$$

10. calculate residual stress in last removed layer, n

$$\sigma_n = \frac{\hat{\varepsilon}_n}{\varepsilon_{nn}} \qquad \text{Equation 5-24}$$

ready to solve next increment, and the algorithm goes to point 5 above.

This method represents a continuous distributed residual stress with stepwise constant residual step blocks as showed in Figure 5-8.

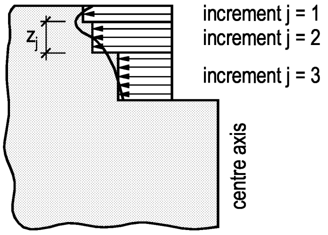

Figure 5-8 Uniform residual stress blocks is a good assumption to continuously residual stress distribution.

In reality there will be three unknown variables in each step, and not just one as in the preceding 2D example; two principal stresses and one unknown angle. To solve this, the same strain gauge rosette configuration as shown in Figure 5-2 will be used, with filaments at 0°, 45° (or 225°) and 90° numbered clockwise here.

The equations needed will be established by considering an arbitrary increment j with thickness z_j at total number of increments n with total hole depth

$$z = \sum_{j=1}^{n} z_j \qquad \text{Equation 5-25}$$

in an infinite wide plate with z << plate thickness. Analogous to Equation 5-12 the surface strain from the arbitrary layer is considered:

$$\varepsilon_{nj} = \overline{A}_{nj}(\sigma_{x,j} + \sigma_{y,j}) + \overline{B}_{nj}(\sigma_{x,j} - \sigma_{y,j})\cos 2\alpha_j \qquad \text{Equation 5-26}$$

The constants $\overline{A}_{nj}$ and $\overline{B}_{nj}$ in Equation 5-26 is found by FE analysis and will be described in Section 5.4.4.

The following equation system for filaments oriented 0, 45 and 90 degrees is analogous to the system of equations in Equation 5-13:

$$\varepsilon_{1,nj} = \overline{A}_{nj}(\sigma_{1,j} + \sigma_{2,j}) + \overline{B}_{nj}(\sigma_{1,j} - \sigma_{2,j})\cos 2\alpha_j \qquad \text{Equation 5-27a}$$

$$\varepsilon_{2,nj} = \overline{A}_{nj}(\sigma_{1,j} + \sigma_{2,j}) + \overline{B}_{nj}(\sigma_{1,j} - \sigma_{2,j})\cos 2\left(-\alpha_j + \frac{\pi}{4}\right) \qquad \text{Equation 5-27b}$$

$$\varepsilon_{3,nj} = \overline{A}_{nj}(\sigma_{1,j} + \sigma_{2,j}) + \overline{B}_{nj}(\sigma_{1,j} - \sigma_{2,j})\cos 2\left(-\alpha_j + \frac{\pi}{2}\right) \qquad \text{Equation 5-27c}$$

The strain relieved exclusively from layer n will be calculated by use of the already known residual stresses in layers j < n and from the measured surface strain, $\overline{\varepsilon}_{k,n}$, at depth increment n and gauge No. k = 1,2 or 3 by use of

$$\hat{\varepsilon}_{k,n} = \overline{\varepsilon}_{k,n} - \sum_{j=1}^{n-1} \varepsilon_{k,nj} \quad k = 1..3 \qquad \text{Equation 5-28}$$

Analogous to Equation 5-14 and Equation 5-15 the principal stresses and their orientation are found to be:

$$\sigma_{1,n} = \frac{\hat{\varepsilon}_{1,n} + \hat{\varepsilon}_{3,n}}{4\overline{A}_{nn}} - \frac{1}{4\overline{B}_{nn}}\sqrt{(\hat{\varepsilon}_{3,n} - \hat{\varepsilon}_{1,n})^2 + (\hat{\varepsilon}_{3,n} + \hat{\varepsilon}_{1,n} - 2\hat{\varepsilon}_{2,n})^2} \qquad \text{Equation 5-29 a}$$

$$\sigma_{2,n} = \frac{\hat{\varepsilon}_{1,n} + \hat{\varepsilon}_{3,n}}{4\overline{A}_{nn}} + \frac{1}{4\overline{B}_{nn}}\sqrt{(\hat{\varepsilon}_{3,n} - \hat{\varepsilon}_{1,n})^2 + (\hat{\varepsilon}_{3,n} + \hat{\varepsilon}_{1,n} - 2\hat{\varepsilon}_{2,n})^2} \qquad \text{Equation 5-29 b}$$

$$\alpha_n = \frac{1}{2}\arctan\left(\frac{\hat{\varepsilon}_{3,n} + \hat{\varepsilon}_{1,n} - 2\hat{\varepsilon}_{2,n}}{\hat{\varepsilon}_{3,n} - \hat{\varepsilon}_{1,n}}\right) \qquad \text{Equation 5-30}$$

If the one-argument arctan function is used, α_n must be adjusted according Table 5-1. The angle, α_n, is from filament No. 1 to the maximum principle axis.

5.4.4 Determination of constants $\overline{A}_{ij}$ and $\overline{B}_{ij}$

By use of axial symmetric unity stresses at the hole surface in successive layers Equation 5-26 is reduced to

$$\varepsilon_{ij} = 2\overline{A}_{ij} \qquad \text{Equation 5-31}$$

where ε_{ij} is obtained from numerical integration over the filament area of the strain from the FE analysis.

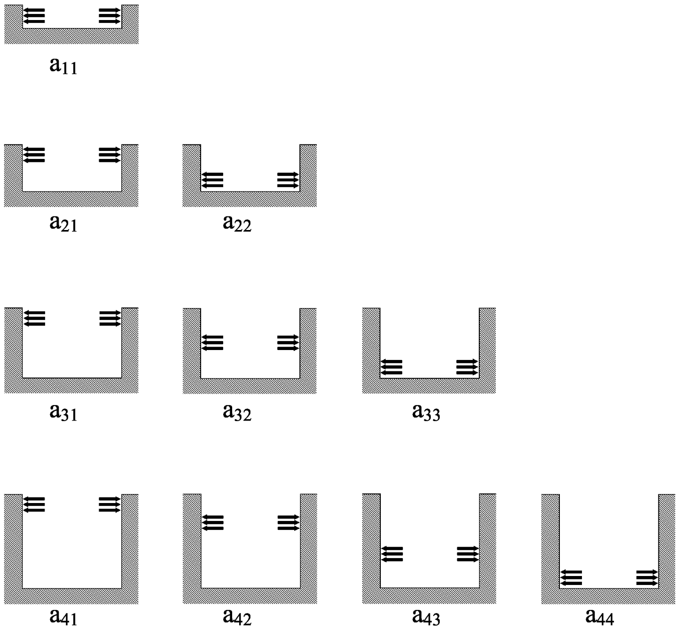

Figure 5-9 Schematic presentation of loads in individual layers and the $\overline{a}_{in}$ matrix.

B_{ij} is found by using a normal stress equal to cos(2α) and a shear stress equal to –sin(2α) on the hole surface in successive layers. Then Equation 5-26 for $\alpha_j = 0$ will give

$$\varepsilon_{ij} = 2\overline{B}_{ij} \qquad \text{Equation 5-32}$$

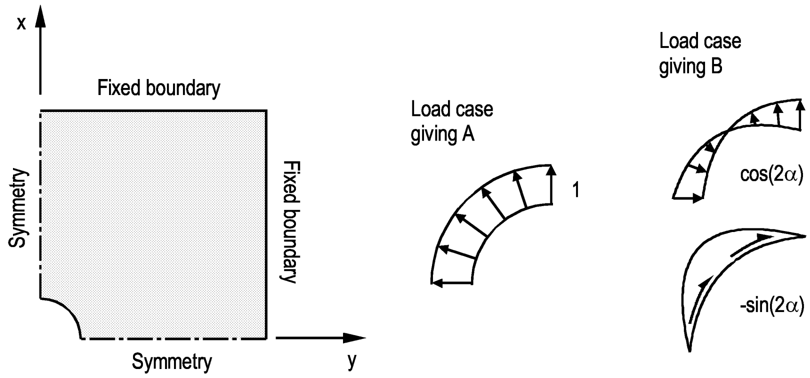

Figure 5-10 Unit-stress distributions for determining A_{ij} and B_{ij} respectively.

The material independent constants (see footnote 21) $\overline{a}_{ij}$ and $\overline{b}_{ij}$ are calculated analogous to Equation 5-16 and Equation 5-17 as:

$$\bar{a}_{ij} = \frac{2\bar{A}_{ij}E}{1+\upsilon}$$

Equation 5-33

$$\bar{b}_{ij} = 2\bar{B}_{ij}E$$

Equation 5-34

When $\bar{A}_{ij}$ and $\bar{B}_{ij}$ are found, a set of $\bar{A}$ and $\bar{B}$ valid for the same material and geometry (gauge, hole-diameter and depth) for the blind hole drilling method will readily be calculated as

$$\bar{A} = \sum_{j=1}^{n} A_{nj}$$

Equation 5-35 a

$$\bar{B} = \sum_{j=1}^{n} B_{nj}$$

Equation 5-35 b

5.4.5 The integral hole drilling method

The incremental hole drilling method was further developed by Schajer [29, 30]. By considering an infinite number of stress blocks simultaneously, the surface strain is found from the integral of the strain contribution from each block.

Consider a biaxial stressed plate with a drilled hole with depth z, where the stress only varies in depth h, $\sigma_r^{''}(\alpha,h) = \sigma(h)$. Analogous to Equation 5-12 and Equation 5-26 the radial strain at the surface, ε_r will be:

$$\varepsilon_r(h) = \frac{1+\upsilon}{E}\int_o^z \bar{A}(z,h)\sigma(h)dh \quad 0 \le h \le z$$

Equation 5-36

where $\bar{A}(z,h)$ is the strain relaxation per unit depth caused by a unit stress at depth h when the hole depth is z. Drilling with a high number of increments, an interpolation procedure will give a continuous distribution for $\bar{\varepsilon}_k(h)$, and $\bar{A}(z,h)$ can also be determined from a number of increments in an FE analysis combined with an interpolation procedure. The unknown residual stress distribution is found by solving the integral Equation 5-36. By using a computer with a suitable code and predetermined $\bar{A}(Z_i,H_j)$ and $\bar{B}(Z_i,H_j)$, this integral equation is approximated by a finite number of increments with the material independent $\bar{a}(Z_i,H_j)$ and $\bar{b}(Z_i,H_j)$ given as:

$$\bar{a}_{ij} = \bar{a}(Z_i,H_j) - \bar{a}(Z_i,H_{j-1})$$

Equation 5-37

$$\bar{b}_{ij} = \bar{b}(Z_i,H_j) - \bar{b}(Z_i,H_{j-1})$$

Equation 5-38

where

$$H_j = \frac{2}{D}\sum_{m=1}^{j} z_j$$

Equation 5-39

5.5 Computer code for integral hole drilling method

The only commercially available computer code for residual stress determination known to the author is Restran 3.3.1 also called SINT [32]. This code is distributed through Hottinger Baldwin Messtechnik (HBM) [15]. A new version of Restran version 3.3.2.a is now available, but only the user interface is changed with the computational aspects remaining unaltered[22]. The software source code is not accessible. The only possible way to verify the program is to calculate residual stress distributions manually, and to compare the residual stress output with that from Restran 3.3.1.

5.5.1 Calculation of constants $\bar{a}(Z_i,H_j)$ and $\bar{b}(Z_i,H_j)$

There are no known published accounts of $\bar{a}(Z_i,H_j)$ and $\bar{b}(Z_i,H_j)$ for HBM-gauges. Initially a very limited number of $\bar{a}(Z_i,H_j)$ and $\bar{b}(Z_i,H_j)$, and subsequent FE models, were planned for the present work, to serve only as verification of Restran 3.3.1. A 3D FE model was then chosen, despite it being more time consuming than 2D axi-symmetric modelling with circumferential sin-cos distribution of loads, because there was no pre-existing experience at the institute with that particular kind of 2D modelling at that time. Models with higher levels of accuracy became necessary when the accuracy of Restran was questioned. A Fortran code had already been developed to automatically generate 3D FE model input files for Abaqus 5.8 and it was therefore more convenient to use 3D-modelling despite the more CPU intensive solution load.

3D-models are time consuming, therefore a study of model size, mesh density and element type was performed to optimize the FE performance. The boundary conditions are shown in Figure 5-10, and the one-quarter model meshed was 35*35 mm in width and 6.17 mm thick (equivalent to 1.2D which is considered thick by ASTM [4]). The element density used in the x-y plane throughout the FE analysis is shown in Figure 5-11. By using an automatically generated through-hole ($\phi = 2R_0/D = 0.4$) model with the optimised mesh density, A and B from Equation 5-8 were found to match perfectly (< 0.1% error and -0.25% error, respectively) compared with the FE analysis. The integration over the filament areas was performed by a Matlab routine. This routine uses two paths of node values (seen in Figure 5-11 and Figure 5-12) for a Cubic Spline [10] interpolation, and integrates across the gauge by a second order polynomial function. Calculated $\bar{a}$ and $\bar{b}$ for the M&M 062-RE gauge from Equation 5-18 and Figure 5-19 is found 0.3 and 1.1 % respectively from FE analysis with numerical integration. $\bar{a}$ and $\bar{b}$ found for the HBM gauge RY-61 was -0.2% and 0.2% off compared to the analytical solution. For both gauges the numerically integrated $\bar{a}$ was found with almost the same accuracy as A along the centre-line in Figure 5-13, but the accuracy of the numerically integrated $\bar{b}$ differed for the M&M gauge compared to the accuracy of B. This is explained by the steep transverse strain gradient in the filament area for the M&M gauge compared to the HBM gauge seen in Figure 5-12, which will decrease the accuracy in the transverse second order polynomial used in the numerical integration.

---

[22] Confirmed through E-mail communication with Thomas Kleckers at HBM 24.10.01 and 26.10.01.

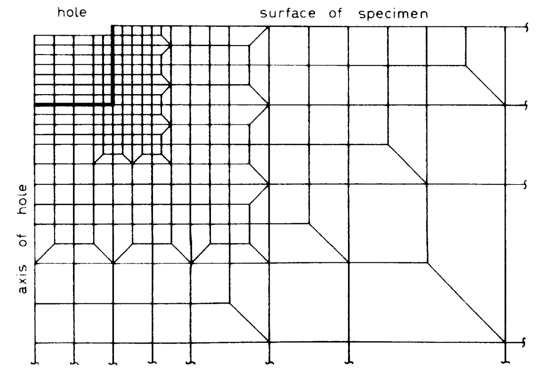

Figure 5-14. 2D-axisymmetric mesh used by Schajer. [30]

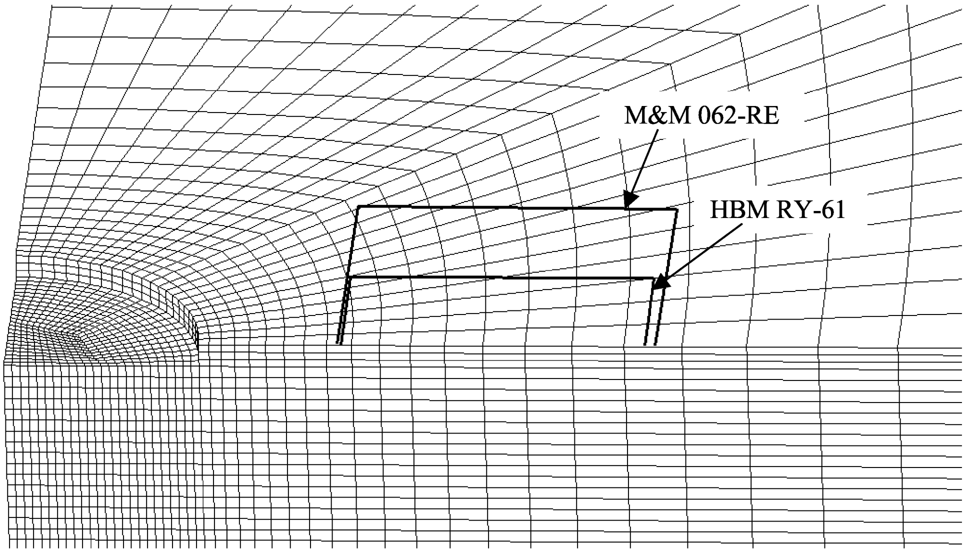

Figure 5-15. 3D-view of mesh with HBM RY-61 and M&M 062-RE. $\phi = 0.4$

Z \ H	0.00	0.05	0.10	0.15	0.20	0.25	0.30	0.35	0.40	0.45	0.50
0.00	0.0000										
0.05	0.0000	-0.0208									
0.10	0.0000	-0.0274	-0.0486								
0.15	0.0000	-0.0321	-0.0588	-0.0779							
0.20	0.0000	-0.0354	-0.0655	-0.0893	-0.1051						
0.25	0.0000	-0.0377	-0.0701	-0.0965	-0.1161	-0.1283					
0.30	0.0000	-0.0393	-0.0733	-0.1013	-0.1228	-0.1381	-0.1469				
0.35	0.0000	-0.0404	-0.0754	-0.1044	-0.1272	-0.1439	-0.1551	-0.1610			
0.40	0.0000	-0.0411	-0.0768	-0.1066	-0.1301	-0.1476	-0.1599	-0.1676	-0.1712		
0.45	0.0000	-0.0412	-0.0772	-0.1072	-0.1310	-0.1489	-0.1617	-0.1702	-0.1752	-0.1770	
0.50	0.0000	-0.0416	-0.0778	-0.1081	-0.1322	-0.1505	-0.1637	-0.1726	-0.1780	-0.1808	-0.1813

Table 5-2. Constants $\overline{a}(Z_i, H_j)$ valid for M&M 062-RE. $\phi = 0.4$.

Z \ H	0.00	0.05	0.10	0.15	0.20	0.25	0.30	0.35	0.40	0.45	0.50
0.00	0.0000										
0.05	0.0000	-0.0378									
0.10	0.0000	-0.0477	-0.0881								
0.15	0.0000	-0.0550	-0.1044	-0.1433							
0.20	0.0000	-0.0604	-0.1156	-0.1626	-0.1979						
0.25	0.0000	-0.0642	-0.1237	-0.1754	-0.2176	-0.2480					
0.30	0.0000	-0.0669	-0.1292	-0.1842	-0.2301	-0.2664	-0.2918				
0.35	0.0000	-0.0688	-0.1331	-0.1902	-0.2386	-0.2778	-0.3080	-0.3288			
0.40	0.0000	-0.0700	-0.1357	-0.1942	-0.2442	-0.2853	-0.3178	-0.3424	-0.3592		
0.45	0.0000	-0.0706	-0.1368	-0.1960	-0.2468	-0.2889	-0.3227	-0.3490	-0.3687	-0.3820	
0.50	0.0000	-0.0711	-0.1380	-0.1979	-0.2494	-0.2923	-0.3270	-0.3544	-0.3754	-0.3910	-0.4014

Table 5-3. Constant $\overline{b}(Z_i, H_j)$ valid for M&M 062-RE. $\phi = 0.4$.

The constant is sensitive to the measured hole radius. A difference of only 0.01 mm in measured hole diameter, which is well below what can be expected from the experimental determination will according to Equation 5-18 and Equation 5-19 give 0.4% and 0.2% difference in A and B respectively. Furthemore, the inaccuracy from FE analysis and numerical integration is expected to be well contained within the level of experimental noise discussed in Section 5.6.

Three sets of $\overline{a}(Z_i, H_j)$ and $\overline{b}(Z_i, H_j)$ for HBM RY-61 $\phi = 0.3$, 0.4 and 0.5 were obtained from FE analysis. From these sets a new set $\overline{a}(Z_i, H_j)$ and $\overline{b}(Z_i, H_j)$ for the value of ϕ of interest will be interpolated by a second order polynomial interpolation.

From the value of $\overline{a}(Z_i, H_j)$ and $\overline{b}(Z_i, H_j)$ and for the value of ϕ of interest with tabulated Z interval, a new set of $\overline{a}(Z_i, H_j)$ and $\overline{b}(Z_i, H_j)$ is interpolated by Cubic Spline with depth increments of interest (regardless of increment numbers). The interpolated calibration surfaces are rather complex, and this last interpolation procedure was verified by comparing interpolated $\overline{a}(Z_i, H_j)$ and $\overline{b}(Z_i, H_j)$ values with values from FE analysis for the dimensionless hole diameter $\phi = 0.4$, valid for M&M 062-RE. The extreme points (max. distance from tabulated points: $Z = 0.025{*}i, i \in [1,3,5]$; $H = 0.025{*}j, j \in [1,3,5]$) differed by approximately 1%, except $\overline{a}(0.025, 0.025)$ and $\overline{b}(0.025, 0.025)$ (at arrow in Figure 5-16) which differed by approximately 7%. Z = 0.05 for the two gauges in this study is 0.06 mm, and this hole depth is close to the practical limit where determination of the hole depths with sufficient accuracy is possible.

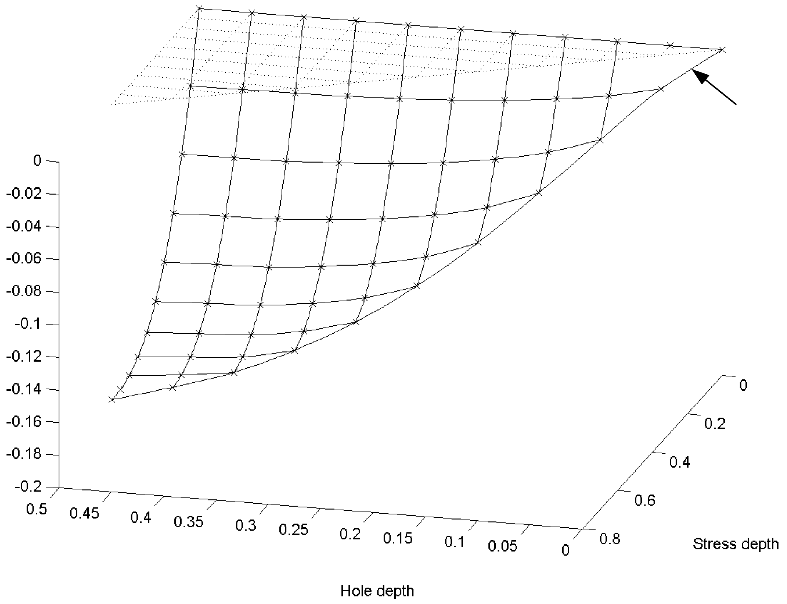

Figure 5-16. Calibration surface $\overline{a}(Z_i, H_j)$ for M&M 062-RE with $\phi = 0.4$. Arrow indicating the point of least interpolation accuracy.

5.5.2 Residual stress determination

A Matlab routine was written using the procedures presented above to determine the residual stress from strain readings using $\overline{a}(Z_i, H_j)$ and $\overline{b}(Z_i, H_j)$ for the hole diameter and increments of interest. The residual stresses calculated from the in-house routine **did not** match the residual stresses calculated from the Restran 3.3.1, and a detailed investigation to determine the cause was initiated. No errors were found in the in-house codes, and the source code for the Restran 3.3.1 was not available. However, using the $\overline{a}(Z_i, H_j)$ and $\overline{b}(Z_i, H_j)$ constants calculated by Schajer [30] in the in-house Matlab routines and the same strain readings for both the in-house Matlab routines and Restran, perfect mach was found (<0.1%) for the principal stresses and angle. The tabulated Schajer values for $\phi = 0.4$ ($R_0 = 1.028$ mm) with Z increments of 0.05 was used. This proves Restran 3.3.1 is using the constants calculated by Schajer, in spite of specifying HBM RY-61 gauges when using Restran and not the M&M 062-RE gauges that Schajer used in his calculations. In other words; the HBM software calculates correct residual stresses for the gauges supplied by the Measurements Group, and the residual stresses are calculated **erroneously** for the HBM gauges.

The difference in residual stress obtained using Schajer's constants, and those calculated by means of the in-house constants is small at shallow depths, but increases steadily to 10% at maximum depth as seen in Figure 5-17.

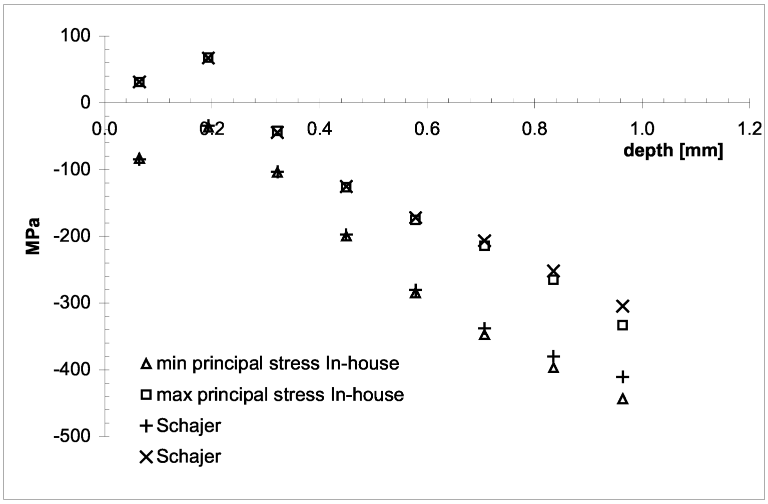

Figure 5-17. Residual stress calculated by $\overline{a}(Z_i, H_j)$ and $\overline{b}(Z_i, H_j)$ from Schajer and in-house. Input strain data Figure 5-22.

Additionally, in Restran 3.3.1 the averaged angle of the total relieved strains calculated from Equation 5-15 is **erroneously** presented, and not the correct angle of each increment calculated from Equation 5-30. The angle for each increment is presumably available in the Restran source code, as this angle is necessary in Equation 5-27 and the result from Equation 5-27 is correctly calculated in Restran 3.3.1. Use of the average angle will give erroneous results in residual stress fields where the residual stress in the direction of maximum principal at shallow depth decreases and becomes the minimum principal stress in depth. From Equation 5-40 the residual stress distribution is found for an arbitrary measured strain set in the direction of gauge No. 1 when $\alpha_j = 0$ and is presented in Figure 5-18.

$$\sigma_j = \frac{\sigma_{1,j} + \sigma_{2,j}}{2} + \frac{\sigma_{1,j} - \sigma_{2,j}}{2}\cos(2\alpha_j) \qquad \text{Equation 5-40}$$

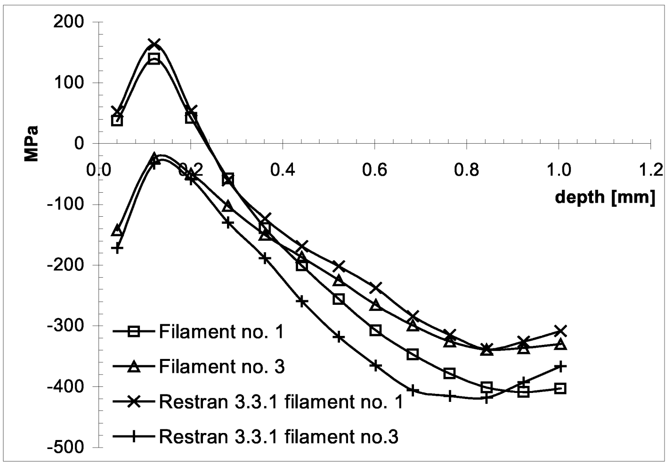

Figure 5-18. Difference in stress between Restran 3.3.1 using inappropriate constants and angle to calculate the residual stresses in direction of filament No. 1 and 3 compared with residual stress from appropriate constants and the correct angle. Input strain data hole No. 4 in Figure 5-36 - Figure 5-38.

Varying the depth increments for residual stress evaluation gave only small differences in calculated residual stress, but the use of too many increments in the surface layer made the calculations becoming unstable at deeper layers, calculating non-existing large residual stress fluctuations. This is caused by the interpolation procedure for $\bar{a}(Z_i, H_j)$ and $\bar{b}(Z_i, H_j)$, as this phenomenon was not observed to the same magnitude in Restran 3.3.1, which most likely has a better interpolation procedure for the determination of $\bar{a}(Z_i, H_j)$ and $\bar{b}(Z_i, H_j)$ at values of Z other than those tabulated. The problem of unstable solutions is well known, and generally the recommendation is to have progressively larger increments in the depth direction and to use as few as 4-5 hole increments [17]. In this work, up to 16 constant sized increments were used with a best-fit interpolation procedure to minimise strain reading scatter (See Figure 5-18). Additionally, maximum and minimum stresses might be underestimated if it is located in between calculation points with too large depth increments.

5.6 Limitations of hole drilling methods

The hole drilling methods are based upon a number of assumptions. Unfortunately not all users of the method are aware of them. In the list given below, the first eight limitations apply to all hole drilling methods, while number 9 is not applied to the integral method. The limitations are:

1. isotropic linear-elastic material behaviour.
2. infinitely wide plate, and thickness equal to the thickness used in calibration.
3. the hole geometry is perfect compared to the FE geometry and concentric with the gauge centre.
4. no introduction of residual stresses during drilling.
5. good reproducibility in strain readings.
6. normal stress and shear stress perpendicular to the surface are neglected.
7. the strain gauge geometry is in agreement with the manufacturer's specifications.
8. constant stress around the hole surface within each increment.
9. constant stress in depth direction

The stress concentration factor at a hole in an infinite plate is 3 (see Equation 3-2), and all stresses, residual or applied, are magnified by this factor. Therefore local plasticity will occur at relatively low stresses and this will violate the basic assumption of having an elastic stress field. The problem of loss of accuracy in the hole drilling method at high levels of residual stress is dealt with in several publications, e.g. [4, 6, 8, 17, 20]. Generally, it has been found that a residual stress below 70% of yield stress will give negligible error [20]. A 2D uniaxial stressed plate ($\sigma_2 = 0$) with $\phi = 0.4$ and an element density as shown in Figure 5-11 was used to study the error introduced by plasticity. One reference solution was made with a linear-elastic material, and was compared with various stress levels with a true stress/strain curve as presented in Figure 5-19, with von Mises yield criterion and 515 MPa in yield stress. Two element strains at the symmetry line at each end of the M&M strain filament were averaged and used in the comparison. As seen in Figure 5-19, a residual stress equal to 70% of yield stress is overestimated by 8% in the through hole drilling method. However, the amount of plasticity depends on the complexity of the stress field at the hole. As noted before, for a uniaxial stress as used in this example, the stress concentration factor is 3, whereas the stress concentration factor is 2 in an equi-biaxial stress field [24]. The values listed in Table 5-4 are as expected somewhat higher than the equi-biaxial plane stress state analysed by Gibmeier et al. [13] and are in good agreement with results from various workers summarised by Nobre et al. [22, 23].

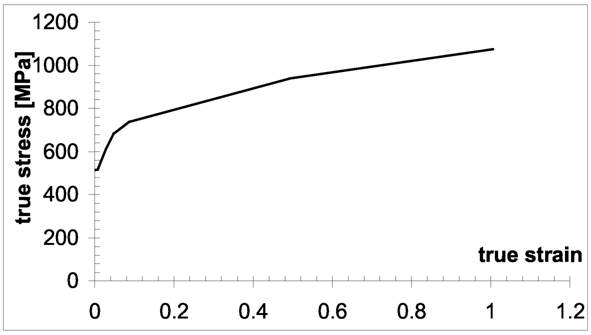

Figure 5-19. True stress/strain curve used in FE analysis.

Plate stress	$\varepsilon_{true} / \varepsilon_{estimated}$
0.33 $Rp_{0.2}$	1.00
0.50 $Rp_{0.2}$	0.99
0.60 $Rp_{0.2}$	0.96
0.70 $Rp_{0.2}$	0.92
0.80 $Rp_{0.2}$	0.88
0.90 $Rp_{0.2}$	0.84
0.95 $Rp_{0.2}$	0.80
1.00 $Rp_{0.2}$	0.97

Table 5-4. Error in estimated residual stress as function of residual stress

The values in Table 5-4 do not apply to a stress field with a gradient in the thickness direction. Considering two plates, the first with residual stresses high enough to give strain influenced by plasticity around the hole, and the second with low residual stresses giving no plasticity adjacent to the hole. Now, considering these plates as the first two increments measured where their intersection follows the rule of kinematic compability (glued together). The increments will incfluence each other, thereby possibly reducing the strain in the first increment below yield. It is not possible however, to decide in general terms when a strain gradient is influenced by plasticity around the hole, and to what extent. This assumption is supported by the observations made by Nobre et al [22, 23]. They found that the incremental hole drilling measurements disagreed with the residual stress measured by x-ray diffraction only in the layer of high compressive stresses at the surface, whereas good agreement was found in deeper regions where residual stresses are lower.

The assumption of an infinite flat plate without stress concentrations is frequently overlooked. This assumption may be violated when using special strain gauges "useful where measurements need to be made near an obstacle", ASTM [4].

A flat plate with $\phi = 0.4$ was modelled by 2D elastic 8-node thin shell elements and solved by I-DEAS Master Series 7 to investigate the influence from various boundaries. The stress in this investigation was localised at R1 and R2 (see Figure 5-20), and compared to A and B in Equation 5-8. A reference model without any influence from a free boundary was found to give results very close to the analytical solutions. The influence form the free boundary is presented in Table 5-5 where the difference between the values for the constants A and B influenced by a free boundary are compared with values for infinite plate.

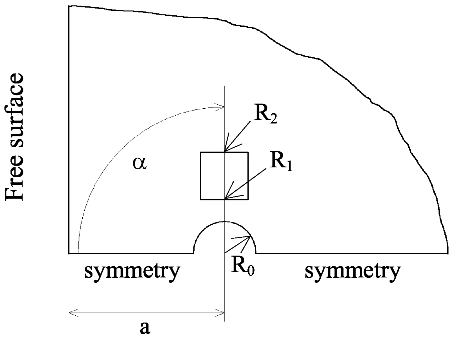

Figure 5-20. Through hole thin shell FE model used to investigate the influence from a free boundary on the constants A and B.

a	$\alpha = 0°$		$\alpha = 90°$		$\alpha = 180°$	
	A	B	A	B	A	B
D	92.7	86.7	97.5	99.9	96.3	98.1
2D	98.6	97.7	99.3	99.4	99.0	99.4

Table 5-5. A and B calculated close to free surface compared with the value for an infinite plate given in %.

Residual stress measurements made on a curved surface such as a pipe wall will possibly be influenced by the curvature. For verification purposes a pipe with radius 48 mm was used in this investigation. For a blind hole with the dimensionless depth of 0.15 the effect of the curvature on the blind hole calibration coefficient was approximately 0.3%.

In the ASTM standard E-837-95 [3] it is stated that the assumption of infinite plate thickness is valid for plate thickness above 1.2D, when the hole is drilled to a depth of 0.4D. In the case of the integral method, the first calculation step is of the order of Z = 0.05, and studies in this work find acceptable accuracy in the shallow hole increments at plate thickness equal to D/2. However, it is possible to calculate values of $\overline{a}(Z_i, H_j)$ and $\overline{b}(Z_i, H_j)$ valid for any particular plate thickness if necessary.

Off-centre positioning of the hole relative to the gauge gives a complex strain situation to solve. Several publications deal with this topic for the through hole method [26, 34]. When the hole is positioned off-centre, for example in the axis of filament No.1 in Figure 5-2, the strain measured by filament No. 1 will obviously be changed. This can be treated numerically for a through hole by using Equation 5-18 and Equation 5-19. For example, a hole positioned 0.05 mm off-centre towards the strain gauges for the M&M 062-RE gauge gives 4% error in $\overline{a}(Z_i, H_j)$ and $\overline{b}(Z_i, H_j)$. An off-centre in the direction of gauge No. 1 causes a change in D for gauge No. 2, and gauges No.2 and 3 will also be influenced by the decomposed tangential strains caused by the off-centre, see Figure 5-21. The recommendation for the ASTM standardised method is a maximum allowable off-centre position of ±0.004D or ±0.025 mm, whichever is greater. This recommendation is approximately the limit of what is possible to determine with a standard travelling microscope.

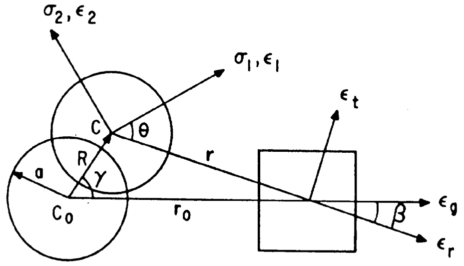

Figure 5-21. Schematic presentation of off-centre positioning and its influence on the strain reading. [34]

The physical hole shape was checked on several occasions during this work [16], and found to be in good agreement with the FE model which has parallel walls and a flat bottom without a transition radius. This is achieved by an ultra-high speed mill driven by an air turbine rotating at 200 000 – 300 000 rpm. This is considered to be the best drilling method because of the perfect hole shape and very small residual stresses introduced [4, 17, 20, 23]. It is strongly recommended to replace used mills before drilling a new hole, in order to minimise introduced residual stresses by having a cleaner cut and to avoid fracture of cutting faces of the mill. Damage to the mill has happened on some occasions during this work, and this will generally give highly irregular strain readings. Fracture of the mill blades is easily spotted after drilling by examination under a travelling microscope, and the irregular hole surface caused by a broken mill is easily detected through the microscope used to position the drilling device at the gauge centre. It is possible to measure the hole depth by a micrometer screw or better by measuring the relative distance between the plate and drilling device. The accuracy in the hole depth is equally important as accurate strain readings in obtaining high quality input data for the residual stress gradient evaluation.

ASTM requires reproducibility in strain measurements of $\pm 2*10^{-6}$ for the standardised method. When the integral method is used the strain relief between two measurements will be relatively low. To obtain an acceptable accuracy the minimum reproducibility should be $0.5*10^{-6}$, which in the case of Figure 5-22 is 10% of the value from gauge No. 2 at 0.2 mm depth. It is only possible to fulfil such a strict requirement with good laboratory equipment and skilled technicians. See also Section 5.9.

The residual stress calculations in this Chapter are based upon the strain readings from an indentation on a steel pipe (See Section 5.7). As seen in Figure 5-22 the absolute value of strain, as well as the slope, are very small at shallow depths. Measurement scatter will be significant given the small values of strain. After a transition region, the strain readings will level off which limits the integral hole drilling method to maximum depths of about 0.15 – 0.2D [17]. By using gauges scaled to a larger diameter D, deeper measurements are possible. ASTM [4] recommends a hole diameter approximately $0.3 < \phi < 0.6$ to maximize the strain output signal, and minimize the influence from drilling (See [4] for details).

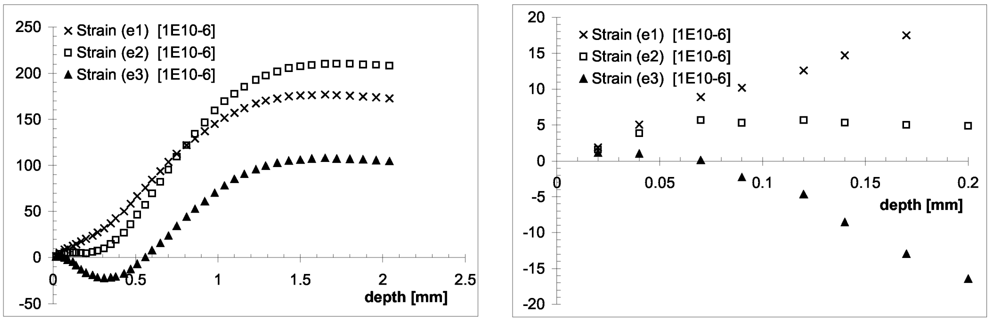

Figure 5-22. Strain reading from the indention experiment presented in Section 5.7.

The shear stress and normal stress perpendicular to the surface are generally small close to the surface since they are equal to zero at the surface, but they are impossible to determine by hole drilling methods. Their influence on the constants $\overline{a}(Z_i, H_j)$ and $\overline{b}(Z_i, H_j)$ is possible to determine by FE analysis, but this is not carried out in the present work.

5.7 Introducing residual stress by surface cold working

Residual stress was introduced into a smooth pipe surface by a specially designed cold rolling rig. The rig was designed for cold rolling of threads, but the verification of the residual stress measurement and FE analysis was made on an unnotched pipe with just a surface indentation. The reason for this is described in Section 5.8.

Three 60 mm diameter rolls placed 120 degrees apart and with a transverse radius of 100 mm were made from Rigor high strength steel produced by Uddeholm (specified $Rp_{0.2} = 2000$ MPa and $E = 1.90*10^5$) (See Figure 5-23 and Figure 5-25). After heat treatment the roll hardness was measured as 57 Vickers.

A hand driven hydraulic pump was used to obtain the intended roller force by means of an actuator. A digital meter calibrated against a load cell was used to read the oil pressure, and the load is accurate to within 2%.

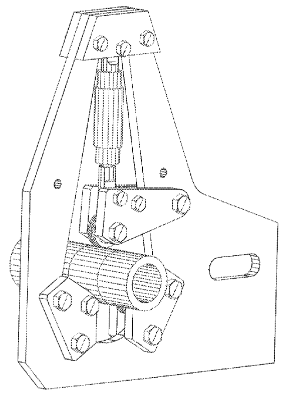

Figure 5-23. The rolling rig used to make indentations in the test specimen.

5.7.1 Test material

The specimen used in this study was a smooth pipe of 68 mm inner diameter. After turning off several mm by normal machine shop procedures the final outer diameter was 96 mm.

To determine the mechanical properties of the pipe material two specimens oriented in the circumferential direction and two specimens in the longitudinal direction were tested. The results are presented in Table 5-6. As expected the material is reasonably homogeneous, and the true stress strain curve found in longitudinal direction (presented in Figure 5-19) was the one used in the FE simulations.

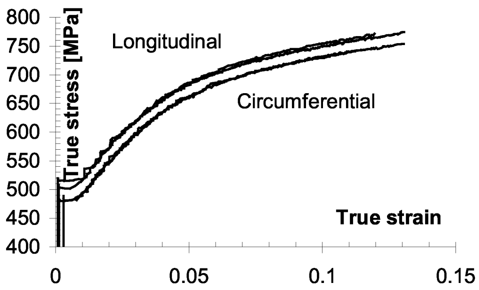

Figure 5-24. True stress-strain curves from tensile tests.

	$Rp_{0.2}$	UTS
Longitudinal	512	684
Circumferential	480	666

Table 5-6. Tensile test data.

5.8 Finite element analysis of residual stress fields

The general static non-linear FE analyses was solved by Abaqus Standard v. 5.8, where the increment is computed automatically (the arc-length method). Simulation of a cold-rolling process is strongly non-linear with material hardening and contact formulation. Several modelling alternatives and mesh densities in the contact region were investigated to get useful experience for the analysis of an actual thread profile that was planned. From a 2D model, simulating rolling of an infinitely long pipe between infinitely long rolls, the necessary rotation to get a stabilised solution uninfluenced by the stop / start positions was approximately 20 degrees. It soon became clear that the solution time for a rolling process would be extremely long, and it was decided to omit the cold rolling analysis of the smooth pipe. Instead, only an indentation analysis was performed, in order to save time for the more important analysis of thread rolling. The final model used for the indentation analysis and residual stress verification is by no means optimal, but the solution converged to the same result from different models and confidence in the results was therefore achieved.

5.8.1 FE model

One quarter of the system was modelled, using symmetric boundary conditions. Various boundary conditions were used, all giving identical residuals stress. The roller force used was of 13.7 kN.

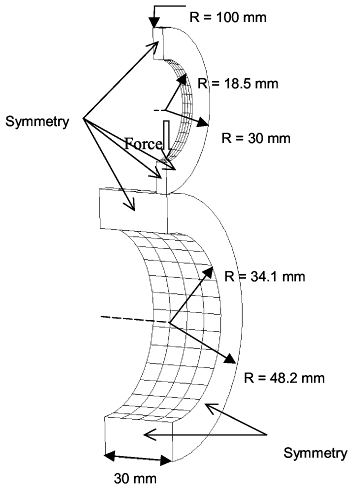

Figure 5-25. FE model.

5.8.2 Element formulation and material model

As recommended for contact analysis by Abaqus, the element C3D8R was used [1] after other element formulations had been tried. A very small difference is observed in the residual stress calculated between full and reduced integration (see Figure 5-26), but the time consumption was reduced by 12%.

The von Mises yield criterion was used throughout this study. Pure isotropic hardening and a mix of 15% kinematic and 85% isotropic hardening gave no difference in computed residual stress. A small difference was observed between analyses using the stress-strain curves obtained from longitudinal and circumferential tests (see Figure 5-24 and Figure 5-27). Fatigue cracks will normally propagate circumferentially and hence the longitudinal direction was used in the FE analysis.

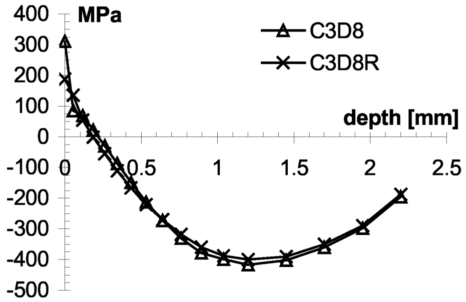

Figure 5-26. Differences in residual stresses from reduced and fully integrated element.

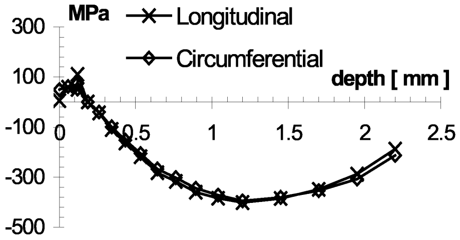

Figure 5-27. Residual stresses from differences in material parameters.

A roll modelled by a rigid surface exaggerated the residual stresses compared to an elastic roll as presented in Figure 5-28. No difference was found between E = 1.9*10^5 MPa suggested by the roll-steel manufacture and E = 2.1*10^5 MPa.

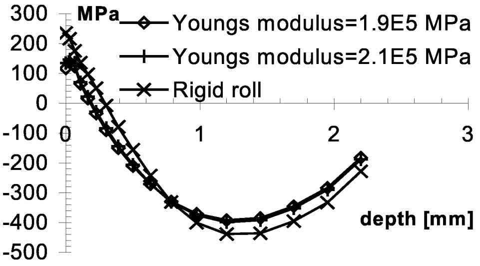

Figure 5-28. Rigid roll surface exaggerated the residual stresses.

5.8.3 Optimisation of mesh model

The FE analysis for this problem required extremely long computer runs, and several different meshes are evaluated to optimise the CPU time against accuracy. To minimise the number of variables, slave nodes are used as illustrated in Figure 5-29. A high density reference mesh was used to evaluate the optimised mesh; the result is presented in Figure 5-30.

5.9 Measurements of residual stresses at the indentation

The high residual stress gradients in the plane parallel to the surface influence the measurements if the hole or the strain gauge is located off-centre relative to the indentation centre. An off-centre hole will not significantly influence the measurement of longitudinal residual stress, especially not in the more shallow regions as seen in Figure 5-32 and Figure 5-33. The susceptibility to an off-centre position in the circumferential direction is much more pronounced, particularly in the deeper regions.

In the integral hole drilling methods, residual stress is assumed to vary only in the depth and to remain constant along the circumference. However, this is not the case in the verification model, and the assumption of constant stress all around the hole surface within each increment is violated (See Section 5.6). Obviously, the removed stresses on the part of the hole surface closest to the strain gauge dominate the strain reading, and are used in the comparison with the measured residual stresses.

Four indentations were made and HBM RY-61S gauges were attached in the centre of the indentations according to the manufacturer's guidance. The orientation was with gauge No. 1 in the circumferential direction, and gauge No. 3 in the longitudinal direction. High speed hole drilling equipment, a MTS 3000, rotating at 300 000 rpm[23] was used for the residual stress measurements. The equipment is manufactured by SINT and marketed by HBM. After centring the milling unit above the strain gauge, the incremental step drilling procedure is fully computer controlled. An electrical circuit is obtained as the mill is lowered by 0.15 mm/min and drilled through the gauge foil and touches the metal surface, and the depth gauge is zeroed. The hole is drilled at 0.1 mm/min by a stepping motor, and stopped at each increment for 3 seconds, after which time the computer controlled HBM Spider8 digital amplifier automatically made strain readings. In order to minimise electrical noise, a dummy gauge, new wires and new solder tin were used for each hole. A curve fitting procedure was used to determine the strain input for the strain-stress transformation to minimise noise.

The strain measurements are presented in Figure 5-36, Figure 5-37 and Figure 5-38. The magnitude on the relieved strain depends of the hole size, but as seen in Table 5-7 the variation in hole diameters is small. Holes No. 2 and 4 were off-centre in the direction of the axis of filament No. 1 (circumferential), above the recommended ASTM limit. This direction is also found most critical in Section 5.8.4, and the result is more scatter in the circumferential strain reading found in Figure 5-36 compared to the longitudinal strain reading presented in Figure 5-38. Obviously, also the reading from filament No. 2 is also influenced by an off-centre positioning of the hole relative to the strain gauge centre in circumferential direction, as seen in Figure 5-37.

---

[23] Value given by HBM.

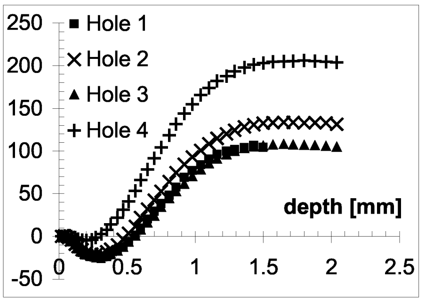

Figure 5-36. Strain reading from filaments No. 1.

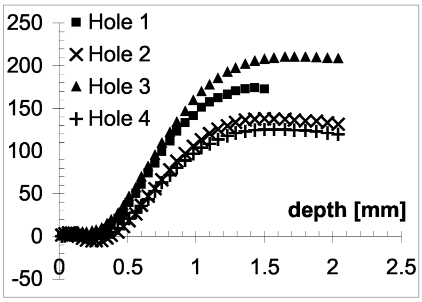

Figure 5-37. Strain reading from filaments No. 2.

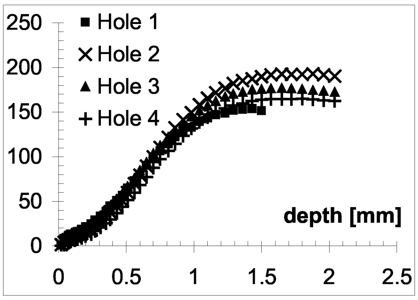

Figure 5-38. Strain reading from filaments No. 3.

The hole geometry data and off-centre relative to the gauge centre were measured by a stationary microscope and are presented in Table 5-7. The procedure according the MTS 3000 manual using the microscope attached to the MTS 3000 and dial gauges is found to give inaccurate hole data and was not used.

	Diameter in the axis of filament No. 1 [mm]	Diameter in the axis of filament No. 3 [mm]	Position of hole centre relative to gauge centre in direction of:	
			filament No. 1 [mm]	filament No. 3 [mm]
Hole 1	0.86	0.855	-0.005	-0.005
Hole 2	0.89	0.87	-0.03	-0.01
Hole 3	0.903	0.893	0.013	0.008
Hole 4	0.913	0.88	0.038	0.00

Table 5-7. Hole data.

5.10 Discussion

In the region from 0.1 - 0.9 mm of the hole depth, strain magnitude and strain gradient are sufficient for an accurate residuals stress determination [17], and a perfect match between the longitudinal residual stress from measurement and FE analysis as seen in Figure 5-40 were found. The grinding prior to strain gauge attachment, and also the shallow groove from the indentation, might have influenced residual stresses in the surface region as this does not match the FE analysis well, or it might simply be inaccuracy in the FE analysis of indentation, inaccurate calibration surfaces for stress-strain transformation, noise in strain and hole depth measurement, or a combination of these factors.

The dotted measurement does not fulfil the ASTM requirement for maximum allowable off-centre positioning of max. 0.025 mm or 0.004D as seen in Table 5-7.

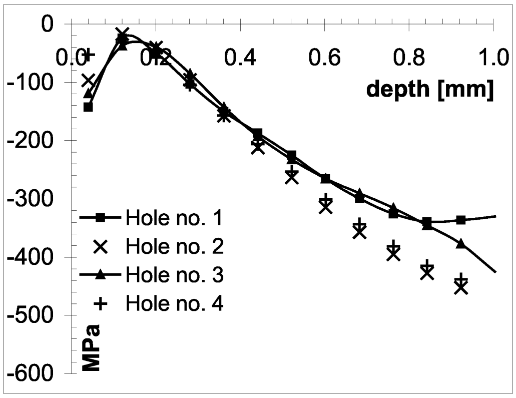

Figure 5-39. Longitudinal residual stress measurements. Lined measurements are fulfilling the ASTM requirement and in depth region where strain gradient are sufficient for accurate residual stress determination.

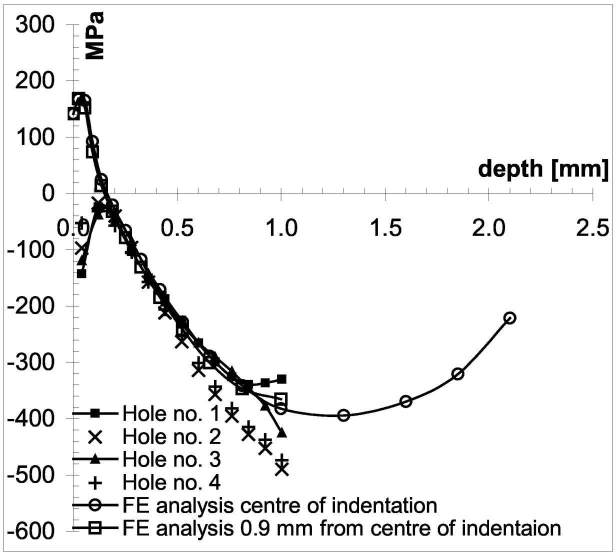

Figure 5-40. Longitudinal residual stress from measurements compared to FE analysis 0.9 mm from centre of indentation in longitudinal direction and in the centre of indentation.

As expected, more scatter is observed in the circumferential residual stress than in the longitudinal residual stress. This is seen in Figure 5-43 where the measurements are more or less within the residual stress found in the centre of the indentation and 0.9 mm from the indentation centre where the hole is located.

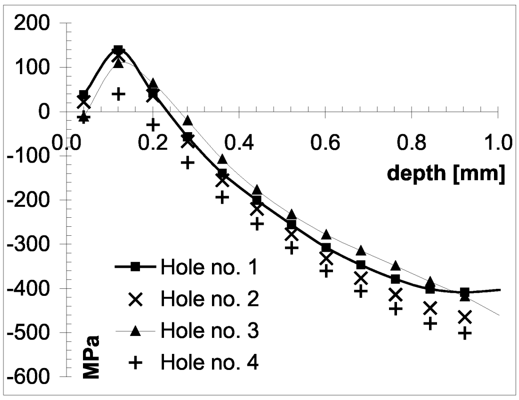

Figure 5-41. Circumferential residual stress measurements. The curves represent data that satisfy the ASTM requirement.

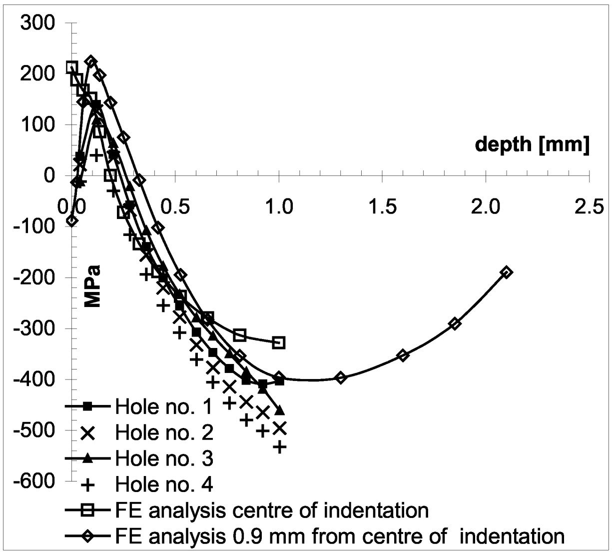

Figure 5-42. Circumferential residual stress from measurements compared to FE analysis 0.9 mm from centre of indentation in circumferential direction and in the centre of indentation.

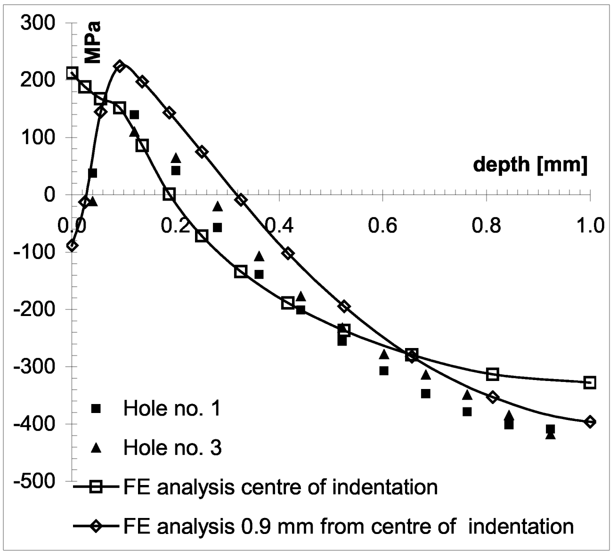

Figure 5-43. The circumferential residual stresses measured are in good agreement with residual stresses from FE analyses.

Residual stress measurements outside the indentation were found to be small, and located close to the surface (from turning) compared to the one found after indentation as expected.

As described in Section 5.6, a key assumption is that residual stresses give none or only small amounts of plasticity at the hole. The residual stresses measured in these measurements are not expected to give any plasticity sufficient to influence the measurement.

5.11 Conclusions

Within it's limitations, the integral hole drilling method is found to be relatively inexpensive and robust. Measurements in layers 0 - 0.1 mm are shown to be prone to inaccuracy due to the small amount of relieved strain, and the relatively inaccurate determination of the hole depth. Other factors contributing to the observed scatter in the verification measurements are:

1. Off-centre positioning of strain gauge relative to centre of indented area.
2. Off-centre positioning of the hole relative to the strain gauge.
3. Stress gradients parallel with the surface as seen in the FE analysis.
4. Inaccuracy in hole geometry.
5. Electrical noise in strain readings.

However, the measured longitudinal residual stress was found to match the residual stress determined by FE analysis in the depth region 0.1 – 0.9 mm which is also the region recommended in the literature for the strain gauge. Both methods are thereby found to give accurate determination of the residual stress field. Very good agreement is also found in the literature between x-ray diffraction with local electrolytic layer removal, and the integral hole drilling method [22, 23].

Two errors are found in the only commercially available software package for the calculation of residual stresses by the incremental hole drilling method. The errors seriously reduce the accuracy of the computed residual stresses, and in certain circumstances the residual stresses are invalid.

The true stress-strain curves for the material used in the indentation tests was determined in both the circumferential and longitudinal directions, indicating only a small amount of anisotropy. Accordingly, FE analyses, with the material hardening characteristics in the longitudinal and circumferential directions respectively, were found to give the same residual stresses to within a few percent.

Very high element density was necessary for the FE analyses described in this Chapter. Highly non-linear material properties and contact modeling give very time consuming computer runs. The importance of modeling the roll with elastic, rather than a rigid, body was demonstrated.

5.12 References:

1 Abaqus (1998) Contact in Abaqus/Standard. Hibbitt, Karlsson & Sorensen, Inc.

2 Ajovalasit A., Petrucci G. and Zuccarello B. (1996) Determination of nonuniform residual stresses using the ring-core method. *Journal of Engineering Materials and Technology* 118, 224-228.

3 ASTM (1995) Standard test method for determining residual stress by the hole-drilling strain-gage method. E 837 - 95. Annual book of ASTM standards 1995. ASTM, Philadelphia. pp 642

4 ASTM (2000) Standard test method for determining residual stress by the hole-drilling strain-gage method. E 837 - 99. Annual book of ASTM standards 2000. ASTM, Philadelphia. pp 670

5 ASTM (2000) Standard test method for determining the effective elastic parameter for x-ray diffraction measurements of residual stress. E 1426 - 98. In Annual book of ASTM standards 2000. ASTM, Philadelphia. pp 916-919.

6 Beghini M. and Bertini L. (1998) Recent advance in the Hole Drilling method for residual stress measurement. *Journal of Materials Engineering and Performance* 7, 163-172.

7 Beghini M. and Bertini L. (2000) Analytical expressions of the influence functions for accuracy and versatility improvement in the hole-drilling method. *Journal of strain analysis* 35, 125-135.

8 Beghini M., Bertini L. and Raffaelli P. (1995) An account of plasticity in the hole-drilling method of residual stress measurement. *Journal of strain analysis* 30, 227-233.

9 Beghini M., Bertini L. and Rosellini W. (2000) Generic algorithms for variable through thickness residual stress evaluation. *Materials Science Forum* 347-3, 138-143.

10 Faires J.D. and Burden R.L. (1993) Numerical Methods. PWS publishing company, Boston.

11 Finch D.M. (1994) A review of non-destructive residual stress measurement techniques. ERA Technology report 94-0101R. pp 1

12 Flaman M.T. and Manning B.H. (1985) Determination of residual-stress variation with depth by the hole-drilling method. *Experimental mechanics* 205-207.

13 Gibmeier J., Kornmeier M. and Scholtes B. (2000) Plastic deformation during application of the Hole-drilling method. *Materials Science Forum* 347-3, 131-136.

14 Holmgren M. and Näsström M. (1994) Mätning av restspänningar: jämförelse mellan olika metoder och redovisning av round-robin provning.

15 Hottinger Baldwin Messtechnik (1999) HBM - Strain gauges and accessories G24.01.9e.

16 Kristoffersen S. and Haagensen P.J. (1998) Determination of residual stresses in plates by the hole-drilling technique. In Proceeding: INALCO'98. pp S21A 1-S21A13.

17 Lu J. (1996) Handbook of Measurement of Residual Stresses. The Fairmont Press.

18 Mathar J. (1934) Determination of initial stresses by measuring the deformation around drilled holes. *Transactions of the ASME* 56, 249-254.

19 Measurement Group (1993) Catalog 500. Measurement Group.

20 Measurement Group (1993) Measurement of residual stresses by the hole-drilling strain gage method. Tech note TN-503-4 Residual stress measurement. pp 1

21 Niku-Lari A., Lu J. and Flavenot J.F. (1985) Measuremet of residual-stress distribution by the incremental hole-hole drilling method. *Journal of Mechanical Working Technology* 11, 167-188.

22 Nobre J.P., Kornmeier M., Dias A.M. and Scholtes B. (2000) Use of the hole-drilling method for measuring residual stresses in highly stresses shot-peened surfaces. *Experimental mechanics* 40, 289-297.

23 Nobre J.P., Kornmeier M., Dias A.M. and Scholtes B. (2000) Comparative analysis of shot-peening residual stresses using hole-drilling and x-ray diffraction methods. *Materials Science Forum* 347-3, 138-143.

24 Pilkey W.D. (1994) Formulas for stress, strain, and structural matrices.

25 Rendel S. and Vigness I. (1966) Hole-drilling strain-gage method of measuring residual stresses. In Porc. SESA XXIII. pp 577-586.

26 Sander J.P. and Bowie G.E. (1978) Residual stress by blind-hole method with off-center hole. *Experimental mechanics* May,

27 Schajer G. (2000) Improved resiudal stress measurement methods. Advarticement for graduent students. *Internet*

28 Schajer G.S. (1981) Application of finite element calculation to residual stress measurements. *Journal of Engineering Materials and Technology* 103, 157-163.

29 Schajer G.S. (1988) Measurement of non-uniform residual stresses using the hole-drilling method. Part I - Stress calculation procedure. *Transactions of the ASME* 110, 338-343.

30 Schajer G.S. (1988) Measurement of non-uniform residual stresses using the hole-drilling method. Part II - Practical application of the integral method. *Transactions of the ASME* 110, 344-349.

31 Scott P. (1986) Comparison of the blind-hole drilling and the BCD chip-removal technique for determining residual stresses. In 1986 Spring conf. on experimental mechanics, New Orleans, 8-13 Jun 1986. pp 209-215.

32 SINT (1998) Manual for use and maintenance. System for measuring residual stresses by the hole drilling method (RESTAN).

33 Smith D.J., Leggatt R.H., Webster G.A. and Mills G. (1988) Neutron diffraction measurements of residual stress and plastic deformation in an aluminium alloy weld. *Journal of strain analysis* 23, 201-211.

34 Wang H.-P. (1979) The alignment error of the hole-drilling method. *Experimental mechanics* January, 23-27.

35 Wu Z., Lu J. and Joulaud P. (1997) Study of residual stress distribution by Moiré interferometry incremental hole drilling method. In Proceeding of 5'th international conf. on residual stress - ICRS 5. pp 804-809.

6 Full scale testing

6.1 Notation

ε_f	true fracture strain = $\ln(A_0/A_f)$
σ	stress [MPa]
σ_b	stress from bending [N/m^2]
σ_f	true fracture stress = F/A_f [N/m^2]
$\varnothing$	diameter [m]
A_0	initial cross-section area [m^2]
A_f	cross-section area of fracture [m^2]
F	axial force [N]
I_{nom}	the moment of inertia [m^4]
K_t	stress concentration factor
M	moment [Nm]
$Rp_{0.2}$	0.2 % offset yield stress [MPa]
UTS	ultimate tensile strength = F/A_0 [MPa]

6.2 Introduction

The use of used drillstring connections would involve expensive re-cutting of both pin and box threads. These operations would be necessary in order to remove all defects and damage incurred from drilling operations thus obtaining a specimen with similar fatigue strength to a new one. Instead, pipes cut from scrapped drillstrings were used to produce large scale test specimens with a notch geometry similar to that found in the thread at the pin.

6.3 Fatigue test specimens

The fatigue test specimens were fabricated from used drillstings in two material qualities, called AC-95 and P-110. Two tensile test specimens oriented in the longitudinal direction were extracted and tested from each of the two materials, 6 mm diameter for the AC-95 specimens and 5 mm diameter for the P-110 specimens. The mechanical properties are presented in Table 6-2 and Figure 6-1.

The microstructure of the seamless steel pipes was tempered martensite with chemical compositions presented in Table 6-1.

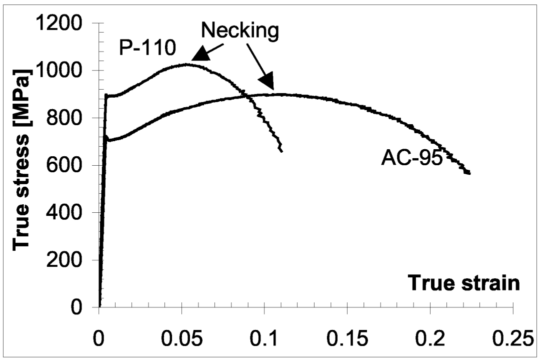

Figure 6-1. True stress/strain curve for AC-95 and P110.

Elements	AC-95	P-110
C	0,28	0,34
Si	0,28	0,24
Mn	0,49	0,71
P	0,016	0,010
S	0,002	0,001
Cr	0,94	0,99
Ni	0,018	0,079
Al	0,069	0,027
Cu	0,015	0,19
Mo	0,45	0,19
Nb	0,002	0,001
V	0,005	0,003
Ti	0,004	0,002
Co	0,004	0,011
B	0,0019	0,0001
W	0,01	0,01
As	0,004	0,012
Sn	0,001	0,009

Table 6-1. Chemical elements in %[24].

From each tubing, four fatigue specimens 2200 mm long were cut, respectively 32 AC-95 specimens and 41 P-110 specimens. The test area was manufactured with the thread profile start and stop positions on the surface reaching full depth within 180° and four full V-0.038R threads. See Figure 6-2 and Table 6-2. The machining procedure and surface quality was according to normal oil-tool manufacturing procedures.

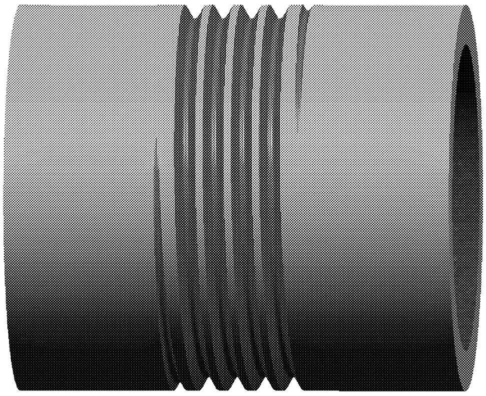

Figure 6-2. Full scale fatigue test geometry.

	P-110	AC-95
Thread height	3.10mm	3.10 mm
Thread root radius	0.97 mm	0.97 mm
Thread pr. inch	4	4
Outer radius	43.5 mm	43.5 mm
Inner radius, approx.	35.0	33.0 mm
$Rp_{0.2}$	887 MPa	701 MPa
UTS	973 MPa	818 MPa
σ_f	1890 MPa	1750 MPa
ε_f	1.17	1.35

Table 6-2. Test geometry and mechanical data. Mechanical test cylindrical tension bar: P-110, 5 mm diameter; AC-95, 6 mm diameter.

---

[24] Optical emission spectrometry (OES)

The bearings in the four-point rotating bending fatigue test rig were positioned 600 mm apart, with the machined test area located at mid-span.

6.4 Test setup

The four-point rotating bending fatigue test rig was designed and built for the project. (see Figure 6-4 and Figure 6-5). A 100 kN hydraulic actuator and an analogue controll unit were used, however, at speeds higher than 180 rpm (3 Hz) the response of the hydraulic system was too slow to compensate for small eccentricities in the test specimens. The result was fluctuations in the load amplitude that were far higher than the normal requirement of 2% accuracy in fatigue testing. A 'clean' sinusoidal load signal was generated with amplitude and phase tuned by an oscilloscope monitoring the load cell-signal to minimise the load fluctuations. Typical load variations due to eccentricity before and after active load control was incorporated are shown in Figure 6-3. Another serious problem, that took a large effort to reduce to an acceptable level, was a significant noise in the signal from the load cell. The problem was generated by the electronic circuits controlling the electric motor.

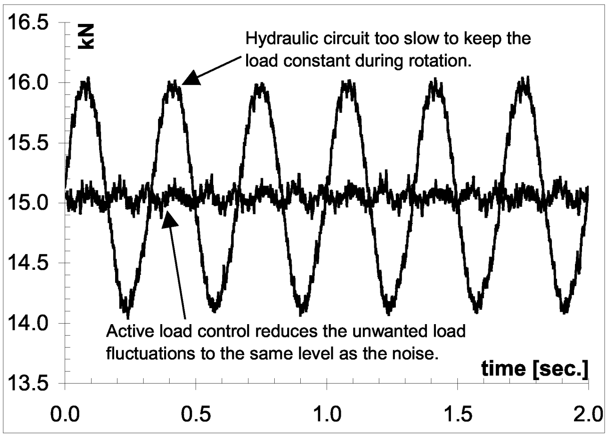

Figure 6-3. Load variation with and without active damping of the load fluctuations caused by small eccentricities in the test specimen. When active damping was used, the remaining load fluctuations were of the same magnitude as the noise.

The number of rotations was counted by a trigger arm attached to the end of the pipe which activated a photocell. Displacement and load was monitored automatically by the actuator load cell, once either was outside the acceptance window, both the hydraulics and the electrical motor rotating the pipe were shut down.

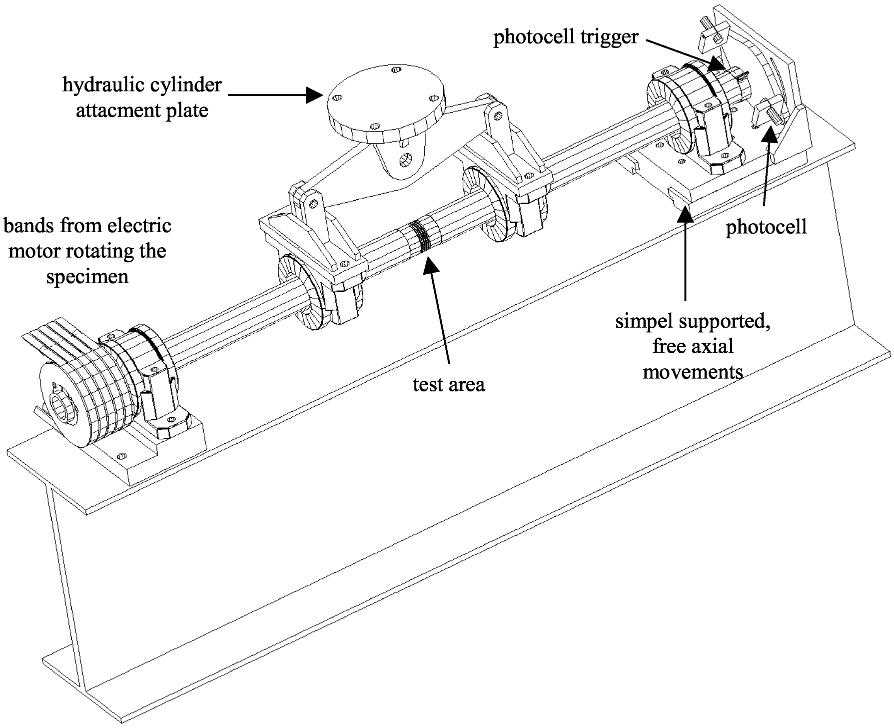

Figure 6-4. Rotating bending fatigue test-rig.

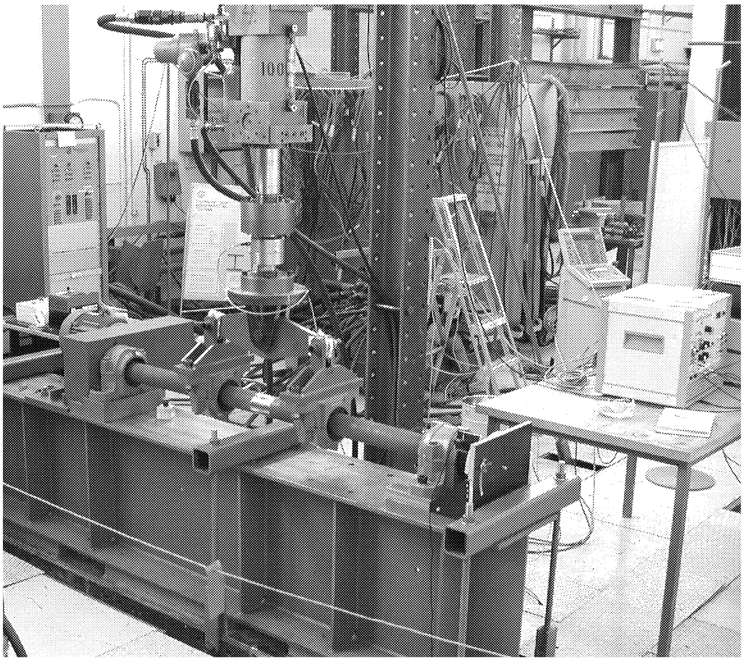

Figure 6-5. Four-point rotating bending test rig.

6.5 Stress concentration factor for notched pipe specimen

The stress concentration factor is defined as

$$K_t = \frac{\sigma}{\sigma_b} = \frac{I_{nom}\sigma}{M \cdot y} \qquad \text{Equation 6-1}$$

where I_{nom} is the moment of inertia at the thread root. Ideas Master Series 8 software was used to generate the element model to be solved by Abaqus Standard v. 5.8 using second order C3D10 elements and isotropic elastic material properties. The solution was found to converge by using element refinement, and the values of K_t found are presented in Table 6-3. As seen in Table 6-3, K_t at the thread root is practically the same for both specimens and is highest at threads 1 and 4. K_t for the inner surface is highest at threads 2 and 3, and almost equal for both specimens.

	Thread 1 and 4		Thread 2 and 3	
	Thread root	Pipe inner surface	Thread root	Pipe inner surface
AC-95	2.79	0.52	2.45	0.61
P-110	2.74	0.44	2.39	0.62

Table 6-3. K_t for specimens used in full scale fatigue testing.

As seen in Figure 6-6 the stress gradient is very steep, and FE analyses are therefore sensitive to the element mesh density close to the thread root.

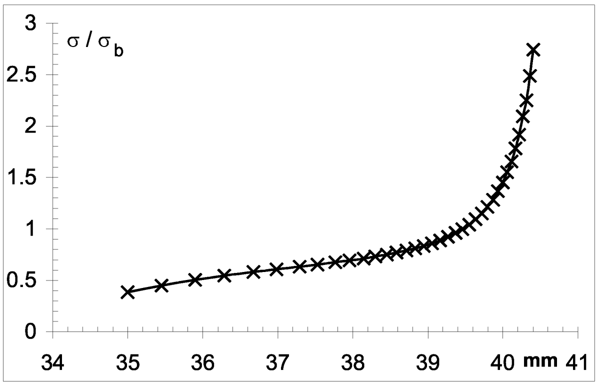

Figure 6-6. σ / σ_b vs mm from pipe centre.

6.6 Reference data

Care was taken to machine the pipe such that the centre of the test area was as close to the symmetry line as practical. After crack growth lead to a pipe deflection outside the automatic stop limits, the test was stopped, the remaining cross-section was partly cut by sawing and was broken free. The cross-section was measured, and the test's local nominal stress where the crack presumably initiated was calculated as:

$$E = \frac{FOD - ID}{2} - MT \qquad \text{Equation 6-2}$$

$$z = \frac{\frac{FOD^3}{2} - ID^2\left(\frac{FOD}{2} - E\right)}{FOD^2 - ID^2} \qquad \text{Equation 6-3}$$

$$M = \frac{(S1 + S2)F}{4} \qquad \text{Equation 6-4}$$

$$I = \pi \left(\frac{FOD^4 - ID^4}{64} + \frac{FOD^2 \left(z - \frac{FOD}{2} \right)^2 - ID^2 \left(z - \frac{FOD}{2} + E \right)^2}{4} \right) \qquad \text{Equation 6-5}$$

$$\sigma = \frac{M}{I} z \qquad \text{Equation 6-6}$$

with definitions as presented in Figure 6-7 and Figure 6-8.

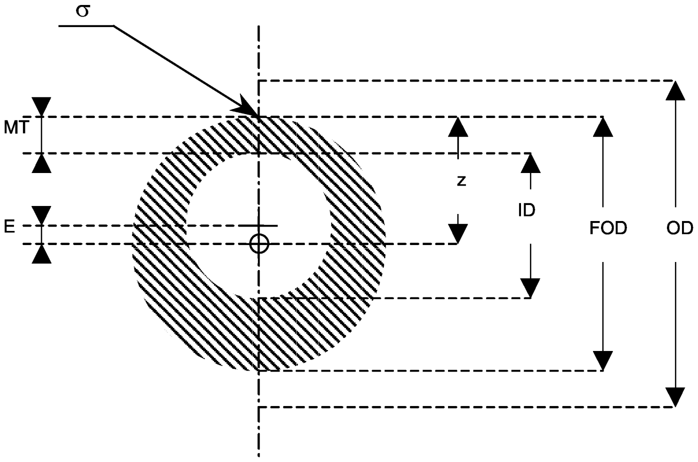

Figure 6-7. Crack cross-section definitions.

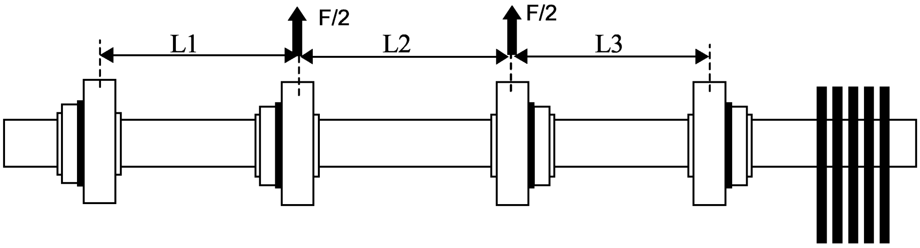

Figure 6-8. Length definitions.

The fatigue data from testing of the unrolled specimens are presented in Figure 6-9. There is no statistical difference between the two sets, and the regression line is

$$\log(N) = 17.690 - 4.72 \log(\Delta\sigma) \qquad \text{Equation 6-7}$$

with st.dev. = 0.11 and 258 MPa fatigue limit (N = $2*10^6$).

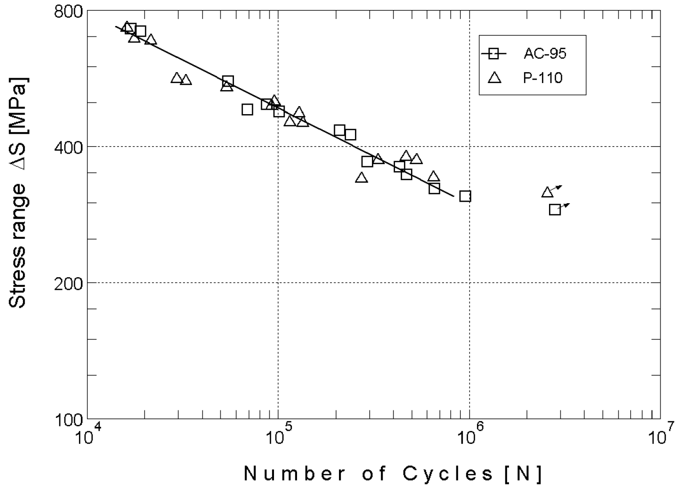

Figure 6-9. Reference test on unrolled pipes.

6.7 Cold rolling setup

The cold rolling rig is shown in Figure 5-23. A calibrated hydraulic pump was used to maintain correct oil pressure during rolling, which was made by hand at approximately 1.5 rpm. One profiled roll (see Figure 6-10) 30 mm in radius with 50° thread angle and thread root radius 0.96 or 1.05 mm, and two flat rolls with 30 mm radius and 34 mm wide, all made of Rigor steel (see Section 5.7) were used. The plastically deformed thread root area was small, and rolling with a 30 kN roll force resulted in a reduction of the pipe diameter at the root of 0.12 mm (this is a very high roll load compared to what was normally used).

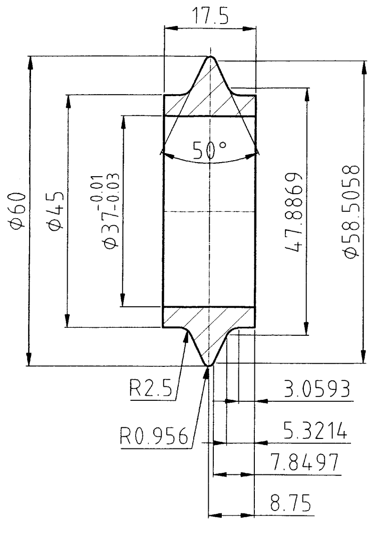

Figure 6-10. Roll used for cold rolling of threads.

6.8 Visual crack inspection and fracture surfaces

The fracture surfaces for the cold rolled specimens typically showed a distinctly different pattern compared to those of the non-rolled specimens. Depending on the fatigue test load, a number of initiation sites were easily identified as seen in Figure 6-11 on the unrolled specimen. These features were counted under low-magnification optical examination, and presented in Figure 6-12.

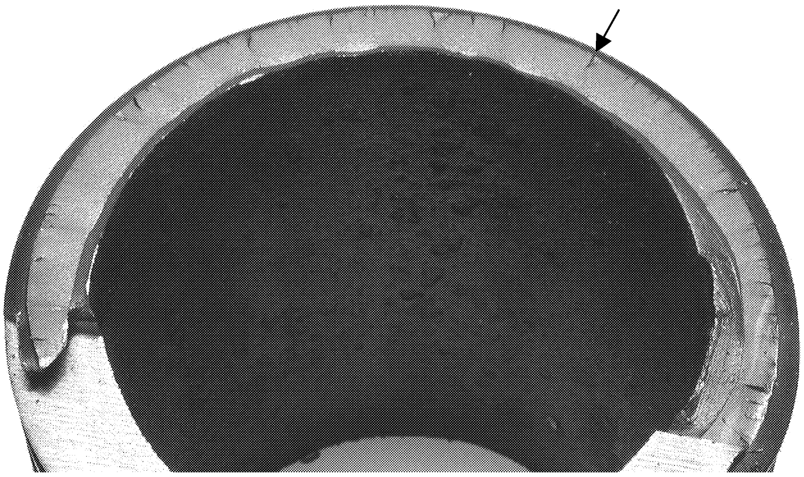

Figure 6-11. Fracture surface for an unrolled specimen. Failure after 100 850 cycles. Note the radial ductile fracture at the thread root connecting small cracks initiated at different planes (one is pointed out).

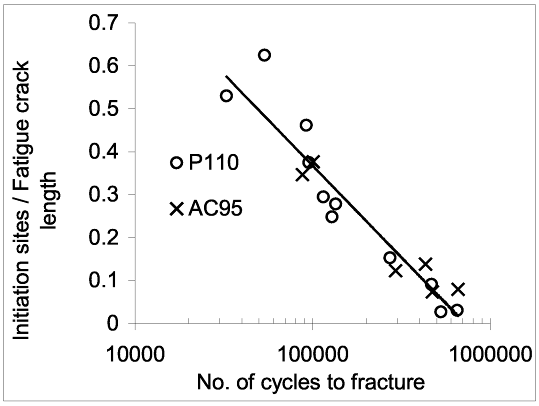

Figure 6-12. Number of initiation sites vs number of cycles to fracture.

The crack growth pattern in fracture surfaces from rolled specimens was totally different as seen in Figure 6-13, where a crack has initiated at the thread root surface and at the pipe inner surface. Another example is shown in Figure 6-15 where three crack initiation sites at the pipe inner surface were found.

These cracks were not connected to the final fatigue crack.

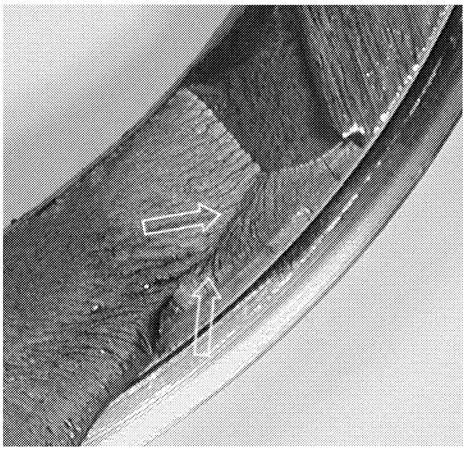

Figure 6-13. Fracture surface for a rolled specimen. Arrows indicating crack growth direction. Ridge between the arrows is from ductile fracture. Note typical flat featureless region directly beneath the thread root.

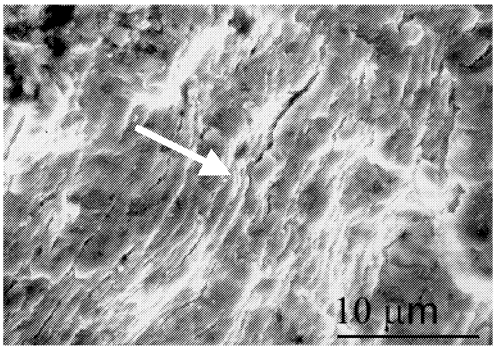

Figure 6-14. Example of striations found at the arrows in Figure 6-13.

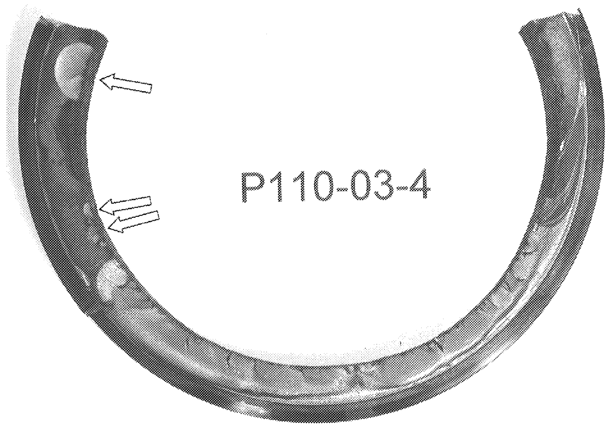

Figure 6-15. Fracture surface of a rolled specimen with three semi-elliptical cracks that had started from pipe inner surface.

To follow up these observations, one unrolled and one rolled specimen were systematically investigated by dye penetrate inspection. With inspection intervals of 5000 cycles cracks were found after 10 000 cycles for the unrolled and 20 000 cycles for the rolled specimen, but the number of cycles spent in crack growth was dramatically increased by rolling (see Figure 6-16).

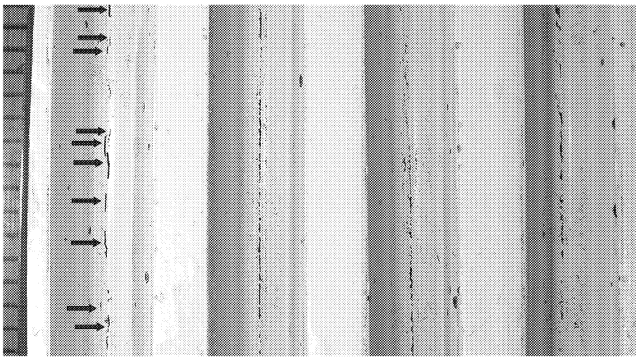

Figure 6-16 a. Crack development of a cold rolled fatigue test stopped every 5000 cycles. The cracks were first detected after 20 000 cycles by dye penetrant. In the unrolled specimen cracking was found after 10 000 cycles. The same load was used in the two tests.

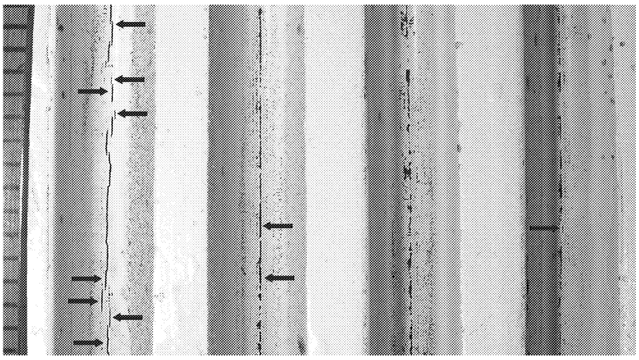

Figure 6-16b. Crack pattern at 30 000 cycles. Arrow indicating new cracks or crack growth.

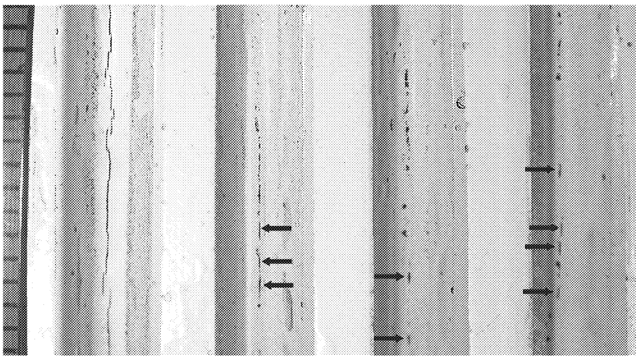

Figure 6-16c. Crack pattern at 35 000 cycles.

Figure 6-16d. Crack pattern at 40 000 cycles

Figure 6-16e. Crack pattern at 50 000 cycles. Unrolled specimen fractured after 55 000 cycles.

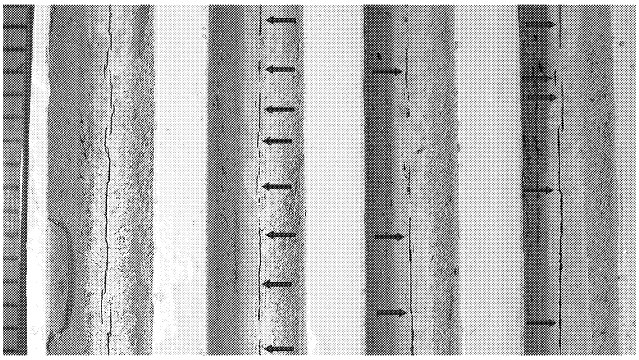

Figure 6-16f. Crack pattern at 80 000 cycles. Unrolled specimen reached this level of cracking after 30 000 cycles.

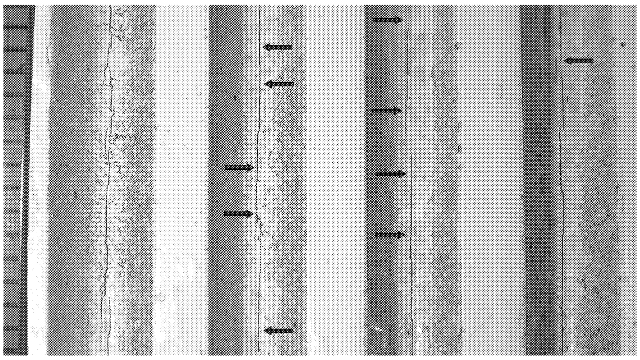

Figure 6-16g. Crack pattern at 200 000 cycles. The test was stopped due to severe deflection after 307 200 cycles in the second thread from left. Crack grew from inside pipe surface.

The rolled specimen was stopped automatically due to excessive deflections at 307 200 cycles, and 4 cross-sections were cut open for investigation. The pipe inside had severe corrosion pitting attacks, similar to the majority of the pipes. The crack was following a path formed by pits as shown in Figure 6-17. A crack was found in the bottom of all threads.

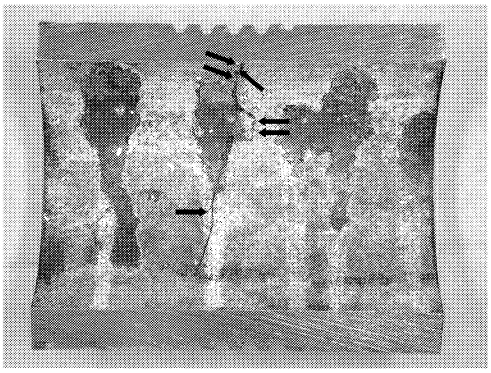

Figure 6-17. The crack on the inside crossed several pittings indicated by arrows. Fatigue crack development was followed in Figure 6-16.

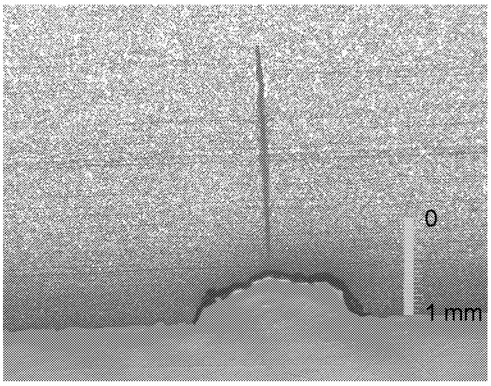

Figure 6-18. Fatigue crack initiated from pitting. Inner surface shown in Figure 6-17. The crack looks wider in the deepest part of the crack due to more severe etching.

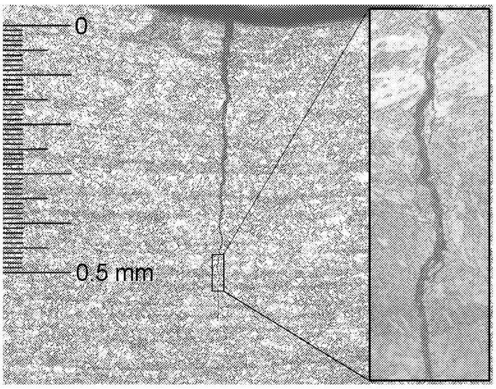

Figure 6-19. Cross-section at bottom of thread in specimen followed in Figure 6-16. Cracks were found in all thread roots. Typical crack lengths were 0.3 – 0.5 mm.

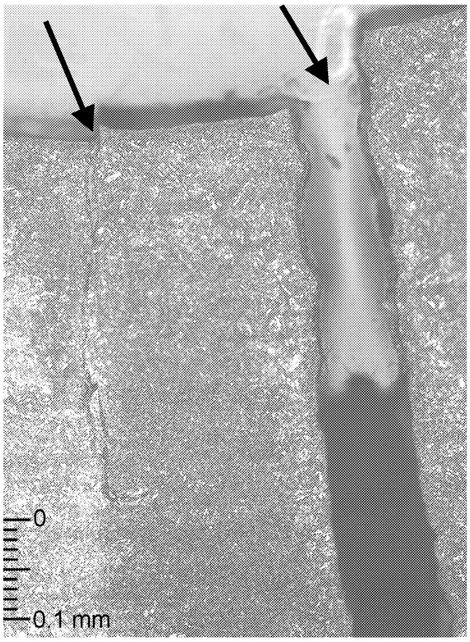

Figure 6-20. Crack surface mismatch (at arrows) due to relieved residual stresses. Left crack initiated at the thread root, right crack initiated at the pipe inner surface. Crack development followed in Figure 6-16.

In order to confirm the sensitivity of the dye penetrant method to find cracks, another specimen was prepared with a similar rolling force and cycled at similar load level as the specimen investigated in Figure 6-16. This specimen was also examined at regular intervals by dye penetrant inspection. When a number of crack initiation sites were detected at 30 000 cycles, the test was stopped. Several crack initiations were marked for further investigation (see Figure 6-21) and the surface crack length (as indicated by dye penetrant) were measured. After preparation by sawing and grinding, the crack initiation sites were examined under a microscope, and the crack depth measured. All dye penetrant indications were found to be shallow cracks, less than 0.4 mm deep.

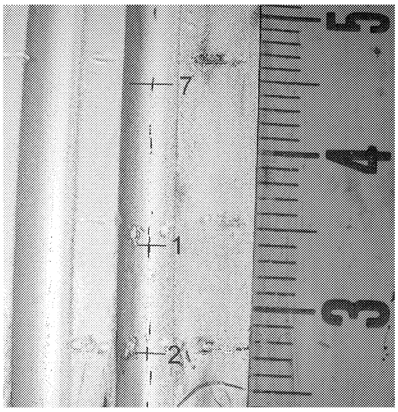

Figure 6-21. Crack initiation sites cut and investigated in microscope.

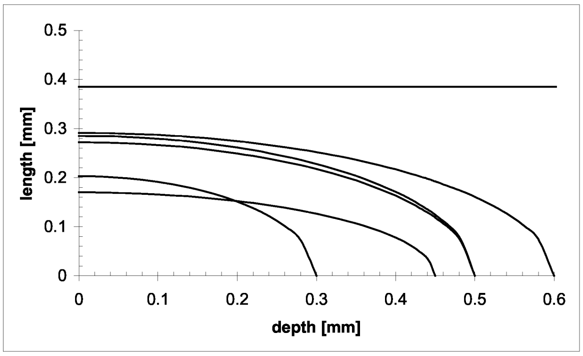

Figure 6-22. Approximate crack shape development from surface indication and crack depth measurements.

It is clear from these investigations that the crack initiation period is longer for rolled specimens compared with unrolled, but the increase is very small compared to the increased fatigue life following crack arrest. The cracks leading to failure in rolled specimens were initiated at corrosion pits on the pipe inner wall.

6.9 Rolling parameters

After the observation of crack initiation from the inner surface all successive fatigue tests were done at high load, with typical fatigue live of 10 000 – 30 000 cycles for unrolled specimens. This is due to what appears to be a steeper slope for cracks initiated from the inner surface compared to the high quality thread surface, as seen in Figure 6-23.

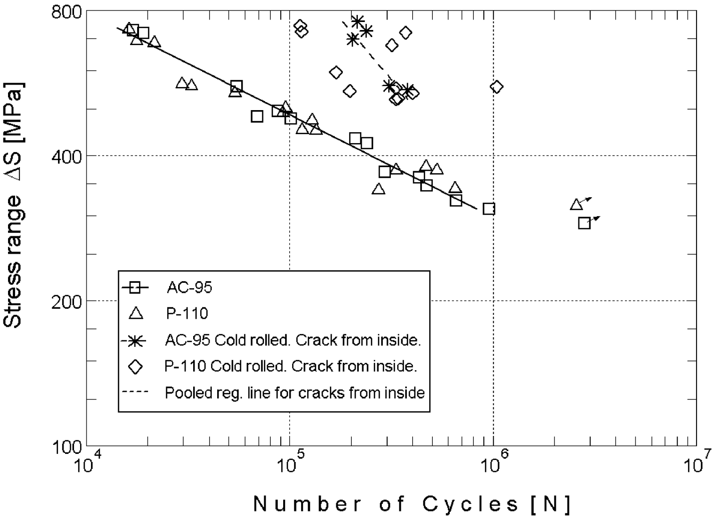

Figure 6-23. Comparison of unrolled threads, and cold rolled threads where the final crack grew from the pipe inner surface.

The test's exact nominal stress was not known until the fatigue tests were completed and the geometry of the cross-section was measured. To be able to compare test results from slightly different nominal stresses, the fatigue life was adjusted assuming a slope equal to 5.

6.9.1 Rolling load

As expected, higher rolling loads led to longer fatigue lives. Also, the difference in material toughness gave different fatigue improvement. The AC-95 specimens will reach yield introducing residual stresses at a roller force at which P-110 still have elastic strain response. Increasing roller load will increase plastic strain and level of residual stress until maximum strain hardening is reached. As expected, at equal roller force AC-95 specimens had longer lives than P-110 specimens (see Figure 6-24). However, at optimised roller force, which will be higher for P-110 than AC-95, P-110 has more strain-hardening and hence higher residual stresses than AC-95.

An optimisation of the roller force was not possible due to failure from cracks initiated at pits on the pipe inner surface. However, at 30 kN the thread helix was deformed severely during rolling of one specimen. In the literature small cylindrical steel bars with typical cross-sectional radii from 7 to 15 mm and a notched radius of 1 mm have been cold rolled with roller loads from 1.27 to 10 kN [1, 2].

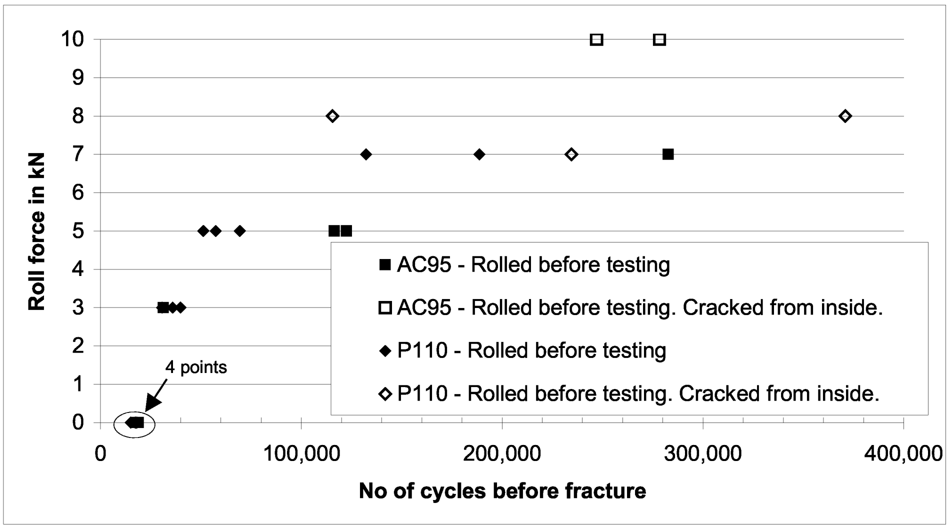

Figure 6-24. Fatigue testing with increasing cold rolling force.

6.9.2 Roll radius

An oversized roll with a nose radius of 1.045 mm was used, and found to need an increased rolling force to give a fatigue life increase equal to that from the roll sized slightly less than the thread root radius of 0.96 mm.

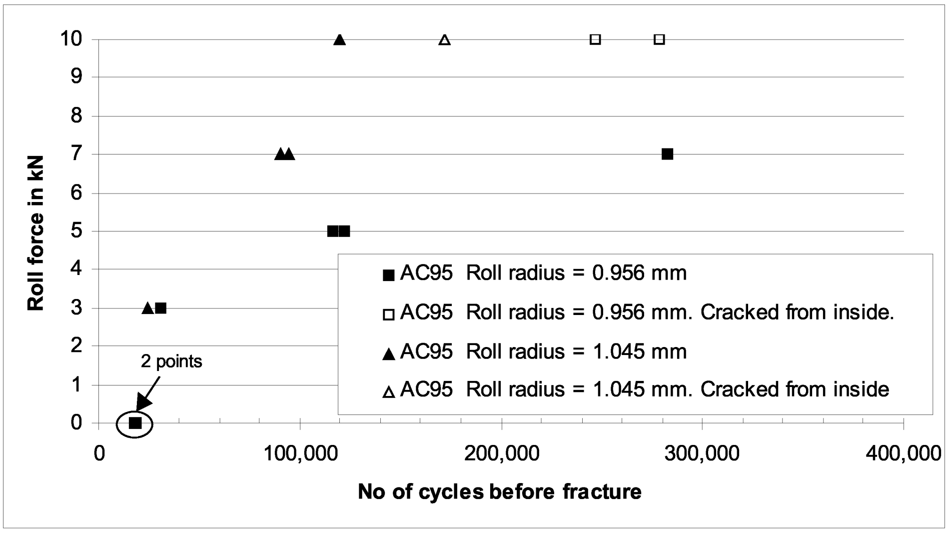

Figure 6-25. Fatigue tests from rolling of an oversized roll compared to equal sized roll.

6.9.3 Re-rolling

Re-rolling after expiry of 50% of the expected life for rolled specimens with shallow cracks present further increased the fatigue life as seen in Figure 6-26 marked with filled triangles.

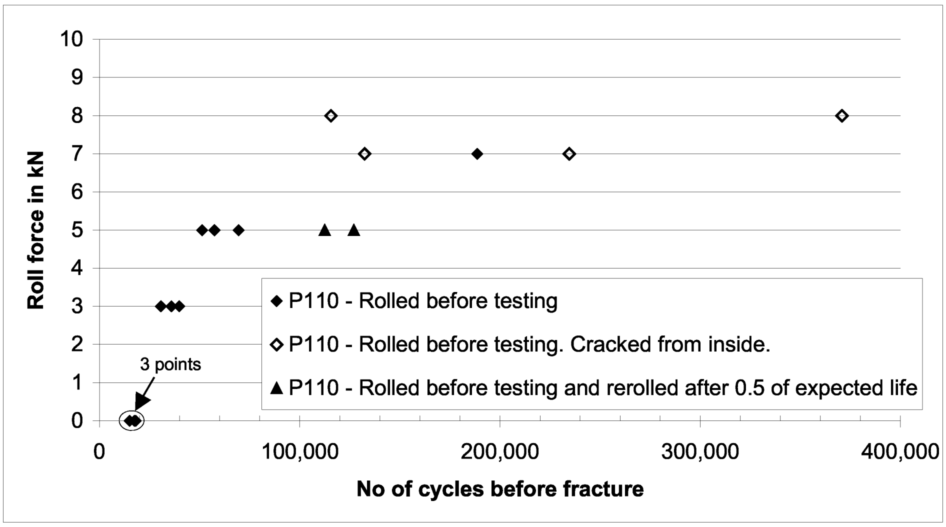

Figure 6-26 Fatigue testing with re-rolling at 50% of expected fatigue life for specimens with initial cold rolling.

6.10 Conclusions

Two different steel qualities typical of drillstring elements were tested in four-point rotating bending. Due to efforts to reduce noise in the closed loop control system for the test equipment, and to compensate for the eccentricity in the test specimens, reference fatigue data were obtained with small standard deviations, thus indicating good reproducibility.

An increased fatigue initiation period with cracks initiating at the thread root was obtained for cold rolled pipe specimens. However, the major contribution to the increased life came from longer crack propagation life. In fact, the cracks at the thread root would typically arrest and the final fatigue cracking to failure took place initiated at the pipe inner surface for the rolled specimen. For this reason it was not possible to optimise the roller geometry and the rolling procedure in terms of load and number of rolling passes.

From this investigation a roller with the same geometry as the thread root profile is recommended, as an increased fatigue life could be obtained with a lower rolling force. Based on the experience gained in this work, the recommended rolling force for the material investigated is around 20 kN, since the optimum roll force is higher than 7 kN for a roll with the same curvature as the thread, and lower than 30 kN to avoid damage to the thread profile.

Re-rolling with shallow cracks less than approximately 0.5 mm deep increased the remaining fatigue life significantly. An implication from this observation is the possibility to roll a used drillstring, following inspection to ensure that cracks deeper than approximately 0.25 mm are not present. However, such a procedure would need to be verified by full scale testing of treated drillstring connections.

It is however important to remember that the tests described in this chapter were performed at R = -1, and for the reasons discussed in Section 9.2, would apply to the threads in the box only.

6.11 References:

1 Bai-ping D. and Nian L. (1992) Relation between fatigue threshold and fatigue limit for surface-rolled specimens. *International Journal of Fatigue* 14, 403-409.

2 Kloos K.H., Fuchsbauer B. and Adelmann J. (1987) Fatigue properties of specimens similar to components deep rolled under optimized conditions. *International Journal of Fatigue* 9, 35-42.

7 FE analysis of cold rolling

7.1 Notation

$\sigma_{res,zz}$	longitudinal residual stress [MPa]
F_{zz}	axial force in longitudinal direction [N]
r	radius [mm]
r_1	inner radius [mm]
r_2	outer radius [mm]

7.2 Introduction

The in-depth residual stress distribution at the thread root is impossible to measure by the hole drilling method, and x-ray diffraction would require a large effort in removing material by electro-polishing. Numerical analysis of cold rolling of a thread profile is quite similar to the simulation of the indentation performed in Section 5.8, the result of which was found to agree well with residual stresses measured by the integral hole drilling method. The results from Section 5.8, and the large number of publications on residual stress simulations in the literature, from expanded holes for example, would suggest that similar methods could be applied to the cold rolling process of threaded profiles. However, the rotation that is necessary adds to the complexity of the problem. The only 3D cold rolling simulation found in literature is a work done by Guagliano and Vergani [3]. Based on the results obtained in Section 5.8, the element density used is considered too coarse[25]. The simplification of using a completely rigid roller used in their study was found to give an unacceptable level of error in the study in Chapter 5, as illustrated in Figure 5.28. In addition, when the roller passes a volume of material, the material ahead is not strain-hardened whereas the material beneath and behind is both deformed and strain-hardened. As a result, the assumption of symmetrical boundaries used by Guagliano and Vergani is incorrect for rolling simulations, but correct in indentation studies.

7.3 Rolling distance required for obtaining steady state conditions

When the rolling simulation is only partial, in order to save computational time, the start and stop location represents a boundary between deformed and undeformed material. At these locations the residual stress field will differ from that found at some distance away where rolling has been performed. The residual stress field will gradually become homogeneous in the circumferential direction with increasing distance from the start and stop locations, which is what happens during an actual cold rolling process. A 2D plane strain (CPE4-element) model was used to investigate the

---

[25] 6 * 20 first order elements in the contact area (3 * 10 in the ¼ modelled) and 7 elements over the first 2.5 mm in thickness.

necessary rolling distance to obtain steady state residual stresses uninfluenced by start and stop. From this investigation, a 16° rotation equivalent to 11 mm of the pipe surface was found necessary in order to obtain results in the centre of the rolled area that were independent of start and stop conditions. In the work by Guagliano and Vergani only 1.3 mm of the surface was rolled.

7.4 Roll indentation of threaded profile

The FE mesh was generated in I-DEAS series v. 8.1. Based on the experiences gained from Section 5.8 and Section 7.3, the density of the elements in the contact region were chosen such that the indentation model could also be used for the case of a rotating roller with only minor changes. Element density in the contact area and depth is therefore similar to the optimised model found in Section 5.8.3. The computer processing time was reduced as much as possible by reducing element density with reasonable time consumption for the meshing process in the periphery regions. The finite element model used for the pipe is shown in Figure 7-1.

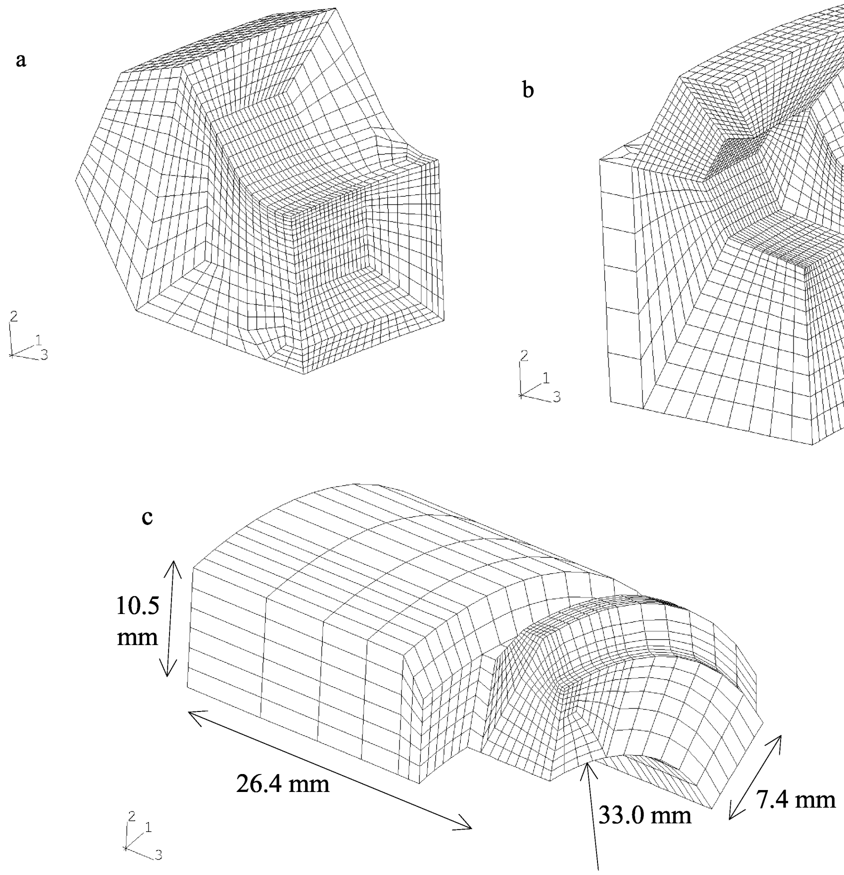

Figure 7-1. Pipe model. Part a) is the sub-structure that fits into the cut-out in b) which fits into the cut-out in c). 1/12 of pipe modelled using symmetry boundary conditions.

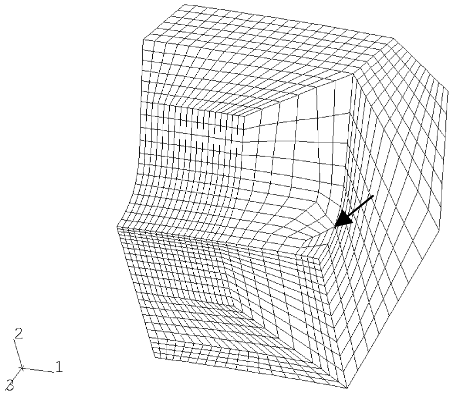

Figure 7-2. High density element area. Tilted. Arrow pointing on distorted element area for cold rolling model.

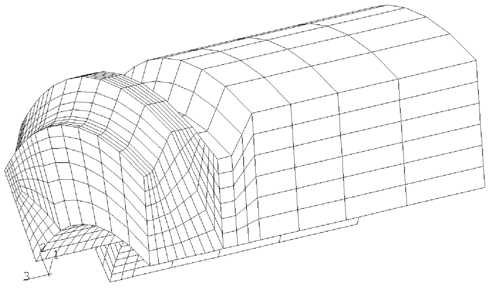

Figure 7-3. FE model. Symmetry boundary view.

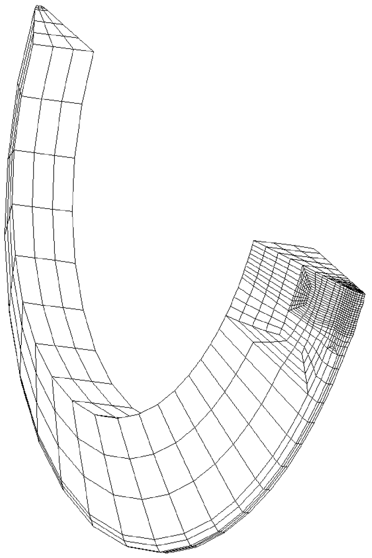

Figure 7-4. Roll mesh. ¼ modelled using symmetry boundary condition. Distributed load on the inner surface.

The element model was exported to Abaqus Standard v. 5.8. The resulting input file was manually edited before running the analysis. The reduced 8-node element formulation with hour-glass control (C3D8R) used in the analysis is recommended for contact problems by HKS, the makers of Abaqus [1, 2].

The AC-95 specimen was modelled with an isotropic hardening material model, the von Mises yield criterion and stain-hardening given in table form for the FE simulation. The roll was modelled with elastic material properties, with no friction between the contact surfaces.

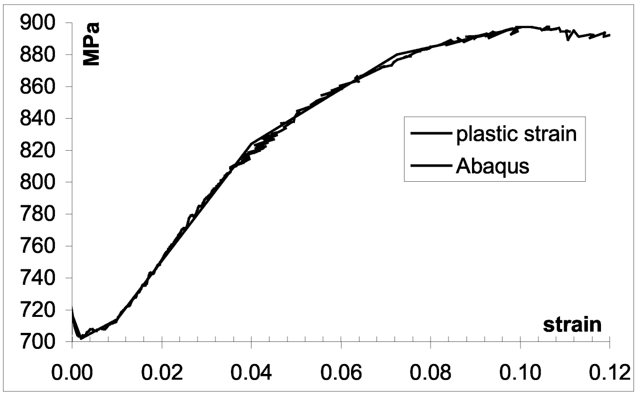

Figure 7-5. Plastic strain from tension test vs plastic strain used in FE simulation.

The number of degrees of freedom was 74991, requiring approximately 60 000 CPU seconds on a modern desktop computer.

The plastic strain at the maximum indentation load is plotted from the centre of indentation through the thickness of the pipe in Figure 7-6 to Figure 7-8, and the resulting longitudinal residual stress presented in Figure 7-9.

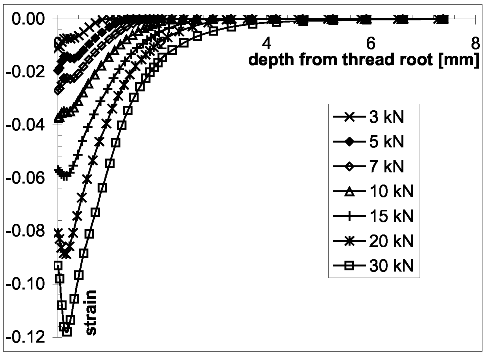

Figure 7-6. Radial plastic strain at the centre of indentation through the thickness, AC-95 specimen.

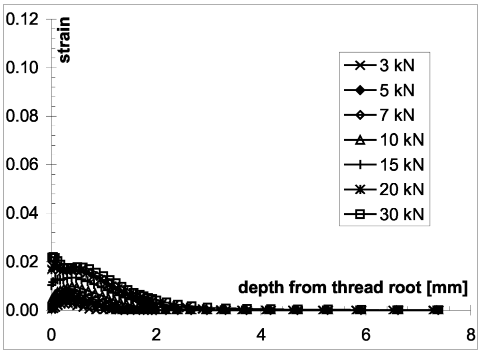

Figure 7-7. Circumferential plastic strain at the centre of indentation through the thickness, AC-95 specimen.

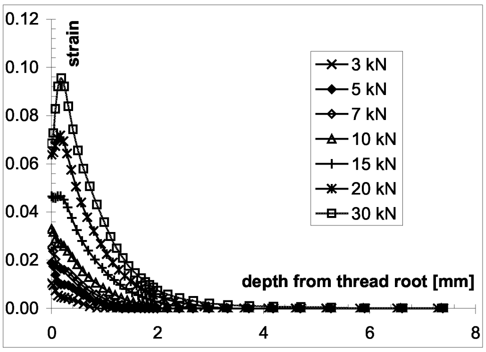

Figure 7-8. Longitudinal plastic strain at the centre of indentation through the thickness, AC-95 specimen.

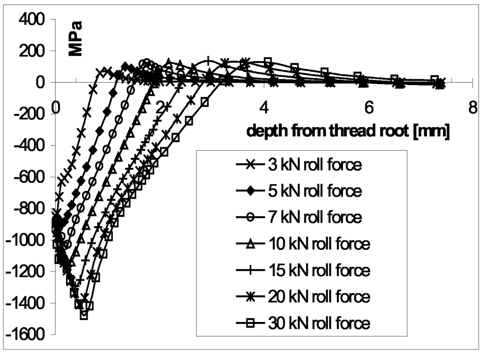

Figure 7-9. Longitudinal residual stress at the centre of indentation through the thickness, AC-95 specimen.

By assuming uniform longitudinal residual stresses circumferentially and integrating the residual stresses in Figure 7-9 as

$$F_{zz} = \int_{0}^{2\pi}\int_{r_1}^{r_2} \sigma_{res,zz} dr d\theta \neq 0 \qquad \text{Equation 7-1}$$

the longitudinal residual stress was found to not be in self equilibrium and hence the longitudinal residual stress presented in Figure 7-9 is not representative for the rolled analysis.

7.5 Rolling of thread profile

By reflecting the elements across the symmetry plane at the centre of the highly dense element area, a 60° arc of the pipe and the whole roll was modelled. By assuming no friction between the contact surfaces, there was no need to rotate the roll (frictionless gliding). A "general multi-point constraint" (MPC) called CYCLSYM [1] was used on the boundaries to circumferentially constrain the pipe, and three rolls spaced 120° apart were modelled. A steady state residual stress was obtained in the contact area by initially rotating the pipe 8° before starting the analysis. However, the element at the arrow in Figure 7-2 was initially too distorted during the effort to reduce the number of degrees of freedom, and the analysis failed when the roll was approaching these elements.

The only solution for this problem was a full remeshing exercise, which would have taken too much time. In addition, the number of degrees of freedom in this analysis was 147 050, which was an insurmountable limiting factor when processing on an SGI Origin 3000 at the national computer centre located at NTNU. The estimated solution time was one month.

7.6 Conclusion

Numerical simulations of cold rolling of threads are extremely difficult to perform. A highly non-linear contact problem with frequent changes in the nodes of contact, and highly non-linear material behaviour, leads to a great number of iterations for each simulation. Keeping the computing time within reasonable limits necessitates a very large effort to decrease the element density outside the contact region where the residual stress is to be obtained. This led to distorted elements, which gives numerical problems particularly with first order elements, however, such element types are strongly recommended by Abaqus for use in contact analyses. Within the time available to this project, remeshing to improve the elements with subsequent additional computing time was not considered cost-effective.

7.7 References:

1 Abaqus (1998) ABAQUS/Standard User's manual. Version 5.8.

2 Abaqus (1998) Concact in ABAQUS/Standard.

3 Guagliano M. and Vergani L. (1995) Residual stresses induced by deep rolling in notched components. In Computer Methods and Experimental Measurements for Surface Treatment Effects II, Sec. int. conf. on computer methods and exp. measurements for surface treatment effects. Edited by Aliabadi M.H. and Terranova A. Computational Mechanics Publications, Southampton, Boston. pp 109-119.

8 Small scale fatigue tension bar with pretension

8.1 Notation

ε_f	true fracture strain = $\ln(A_0/A_f)$
σ	stress [MPa]
σ_f	true fracture stress = F/A_f [N/m^2]
σ_y	yield stress [MPa]
$\Delta\sigma$	nominal stress range = σ_{max} - σ_{min} [MPa]
σ_{max}	maximum cyclic stress [MPa]
σ_{min}	minimum cyclic stress [MPa]
A_0	initial cross-section [m^2]
A_f	cross-section area of fracture [m^2]
F	axial force [N]
K	stress intensity factor [MNm$^{-3/2}$]
ΔK_{eff}	effective stress intensity range = $K_{max} - K_{op}$ [MNm$^{-3/2}$]
$\Delta K_{eff,\ th}$	effective stress intensity threshold [MNm$^{-3/2}$]
K_{max}	stress intensity factor at max load [MNm$^{-3/2}$]
K_{op}	opening stress intensity factor [MNm$^{-3/2}$]
K_t	stress concentration factor
m	slope of SN-curve in log-log scale
d_{min}	notch cross-section diameter [mm]
R	stress ratio = $\sigma_{min}/\sigma_{max}$
R_{notch}	R at the notch surface
$Rp_{0.2}$	0.2 % offset yield stress [MPa]
UTS	ultimate tensile strength = F/A_0[MPa]
W	½ test plate width in crack plane for centre crack specimen [mm]

8.2 Introduction

The FE analysis of cold rolling proved extremely time-consuming, both in terms of computer time and modelling. This was due to the regions with high stress gradients, the use of contact elements, and large plastic strains encountered. Also, an analysis of the growth of short cracks is extremely time costuming due to the fine mesh required.

The use of a 2D-mesh is a practical solution for studying residual stress relaxation and redistribution in the analysis of growth of short cracks. By using axi-symmetric models, the problem of having plane stress at the specimen edges and plane strain in the interior of the specimen is also avoided. An approach to cold rolling is the use of axial loaded notch specimen, which will give a residual stress field with a longitudinal component close to that which is expected from rolling. This will give a small 2D FE model where shallow circumferential cracks are easily incorporated by modelling contact surfaces at the crack mid-plane. Residual stress analyses of prestressed specimens are found in the literature, e.g. [4, 11], where both studies examine crack closure.

8.3 Material and fatigue test specimens

Fatigue test specimens were machined from cylindrical steel bars of 25 mm in diameter. The material was selected to be as close as possible in chemical composition and mechanical properties to the material used in the four-point rotating bending fatigue testes presented in Chapter 6. The steel bars were from four different batches; the chemical composition and mechanical properties are presented in Table 8-1 and Table 8-2. Typical stress strain curves for the material are shown Figure 8-1. The fatigue test specimens are shown in Figure 8-2 and Figure 8-3. The notch surface is in the as-turned condition, and the unnotched specimen is prepared by sandpaper grade 320.

Second order axial-symmetric elements (CAX8R) were used for the stress analysis by Abaqus Standard v. 5.8. The typical element size in the notch region was 0.06 mm. For the test specimen with d_{min} = 14.00 mm, a K_t value (max. notch stress / nominal stress) of 3.09 was found, while d_{min} = 12.00 mm gave K_t = 2.91. K_t for the unnotched specimen was 1.02.

Elements	Bar A	Bar B	Bar C	Bar D
C	0,37	0,37	0,38	0,37
Si	0,27	0,31	0,31	0,31
Mn	0,71	0,64	1,13	1,12
P	0,029	0,009	0,008	0,008
S	0,028	0,026	0,031	0,028
Cr	1,36	1,35	1,48	1,48
Ni	1,38	1,41	1,42	1,42
Al	0,017	0,012	0,017	0,014
Cu	0,20	0,24	0,18	0,18
Mo	0,17	0,16	0,16	0,16
Nb	0,003	0,003	0,003	0,003
V	0,006	0,008	0,005	0,005
Ti	0,003	0,004	0,005	0,005
Co	0,023	0,017	0,019	0,019
B	0,0002	0,0003	0,0002	0,0001
W	0,01	0,01	0,01	0,01
As	0,013	0,010	0,013	0,013
Sn	0,009	0,011	0,008	0,008

Table 8-1. Chemical elements in %.[26]

---

[26] Analysis by optical emission spectrometry (OES)

	Bar A	Bar B	Bar C	Bar D
$Rp_{0.2}$	914 MPa	878 MPa	963 MPa	954 MPa
UTS	1029 MPa	1002 MPa	965 MPa	957 MPa
σ_f	2050 MPa	2140 MPa	1727 MPa	1737 MPa
ε_f	1.06	1.11	0.92	0.93

Table 8-2. Mechanical properties from cylindrical tension bars.

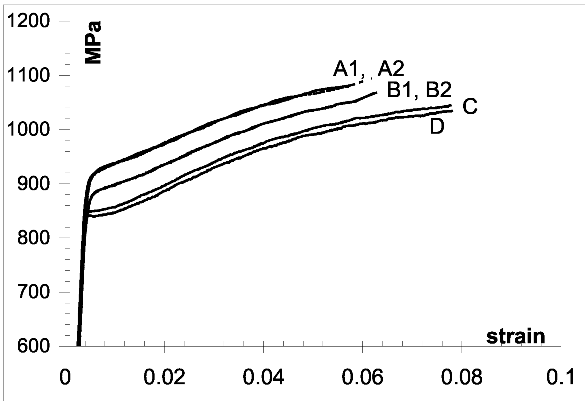

Figure 8-1. True stress – strain curve until necking for four different bars used in the small scale fatigue test specimens.

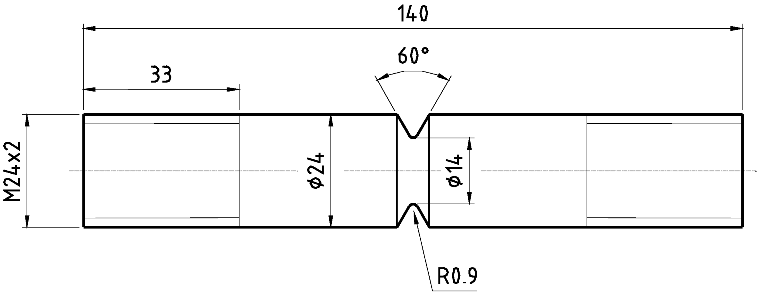

Figure 8-2. Sketch of fatigue tension test specimen with d_{min} = 12.00 or 7.00 mm.

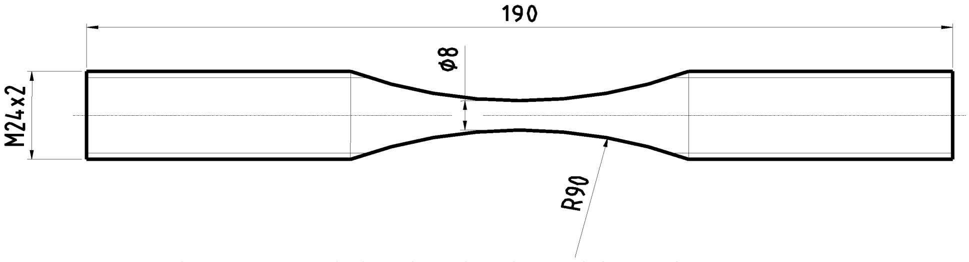

Figure 8-3. Unnotched specimen for reference fatigue testing. K_t = 1.02.

8.4 Test setup

The threaded ends of the specimens were connected to ball-joints. This arrangement was used in the 250 kN servo-hydraulic machine used for pretensioning, and in the 100 kN servo-hydraulic Instron model 1332 test machine used for the fatigue testing. Both machines were equipped with Instron Track 8800 digital control units. The specimens were tested in air under constant amplitude cyclic tension-tension loading. The prestraining was performed with a maximum load hold time of 2 min before unloading. A sinusoidal load-time history at 1 cycle/min was used in dynamic prestraining.

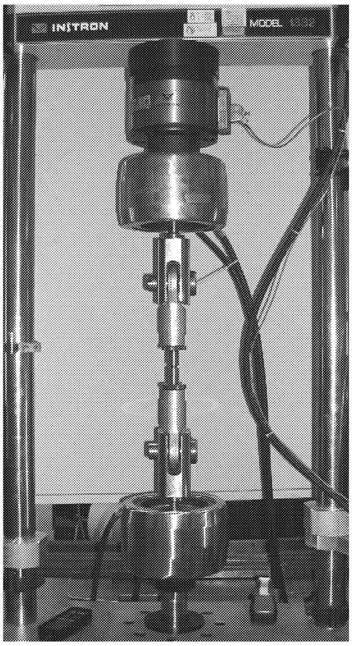

Figure 8-4. 100 kN servo-hydraulic fatigue test rig used.

8.5 Fatigue test results

Pretensioning nominal stress levels from 1200 MPa to 1625 MPa were used. 1625 MPa was the fracture stress for the d_{min} = 14.00 mm specimen from bar C. An increased prestress gives increasing fatigue life in general as indicated in Figure 8-5 to Figure 8-7, similar to the results obtained in the full scale pipe fatigue test (see Figure 6.24 – Figure 6.26). An infinite life is obtained after prestress at 1625 MPa and tested at R = 0.05 in comparison to a fatigue life of approximately 50 000 cycles for no pretensioning, see Figure 8-5. The fatigue life improvement gradually decreases with increasing R-ratio. At R = 0.4 and d_{min} = 12.00 mm no increase was observed, while d_{min} = 14.00 mm gave an improvement similar to the improvement from polishing (see Figure 8-7). At R = 0.6 no increase where observed.

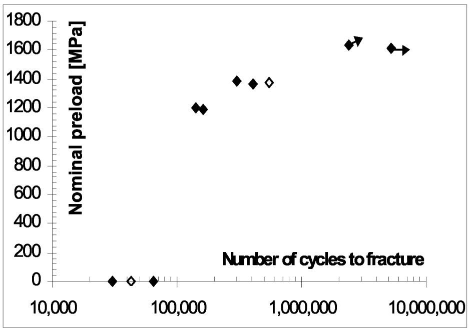

Figure 8-5. Fatigue life increase due to pretensioning. $\Delta\sigma = 430$ MPa, $R = 0.05$. One broke as a result of crack in fixture (marked →) and one runout. $d_{min} = 14.00$ mm. Bar A: filled marks, bar C: open marks

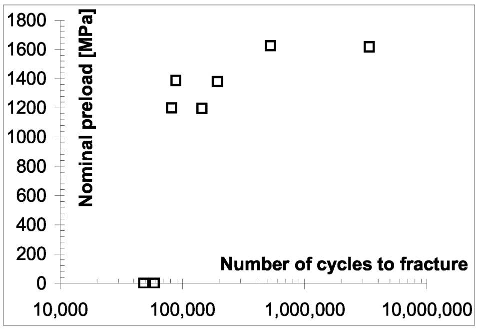

Figure 8-6. Fatigue life increase from pretension. $\Delta\sigma = 400$ MPa, $R = 0.2$, $d_{min} = 14.00$ mm and bar B.

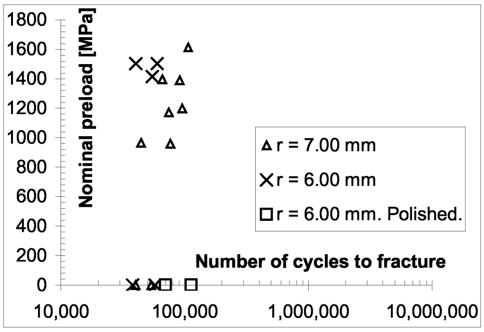

Figure 8-7. Fatigue life increase from pretensioning, $R = 0.4$.
$d_{min} = 12.00$ mm: bar B, $\Delta\sigma = 360$ MPa.
$d_{min} = 14.00$ mm: bar D, $\Delta\sigma = 345$ MPa.

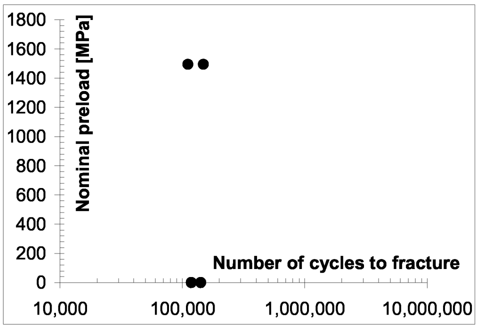

Figure 8-8. No fatigue increase from residual stresses at $R = 0.6$. $\Delta\sigma = 247$ MPa, bar C and $d_{min} = 14.00$ mm.

An interesting observation is the reduced fatigue life from 5 cycles of pretensioning compared to the monotonic pretreatment as seen in Figure 8-9. Unfortunately, two different batches are used, however a lower yield stress will give an increased residual stress depth and hence a prolonged life (see Figure 6-24). As expected, one specimen of bar C with the same monotonic pretensioning as bar A tested at $R = 0.05$ and 1380 MPa nominal pretension resulted in slightly longer fatigue life. Assuming there are no differences in the fatigue life caused by the small difference in material properties (this is then a conservative assumption), the probability of 3 specimens pretensioned by 5 cycles all having fatigue life shorter than the other 5 specimens monotonically prestressed is 1/56. In tests at $R = 0.05$, 40 pretensioning cycles gave an increased life compared to monotonic pretensioning (see Figure 8-9). This is different from tests at $R = 0.2$, as seen in Figure 8-10, which shows no difference. However, firm conclusions cannot be drawn from three test results alone.

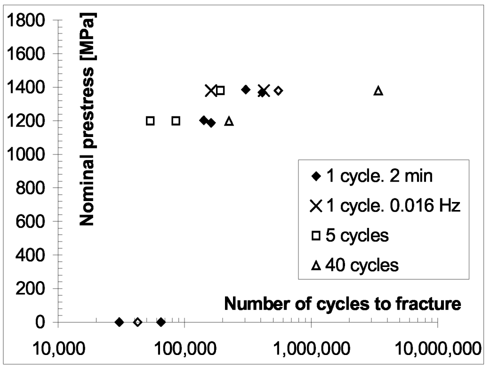

Figure 8-9. Fatigue life increase from repeated overloads. Tested at R = 0.05, Δσ = 430 MPa and d_{min} = 14.00 mm. Bar A: filled marks, bar C: open marks

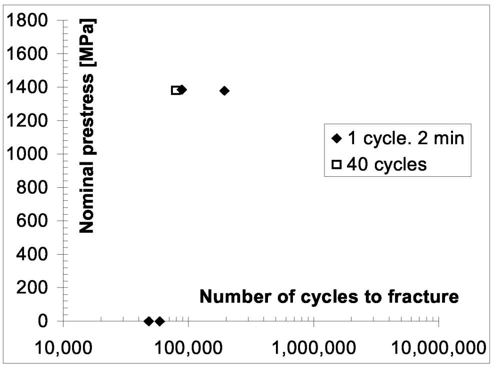

Figure 8-10. Fatigue life increase from repeated overloads. Tested at R = 0.2, Δσ = 360 MPa and d_{min} = 14.00 mm. Bar A: filled marks, bar C: open marks

The possibility of dependency on the max. prestress time was investigated by testing with one and five pretension cycles at one cycle/min (see Figure 8-9). Two specimens with one cycle of prestress supports the theory of prestress time dependency since the mean life of these two is shorter than the mean life of three monotonic prestressed specimens. From these tests and this discussion, the effect of pretension seems to depend on the holding time at max prestress.

The unnotched cylindrical specimens were tested in axial loading at R = 0.05. As seen, the slope of the SN-curve obtained from the three fractured specimens and the run-out at the highest stress level was flat with m = 28 (The number of specimens are not sufficient for a satisfactory statistical analysis). As can be seen, the fatigue limit is approximately 760 MPa nominal stress, giving 775 MPa at the outermost fibre ($K_t = 1.02$) compared to 1330 MPa for notched specimen (Δσ * K_t). Compared to smooth specimens, the improvement from pretension of the notched specimens was clearly evident.

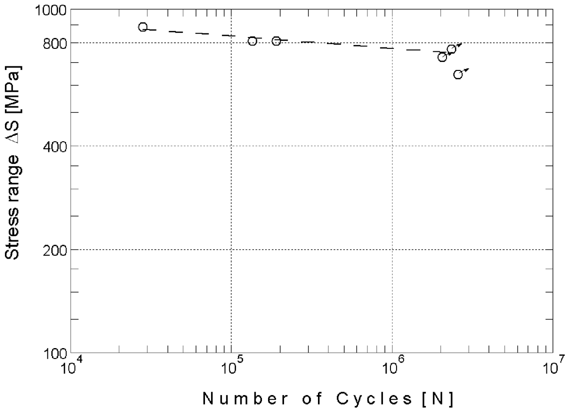

Figure 8-11. Fatigue data from smooth specimen. All test data exceeding 2 000 000 are run-outs. R = 0.05.

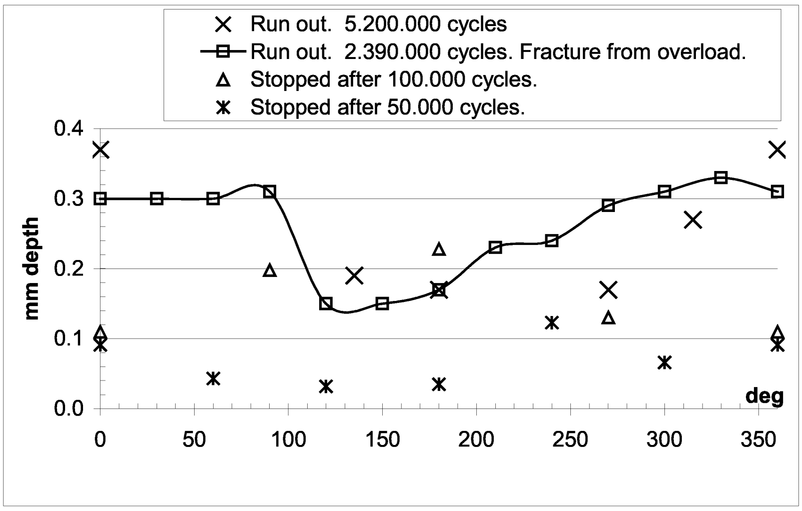

Figure 8-21. Crack depth. Δσ = 430 MPa, R = 0.05, d_{min} = 14.00 mm prestressed at 1625 MPa.

Figure 8-22. Fatigue specimen failed from non-axial loading as a result of crack in fixture after 2 390 000 cycles. Non-propagating crack depths measured at 30° intervals marked with thin white lines in figure and plotted in Figure 8-21.

The average length of non-propagating cracks found in the specimen tested at R = 0.05 and Δσ = 430 MPa, with 40 pretension cycles at 1380 MPa, was 0.40 mm. This result was obtained from 11 measurment points with a standard deviation of 0.06 mm. This is longer than the cracks presented in Figure 8-21.

8.8 Crack growth in a residual stress field

Crack growth in a residual stress field was simulated by first applying prestress in order to introduce residual stresses, before removing the longitudinal boundary condition on the symmetry plane after each second subsequent load-cycle at max-load. The boundary condition was subsequently removed node by node starting at the notch surface[28]. A contact surface at the symmetry plane was used to obtain crack closure. The crack was open at σ_{max} in this model until it reached the crack depth presented in Table 8-4, where after the crack remained completely closed even though the node was not restrained, simulating lack of atomic bonding. The depth of the non-propagating crack as defined herein is that length at which the crack tip is completely closed during the whole cycle, and not the criterion normally used in fracture mechanics calculactions, i.e. $K_{eff} < K_{eff,\, th}$. (See Section 4.11.3.)

From the FE analyses, all except one of the pretensioned specimens at the load ranges investigated should have infinite fatigue life, which contradicts the observations in Figure 8-5 - Figure 8-7. Additionally, the specimen prestressed at 1625 MPa and cycled at $R = 0.05$ and $\Delta\sigma = 430$ MPa should have no crack growth at all, which is also in contradiction to the test results.

Residual stress relaxation is a plausible explanation because this would decrease the crack closing load. FE analyses with monotonic strain hardening and subsequent cyclic stress strain (CSS) softening is very difficult to perform. In addition, the simulation requires strain hardening data from cyclic tests, and these data will depend on prestrain level as well as the magnitudes of R and $\Delta\sigma$ during subsequent cycling. However, assuming elastic-perfect plastic behaviour with $\sigma_y = 885$ MPa, no hardening and tuning of the artificial prestress level to match the residual stress from monotonic hardening (see Figure 8-23), a relatively good match to the observations in Figure 8-5 - Figure 8-7 was achieved. Perfect plasticity with $\sigma_y = 840$ MPa, still without hardening, did not give much difference in the non-propagating crack length.

The choice of a constitutive model for hardening and relaxation can have a major impact on crack closure also without residual stresses present [7].

---

[28] Various crack tip node release scheme was investigated [7] for constant amplitude fatigue test without prestress.

Bar	Prestress [MPa]	R	Crack closed [mm]
A	1200	0.05	0.05
B	1200	0.20	0.14
B	1200	0.40	open
A	1625	0.05	totally closed
B	1625	0.20	0.04
B	1625	0.40	0.17

Table 8-4. Calculated non-propagating crack length where after the crack tip will be kept completely closed during the applied cyclic loading.

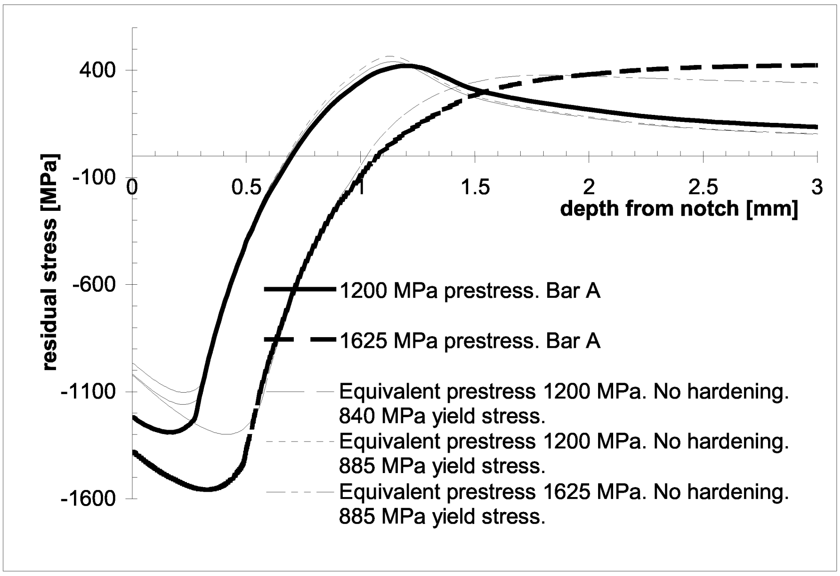

Figure 8-23. Equvalent prestress for bar without hardening simulating residual stress relaxation.

yield stress	Equivalent prestress [MPa]	R	Crack closed [mm]
885	1200	0.05	0.17
840	1200	0.05	0.22
885	1625	0.05	0.17
885	1625	0.20	0.22

Table 8-5. Calculated non-propagating crack length where after the crack will be kept closed during the applied cyclic loading. Material has no hardening.

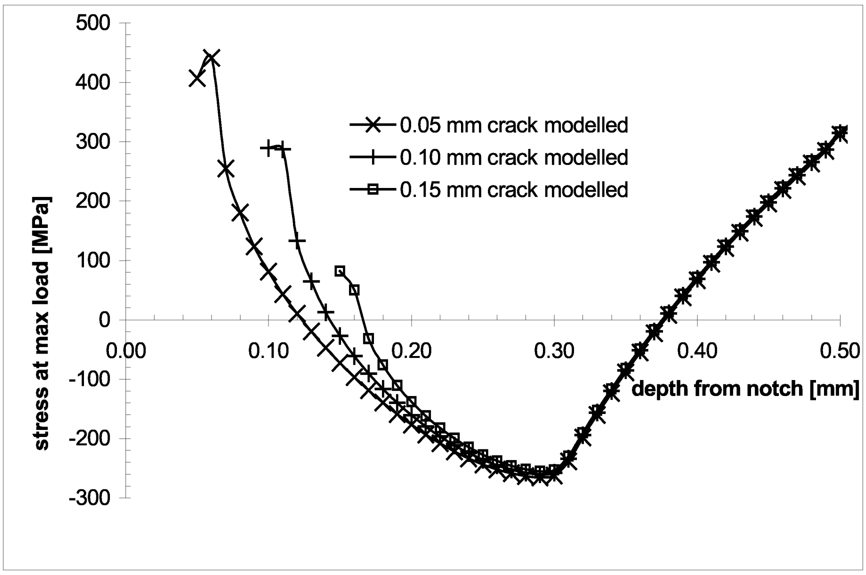

Figure 8-24. Stress at maximum load during cyclic loading with crack modelled. R = 0.05, Δσ = 430 MPa. Equivalent prestress 1200 MPa. Perfect plastic material with 885 MPa yield stress. These specimens fractured during testing.

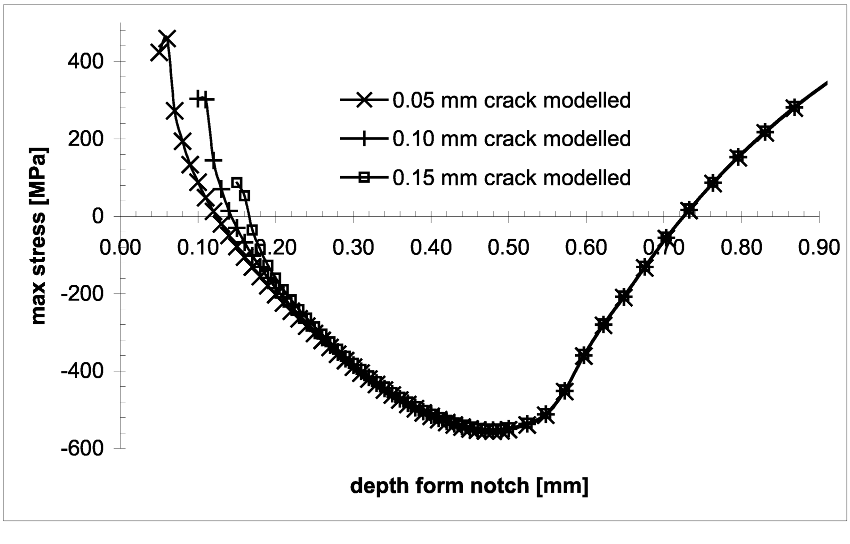

Figure 8-25. Stress at max load during cyclic loading with crack modelled. R = 0.05, Δσ = 430 MPa. Equivalent prestress 1625 MPa. Perfectly plastic material with 885 MPa yield stress.

A small amount of bending stress present will produce an asymmetric crack, which further increases the eccentricity, and might be enough to overcome the crack closing residual stresses in the region 0.17-0.38 mm in Figure 8-24. However, further residual stress relaxation is a more likely cause for the difference between simulation and observations. The case with yield stress at 840 MPa, R = 0.05 and

$\Delta\sigma$ = 430 MPa prestressed equivalently at 1200 MPa gives a maximum load of –192 MPa at 0.3 mm depth compared to -253 MPa where σ_y = 885 MPa.

Below a depth of 0.30 mm, the max stresses in Figure 8-24 and Figure 8-25 are remarkably similar, indicating equal crack growth rates until the non-propagating crack length is reached for the specimens that were prestressed at 1625 MPa.

Using the perfectly plastic model with σ_y = 840 MPa, one simulation was made without prestress and another with the equivalent of 1495 MPa in prestress. Cycling at R = 0.6 and $\Delta\sigma$ = 247 MPa gave R_{notch} = 0.15 and 0.24 respectively for non-prestressed and prestressed specimens, with almost identical stress in front of the crack tip until 0.2 mm crack depth. At greater depths, the difference in simulated crack tip stress was more pronounced as can be seen in Figure 8-26. Numerically both models led to fracture, but with shorter fatigue life for the non-prestressed specimen compared to the prestressed. The fatigue test however gave equal fatigue life (see Figure 8-8). The reason might be that the crack spends the greater part of the fatigue life in the crack initiation and short crack region, where the difference is small between the crack tip stresses in specimens with and without residual stress introduced. In addition, after crack initiation and short crack growth, one crack can easily become dominant and produce a small eccentricity that will increase the local stresses leading to an even faster growing crack.

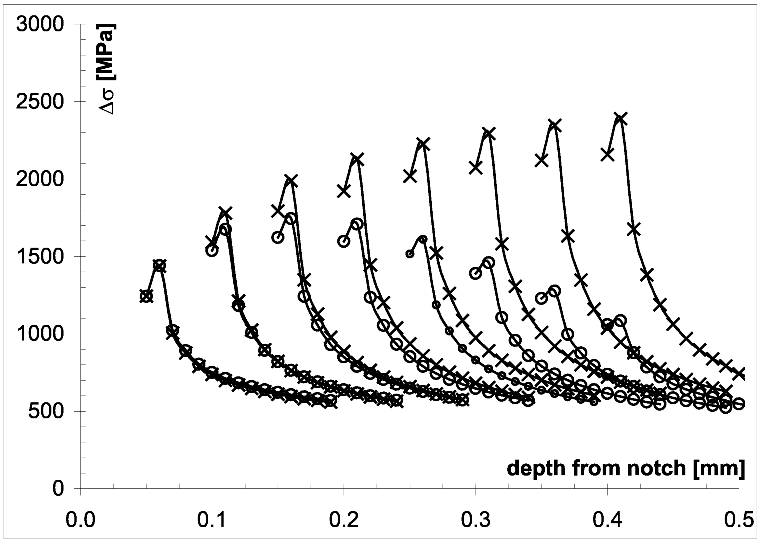

Figure 8-26. Residual stress in front of crack tip at 0.05 mm increments in crack length for non-prestressed (marked x) and prestressed (marked o) model at equivalent 1495 MPa pretension with yield stress 840 MPa (Bar C) cycled at R = 0.6 and $\Delta\sigma$ = 247 MPa.

Moshier and Hillberry [10] investigated a notched 2024-T3 aluminium plate 2.54 mm thick with K_t = 3.17 prestressed at four different levels to introduce compressive residual stresses and tested the plates at R = 0.275 with σ_{max} = 200 MPa. They used a true stress-strain curve from a uniaxial-monotonic tension test, the von Mises yield criterion, isotropic hardening material and Abaqus

Standard to simulate the residual stresses. A life prediction model using a fracture mechanics approach called FASTRAN II, which they modified to incorporate residual stresses (FASTRAN II-R), was used to predict crack growth rate. The predicted growth rate agreed well with the experimentally obtained rate. The predicted fatigue life scatter band was wide, but covered the experimental data. Neither residual stress relaxation nor cyclic stress-strain behaviour was discussed.

8.9 Conclusions

Notched specimens from material similar to the material tested in four-point rotating bending (Chapter 6) were tested in cyclic tension. A remarkably increased fatigue life was observed due to residual stresses after axial preload tested at R = 0.05. However, the increase in fatigue life was gradually reduced with increasing R-ratio, and in the region R = 0.4-0.6, the increase in fatigue life from residual stresses was totally lost in these fatigue tests.

FE analysis showed high hydrostatic residual stresses, giving longitudinal residual stress levels much higher than σ_y. This phenomenon is geometry dependent, and notched thin plates, for instance, will not have hydrostatic residual stresses of the same magnitude. The residual stress lowered the R-ratio at the notch surface. From observations in Chapter 6 and the results reported in this Chapter, the crack initiation period is very short compared with the proportion of life spent in crack propagation when residual stresses are present tested at low values of R. Numerical simulations of fatigue tests at R = -1 indicate a large immediate residual stress relaxation at the surface, with deeper layers still benefiting from the residual stresses.

The residual stress level derived from FE analysis with monotonic strain hardening material behaviour did not predict crack growth in cases where crack growth was observed in tests. Eccentricities in the axial fatigue test will introduce bending moments, and increase the crack growth rate locally. This will further increase the eccentricity and the actual fluctuating stress at the crack tip will be higher than that predicted in the symmetric FE model. This will increase the non-propagating crack depth locally. This phenomenon was evident in the fracture surfaces as variable crack depth. However, this effect was not sufficient to explain the difference between experimental observations and FE analysis. Assuming that the maximum compressive residual stress level at the notch is relaxed by cycling to a level similar to the initial yield stress (the effect of hardening is totally removed), relatively good agreement was found between the observed non-propagating crack length and the crack length at which the crack remained closed during cycling in the FE analysis. In addition, the residual stress did not relax due to crack growth. This proves that the residual stress is relaxed close to the level where no effect of hardening is observed, or lower.

From the fatigue tests performed in this work, the residual stress depends on time at max. prestress. It is not clear from these tests, however, whether the number of prestress cycles also influences the residual stress level. This effect is expected as long as the material exhibits cyclic hardening, as discussed in Chapter 4.

From the fact that no increase in fatigue life tested at R = 0.6 after pretensioning was observed for notched specimens, strain hardening by itself is unlikely to influence the fatigue life significantly; this is also in agreement with the literature referred to in Section 4.12. Additionally, the benefit from the small difference in local R_{nocth}-ratio discussed in Section 8.6 seems insignificant. FE analysis of crack tip stresses in pretensioned specimens, fatigue cycled at R = 0.6, were similar to non-pretensioned crack tip stresses to a depth of 0.2 mm, after which the crack tip stress was reduced by residual stresses for the prestressed specimen.

When comparing observations with results from the literature, it is important to keep in mind the triaxial nature of the residual stresses in these specimens, and also the triaxiality of the cyclic stress local to the notch during fatigue testing of these notched specimens. Stress biaxiality is reported to have an effect on closure behaviour [7, 8, 12].

The material modelling problems discussed above are in addition to the problems related to crack closure without any residual stress present that were discussed in Section 4.8.

8.10 References:

1 Abaqus (1998) ABAQUS/Standard User's manual. Version 5.8.

2 Banks-Sills L., Dagani E., Eliasi R., Reinberg E. and Schwartzman R. (1994) Analysis and testing of surface cold-work procedures applied to notched, flat elements. *Fatigue Fract Engng Mater Struct* 17, 1371-1381.

3 Holm D.K., Blom A.F. and Suresh S. (1986) Growth of cracks under far-field cyclic compressive loads: numerical and experimental results. *Engineering Fracture Mechanics* 23, 1097-1106.

4 Leitao V.M.A., Aliabadi M.H., Rooke D.P. and Cook R. (1998) Boundary element methods for the analysis of crack growth in the presence of residual stress fields. *Journal of Materials Engineering and Performance* 7, 352-360.

5 McClung R.C. (1991) Crack closure and plastic zone sizes in fatigue. *Fatigue Fract Engng Mater Struct* 14, 455-468.

6 McClung R.C. (1991) The influence of applied stress, crack length, and stress intensity factor on crack closure. *Metallurgical Transaction A* 22A, 1559-1571.

7 McClung R.C. and Sehitoglu H. (1989) On the finite element analysis of fatigue crack closure - 1. Basic modeling issues. *Engineering Fracture Mechanics* 33, 237-252.

8 McClung R.C. and Sehitoglu H. (1989) On the finite element analysis of fatigue crack closure - 2.Numerical results. *Engineering Fracture Mechanics* 33, 253-272.

9 McClung R.C., Thacker B.H. and Roy S. (1991) Finite element visualization of fatigue crack closure in plane stress and plane strain. *International Journal of Fracture* 50, 27-49.

10 Meshii M., Shetty D.K. and Ochiai Y. (1974) Cyclic creep of metals. In Mechanical behavior of materials, Proceeding of the 1974 Symposium on Mechanical Behavior of Materials. The Society of Materials Science.

11 Moshier M.A. and Hillberry B.M. (1999) The inclusion of compressive residual stress effects in crack growth modelling. *Fatigue Fract Engng Mater Struct* 22, 519-526.

12 Riemelmoser F.O., Gumbsch P. and Pippan R. (2000) Plastic deformation at short edge cracks under fatigue loading. *Engineering Fracture Mechanics* 66, 357-374.

13 Riemelmoser F.O., Gumbsch P. and Pippan R. (2001) Dislocation modelling of fatigue cracks: An overview. *Materials Transactions* 42, 2-13.

14 Riemelmoser F.O. and Pippan R. (1999) On the ΔK_{eff} concept: An investigation by means of a discrete dislocation model. In Advances in fatigue crack closure measurement and analysis. Edited by McClung R.C. and Newman J.C. ASTM. pp 1-13.

URN:NBN:no-2334

9 General discussion, conclusions and recommendations for further work

9.1 Notation

CT	compact tension
FE	finite element
LET	last engaged thread
R	stress ratio = $\sigma_{max} / \sigma_{min}$

9.2 Discussion of cold-rolling effects on drillstring threaded connections

Fatigue improvement from cold rolling is due to three effects: strain hardening; surface polishing; and residual stresses.

Notched axi-symmetric specimens fatigue tested at $R = 0.6$ with fatigue failure at 130 000 cycles showed no effect on fatigue life from residual stress or strain hardening after pretension (see Figure 9-1). In the literature small benefits from strain hardening of smooth specimens are often reported, but this could possibly be caused by residual stress present in the specimen after pretensioning and fatigue testing at low R-ratios.

Cold rolling of threads introduces high residual stresses and a significant amount of strain hardening at the thread root. The make-up torque used on threaded drillstring connections gives a nominal locked-in stress equivalent to approximately 60% of yield at the most critical cross-section of the pin or box [1]. The SCF of the pin last engaged thread (LET, see Figure 1-4) is around 4 depending on the drillstring element geometry [2]. The local pin root mean stress at the LET will be very high from the make-up torque, hence no fatigue improvement is expected from residual stress. Neither strain hardening nor residual stress improved the fatigue life for the notched specimens tested at $R = 0.6$. Only low mean stresses caused by the make-up torque are present at the box LET, and a highly significant improvement from the cold rolling residual stress is likely to take place, as discussed in Chapter 6 and 8.

The pretensioning of notched specimens discussed in Chapter 8 will not however give rise to any benefit from surface polishing. Even though no fatigue improvement was found for the notched specimen tested at $R = 0.6$, the polishing effect from cold rolling will prolong the fatigue initiation life, as seen for the cold rolled specimen discussed in Chapter 6 for both the pin LET and the box LET.

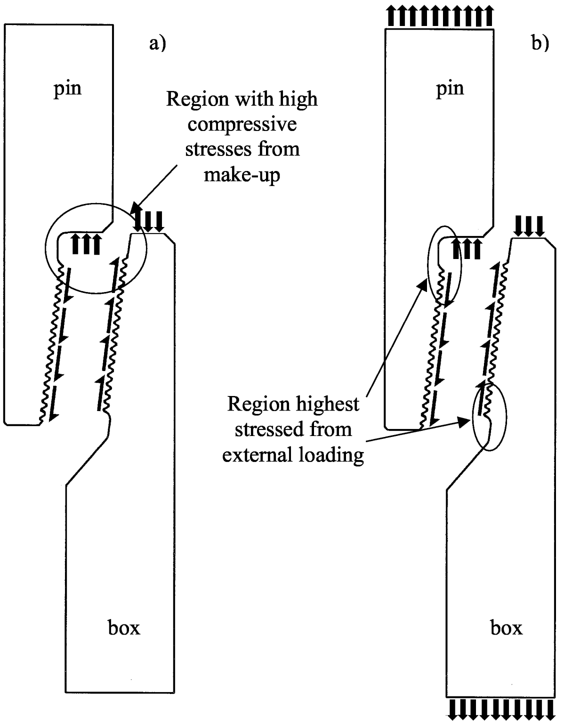

Figure 9-1. Load distribution from a) make-up and b) make-up and external loading.

The materials used in the fatigue tests in the present work were either taken from drillpipes, or had chemical composition and mechanical properties close to drillstring material.

9.3 Conclusions

Generally, non-linear material properties need be to used in FE simulations of cold rolling. Non-linear material behaviour and contacting surfaces make cold rolling simulations highly non-linear and very time consuming. In addition, symmetry must be used with great care for non-symmetric conditions in the rolling plane (no residual stresses and strain hardening in front of the roll). Cold rolling simulations of threaded connections require a 3D simulation and a very high density of elements adjacent to the contact area. In order to obtain residual stresses not influenced by start/stop, a surface rolling length of 11 mm was necessary. A relatively high element density was also required with the contact algorithm used in Abaqus v. 5.8. Employing rigid rolls reduced the problem size but gave significantly higher values of residual stresses, and hence were not utilized further. A time consuming modelling effort aiming to minimise the number of degrees-of-freedom resulted in distorted elements, which caused the cold rolling simulation to fail. Cold rolling analyses of notches with sufficient accuracy for research purposes are extremely time consuming, even on high-capacity work-stations or mainframe computer facilities available today, if numerical problems during the solution are to be avoided.

Most of the FE problems associated with cold rolling were avoided by using a 2D axi-symmetric model of a notched specimen, prestressed to introduce residual stresses, and the solution time was acceptable. Prestressing of notched steel specimens with similar chemical composition and mechanical properties as typical drillstring components, gave an improvement in fatigue life from approximately 50 000 cycles to infinite life, a highly significant improvement. Following fatigue testing, a few run-out specimens were sectioned longitudinally. The cross-section was polished and examined in an optical microscope. Non-propagating cracks approximately 0.4 mm deep were found. By fatigue testing and sectioning equally prestressed specimens where the fatigue testing had been prematurely stopped after different numbers of fatigue cycles, the fatigue cracks were found to have initiated early, and to have propagated at a decreasing rate until final arrest. This is in agreement with observations reported in the literature. FE simulations with a crack did not support the observation of non-propagating cracks, as the entire load cycle at the crack was compressive (from residual stresses). However, when the initial residual stress after pretension was relaxed to a level where no strain hardening remained in the material, good agreement between the FE simulations and observations was found. This observation is in agreement with results for strain hardened steel found in the literature where a rapid and almost instant relaxation to a certain level of residual stress is found when fatigue life to failure is of the order of 10 000 cycles. In addition, the prestrains used in this work are of a level where wavy-slip metals exhibit a history dependency similar to planar-slip metals. This means that the results in this work should be equally valid for stainless steel drillstring components.

The benefit obtained from holding the maximum load constant for two minutes, compared with a cyclic preload at one cycle/min, is important since cold rolling of threads must be done at a determined speed for quality control of the process. With subsequent preload cycles, further cyclic strain hardening and increased residual stress is expected. However, at five preload cycles applied at one cycle/min, fatigue improvement was less than for one cycle held for 2 min. at max. preload. At 40 cycles a significant improvement was observed. More tests are necessary to obtain a more sound statistical basis for these observations.

For proper FE simulations of cold rolling and subsequent fatigue loading, a very complex material routine must be used where important features such as additional strain hardening from cyclic preload, time dependency at max. preload and cyclic softening from fatigue loading is incorporated. Such a material model requires a series of material tests with various amounts and numbers of pretensions, various cyclic stress amplitudes and frequencies, and also most likely different R-ratios. As long as the relaxation is not properly modelled, crack closure is not correctly calculated, as demonstrated, and fracture mechanics models are of limited use for calculating fatigue improvement caused by residual stresses.

Significant improvement in fatigue strength from cold rolling was found in four-point rotating bending tests on drillstring pipes with thread profiles. Unfortunately, with properly cold rolled threads, cracks would initiate from pitting on the inside surface of the pipe. The corresponding S-N curve for these points had a steeper slope in the S-N diagram than the curve representing cold rolled threads. Therefore, to study the maximum benefit from cold rolling in this study, fatigue loading was used that gave lives of the order of 20 000 cycles for unrolled specimens and some 100 000 cycles for rolled specimens, where crack initiation occurred on the inside pipe surface. The fatigue initiation period was increased, but the major portion of the increased fatigue life after rolling was provided due to slower crack propagation. In fact, 90% of the fatigue life to failure from cracks initiated at pitting inside the pipe was with cracks present at the thread root. This is in good agreement with the results obtained from notched small scale axially-loaded specimens.

Both the axially-loaded, notched and pretensioned specimens, and the rolled specimens, showed increases in fatigue life with increased cold working. It was not possible to determine optimised fatigue conditions for the two types of specimen. The axially-loaded specimen was prestrained close to fracture and hence no further increase in residual stress was possible. However, self-balancing stress analysis showed that this level of residual stress was close to the theoretical maximum. The rolled specimen fractured from cracks initiating from pits inside the pipe, hence, further increases in fatigue life from increased roller force was impossible. Moreover, it was not possible to determine the optimised roll geometry for the same reason. However, a roller with the same radius as the thread profile gave significantly higher improvement at a lower roll force than an oversized roll, and this geometry is therefore recommended, since this minimises the possibility of deforming the thread helix beyond acceptable limits. Based on these experiments, a roller force of around 20 kN is recommended.

Re-rolling after crack initiation increased the fatigue life significantly. The major advantage from this observation is the possibility of treating initially unrolled drillstring connections already used in service after crack inspection (where small cracks might remain undetected) without harming the connection due to cold rolling.

As described in the literature, the fatigue improvement from residual stress was highly dependent on R-ratio. A continuously decreasing level of fatigue improvement was obtained with increasing R-ratio until $R = 0.6$, whereupon the benefit was completely lost. In addition, the observation of no benefit from pretension at $R = 0.6$ (where crack closure from residual stress is not contributing) strongly indicates that there was no fatigue benefit from strain hardening. Hence, as stated in Section 9.2, residual stress will not increase the fatigue performance of the pin LET, and a moderate increase in fatigue life from the cold rolling process is expected for the cold-rolled pin LET and pin stress relief groove due to the polishing effect.

A significant increase in fatigue life is expected for drillstring components where the fatigue crack initiates at the box LET. However, is very important to bear in mind the adverse effect from compressive overloads, which cause local yielding and remove, or even introduce damaging, tensile residual stresses. From FE analysis it is evident that cycling the notched axial loaded specimen at $R = -1$ immediately reduces the compressive residual stresses at the notched surface by 70%, but the residual stresses remain at deeper layers supporting the significant improvement obtained for the cold-rolled rotating bending pipe specimens.

The use of residual stress measurements of surface layers at the pin LET and stress relieve groove sites during service is not recommended as a means of tracking residual stress relaxation. The surface residual stress is expected only to give a minor increase in fatigue life, due to the high mean stress from the make-up torque. An immediate and large relaxation of residual stresses in the surface layer of the thread root is also likely to occur in the bottom hole assembly (BHA) box LET during severe bending loads, e.g. caused by dog-legs. However, due to the protective action of deeper layers in compression, any fatigue cracks that may initiate will experience arrest or a significantly reduced rate of crack growth.

Finite element analyses of residual stresses after cold working are presently widely used. During verification of residual stresses by hole drilling, two significant errors were found in Restran v. 3.3.2a distributed by HBM, which is the latest version of the only commercial available non-uniform residual stress evaluation software for hole drilling measurements. Very good agreement between FE simulation and experimental measurement was found by using in-house routines developed for Matlab.

9.4 Recommendations for further work

The main benefit from cold rolling of the pin LET appears to be due to improved surface condition and, possibly, strain hardening. Therefore full scale testing of threaded connections is recommended to investigate the cost-benefit that could be obtained from cold rolling. With the fatigue improvement of the box LET, crack initiation and growth at another location is likely. However, the stress-strain behaviour of a drillstring connection is difficult to model due to the transient strain hardening effect and hence changes in the make-up stresses and relaxation of residual stresses introduced by thread rolling. Since full scale testing is expensive and the results difficult to interpret, cold rolling of small scale tests should be used to obtain a better understanding of the various factors that influence the fatigue life of threaded connections under service loading

In order to fully understand and model the behaviour of fatigue crack initiation and growth in residual stress fields, tests could be made on specimens with cold expanded holes or prestrained CT-specimens, in order to introduce residual stresses in a material that does not strain harden either monotonically or in cyclic tests. Crack growth is easily measurable in cold expanded holes and CT-specimens, in contrast to the notched specimens used in this study. In addition, crack opening/closing could be measured with necessary attention to the problems involved with such measurements. X-ray diffraction measurements of residual stress adjacent to the crack tip would be very useful to verify and calibrate the numerical model.

The next step would be to use a material that hardens monotonically. A detailed study needs to be performed to determine the necessary cyclic stress-strain material parameters and strain rate dependency. The material model should be incorporated in a FE program and used on a cold expanded hole or CT-specimen in a numerical and experimental study for verification purposes, as described above.

The effect of surface improvement, or the polishing effect due to rolling, needs to be investigated further before being incorporated into a fatigue improvement model. Furthermore, more tests should be performed in order to form a firmer statistical basis for the observation that strain hardening does not contribute to fatigue improvement.

9.5 References:

1 American Petroleum Institute (1997) API specification 7, 39'th edition. Specification for Rotary Drill Stem Elements.

2 Macdonald K.A. (1996) Fatigue of drillstring threaded connections. PhD Thesis, Aberdeen University

URN:NBN:no-2334

10 Appendix A: Full scale fatigue test data.

Pipe ID	Rolling load [kN]	Roller radius [mm]	RPM	Nominal stress amp. [MPa]	No of cycles	Comments
AC-01-1	10	1.05	180	382	80,686	
AC-01-4			180	185	293,000	
AC-02-2	5	0.96	180	351	132,179	
AC-02-4	10	1.05	180	355	128,715	
AC-03-2	20	0.96	180	279	307,200	Fracture from pit.
AC-03-3			180	241	69,268	
AC-03-4	7	1.05	180	350	103,768	
AC-04-2	5	0.96	180	358	126,000	
AC-04-4			180	247	87,464	
AC-05-2			180	212	239,000	
AC-05-4	7	0.96	180	383	207,425	
AC-06-2	3	0.96	180	364	29,678	
AC-06-3			180	155	957,258	
AC-06-4	10	0.96	180	363	237,000	Fracture from pit.
AC-07-1	10	1.05	180	348	203,890	Fracture from pit.
AC-07-2			180	217	209,300	
AC-07-3	7	1.05	180	352	105,765	
AC-07-4			180	145	2,815,000	Run out.
AC-08-1			180	239	100,850	
AC-08-3	20	0.96	180	274	380,100	Fracture from pit.
AC-08-4	10	0.96	180	379	215,310	Fracture from pit.
AC-09-1			120	364	17,000	
AC-09-4			180	173	471,515	
AC-10-2			180	359	19,077	
AC-10-3			180	161	658,000	
AC-11-1			180	180	431,500	
AC-11-3			180	278	54,800	
AC-11-4	3	1.05	180	368	21,640	
P-01-1	3	0.96	180	351	45,290	
P-01-2	30	0.96	180	200	2,003,370	Distorted helix. Run out.
P-01-2-2	30	0.96	180	263	341,000	Fracture from pit.
P-01-4			180	188	528,200	
P-02-1			180	159	2,557,000	Run out.
P-02-1-2			180	228	114,800	
P-02-2	5	0.96	180	361	125,250	Re-rolled after 25,900 cycles.
P-02-3	20	0.96	180	276	331,100	Fracture from pit.
P-02-4			180	345	21,536	
P-03-1			180	284	29,481	
P-03-2			180	368	16,155	
P-03-4	20	0.96	180	298	168,630	Fracture from pit.
P-04-1	5	0.96	180	375	41,800	
P-04-3	5	0.96	180	366	103,570	Re-rolled after 25,900 cycles.
P-04-4			239	172	650,590	
P-05-1	10	0.96	150	270	400,700	Fracture from pit.

P-05-2	3	0.96	180	366	33,121	
P-05-3			150	171	273,062	
P-06-2			120	191	466,776	
P-06-3	10	0.96	180	278	1,038,540	Fracture from pit.
P-06-4	3	0.96	180	366	28,228	
P-07-1	7	0.96	180	339	316,820	Fracture from pit.
P-07-2			180	349	17,630	
P-07-4			180	227	134,707	
P-08-4	8	0.96	180	361	113,940	Fracture from pit.
P-09-1	8	0.96	180	360	370,800	Fracture from pit.
P-09-3	20	0.96	180	272	196,670	Fracture from pit.
P-09-4			103	272	53,658	
P-10-1	30	0.96	180	262	331,100	Fracture from pit.
P-10-3	7	0.96	180	365	176,070	
P-10-4			120	239	128,650	
P-11-3	7	0.96	180	372	112,300	
P-12-1	5	0.96	180	365	64,820	
P-12-3			120	253	95,260	
P-13-1			180	247	92,200	
P-13-2	5	0.96	180	372	48,696	
P-13-3			180	188	332,600	
P-14-2			180	281	32,788	

11 Appendix B: Small scale fatigue tension bar test data.

Monotonic preload held at max load for 2 min. Cyclic preload with one minute sinusoidal wave length.

Serie ID		Preload		Test d.	Freq	$\Delta\sigma$	R-ratio	No. of	Comments
		[kN]	No. cycles	[mm]	Hz.	[MPa]		cycles	
A	1			14	15	380	0.05	1,704,115	Run out.
A	3	185	Monotonic	14	15	430	0.05	141,538	
A	4			14	15	430	0.05	64,910	
A	5	251	Monotonic	14	15	430	0.05	2,390,970	Fractured in fixture.
A	7			14	15	430	0.05	30,424	
A	8	211	Monotonic	14	15	430	0.05	411,193	
A	9	183	Monotonic	14	15	430	0.05	162,379	
A	11	248	Monotonic	14	15	430	0.05	5,212,432	Run out.
A	12	213	Monotonic	14	15	430	0.05	304,496	
B	1	148	Monotonic	14	15	359	0.40	76,483	
B	2	250	Monotonic	14	15	400	0.20	525,104	
B	3	185	Monotonic	14	15	400	0.20	81,613	
B	4			14	15	260	0.40	1,633,860	
B	5	215	Monotonic	14	15	359	0.40	65,931	
B	6	213	Monotonic	14	15	400	0.20	88,685	
B	7	214	Monotonic	14	15	359	0.40	91,199	
B	8			14	15	322	0.40	73,675	
B	9			14	15	400	0.20	59,053	
B	10	181	Monotonic	14	15	359	0.40	74,220	
B	11	248	Monotonic	14	15	359	0.40	106,797	
B	12			14	15	240	0.40	3,500,000	Run out.
B	13			14	15	307	0.40	92,312	
B	14	185	Monotonic	14	15	359	0.40	95,426	
B	15			14	15	292	0.40	417,422	
B	16			14	15	359	0.40	39,966	
B	17	249	Monotonic	14	15	400	0.20	3,375,250	
B	18			14	15	359	0.40	53,615	
B	19	149	Monotonic	14	15	359	0.40	44,425	
B	20			14	15	386	0.40	29,815	
B	21	184	Monotonic	14	15	400	0.20	144,720	
B	22			14	15	400	0.20	48,237	
B	23			14	15	380	0.20	91,669	
B	25			14	15	260	0.40	98,357	
B	26	212	Monotonic	14	15	400	0.20	194,005	
B	27			14	15	413	0.20	28,345	
B	28			14	15	278	0.40	175,053	
C	2	213	40 cycles	14	15	430	0.05	3,407,884	
C	3	213	40 cycles	14	15	400	0.20	79,557	
C	4			14	15	430	0.05	42,360	
C	5	213	Monotonic	14	15	430	0.05	549,343	
C	6	185	5 cycles	14	15	430	0.05	53,499	
C	7	185	5 cycles	14	15	430	0.05	85,497	

C	8			14	10	247	0.60	141,981	
C	9			14	10	247	0.60	118,588	
C	10	230	Monotonic	14	10	247	0.60	148,783	
C	11	230	Monotonic	14	15	247	0.60	111,188	
C	12	185	40 cycles	14	15	430	0.05	224,089	
C	13	213	5 cycles	14	15	430	0.05	191,990	
C	15	213	1 cycle	14	15	430	0.05	422,874	
C	16	213	1 cycle	14	15	430	0.05	161,823	
D	1			12	15	380	0.40	37,007	
D	2			12	15	399	0.40	46,884	
D	3			12	15	360	0.40	28,741	
D	4			12	15	340	0.40	67,319	
D	5			12	15	350	0.40	37,115	
D	6			12	15	345	0.40	57,486	
D	7	160	Monotonic	12	15	345	0.40	54,776	
D	10	170	Monotonic	12	15	345	0.40	40,254	
D	11	170	Monotonic	12	15	345	0.40	59,980	
D	12			12	15	345	0.40	37,970	
D	13			12	15	345	0.40	69,735	Polished
D	14			12	15	345	0.40	112,441	Polished

12 Appendix C: Small scale fatigue tension bar test data, reference test on unnotched specimen.

Serie ID	Test d. [mm]	Freq Hz.	$\Delta\sigma$ [MPa]	R-ratio	No. of cycles	Comments
C 21	8	15	807	0.05	189,819	
C 22	8	15	645	0.05	2,557,030	Run out
C 23	8	15	724	0.05	2,041,659	Run out
C 22	8	15	807	0.05	135,079	
C 23	8	15	887	0.05	28,107	
C 24	8	15	764	0.05	2,332,483	Run out

URN:NBN:no-2334

DEPARTMENT OF STRUCTURAL ENGINEERING
NORWEGIAN UNIVERSITY OF SCIENCE AND TECHNOLOGY

N–7491 TRONDHEIM, NORWAY
Telephone: +47 73 59 47 00 Telefax: +47 73 59 47 01

"Reliability Analysis of Structural Systems using Nonlinear Finite Element Methods",
C. A. Holm, 1990:23, ISBN 82-7119-178-0.

"Uniform Stratified Flow Interaction with a Submerged Horizontal Cylinder",
Ø. Arntsen, 1990:32, ISBN 82-7119-188-8.

"Large Displacement Analysis of Flexible and Rigid Systems Considering Displacement-Dependent Loads and Nonlinear Constraints", K. M. Mathisen, 1990:33, ISBN 82-7119-189-6.

"Solid Mechanics and Material Models including Large Deformations",
E. Levold, 1990:56, ISBN 82-7119-214-0, ISSN 0802-3271.

"Inelastic Deformation Capacity of Flexurally-Loaded Aluminium Alloy Structures",
T. Welo, 1990:62, ISBN 82-7119-220-5, ISSN 0802-3271.

"Visualization of Results from Mechanical Engineering Analysis",
K. Aamnes, 1990:63, ISBN 82-7119-221-3, ISSN 0802-3271.

"Object-Oriented Product Modeling for Structural Design",
S. I. Dale, 1991:6, ISBN 82-7119-258-2, ISSN 0802-3271.

"Parallel Techniques for Solving Finite Element Problems on Transputer Networks",
T. H. Hansen, 1991:19, ISBN 82-7119-273-6, ISSN 0802-3271.

"Statistical Description and Estimation of Ocean Drift Ice Environments",
R. Korsnes, 1991:24, ISBN 82-7119-278-7, ISSN 0802-3271.

"Turbidity Current Modelling",
B. Brørs, 1991:38, ISBN 82-7119-293-0, ISSN 0802-3271.

"Zero-Slump Concrete: Rheology, Degree of Compaction and Strength. Effects of Fillers as Part Cement-Replacement",
C. Sørensen, 1992:8, ISBN 82-7119-357-0, ISSN 0802-3271.

"Nonlinear Analysis of Reinforced Concrete Structures Exposed to Transient Loading",
K. V. Høiseth, 1992:15, ISBN 82-7119-364-3, ISSN 0802-3271.

URN:NBN:no-2334

"Finite Element Formulations and Solution Algorithms for Buckling and Collapse Analysis of Thin Shells", R. O. Bjærum, 1992:30, ISBN 82-7119-380-5, ISSN 0802-3271.

"Response Statistics of Nonlinear Dynamic Systems",
J. M. Johnsen, 1992:42, ISBN 82-7119-393-7, ISSN 0802-3271.

"Digital Models in Engineering. A Study on why and how engineers build and operate digital models for decisison support", J. Høyte, 1992:75, ISBN 82-7119-429-1, ISSN 0802-3271.

"Sparse Solution of Finite Element Equations",
A. C. Damhaug, 1992:76, ISBN 82-7119-430-5, ISSN 0802-3271.

"Some Aspects of Floating Ice Related to Sea Surface Operations in the Barents Sea",
S. Løset, 1992:95, ISBN 82-7119-452-6, ISSN 0802-3271.

"Modelling of Cyclic Plasticity with Application to Steel and Aluminium Structures",
O. S. Hopperstad, 1993:7, ISBN 82-7119-461-5, ISSN 0802-3271.

"The Free Formulation: Linear Theory and Extensions with Applications to Tetrahedral Elements with Rotational Freedoms", G. Skeie, 1993:17, ISBN 82-7119-472-0, ISSN 0802-3271.

"Høyfast betongs motstand mot piggdekkslitasje. Analyse av resultater fra prøving i Veisliter'n",
T. Tveter, 1993:62, ISBN 82-7119-522-0, ISSN 0802-3271.

"A Nonlinear Finite Element Based on Free Formulation Theory for Analysis of Sandwich Structures", O. Aamlid, 1993:72, ISBN 82-7119-534-4, ISSN 0802-3271.

"The Effect of Curing Temperature and Silica Fume on Chloride Migration and Pore Structure of High Strength Concrete", C. J. Hauck, 1993:90, ISBN 82-7119-553-0, ISSN 0802-3271.

"Failure of Concrete under Compressive Strain Gradients",
G. Markeset, 1993:110, ISBN 82-7119-575-1, ISSN 0802-3271.

"An experimental study of internal tidal amphidromes in Vestfjorden",
J. H. Nilsen, 1994:39, ISBN 82-7119-640-5, ISSN 0802-3271.

"Structural analysis of oil wells with emphasis on conductor design",
H. Larsen, 1994:46, ISBN 82-7119-648-0, ISSN 0802-3271.

"Adaptive methods for non-linear finite element analysis of shell structures",
K. M. Okstad, 1994:66, ISBN 82-7119-670-7, ISSN 0802-3271.

"On constitutive modelling in nonlinear analysis of concrete structures",
O. Fyrileiv, 1994:115, ISBN 82-7119-725-8, ISSN 0802-3271.

"Fluctuating wind load and response of a line-like engineering structure with emphasis on

motion-induced wind forces",
J. Bogunovic Jakobsen, 1995:62, ISBN 82-7119-809-2, ISSN 0802-3271.

"An experimental study of beam-columns subjected to combined torsion, bending and axial actions", A. Aalberg, 1995:66, ISBN 82-7119-813-0, ISSN 0802-3271.

"Scaling and cracking in unsealed freeze/thaw testing of Portland cement and silica fume concretes", S. Jacobsen, 1995:101, ISBN 82-7119-851-3, ISSN 0802-3271.

"Damping of water waves by submerged vegetation. A case study of laminaria hyperborea",
A. M. Dubi, 1995:108, ISBN 82-7119-859-9, ISSN 0802-3271.

"The dynamics of a slope current in the Barents Sea",
Sheng Li, 1995:109, ISBN 82-7119-860-2, ISSN 0802-3271.

"Modellering av delmaterialenes betydning for betongens konsistens",
Ernst Mørtsell, 1996:12, ISBN 82-7119-894-7, ISSN 0802-3271.
"Bending of thin-walled aluminium extrusions",
Birgit Søvik Opheim, 1996:60, ISBN 82-7119-947-1, ISSN 0802-3271.

"Material modelling of aluminium for crashworthiness analysis",
Torodd Berstad, 1996:89, ISBN 82-7119-980-3, ISSN 0802-3271.

"Estimation of structural parameters from response measurements on submerged floating tunnels",
Rolf Magne Larssen, 1996:119, ISBN 82-471-0014-2, ISSN 0802-3271.

“Numerical modelling of plain and reinforced concrete by damage mechanics”,
Mario A. Polanco-Loria, 1997:20, ISBN 82-471-0049-5, ISSN 0802-3271.

“Nonlinear random vibrations - numerical analysis by path integration methods”,
Vibeke Moe, 1997:26, ISBN 82-471-0056-8, ISSN 0802-3271.

“Numerical prediction of vortex-induced vibration by the finite element method”,
Joar Martin Dalheim, 1997:63, ISBN 82-471-0096-7, ISSN 0802-3271.

“Time domain calculations of buffeting response for wind sensitive structures”,
Ketil Aas-Jakobsen, 1997:148, ISBN 82-471-0189-0, ISSN 0802-3271.

"A numerical study of flow about fixed and flexibly mounted circular cylinders",
Trond Stokka Meling, 1998:48, ISBN 82-471-0244-7, ISSN 0802-3271.

“Estimation of chloride penetration into concrete bridges in coastal areas”,
Per Egil Steen, 1998:89, ISBN 82-471-0290-0, ISSN 0802-3271.

“Stress-resultant material models for reinforced concrete plates and shells”,
Jan Arve Øverli, 1998:95, ISBN 82-471-0297-8, ISSN 0802-3271.

“Chloride binding in concrete. Effect of surrounding environment and concrete composition”,
Claus Kenneth Larsen, 1998:101, ISBN 82-471-0337-0, ISSN 0802-3271.

“Rotational capacity of aluminium alloy beams”,
Lars A. Moen, 1999:1, ISBN 82-471-0365-6, ISSN 0802-3271.

“Stretch Bending of Aluminium Extrusions”,
Arild H. Clausen, 1999:29, ISBN 82-471-0396-6, ISSN 0802-3271.

“Aluminium and Steel Beams under Concentrated Loading”,
Tore Tryland, 1999:30, ISBN 82-471-0397-4, ISSN 0802-3271.

"Engineering Models of Elastoplasticity and Fracture for Aluminium Alloys",
Odd-Geir Lademo, 1999:39, ISBN 82-471-0406-7, ISSN 0802-3271.

"Kapasitet og duktilitet av dybelforbindelser i trekonstruksjoner",
Jan Siem, 1999:46, ISBN 82-471-0414-8, ISSN 0802-3271.

“Etablering av distribuert ingeniørarbeid; Teknologiske og organisatoriske erfaringer fra en norsk ingeniørbedrift”, Lars Line, 1999:52, ISBN 82-471-0420-2, ISSN 0802-3271.

“Estimation of Earthquake-Induced Response”,
Símon Ólafsson, 1999:73, ISBN 82-471-0443-1, ISSN 0802-3271.

“Coastal Concrete Bridges: Moisture State, Chloride Permeability and Aging Effects”
Ragnhild Holen Relling, 1999:74, ISBN 82-471-0445-8, ISSN 0802-3271.

”Capacity Assessment of Titanium Pipes Subjected to Bending and External Pressure”,
Arve Bjørset, 1999:100, ISBN 82-471-0473-3, ISSN 0802-3271.

“Validation of Numerical Collapse Behaviour of Thin-Walled Corrugated Panels”,
Håvar Ilstad, 1999:101, ISBN 82-471-0474-1, ISSN 0802-3271.

“Strength and Ductility of Welded Structures in Aluminium Alloys”,
Miroslaw Matusiak, 1999:113, ISBN 82-471-0487-3, ISSN 0802-3271.

“Thermal Dilation and Autogenous Deformation as Driving Forces to Self-Induced Stresses in High Performance Concrete”,
Øyvind Bjøntegaard, 1999:121, ISBN 82-7984-002-8, ISSN 0802-3271.

“Some Aspects of Ski Base Sliding Friction and Ski Base Structure”,
Dag Anders Moldestad, 1999:137, ISBN 82-7984-019-2, ISSN 0802-3271.

"Electrode reactions and corrosion resistance for steel in mortar and concrete",
Roy Antonsen, 2000:10, ISBN 82-7984-030-3, ISSN 0802-3271.

"Hydro-Physical Conditions in Kelp Forests and the Effect on Wave Damping and Dune Erosion. A case study on Laminaria Hyperborea",
Stig Magnar Løvås, 2000:28, ISBN 82-7984-050-8, ISSN 0802-3271.

"Random Vibration and the Path Integral Method",
Christian Skaug, 2000:39, ISBN 82-7984-061-3, ISSN 0802-3271.

"Buckling and geometrical nonlinear beam-type analyses of timber structures",
Trond Even Eggen, 2000:56, ISBN 82-7984-081-8, ISSN 0802-3271.

”Structural Crashworthiness of Aluminium Foam-Based Components”,
Arve Grønsund Hanssen, 2000:76, ISBN 82-7984-102-4, ISSN 0809-103X.

“Measurements and simulations of the consolidation in first-year sea ice ridges, and some aspects of mechanical behaviour”, Knut V. Høyland, 2000:94, ISBN 82-7984-121-0, ISSN 0809-103X.

”Kinematics in Regular and Irregular Waves based on a Lagrangian Formulation”,
Svein Helge Gjøsund, 2000-86, ISBN 82-7984-112-1, ISSN 0809-103X.

”Self-Induced Cracking Problems in Hardening Concrete Structures”,
Daniela Bosnjak, 2000-121, ISBN 82-7984-151-2, ISSN 0809-103X.

"Ballistic Penetration and Perforation of Steel Plates",
Tore Børvik, 2000:124, ISBN 82-7984-154-7, ISSN 0809-103X

"Freeze-Thaw resistance of Concrete. Effect of: Curing Conditions, Moisture Exchange and Materials", Terje Finnerup Rønning, 2001:14, ISBN 82-7984-165-2, ISSN 0809-103X

"Structural behaviour of post tensioned concrete structures. Flat slab. Slabs on ground",
Steinar Trygstad, 2001:52, ISBN 82-471-5314-9, ISSN 0809-103X.

"Slipforming of Vertical Concrete Structures. Friction between concrete and slipform panel."
Kjell Tore Fosså, 2001:61, ISBN 82-471-5325-4, ISSN 0809-103X.